Mécano-biologie avec approche multiphasique de la croissance tumorale : application clinique au glioblastome IDH positif.

Stéphane Urcun

HESAM UNIVERSITÉ

UNIVERSITÉ DU LUXEMBOURG

Arts et Métiers Sciences et Technologies

ÉCOLE DOCTORALE SCIENCES ET MÉTIERS DE L'INGÉNIEUR
[IBHGC- Campus de Paris]

THESIS

présentée par : **Stéphane Urcun**
soutenue le : **15 mars 2022**

to obtain the degree of Doctor issued by :

École Nationale Supérieure d'Arts et Métiers

Speciality : **Biomedical engineering**

Faculté des Sciences, de Technologies et de Médecine du Luxembourg

Speciality : **Computational Mechanics**

Mechano-biology of tumor growth with the aim of clinical applications, a reactive multiphase poromechanical approach

Directors of thesis :
[SKALLI Wafa, BORDAS Stéphane P.A.]

Co-directors of thesis :
[SCIUME Giuseppe, ROHAN Pierre-Yves]

Jury

Mr Vittorio CRISTINI	Professor, Houston Methodist	President
Mrs Olga BARRERA	Ass. Professor, University of Oxford	Reviewer
Mr Alfio GRILLO	Ass. Professor, Politecnico di Torino	Reviewer
Mr Hector GOMEZ	Professor, Purdue University	Examiner
Mrs Wafa SKALLI	Professor emeritus, Arts et Métiers ParisTech	Examiner
Mr Stéphane BORDAS	Professor, Université du Luxembourg	Examiner
Mr Pierre-Yves ROHAN	Ass.professor, Arts et Métiers ParisTech	Examiner
Mr Giuseppe SCIUME	Ass. professor, Université de Bordeaux	Examiner

THÈSE

À ma mère

Abstract

We propose the modeling of glioblastoma isocitrate dehydrogenase wild-type (GBMwt) build on the following hypotheses: the brain tissue is a porous medium, the coupling of hypoxia consequences and mechanical interplay between extra-cellular matrix and tumor cells is the driver of the malignant evolution of the disease. In this thesis, a poromechanical model is developed with the aim of a clinical application in oncology. A review, with a large scope, is done on mechanical applications in clinical management of cancer. The model is first validated on *in vitro* experimental data of encapsulated multi-cellular spheroids. Then, a clinical collaboration is initiated with the Neuro-imaging center of Toulouse, and the targeted clinical application is the modeling of non-operable GBMwt. To this end, the model is first adapted to the specificity of brain tissue mechanics. Characteristic features of the disease are modeled: necrotic core, modified extra-cellular matrix production, emerging malignant phenotype and invasion. Clinical imaging data are pre-treated to inform the model in a patient specific basis. A proposition of modeling is provided with an evaluation against clinical data.

Acknowledgements

I warmly thank the team of my supervisors. My mentor, Giuseppe Sciumè, taught me poromechanics with patience and pedagogy. His scientific rigor accompanied by his benevolence was a major encounter. My co-supervisor, Pierre-Yves Rohan, provided me infallible help all along these three years. His enthusiasm and his maieutics were a beacon in the darkness, when doubts and difficulties overwhelmed me. The encounter with my supervisor Stéphane P.A. Bordas was fundamental for the formation of my scientific mind. He taught me how to write articles with the respect of the reader, how to present my research in congress with the respect of the audience. My supervisor Wafa Skalli, professor emeritus, did me the honor to be her student. Through her wise advice along these three years, she gave me the benefits of her rich carrier in clinical application of biomechanics.

I am particularly grateful to the clinical team, who dedicated their precious time to my research, especially during the difficult period of the pandemic. To Vincent Lubrano, neurosurgeon, who patiently advised me and shared with me his precious experience in glioma disease. To Tanguy Duval, for giving me advice on brain atlases and programming in neurology application. To Ruairidh Howells, for dedicating his time on segmentation and formatting the clinical data.

I owe a lot to all the experimenters who collaborated with us and shared their data. To Pierre Nassoy, for our excellent collaboration on cellular capsule technology which resulted in a research article. To Silvia Budday, for her kind comments during the World Congress of Computational Mechanics, and for accepting us to model her data of cortex tissue. To Lance Munn and to Davide Bigoni, for accepting us to reproduce their data on our articles.

I warmly thank all the colleagues and collaborators I met along the way of this thesis. Davide Baroli, who guided me in the jungle to Python libraries, who patiently taught me how to write clean codes. Guillermo Lorenzo, who did me the honor to be my co-author of our review article. His proficiency and his high standards are a model of me. Arnaud Mazier, for all our fruitful discussions on imaging-informed cancer modeling. Jacub Lengiewicz, for his high standards on scientific method, our discussions were very inspiring. Jack Hale, for his help in building FEniCS and Dolfin frameworks on the Iris cluster. To Vincent Le Maout, my first fellow in this thesis, thank you for your initiation in FEniCS and for your rich discussions. To Azita Ahmadi, for her kind guidance of my first steps in the academic world. To Henri Bertin, for his nice

discussions on soil poromechanics. To Jean-Luc Charles and Eric Ducasse, for their advice in teaching and for accepting me in their academic team. To Thomas Lavigne, for his proficiency and his curiosity about my work. To Meryem Abbad Andaloussi, welcome on board! I hope the transmission is going well. To Jean-Luc Barou and Florence Duville, thank you for your support in the difficult moments. To Muriel Ezan Boré and to Odile Marois, our administrative supports who, by their works, allow us for continuing our research in proper conditions.

Contents

List of Figures

List of Tables

Chapter 1

Introduction

L'échec, même répété, parait toujours nouveau,

alors que le succès, en se multipliant,

perd tout intérêt, tout attrait.

Cioran

Context and motivation of the thesis

The basis of this work is the reactive multiphase poromechanical model developed since 2013 by Sciumè *et al* in [214]. The porous system is modeled as a porous solid saturated by two or three fluid phases, interstitial fluid, healthy cells and tumor cells respectively. These fluids have their own constitutive relationships, designed by the same authors in [219]. The porous system mimics a living tissue by the addition of a reactive species, denoted nutrients, but solely considered as oxygen. Indeed, the acute deprivation of oxygen - also known as hypoxia*[1] - due to the tumor cells proliferation will cause the necrosis of the tumor phase, changing its properties. This model was enhanced in 2014 by the same authors with a deformable porous solid in [216], then allowing for modeling the interplay between extra-cellular matrix (ECM) and tumor cells. In [216], the model outputs have been qualitatively compared to *in vitro* experiments of Chignola *et al.* [50] and histological* cuts of skin cancer of Chung *et al.* [51], showing promising results. Additionally, by replacing the tumor phase by a non-proliferative cell phase under hypoxic condition, the model has been proposed to qualitatively reproduce the mechanism of diabetic foot in [218]. Thus, this model proved its potential in cancer modeling and translation in other tissue pathologies.

The motivation of this thesis is the further development of this modeling framework and its translation into a clinical context. We began with a wide state of the art of collaboration between mechanics and clinical oncology. The research

[1] All the terms with an * are in the clinical glossary section 2.5.2

was driven by two questions: which mechanical phenomena are of interest to predict the kinematics and kinetics of tumour growth? How to translate mechanical-based modeling into clinical applications? Regarding the first question, we selected the mechanically-inhibited tumor growth [107, 48, 4] and, as a consequence of stroma mechano-biology, the mechanically-induced phenotype switch [192, 17]. Regarding the second, we chose the image-informed modeling framework, firstly designed in 2002 by Swanson *et al.* in [239], enhanced by Yankeelov *et al.* since 2013 and thereafter intensively used [268, 259, 260, 111, 151, 122, 112]. During the first year of the thesis, we quantitatively validated the model against the *in vitro* experiment of Alessandri *et al.* in [4], termed as cellular capsule technology. With these first results in our hands, we started several attempts of clinical collaborations with research teams working on skin, prostate and endometrial cancers, without fulfillment. Then, we were extremely lucky to start a collaboration with the Toulouse Neuro-imaging Center and M.D. Lubrano, neurosurgeon. From this point, the aimed clinical application becomes the modeling of a non-operable glioblastoma* common subtype, the isocitrate dehydrogenase wild-type. At this stage, the SRAS-Cov2 pandemic started to impact the progress of our work. Imaging staff were transferred to pandemic-related tasks, nonessential clinical collaboration were shut down. During this period, our first move was to build a model of healthy brain tissue, by using literature [108, 59] and experiments [89, 31] to validate it. Hence, the disease was modeled within a porous medium, pre-calibrated for brain tissue. We hypothesized that two phenomena drive the malignant evolution of the disease: hypoxia and cell-ECM signaling. To assess patient-specific measurement, we adopted the imaging-informed framework. To build a code of image-informed modeling, we used public atlases [75]. M.D. Lubrano and his collaborators managed to provide us a patient imaging dataset with two time points, the first at diagnosis, the second after 6 weeks of concomitant radio-chemotherapy. This allowed for testing our hypotheses, now adapted to brain tissue, on hypoxia and cell-ECM interaction, and proposed a calibration of our model. This work was only a first step of the inclusion of poromechanics in patient-specific brain cancer modeling. We hope this inspiring framework will lead to new understanding of the physical description of cancer.

This thesis, by its very nature, is at the crossroads of different fields: physical and biological, mathematical, computational, and clinical. If interdisciplinarity is a common feature in cancer research, this work has its specific flavor, with poromechanics and stroma mechano-biology applied to brain cancer. Along this manuscript, we tried, as much as possible, to clearly present the various aspects of this subject. A glossary of clinical term is provided in section 2.5.2.

From the mathematical point of view, we chose to solve the coupled physical and biological system with the finite element method [52]. The weak form of the partial differential equations system was discretized in continuous Lagrange elements, the boundary conditions of the different cases were in depth studied. As an alternative proposition, the discontinuous approach -precisely the internal penalty method - was also developed. An example is provided in appendix A. The continuous method was chosen under the compromise of results accuracy and computational efficiency. The dynamic problems were solved by an implicit Euler scheme. Different schemes were tested and the solution sensitivity evaluated. The first order implicit Euler scheme appeared to be sufficient as the modeled phenomena had a very slow evolution in

time. Before the calibration of the model parameters, every problem was studied with a variance-based sensitivity analysis [210], namely Sobol indices. The choice of optimization algorithm - Newton-Raphson, conjugate gradient, among others - was then decided. After calibration, the parameters set was validated on an external dataset, if provided.

From the computational point of view, the choice of the finite element method opened a large panel of solvers. We chose the Python interface FEniCS [7] of C++ libraries aggregate denoted as Dolfin [149] for two reasons: i) any well-posed weak formulation can be easily coded in a Python script, ii) for draft codes or for small-scale domains, the FEniCS interface was sufficient. For large domains requiring parallelized codes, the C++ Dolfin libraries could be directly used. An end-to-end Python pipeline was designed to convert the clinical imaging data, in Nifti format, into 3D arrays using the NumPy library, and finally formatted for finite element computations. A tutorial of this process is available online[2].

The chosen case to be modeled was the non-operable glioblastoma* multiforme isocitrate dehydrogenase wild type (GBMwt). Non-operable case represents an opportunity to collect valuable datasets for accessing longitudinal data, hence forecasting the disease evolution, whereas in operable case, maximal resection is the standard of care [233]. GBM is an extremely aggressive brain tumor, almost 100% recurrent, with a median survival rate between 14 and 16 months and a 5-year survival rate around 5%. It also represents almost half of the primary brain tumor case. *De facto*, GBM is currently a major issue in neurosurgery. 90% of GBM are GBM IDH wild-type, the remaining 10% being termed IDH mutants. The IDH wild-type marker is critical in terms of prognosis*, the specificity of this GBM subtype was of great interest in view of our modeling hypotheses: hypoxic environment provokes the production, by the GBMwt cells, of a stiffer ECM [17], which increases the consequences of cell-ECM interplay. The modeling of the heterogeneous tissue in brain by multiphase poromechanics was a first task, followed by its calibration and validation on experimental data. The specificity of the IDH wild-type phenotype, *i.e.* its activation by the coupling of hypoxic stress and mechanical pressure, were modeled. Even non-operable, the patients are subjected to the concomitant radio-chemo-therapy, the second part of the standard of care defined by Stupp *et al.* in [233]. These phenomena and their parameters were added to an adapted version of the model.

Presentation of the manuscript

This manuscript is a cumulative thesis, chapters 2 to 5 are publications. This introduction, the chapter 6 "Perspective and future works", and the appendixes strictly belong to the thesis. The chapters follow the chronological order of the research. In the process of building a model of GBMwt, the chapter 4 constitutes pre-calibration of the poromechanical parameters of the brain tissue. The evaluation of some of our mechano-biological hypotheses - inhibiting pressure and necrosis induced by hypoxia - takes place in chapter 3 with *in vitro* experiments of tumor spheroids encapsulation. Chapter 5 contains our proposition of clinical modeling, *i.e.* the model is informed by the patient imaging data and hypotheses

[2] `https://www.youtube.com/watch?v=hkwK7zP4sas`

specific to the GBMwt - stiffer ECM production and tumor cells phenotype switch - are evaluated.

Chapter 2, "State of the art of mechanical applications in clinical oncology", is accepted for publication as a chapter in the book series Advances in Applied Mechanics. Despite an increasing interest in *in vitro* studies [235, 216, 88], poromechanics is, for now, an unusual framework in clinical oncology. Rare examples, as Frieboes *et al.* in [91] or Ehlers and Wagner in [73], are reported in this review. As a consequence, we were interested to enlarge the scope of the review to solid and fluid mechanics, especially on image-informed modeling. Since the seminal article of Yankeelov *et al.* in 2013 [268], image-informed modeling emerged as an exciting way to translate mechanical-based modeling to patient-specific clinically relevant simulations. Taking advantage of the progress of clinical imaging, we can now retrieve physical quantities required as inputs for mechanical models. This framework termed as image-informed mechanical-based modeling is now well-documented [111] and extensively used [47, 260, 151, 122, 112]. An entire section in the review is devoted to this framework. A last topic is treated in this chapter: the review of mechano-biology of cell-ECM interplay, with a focus on the works of Weaver *et al.* [256, 192, 17, 184], because of its major implication in our modeling. In the review, we show that the collaboration of the biological and mechanical approaches has led to promising advances in terms of modeling, experimental design and therapeutic targets.

Chapter 3, "*In vitro* poromechanical modeling of tumor growth", was published as a research article in PLOS One [247]. It is preceded by an introduction to poromechanics, which presents the basic notion for the reader who would not be familiar with this field. The article constitutes the main part of the first year's thesis, before the choice of the clinical application. We were aiming to validate a first version of the model on experimental data, *i.e.* calibrate the parameters on one experimental dataset and validate them on an external dataset. The sensitivity and the correlation of the model parameters on hypoxia and compressive stress are also explored through Sobol indices analysis. To test these mechano-biological hypotheses, the experimental setup of Alessandri *et al.* [4] was ideal. With the same cell line, they designed free and encapsulated growth of multi-cellular tumor spheroids (MCTS), free growth being the control group. Porous alginate shells were used to encapsulated MCTS. The porosity of alginate allowing an optimum flow of nutrients, the MCTS continue to grow until it reaches the capsule diameter. The alginate being a deformable, isotropic and elastic material, the exerted pressure by the MCTS can be analytically retrieved from the alginate deformation. Thus, this setup allowed us for studying the force exerted by MCTS and the impact on its growth of the compressive stress, as a basic action-reaction principle. Some free and encapsulated MCTS being stained, we could also evaluate the distribution of the necrotic state in the model results. This was a proof-of-concept for our model, for its physical relevancy, for the computational framework, and for the validation process.

Chapter 4, "*Ex vivo* cortex tissue poromechanical modeling", was published as a research article in the Journal of Mechanical Behavior of Biomedical Material [248]. The interested reader will find a recent and comprehensive review of

brain tissue mechanics in Budday *et al.* [34]. Starting from the same core as chapter 3, a two-phase flow porous medium is proposed, but without the equation of oxygen conservation, since we modeled *ex vivo* cases. Based on experimental literature, we defined physical acceptable range for a subgroup of the model parameters. This initial parameter setting was tested on two experimental sets: a confined compression, the consolidation test of Franceschini *et al.* [89] and an unconfined compression, an indentation test of Budday *et al.* [31] ($300\,\mu$m depth at $300\,\mu$m/s). After the same process as chapter 3 (variance-based sensitivity analysis and calibration), the parameter values were validated on three other indentation tests of [31], different in diameters and load rates.

Chapter 5, "In vivo image-informed glioblastoma* multiforme modeling" will be submitted to a journal within the next months. We hypothesized that two phenomena drive the malignant evolution of the disease: hypoxia and cell-ECM interaction. We proposed a patient-specific non-operable glioblastoma model consisting of a porous medium, pre-calibrated for brain tissue.To assess patient-specific measurement, we adopted the imaging-informed framework. The same clinical imaging dataset (MRI methods and segmentation), at two time points, was used to initialize and calibrate the parameters. The first point was the pre-operative checkpoint and the second was performed after 6 cycles of concomitant radio-chemotherapy. A last subset of parameters, which do not belong to brain tissue material properties and can not be assessed by imaging, was fixed by clinical and experimental literature. After calibration, we obtained a simulated tumor with a 2.7% error in volume, comparatively to the patient tumor, and which overlaps 81.7% of the patient tumor. Several qualitative results, mechanical inhibition of tumor growth and malignant progression due to cell-ECM interaction are also presented.

Chapter 6, "Perspective and future works", emphasizes the main findings of the thesis as a first step of the inclusion of reactive multiphase poromechanical framework in patient-specific tumor forecasting and treatment response. Possible evolution of the modeling and the computational framework are proposed.

The appendices of this thesis take up half of its volume, they are of critical importance for the transmission of this work. From chapters 3 to 5, the corresponding Python and C++ commented codes are provided. They are augmented with physical and analytical examples, weak formulations and boundary conditions. The codes for designing the meshes are also provided for the case of encapsulated spheroid and for the pre-treatment of clinical data. All the codes of appendices A, B, C can be adapted to any experimental encapsulation (diameter and thickness), any indentation (diameter, load rate and relaxation) or consolidation (sample size and load). The first part of the appendix D provided the framework for patient imaging data pre-treatment, which can be adapted to any patient-specific case. These codes can be provided upon request. All the libraries used in these appendices are free and open-source.

Chapter 2

State of the art of mechanical applications in oncology

This work was accepted for publication in 2021 in the book series Advances in Applied Mechanics.

Contribution (CRediT author statement)

Conceptualization, Methodology, Investigation, Writing – original draft.

Oncology and mechanics: landmark studies and promising clinical applications

Urcun Stéphane[1,2,3], Guillermo Lorenzo[4,5], Davide Baroli[6,7], Rohan Pierre-Yves[1], Sciumè Giuseppe[3], Vincent Lubrano[8], Skalli Wafa[1], Bordas Stéphane P.A.[2*],

1 Institut de Biomécanique Humaine Georges Charpak, Arts et Metiers Institute of Technology, Paris, France

2 Institute for Computational Engineering Sciences, Department of Engineering Sciences, Faculté des Sciences de la Technologie et de Médecine, Université du Luxembourg, Campus Belval, Luxembourg

3 Institut de Mécanique et d'Ingénierie, Université de Bordeaux, Talence, France

4 Oden Institute for Computational Engineering and Sciences, The University of Texas at Austin, Austin

5 Department of Civil Engineering and Architecture, University of Pavia

6 Università della Svizzera Italiana, Euler Institute, Lugano

7 Aachen Institute for Advanced Study in Computational Engineering Science, Rheinisch-Westfälische Technische Hochschule Aachen, Aachen

8 Hôpital Pierre-Paul Riquet, Toulouse

* stephane.bordas@alum.northwestern.edu

Abstract

Clinical management of cancer has continuously evolved for several decades. Biochemical, molecular and genomics approaches have brought and still bring numerous insights into cancerous diseases. It is now accepted that some phenomena, allowed by favorable biological conditions, emerge *via* mechanical signaling at the cellular scale and *via* mechanical forces at the macroscale. Mechanical phenomena in cancer have been studied in-depth over the last decades, and their clinical applications are starting to be understood. If numerous models and experimental setups have been proposed, only a few have led to clinical applications. The objective of this contribution is to propose to review a large scope of mechanical findings which have consequences on the clinical management of cancer. This review is mainly addressed to doctoral candidates in mechanics and applied mathematics who are faced with the challenge of the mechanics-based modeling of cancer with the aim of clinical applications. We show that the collaboration of the biological and mechanical approaches has led to promising advances in terms of modeling, experimental design and therapeutic targets. Additionally, a specific focus is brought on imaging-informed mechanics-based models, which we believe can further the development of new therapeutic targets and the advent of personalized medicine. We study in detail several successful workflows on patient-specific targeted therapies based on mechanistic modeling.

Introduction

Cancer is one name for numerous diseases. Each location leads to a unique physiological framework; within each location, different forms of cancer are identified, and this diversity is subdivided toward patient specific cases. Additionally to individual diversity, cancer should be considered as a multiscale disease at the cellular and sub-cellular scales, where the micro-environment recruitment by tumor cells and genetic instabilities play an equally important role [161, 103].

Despite the challenges posed by the heterogeneous and multiscale nature of cancer diseases, the recent decades have witnessed much progress in their clinical management, as shown in the global cancer statistics for 2020 [238]. Firstly, there has been a reduction in the incidence thanks to the prevention of risk factors present in the lifestyle of transitioned countries, such as tobacco, alcohol and obesity. These risk factors participate in the most common cancers of the lung, colorectal, liver, stomach and bladder. Cancer incidence has also been reduced by treatment of biological causes like bacterial and virus infection, hormone exposure, poor hygiene or flawed food storage. Before these treatments, these factors contributed to cancers of the lower stomach, bladder, liver, breast and cervix. Secondly, cancer mortality has also decreased thanks to the multiple advances in clinical management of tumors, such as the early detection of prostate and breast cancers, treatment breakthroughs in breast cancer and metastatic melanoma, and active surveillance in various cancers (for instance, lung,

breast and thyroid). In addition to prevention and biological management, genetics has brought considerable insights and effects on treatment outcomes in specific locations (*e.g.* breast cancer stem cells [209], lung biomarkers [254]). Thanks to the recent advances in the understanding and treatment of cancer, many recent battles have been won against cancer. Childhood cancer (mostly leukemia) mortality rates have been halved in thirty years despite an increasing incidence [227]. Cervical cancer is now considered almost 100% preventable, thanks to the human papillomavirus vaccine and population screening [238]. Early detection of prostate cancer has lowered the mortality by 21% in ten years [249]. Thanks to early detection and breakthroughs in the treatment of breast cancer (inhibition of human epidermal growth factor receptor 2 (HER2) by monoclonal antibodies [77]), 5-year survival reaches 90% - all stages*[1] averaged - since 2014 in high-income countries.

In spite of this immense progress, cancer remains an important burden for societies worldwide. The changing lifestyle of economically transitioning countries will increase their relative cancer incidence. Some cancers still have a poor prognosis* (pancreas) or their etiology* is poorly understood (prostate or thyroid), with the exception of environmental and genetic risk factors. The authors of [238] predicted that by 2025 the worldwide incidence of pancreatic cancer will be higher than that of breast cancer. There is currently no effective treatment, and pancreatic adenocarcinoma* has a 5-year survival rate of only 9% [199]. Strongly correlated with socio-economic development, the incidence of colorectal cancer will rise in the economically transitioning countries within the next decades, and probably cause important damage. In economically transitioned countries, where screening and treatments are in the state of the art, the 5-year survival rate is near 90% for benign stage* I, but below 10% for metastatic stage* IV [198].

The biological approach, in its broad sense including biochemistry, molecular, genomics and phenotypic* aspects, has brought and still brings numerous insights into cancerous diseases, which have contributed to the aforementioned advances in the clinical management of these pathologies. The mechanical approach, at the tissue and cellular levels, includes solid, fluid, porous medium and electrophysics show effective ways to clinical applications in oncology. In this review, we understand mechanics by its two common definitions: *the science of systems* which are subjected to the fundamental principles of Newtonian mechanics and *the science of building machine*, as the design of experimental setups is from end to end a critical part of the clinical applications we present.

From the experimental side, following a biological approach and ignoring structural mechanical effects could conceal some phenomena. For instance, the wound healing, chronic fibrosis and cancer progression 'triad', comprehensively reviewed by Rybinski *et al.* in [206], implies that stroma* mechanics are a fundamental part of many cancers progression. The mechanical phenomena, implied in stroma* mechano-biology, cannot be reproduced in classical Petri dish 2D cultures [62]. The structural effects of these interplay emerge only in 3D cell cultures, as multi-cellular tumor spheroids [4]. Sev-

[1] all the words marked with a * are in a glossary at the end of this review

eral phenomena, allowed by favorable biological conditions (genetic, immune or environmental), emerge *via* mechanical signaling at the cell's scale and *via* mechanical forces at the macroscale: epithelial* to mesenchymal* transition (EMT) [200, 19], metastatic cell advection by lymphatic and blood fluxes [86], or tumor cell growth inhibition and necrosis* induced by mechanical stress [4, 48]. Among complementary approaches of cancer description, mechanics is now well accepted. For four decades, mechanical phenomena that emerge from cancer have been widely studied: in 2014 a seminal review was produced by Jain *et al.* [119] for the meso and macroscale, and at the cell scale, a recent review has been provided by Northcott *et al.* [184]. In 2020, the review of Jain *et al.* has been augmented by Nia *et al.* [180] to encompass several new multiscale phenomena. This long-term research has matured enough to provide clinical applications and some inspiring examples are given in section 2.3.

It is now established that mechanical stress influences tumor growth, as shown by a range of sources from early *in vitro* studies [107] in 1997 to encapsulated multi-cellular spheroids [4]. This fundamental mechanism is explained in section 2.1.1. Computational fluid dynamics (CFD) describes viscous flow in compressible vessels [78] and is the basis of the design of microfluidic devices to isolate metastatic cells in blood samples [86]. Already effective clinical applications of CFD are presented section 2.3.2. Stroma* mechano-biology, focusing on the extra-cellular matrix* (ECM), fibroblasts* and their interplay with tumor cells, has been an active research field for several years (reviewed in [184], *in vitro* [172], [192], [156], and *in vivo* [19]). These investigations, presented section 2.1.2, enable the design of new targeted drugs, such as focal adhesion* kinases (FAKs) inhibitor [123], and a new clinical prognosis* tool [19], which are presented section 2.3.1. The more mature mechanical field with experimental devices applied to oncology in the physics of electricity. In this review, we will mainly focus on the non-thermal irreversible electroporation. The reader will find the history of this field in the book chapter of Rolong *et al.* [204]. Since the first landmark study in animal models, published in 1957 [236], irreversible electroporation has evolved to a well-established clinical practice for unresectable tumors. Recent developments led to the coupling of irreversible electroporation and immunotherapy with promising clinical applications in pancreatic cancer [144]. Section 2.3.3 of clinical applications of electrophysics is complemented by the presentation of a new paradigm: tumor-treating fields, which open promising opportunities in the standard of care of glioblastoma* multiforme.

Mechanical-based modeling considers the cancer dynamics as a physical system subjected to the fundamental principles, as balance laws. In solid mechanics, the *in vitro* findings of tumor growth inhibition now play a part in patient-specific modeling [151, 122, 1]. As a wide majority of living tissue may be modeled as a composite system of fluids and solids, with a variable permeability, they can be described by poromechanics. This strong coupling of a solid network of fibers saturated by fluids can describe permeable tissue, such as pancreas, liver, brain or lymph node. In this modeling framework, the infiltration of tumor cells or the diffusion of drugs within the tissue can be explicitly modeled *in vitro* [137, 216] and *in vivo* [91, 73, 217]. This emerging framework is presented in section 2.1.3. The interested reader will find in the supporting information (section 2.5) a brief presentation of the constitutive equations of the tumor growth, its different inhibitions

and specificity of poromechanics.

The progress in the understanding of the multiscale mechanisms, and the numerous hypotheses of mathematical models, have led to a consequent increase of potential therapeutic targets. But these advances created new problems: comprehensive clinical trials or patient adapted therapeutic scenario become virtually impossible, the number of parameters to control being overwhelming. Thus, the necessity appears of a systemic *in silico* exploration of therapeutic targets and patient scenarii against clinical evidence. To address this challenge, tumor forecasting has emerged as a viable option [153]. This strategy combines the integration of patient-specific standard clinical and imaging data with biomechanical models to predict the growth and treatment response for individual patients via computer simulations. Indeed, this approach can be compared to the well-established methods of weather forecasting. Since the 2010s, progress in medical imaging has enabled a wide range of translational advances for biomechanical modeling of the growth and therapeutic response of tumors. As claimed in the seminal paper of Yankeelov *et al.* in 2013 [268]: "Magnetic resonance imaging (MRI) and positron emission tomography (PET) have matured to the point where they offer patient-specific measures of tumor status at the physiological, cellular, and molecular levels". Patient-specific clinical data can give information at the gene scale, the micro-scale (cells and capillaries) and the macro-scale. Hence multi-scale models can be initialized by clinical data.

The association of imaging-informed modeling and computational mechanics brings notable advantages on a patient-specific basis, for instance a 3D MRI can be converted into a computational domain, and its segmentation into subdomains. Multi-parametric MRI allows for the monitoring and quantification of many properties, such as fluid proportion, cellular density, cell metabolism and, using dynamic contrast enhanced MRI (DCE-MRI), dynamic physical quantities such as the diffusion of chemical species and the vascular permeability. Since a 3D MRI can be converted into a computational domain, the patient-specific forecast can be directly compared against further clinical imaging data. The clinical imaging methods that can be used within this framework are presented section 2.2.1. Imaging-informed models of cancer growth and therapeutic response can be directly used in the clinic, end-to-end. Model validation can also be assessed using a combination of the same types of imaging and clinical data used for initialization and parameter identification, but collected at one or multiple posterior dates during the course of tumor monitoring or treatment (for instance, see [122, 111]). Detailed workflows of imaging-informed mechanical-based are provided section 2.2.2.

This review specifically aims to present the process by which mechanics can step in clinical management of cancer. We divided the review into three topics:

1. Pre-clinical studies, *in vitro*, *in silico* or in an animal model. Mechanical phenomena or mechanical therapeutic targets can be tested in isolation from their complex micro-environment. These studies also facilitate the collection of wealth of data to calibrate and validate biomechanical models describing such phenomena and therapies;

2. Patient-specific tumor forecasting. Computational mechanics can be used as a diagnostic, staging* and prognostic tool. This section is specifically designed for students;

3. Clinical applications on cancer management directly derived from mechanical findings in cellular mechano-biology, fluid mechanics, and electrophysics.

For each topic, we recommend further specific reviews for the interested reader. At the beginning of each section, we present the major findings, methods and remaining challenges. At the end of each section, we provide a set of short statements to summarize the topic. The review ends with supplementary information in section 2.5. It contains an introduction to the different modeling frameworks, a glossary of clinical terms, and a list of acronyms.

2.1 Pre-clinical studies

In vitro, *in silico* and animal models studies share the same goal of reducing the complexity of cancer phenomena. These simplifications naturally limit the scope of these studies. Nevertheless, some of them have led to new therapeutic targets, which are through clinical trials. We present three facets of mechanical understandings provided by pre-clinical studies: mechanical inhibition of the tumor growth, stroma* mechano-biology and poromechanical modeling of tumor tissue. For each subject, we selected a few studies which clearly expose the mechanical phenomena at play.

2.1.1 Growth inhibited by mechanical stress

In ancient Greece, the palpation of stiffened tumor tissue was one of the only accessible diagnosis tools. This abnormal stiffening is one of the results of mechanical stress concentration. In 1997, the *in vitro* study of Helmlinger *et al.* [107] unveiled part of these mechanisms: high mechanical stress inhibits tumor growth. Elements of the modeling of this phenomenon are briefly presented in the supplementary information (section A). Nowadays, these results could have consequences on treatment management of solid tumors in clinics, such as prostate [151] or breast [122] cancers (see section 2.2.2). The relationships between mechanical stress and tumor growth are complex and non-linear. If a cell line is subjected to a mechanical load considerably higher than its usual osmotic pressure, it will almost certainly lead to a growth inhibition. We here select few examples, each with its specific mechanism:

- non-hypoxic* driven apoptosis* by Cheng *et al.* in 2009 [48] (*in vitro*)
- smooth confinement by spheroid encapsulation by Alessandri *et al.* in 2013 [4] (*in vitro*)
- growth inhibition applied as treatment before surgery by Brossel *et al.* in 2016 [28] (in animal models)

The interested reader could peruse the sections devoted to this topic in the reviews of Jain *et al.* in [119] and Nia *et al.* in [180].

Non-hypoxic* driven apoptosis* Spheroid growth inhibition in agarose gel is a well-known *in vitro* experimental protocol, enhanced by Cheng *et al.* in 2009 [48]. The tumor spheroids are embedded with fluorescent micro-beads in agarose gel and the 3D distribution of micro-beads surrounding growing spheroids is recorded using confocal microscopy. The change in micro-bead density is converted to strain in the gel, thus the compressive stress around the spheroids can be estimated. There is a strong correlation between the solid stress distribution and spheroid shape. It has been shown that if compressed, spheroids overexpress anti-apoptotic* genes [192]. However, regions of high mechanical stress induce apoptotic* cell death (proliferating and necrotic* cells in spheroids were detected with a proliferative cell fluorescence marker, see Figure 2.1A). The important implication if this result is that apoptosis* via the mitochondrial pathway, induced by compressive stress, may be involved in tumor dormancy, in which tumor growth is constrained by the balance of apoptosis* and proliferation.

Smooth confinement by spheroid encapsulation Cellular capsule technology is an *in vitro* experimental protocol developed in [4] where tumor spheroids were cultured within spherical porous alginate capsules. The capsules are generated by co-extrusion using a 3D printed device and the alginate pore's size allows a free flow of nutrients. The capsule dilatation exhibits an elastic deformation with negligible plasticity and no hysteresis. As their size and thickness can be precisely controlled and alginate gel has isotropic and incompressible properties, the internal pressure can be analytically retrieved from the capsule deformation. Hence, when the tumor spheroid comes in contact with the inner wall, the capsule works as a mechanosensor. From their deformation, one can retrieve the stress state within the tumor spheroids.
In this respect, the post-confluent growing tumor can be regarded as a tumor model that grows against the surrounding tissues and organs. A digital twin of this technology was created through multiphase poromechanical modeling by Urcun *et al.* in [247]. It showed that a poromechanical framework is capable of reproduced both the capsule evolution and its inner structure.

Growth inhibition applied as treatment before surgery Gradient of magnetic field is an experimental protocol developed in [28] to show, *in vivo*, the effect of a mechanically constrained tumor growth. The human breast cancer cell line, MDA MB 231, admixed with ferric nanoparticles is grafted subcutaneously in nude mice. Two magnets located on either side of the tumor create a gradient in the magnetic field, acting on the nanoparticles. Through their reaction, the magnetic energy is transformed into mechanical energy, thereby applying a biomechanical stress to the tumor. The mice are divided into four groups. The first group is subjected to a 2-hour exposure per day to a magnetic field gradient for 21 days. The three other groups are control groups: group 2 has a tumor with nanoparticles without exposure to a magnetic field, group 3 has a tumor without nanoparticles but with the same 21 days treatment as group 1, and group 4 has a tumor without nanoparticles and without treatment. All mice are sacrificed on Day 74.
There was a significant difference of 61% between the median volume of treated tumors and untreated controls in the mice measured up to Day 74. This demonstration of the effect of stress on tumor growth *in vivo* suggests that biomechanical intervention may have a high translational potential as a therapy in locally advanced tumors (stage* II-III). To

our knowledge, this experiment is not yet modeled by a mechanical system.

Mechanically-induced inhibition of tumor growth is a well-known phenomenon that has consequences not only on *in vitro* findings, but also *in vivo* modeling (see section 2.2.2). Moreover, the effect of mechanical stress can also be described at the cell's scale, where interaction between fibrous tissue and carcinoma* cells is a common situation. This microscale description leads to critical *in vitro* findings and to new clinical applications (see section 2.3.1).

2.1.2 Stroma mechano-biology

The influence of the tumor microenvironment on disease evolution has become central in cancer research [124]. We focus here on a small part - but critical from the mechanical point of view - of the microenvironment: stroma* cells, precisely fibroblasts*, and ECM. Generally speaking, fibroblasts* associated with tumor cells will lead to a modified ECM. This ECM is denser and stiffer, due to the abnormal collagen production of these fibroblasts* [182]. As the tumor grows and invades the surrounding tissue, the stroma* interplay with tumor cells dramatically changes. The increase of the mechanical stress due to the proliferation of the tumor cells and to the stiffer ECM will lead, at the cell's scale, to internal and external modifications. In other words, mechanical stress leads to a modification of the tumor cells phenotype* [192]. This phenotype*'s switch depends on the cancerous cell line, so may take various expressions. We can list several frequently encountered properties within these cell lines:

- enhanced tumor cell contractility, *i.e.* the cell's mobility is increased;
- the polarity of the tumor cell cytoskeleton is altered, which leads to 'star-shaped' cells, more adapted to a dense environment (see Figure 2.1B);
- inhibition of the tumor cell apoptosis*, since the mechanical stress is maintained, the programmed death of cells is stopped;
- alterations on ECM mechanical properties and architecture. The production of collagen-rich ECM by fibroblasts and matrix metalloproteinase - enzyme which degrades ECM - by cancerous cells deregulates the composition and the architecture of the ECM.

These changes are of critical importance for the disease evolution, as invasiveness and therapy resistance. They also constitute new and promising therapeutic targets, which are exposed in section 2.3.1. The interested reader would peruse the review of cellular mechano-biology of cancer by Northcott *et al.* in [184].

Mechanical stress, integrin and malignant phenotype have been studied by Paszek *et al.* in 2005 [192]. Abnormal tissue stiffness has been historically associated with tumors and, nowadays, breast cancer patients with stiff fibrosis - an excessive activity of fibroblasts - are known to have poor prognosis* [58]. The authors of [192] lead unconfined compression

tests by indentors on both sane and malignant mammalian tissues, mammalian epithelial* cells and fibroblasts*. The samples are associated to collagen gels of various stiffnesses, from $170\,\text{Pa}$ to $1.2\,\text{kPa}$. This range, at its lower bound, corresponds to the common stiffness of adipose mammalian tissue and, at its upper bound, to fibrosis. The cell colonies evolve accordingly to the stiffness of their surrounding environment (for the mammalian epithelial* cell case, see Figure 2.1B, stiffness range from left to right). The differences between these evolution show, *in vitro*, the phenotype*'s switch described at the beginning of the section. Moreover, the authors of [192] expose the key phenomenon involved in the mechanical stress signaling. Their study emphasizes the critical role of $\beta 1$ integrin (wild-type and mutant) in the abnormal evolution in every kind of sample. Integrin is a transmembrane ECM receptor which functions as a mechanotransducer. At the outer surface of the cell's membrane, the integrin protein is bent by the mechanical compression of the external medium. This deformation provokes, in the inner cell's medium, chemical reactions which precede all the biological manifestation of abnormal growth. If the mechanical downstream signaling - the inner chemical reaction - is maintained for several days, an altered phenotype will emerge. Two main mechanisms, belonging to the cellular internal medium, are exposed:

- the Rho-dependent cytoskeletal tension. This mechanism is involved in mesenchymal* stem cell differentiation. Without the signaling of cytoskeletal proteins as integrin, a mesenchymal* stem cell could evolve into a round-shaped adipose cell. If this alternate cytoskeletal tension is activated, the stem cells will adopt a 'spread' shape characteristic of bone cells. The reader is referred to the work of McBeath *et al.* in [163] for a detailed description.

- the epidermal growth factor(EGF)-transformed epithelia. EGF signaling plays a critical role in the initiation of the epithelial* to mesenchymal* transition (EMT). EMT is the deregulation of the highly organized epithelial tissue and is characteristic of malignant carcinoma*. EGF is a transmembrane protein which is responsible for the downregulation of E-cadherin. And E-cadherin, like integrin, is transmembrane protein responsible for cell adhesion. The downregulation of E-cadherin implies an upregulation of the integrin adhesion. This upregulation will lead to the clustering of integrin on the cell membrane and deregulation of focal adhesions*. This specific phenomenon constitutes a new therapeutic target treated section 2.3.1. The interested reader is referred to the work of Lindsey *et al.* in [145], for the specific role of EGF in this phenomenon.

In the last part of their experiment, Paszek *et al.* shows that the inhibition of $\beta 1$ integrin or EGF signaling can revert to the malignant phenotype expressed in the cell-lines undergoing fibrosis condition. This early *in vitro* study pointed out potential therapeutic targets in the malignant evolution of carcinoma*.

Whatever the scale of interest of these phenomena, macro and micro, they share a common interplay between fluids, solids, and biochemical reactions. Poromechanics allows for modeling the chemical agent transport by the fluids, though the solids. To explicitly model this complex interplay, poromechanics emerges as particularly adapted framework.

2.1.3 Reactive poromechanics

This framework allows for explicitly modeling fibrous tissue, cells and surroundings fluids into a strongly coupled physical system. Used since the XIXth century in soil mechanics, poromechanics now emerges as a new framework for living tissue modeling (see *Encyclodedia of biomedical engineering*, chapter *Poroelasticity of living tissue* [159]). In poromechanical modeling, the tumor system is considered as a multiphase continuum: a solid scaffold in which and through which fluids flow. This framework is briefly presented in the supplementary information section A. The flows are driven by pressure gradient, and subjected to the ratio of the solid's permeability under the dynamic viscosity of the fluids. This relationship, in its usual form, is known as Darcy's law. The solid scaffold may be considered as rigid or deformable. If it is deformable, the momentum conservation of the porous system is composed of both fluids contributions (usually isostatic pressure) and solid contribution (elastic, hyperelastic, ...). Living tissue modeling implies reactive biochemical agents, which can be produced or absorbed by both solid and fluid components, and are subjected to advection-diffusion equations. This complete system is denoted as a reactive porous medium. We highlight the potential of this framework with two pre-clinical examples:

- Modeling drug resistance in Non-Hodgkin's lymphoma*, validated by histological* cuts. Tumor inner structures, accordingly to the cell lines, are accurately modeled by Frieboes *et al.* in [91] (animal model);
- Modeling drug delivery in brain by multi-compartment porous medium. In this example, the solid scaffold is deformable. Provide several qualitative results in anisotropic diffusion and pressure interplay in brain tissue, by Ehlers and Wagner in [73] (*in silico*).

Modeling drug resistance in Non-Hodgkin's lymphoma* In the experiment reproduced by Frieboes *et al.* in [91] two cell lines of lymphoma* are injected into two groups of mice. The first cell line is drug-resistant, thereafter denoted p53, and the other is drug-sensitive, denoted Arf. On day 0, five histological sections, equally distributed in space, are performed in three tumors of each type, extracted from sacrificed mice. The stainings (H&E, Ki-67, HIF-1α among others) give cell viability, necrosis*, proliferation, apoptosis*, oxygen diffusion and blood vessel density. These quantities are used to calibrate the model parameters. On day 21, the observations are made *in vivo* by intravital microscopy.
Frieboes *et al.* build a mechanical model belonging to the hybrid category. In mechanical-based modeling, one can distinguish three categories: continuous, discrete and hybrid. Continuous - or homogenized - modeling consider the phenomena at a sufficiently large scale to hypothesize the absence of strong discontinuities within the modeled object. Conversely, the working hypotheses of discrete modeling are at the cell's scale, and each cell - also denoted agent - has its own characteristics, with possible discontinuities between the cells. While continuous modeling, by its homogenization, implies a controlled loss of information, the computational cost of discrete modeling becomes prohibitive as the number of cells grows. Hybrid modeling, a sort of multi-scale modeling strategy, attempts to make the best of both worlds.
The hybrid system, at the lymph node scale, is governed by advection-diffusion within a continuous domain. Here, this

domain is a porous medium, say the tumor cell infiltration within the extra-vascular space is governed by Darcy's law. However, the system parameters are calibrated with information on the cell's scale through histological staining and intravital microscopy. This protocol was described in 2012 by Macklin *et al.* [157] and applied on ductal adenocarcinoma* in situ (a precursor of invasive breast cancer).

The following experimental results are retrieved from the model:

- both types of tumors reach the same size within the lymph node: 5.2 ± 0.5 mm diameter.
- their inner structures of the tumor are different, according to their cell-line. Arf cell-line tumor is denser in the peripheral region, contrary to p53. The high core density of p53 cell-line tumor could be associated with its drug resistance, by decreasing the penetration of chemical agent. The p53 cell-line has a 4-fold higher density of endothelial cells - cells constituting the wall to the blood vessels - in the core of the tumor than the Arf cell-line. The p53 proliferating cells fraction is 2-fold higher than the Arf cell-line. Hypoxia* is higher in the peripheral region of the p53 tumor. The apoptotic p53 cell density in the whole tumor is 2-fold higher than the Arf, suggesting a non-hypoxia* driven apoptosis* in the p53 cell line.

These rich results show the power of this poromechanical multi-scale approach, which could bring considerable insights into *in vivo* modeling.

Modeling drug delivery in brain by multi-compartment porous medium Brain tumors, especially glioblastoma*, are still a challenge from the surgery, therapy and modeling points of view. Since 2005, the protocol presented by Stupp *et al.* in [233] is the only glioblastoma* standard of care. It prescribed maximum surgical resection followed by concomitant radio-chemo-therapy for 6 weeks and chemotherapy maintenance during 6 or 12 months. Nevertheless, the median survival is only 16 months and the 5-year survival remains at 5%.

Invasive drug delivery is an additional way to decrease the tumor progression, recurrence, and resistance (for instance, see the Gliadel wafers [266]). The blood-brain barrier is not permeable enough to ensure a proper drug delivery by intra-venous application, hence perfusion by catheter directly into the brain parenchyma* is needed. During resection of the tumor, the surgeon drills small holes into the skull and place infusion catheters directly into the extra-vascular space of the parenchyma*.

In surgical planning software, solutions are already proposed for the simulation of the chemical agent diffusion by the catheter. The authors of [73] propose to improve these simulations by taking into account the porous interplay of the brain and its heterogeneous permeability and diffusion. W. Ehlers and A. Wagner are the founders of a recent theory of porous medium [72] dedicated to this application. They also worked on model reduction for clinical applications [82]. In [73], they model the brain parenchyma* as a porous medium with two separated fluid compartments: blood and interstitial fluid.

Grey matter regions may be considered isotropic in terms of permeability and diffusion. Experimental observations of white matter tracts show anisotropy in permeability and diffusion [120]. The authors assume, as Tuch *et al.* in [244], that white

matter tracts directions provide the eigenvectors of anisotropy. These directions can be recovered by the DTI MRI method (see section 2.2.1, paragraph *Imaging methods and physical quantities*). The imaging data of this method are leveraged and used to set, on a tensorial basis, the heterogeneous permeability and diffusion of the simulation. The other material properties come from the literature but, as indicated by the authors, they could be provided by other MRI methods.
The authors do not pretend clinical relevance but propose possible interpretations of their numerical results. They simulate 2 catheter flows: 0.3 and $0.6\,\mathrm{ml}\cdot\mathrm{h}^{-1}$. They retrieve for the case of $0.6\,\mathrm{ml}\cdot\mathrm{h}^{-1}$, in accordance with *in vivo* data, an excess of 1.1kPa ($+8$mmHg) in interstitial fluid pressure, which could be life threatening. Due to the interplay between the solid scaffold and the inner fluid, they found that a higher infusion surface is obtained with a constant application rate. Finally, due to the insertion of the catheter, the permeability of the damaged tissue dramatically increases. In the simulation, this provokes back-flows along the catheter shaft and this phenomenon is also acknowledged *in vivo*. Elhers *et al.* suggest that the porous modeling of the brain will help to gain mechanical insights in surgical and therapy management of glioblastoma*.

This last example is in a pivotal position between the pre-clinical section and the patient-specific forecasting section 2.2. Even if it does not pretend clinical relevance, it shares common features presented section 2.2:

- the use of patient imaging data to set the parameters of the mathematical model
- the direct comparison of the model results with *in vivo* data

Thus, poromechanics could be a suitable framework for imaging-informed modeling presented in the next section.

Pre-clinical studies: key points

•The stripped-down *in vitro* environments allow for clearly exposing mechanical phenomena in cancerous disease: mechanically-inhibited tumor growth, mechanically-induced phenotype*'s switch.

•These findings led to clinical applications [151], prognosis* tools [19], and new therapeutic targets [169].

•Poromechanics is an emerging framework in the mechanistic description of cancer and could lead to new and rich physical insights.

Authors	Cell line | Model	Objective
Cheng *et al.* 2009 [48]	non-metastatic murine mammary carcinoma* 67NR | *in vitro*	Measure of the deformation of agarose gels by tumor cells
Alessandri *et al.* 2013 [4]	mouse colon carcinoma* CT26 | *in vitro*	Retrieve inner pressure exerted by tumor cells on alginate capsules
Brossel *et al.* 2016 [28]	human breast cancer cell line MDA MB 231 | nude mice	Release internal tumor stress in animal model by ferromagnetic particles as bioactuators
Frieboes *et al.* 2013 [91]	lymphoma* Eμ-myc Arf-/- and Eμ-myc p53-/- | mice	Forecast inner structure of tumor cell line drug resistance or not in animal model by poromechanical modeling
Elhers *et al.* 2015 [73]	not specified (patient) | *in silico*	Contribute to the modeling of anisotropic drug diffusion within human brain by poromechanics
Paszek *et al.* 2005 [192]	mammalian tissue of MMTV-Her2/neu, Myc, and Ras transgenic mice ; nonmalignant MCF10A ; HMT3522 S-1 MECs | *in vitro*	Understanding mechanical signaling involved in tumor cell phenotype switch

Table 2.1: **Mechanical understandings of cancer in pre-clinical studies.** For further readings, the interested reader would refer to the reviews of Nia *et al.* [180] and, for mechano-biology specifically, Northcott Nia *et al.* [184].

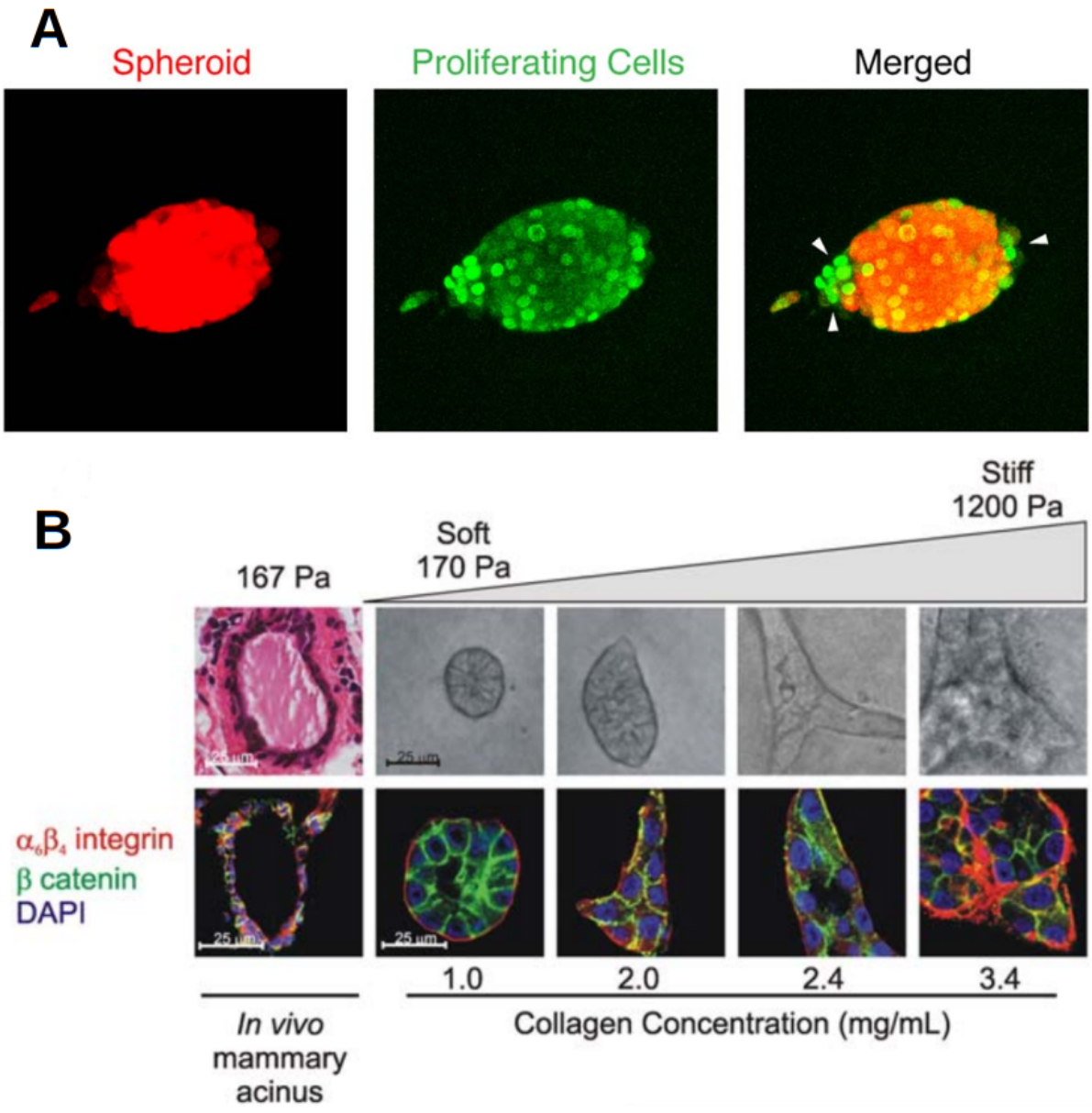

Figure 2.1: **In vitro mechano-biology of tumor growth, landmark studies.** The two panels illustrate the complex relationship between mechanical stress and tumor growth. If a cell line is subjected to a mechanical stress considerably higher than its usual osmotic pressure, it will lead to a growth inhibition. However, for some cell lines, it exists a window where a high mechanical stress will lead to phenotype alterations and a more aggressive behavior **Panel A** Mechanical inhibition of tumor growth by Cheng *et al.* in 2009 [48]. Cancer cell proliferation (green) in tumor spheroids (red) is suppressed in the direction of higher mechanical stress (*i.e.*, in the direction of the minor axis of oblate spheroids). On day 30, the compressive stress is estimated at $3.8\,\mathrm{kPa}$. Arrow heads indicate the regions with more cell proliferation. Scale bar $= 50\,\mu\mathrm{m}$. **Panel B** Mechanically induced phenotype switch: matrix rigidity regulates growth, morphogenesis, and integrin adhesions in Paszek *et al.* in 2005 [192]. Top: phase images and H&E (hematoxylin and eosin) stained tissue showing typical morphology of a mammary gland duct in a compliant gland ($167\,\mathrm{Pa}$), compared with mammalian epithelial* cell (MEC) colonies grown in collagen (BM/COL I) gels of increasing stiffness ($170 - 1200\,\mathrm{Pa}$). Bottom: confocal immunofluorescence images of tissue section of a mammary duct and cryosections of MEC colonies grown as above, stained for β-catenin (green), $\alpha 6$ or $\beta 4$ integrin (red), and nuclei (blue). The increasing size of the colonies is directly related to the increasing stiffness of the collagen.

2.2 Tumor growth forecasting: imaging-informed patient-specific modeling

This modeling paradigm was first developed by Swanson *et al.* in [239] in 2002, and after in [240, 202]. In 2013, with the progress of imaging methods, this framework was further extended by many groups (see the review of Mang *et al.* in [160]), and especially by Yankeelov *et al.* [268]. We start with a brief presentation of the clinical imaging methods that can be used to set the value of the parameters of the mathematical models. These parameters can define the material properties (diffusion, permeability, stiffness) or the material component (fluid, solid, cellular density). Moreover, the clinical imaging data provide patient-specific geometry [268], and this is a crucial gain for the relevance of the model results. However, the challenges involved in the uncertainty quantification and the use of these imaging methods in certain clinical settings may reduce their extensive use across different hospitals. Likewise, the adaptability of the mathematical models to these imaging data sources is still under investigation [222].

The second part of this section is devoted to detailed presentation of three clinically-relevant applications. In a few words, these models describe tumor growth and therapeutic response by means of reaction-diffusion equations that are constrained by the mechanical stress field induced by the development of the tumor.While they share the same modeling core, each model is adapted to the specificity of the cancer location.

2.2.1 Clinical imaging methods

Imaging methods and physical quantities Currently, the imaging methods performed in clinical oncology for diagnosis, monitoring, and assessment of treatment efficacy are:

- Computed tomography (CT) scans, used for cancer early diagnosis. CT scans results from the mathematical reconstruction of multiple axial X-ray images [237]. This reconstructed image of a large part of a body can be created in a few seconds, allowing for cancer detection throughout the body. Apart from bone material, the contrast of the various soft tissue can be enhanced by a radio-contrast agent like iodine or barium.

- Positron emission tomography (PET) scans, which consist of an intravenous injection of a positron-emitting radiopharmaceutical, like ^{18}fluor-fluorodeoxyglucose (F-FDG). The compound is partially metabolized by cells such that it accumulates mostly in cells with the higher metabolic rate, this accumulation being then detected [153]. Contrary to CT scans, 3D images are directly obtained in a PET scan, but the length of diffusion of the degraded compound implies a maximum of 2 millimeters precision [225]. When a precise measurement is required, a PET scan is complemented by other methods.

- Magnetic resonance imaging (MRI), the most commonly used technique for cancer diagnosis and screening. The various MRI methods are capable of providing information about anatomic, functional, and metabolic changes [237]. The signals in MRI originate from stable nuclei with magnetic properties that can be measured through nuclear magnetic resonance.

We will mainly focus on the latter, since MRI methods have been extensively used in the context of computational oncology [111, 153, 203, 268]. Usual MRI methods, T1 and T2 sequences, also termed anatomical methods, allow to coarsely separate solid and fluid phases. The contrast in T1 method is given by the characteristic time it takes for water protons to synchronize, which depends on the surrounding tissue. This time is denoted inversion time T1. Fluid phase, like cerebrospinal fluid (CSF) in the brain, remains dark with the short time sequence of radio frequency/echo measurement of T1 method (T1 ≈ 200 ms), but becomes bright with a very long sequence T1 method (T1 ≈ 3000 ms), denoted FlAIR (standing for fluid attenuated inversion recovery). Conversely, the contrast of T2 method is given by the loss of synchronicity of protons (see [237], ch.4). The characteristic time T2 of synchronicity loss depends on the tissue type, for instance, T2 ≈ 100 ms for fat and T2 ≈ 2000 ms for CSF. The T1 method can be enhanced by the addition of the vascular network of a radiotracer such as Gadolinium, which remains bright under T1 sequence. This method is termed T1 contrast enhanced (T1-CE).

Another class of methods used in imaging-informed modeling is the dynamic contrast enhanced MRI (DCE-MRI). It has been firstly used to obtain information on peripheral perfusion, for vascular-related disease of brain, heart and muscular system [98]. In DCE-MRI, a Gadolinium-based contrast agent is injected into the vascular system and T1 sequences are acquired every few seconds before, during, and after the injection. Specifically on brain tumors, the relative cerebral blood volume (rCBV) method is a class of DCE-MRI and can be used as a prognosis* tool itself [24]. By this method, a leaky vasculature will be revealed. This is a fundamental feature in the case of brain cancer: the blood-brain barrier, strictly impervious to blood flow, with an abnormal permeability will indicate a potential tumorous neo-vasculature. From the modeling point of view, the rCBV method allows quantifying the permeability between intra- and extra-vascular space [74].

A third class of MRI is used to set the parameters of mathematical models: the diffusion-weighted MRI (DW-MRI). This method has been designed to measure the diffusion of water within tissue. This sequence corresponds to a magnetic field with a linearly varying intensity, which is prescribed successively in two opposite directions [16]. In short, the respective intensities of the magnetic field can be retrieved in both directions, and their spatial evolution characterizes the heterogeneous diffusion of water within the excited tissue. This quantity is expressed as the apparent diffusion coefficient (ADC) of water, and it is inversely correlated to cellular density [268]. In case of organized fibrous tissue, the water diffusion increases in the parallel direction of the fiber and decreases in the perpendicular direction [5], such that diffusion is then denoted as anisotropic. DW-MRI can be extended to the 3D case to render this anisotropy, leading to a method termed diffusion tensor imaging (DTI). In DTI-MRI, the diffusion is evaluated at the minimum of 6 non-colinear vectors - as the resulting tensor is symmetric - with preferably equal angles [16, 5]. DTI-MRI can be used to map the white matter tracts in the brain. However, this method is not used routinely: an acquisition lasts for more than an hour, and this duration could be an additional burden for the patient.

These mechanical quantities measured by MRI can be completed by measurements of the metabolism of key chemical quantities, such as oxygen and glucose. The quantification of oxygen levels, and therefore the hypoxia*, is a critical feature for cancer staging[190]. On a patient-specific basis, this quantification may hold importance in future modeling. The PET scan Cu-ATSM - standing for Cu-diacetyl-bis(N^4-methylthiosemicarbazone) - has very promising *in vitro* results and is still in development for clinical applications [57]. Cu-ATSM is a radiotracer which accumulates in hypoxic tissue due to the chemical imbalance of low oxygenation. Among MRI methods, there is the blood oxygen level dependent method which can distinguish, by modified T2 sequence, oxygenated and non-oxygenated haemoglobin by their different magnetic properties. However, this method is more useful for acute hypoxia* than for chronic hypoxia*, characteristic of cancer [190]. To quantify the glucose metabolism of cancer, the PET radiotracer used is F-FDG. Analogous to glucose, it becomes radioactive by addition of the isotope fluor 18. As tumors have an important consumption of glucose, F-FDG is preferentially trapped by them, even if it does not have the energy properties of glucose. This method is routinely used for cancer diagnosis and treatment response [6].

Segmentation This procedure consists of the delineation of different regions of interest in the imaged tissue and provides the anatomical input to define the geometry and spatial parameter maps in mathematical models of cancer growth and treatment response. Segmentation has been traditionally performed by radiologists and specialized physicians. However, manually performing this task can be difficult, time-consuming, and prone to high intra- and inter-observer variability. During the past two decades, several semi-automatic or automatic methods have been developed, such as hidden Markov chain in 2001 [274], supervised learning and convolutional neural network (CNN), which are still under development in 2020 [45]. CNN is now the leading method for semi-automatic and automatic segmentation. Some examples of its applications are DeepMedic in the brain [126] and 3D AxelNet in the prostate [45]. These methods are 3D CNN, which means that the weights within the layers of the neural network are not linked to a specific MRI slice, but directly influence the treatment of the entire 3D data space. Nevertheless, the training of CNN requires an important amount of data. A well-known example is the brain tumor segmentation (BraTS) dataset [15], used to benchmark the brain tumor segmentation. BraTS contains 542 imaging datasets of patients with high- and low-grade glioma*, composed of anatomical methods, contrast enhanced and FLAIR sequences. The imaging data are interpolated to a uniform 3D space with isotropic resolution, allowing for a 3D CNN implementation. The patient cohort is divided in three subgroups: the training set (242 patients), which is used to calibrate the weights of the CNN; the validation set (66 patients), which is used to assess the calibrated weights; and the testing set (191 patients), which is used to evaluate the accuracy of the CNN. Thus, the training of a CNN for MRI segmentation - *a fortiori* for the forecast of cancer evolution (see [94, 171]) -, requires an amount of homogeneous data which is not always available.

2.2.2 Patient-specific approaches in clinical scenarios

Computational oncology is becoming an increasingly rich and prominent field of cancer research [268, 153, 203]. Multiple patient-specific biomechanical models have been proposed to reproduce and forecast the growth and treatment response of different types of cancers in several clinically-relevant applications, e.g., in brain [10, 1, 160, 112], breast [122, 252], prostate [153, 151], kidney [47], and pancreatic tumors [263]. In this section, we proceed to describe in detail a small selection of some illustrative recent studies in breast, brain, and prostate cancer. The examples considered herein share the same framework of tumor growth inhibited by solid stress. Clinical imaging data from individual patients are used to initialize the model, estimate parameters, and assess model forecasts after calibration. The integration of clinical data within the mechanistic framework is briefly described. For a more detailed review of imaging types, clinical applications, modeling paradigms, and computational methods for patient-specific models of cancer growth and therapeutic response, the interested reader is referred to [153].

Breast cancer Neoadjuvant therapy (NAT) is widely regarded as a standard-of-care treatment for locally advanced breast cancer before surgery [272]. Patients who achieve a pathological complete response (i.e., no residual disease) at the completion of NAT have a greater likelihood of recurrence-free survival [133]. Thus, the early determination of response to NAT would enable physicians to modify the therapeutic regimen of a non-responding patient (e.g., by changing dosage, dose schedule, prescribed drugs), and thereby improve treatment outcomes while avoiding unnecessary toxicity. To address this challenge, Jarrett *et al.* [122] propose to use personalized, computational forecasts of tumor response to NAT regimens obtained with a mechanistic model calibrated with patient-specific longitudinal quantitative MR data acquired early in the course of NAT.

In [122], Jarrett *et al.* describe breast cancer growth in terms of tumor cell density as a combination of tumor cell mobility and proliferation, which are modeled with a diffusion operator and a logistic term, respectively [12, 258, 121]. Additionally, Jarrett *et al.* introduce a sum of linear terms in the tumor dynamics equation to describe the NAT drug-induced death of tumor cells [121]. Each of these therapeutic response terms corresponds to one drug included in the patient's NAT regimen and is proportional to the local drug concentration in the breast tissue and the local tumor cell density. The initial spatial distribution of each NAT drug concentration in the breast tissue after infusion is estimated from DCE-MRI data and it follows an exponential decay in time, which reasonably approximates the relevant drug pharmacokinetics during the time scale of NAT. Additionally, the model presented by Jarrett *et al.* is coupled with quasistatic linear mechanics to account for the tumor mass effect. To model the forces exerted by the tumor, the authors use a pressure term that is proportional to the local tumor cell density [54, 258]. Then, to model the mechanical inhibition induced by the tumor mass effect, the authors constrain the tumor cell diffusion coefficient with an exponentially decaying function of the Von Mises stress [258]. Additionally, an earlier study of a simpler version of this breast cancer model by Weis *et al.* explored the differences in tumor forecasting when using a linear elastic versus a neo-Hookean nonlinear hyperelastic constitutive law, with which

they implemented several highly incompressible cases [260]. Weis *et al.* reported differences in tumor volume and total tumor cellularity below 10% with respect to the linear elastic case even in a highly incompressible scenario. Assuming the same Poisson ratio in both constitutive laws, the differences in these quantities were below 0.5%. Thus, Weis *et al.* concluded that the error in assuming a linear elastic constitutive model is admissible for this tumor forecasting application, especially since it would be included within the uncertainty of MR measurements of tumor cell density [260, 261, 229].

Jarrett *et al.* [122] use longitudinal anatomic and quantitative MR imaging datasets to initialize, parameterize, and assess the predictions of their model for each patient during the course of NAT. To this end, the authors present a robust imaging preprocessing pipeline. In brief, they first rigidly register the DCE-MRI and DW-MRI images acquired within each scan session using *imregister* in MATLAB. Second, tumor regions of interest are segmented on postcontrast DCE-MRI data from each scan session by means of a fuzzy c-means-based clustering algorithm developed in MATLAB [46, 264]. In addition, ADC maps are extracted from DW-MRI data using standard methods [261, 258] and the DCE-MRI data are analyzed using the Kety-Tofts model [267] to estimate parameters characterizing the local vasculature. Third, the contrast-enhanced images obtained from DCE-MRI data from each scan session are longitudinally registered using a non-rigid registration algorithm with a tumor-volume preserving constraint [142]. The resulting deformation map is applied to the other MRI modalities. Finally, the authors calculate several imaging-based fields that are required to initialize and parameterize the model: (i) the registered contrast-enhanced images are used to manually contour the breast domain and to generate adipose and fibroglandular tissue masks by means of a k-means clustering algorithm, which enable the definition tissue-specific material properties [258]; (ii) the Kety-Tofts parameters obtained from DCE-MRI data are used to calculate a normalized blood volume spatial map, which is used to define the initial NAT drug concentration fields mentioned above; and (iii) tumor cell density maps at each scan date are calculated by leveraging an inverse linear relationship with the ADC maps extracted from DW-MRI data [12, 258].

While most patients in the cohort ($N = 21$) analyzed by Jarrett *et al.* in [122] received two NAT regimens, the authors center their analysis exclusively on the first one. Hence, Jarrett *et al.* use the tumor cell density maps extracted from two consecutive scans for model calibration: one shortly before the onset of NAT to set initial conditions, and another within the first cycle of NAT to set a model-data mismatch functional. Their calibration method consists of a Levenberg-Marquardt least-square algorithm implemented in MATLAB [109, 122, 258], which aims at minimizing the aforementioned functional and hence yield constant values of baseline (i.e., unconstrained) tumor cell diffusivity, NAT drug efficacy, and NAT drug temporal decay along with a spatial map of the tumor cell proliferation rate on a patient-specific basis. The rest of the model parameters are fixed from the literature or from MRI measurements [122]. The calibrated model is then initialized using the datasets from the second scan and solved in time until the date of a third scan after the conclusion of the first NAT regimen. At this time point, the authors assess their model predictions of tumor cell density by comparing them with the corresponding tumor cell density map extracted from the third DW-MRI dataset. During both calibration and fore-

casting, the model is solved by means of a fully explicit finite-difference scheme implemented in MATLAB [122, 109, 153].

In [122], Jarrett *et al.* show that the imaging-computational framework described above renders highly accurate predictions of breast cancer response to NAT. To illustrate this computational technology, Figure 2.2A shows an example of a patient-specific model forecast against corresponding imaging data at the same date. In particular, the authors report a significant correlation between model forecasts and imaging measurements of total tumor cellularity, tumor volume, and tumor longest axis in a subgroup of 13 patients exclusively receiving chemotherapy for their first NAT regimen, with corresponding concordance correlation coefficients above 0.90 ($p < 0.01$). Additionally, Jarrett *et al.* leverage their model to explore a clinically feasible strategy to optimize NAT chemotherapeutic regimens on a patient-specific basis *in silico*. First, they define a set of alternative NAT regimens by fixing the total dose prescribed in the standard treatment for each patient while varying the number of doses, their frequency, and the corresponding drug dosage. In particular, the authors consider four alternative NAT regimens by equally dividing each original dose in two, three, four, or daily fractions that are delivered more frequently than in the standard treatment assuming an evenly distributed schedule based on the original NAT plan. Then, the authors run a simulation of their calibrated model for each of these alternative regimens accordingly and assess their performance in controlling breast cancer growth at the conclusion of NAT for each patient. Jarrett *et al.* report that an additional $0 - 46\%$ reduction in total cellularity (median 17%) might have been achieved across the patient subgroup ($N = 13$) compared to their original chemotherapeutic regimen according to standard-of-care NAT protocols. Indeed, the authors also report that alternative NAT regimens rendering a superior control of the patient's breast tumor were also found to significantly outperform the standard regimens ($p < 0.001$), thereby suggesting that standard regimens may not be the most effective for every patient and calling for the personalization of NAT to optimize therapeutic outcomes.

Brain cancer Tumors originating in the brain have received a large attention from the computational oncology community since the ability to early identify, or even predict, progression through patient-specific model forecasts would facilitate treatment personalization of these highly lethal diseases, which would ultimately translate into a major impact on survival, functional status, and quality of life [10, 1, 160, 112, 255, 54, 240, 177, 201, 147]. Here, we focus on a recent study by Hormuth *et al.* [112] on high-grade gliomas*. These brain malignancies exhibit a very aggressive behavior characterized as a highly heterogeneous and infiltrative disease, which ultimately influences the high recurrence rates in these tumors despite the advances in therapeutic strategies combining surgery followed by adjuvant radiotherapy plus chemotherapy [186]. Hormuth *et al.* posit that patient-specific computational forecasts of cancer growth and treatment response characterizing the unique underlying biology of the patient's tumor could enable the early identification of aggressive disease progression and the selection of more effective therapies on a personalized basis.

Hormuth *et al.* [112] present a family of 40 biologically-inspired, MR-informed models to describe the growth of high-

grade gliomas* and their response to chemoradiation, which they analyze in a model selection framework to determine the model that best balances predictive accuracy and formulation complexity. Each model is constructed by choosing three key components in their formulation: (i) a biomechanical model describing tumor dynamics, featuring either one or two cancerous species; (ii) a global value versus a spatially varying map to define the tumor cell proliferation rate; and (iii) one out of ten alternative formulations for the tumor response to chemoradiation. The model featuring a single cancerous cell species describes the growth of high-grade gliomas* using the same reaction-diffusion paradigm as the breast cancer model [240, 255, 113]. Inspired by an earlier work by Gatenby *et al.* [92], the authors extend this reaction-diffusion paradigm to a two-species formulation including both the enhancing tumor fraction observed in post-contrast T1-weighted MR images as well as the non-enhancing fraction showing an hyperintense signal in T2-FLAIR MR images. These two fractions are modeled as two different tumor cell densities following reaction-diffusion dynamics and also featuring a biological competition mechanism within the logistic term that describes tumor cell proliferation. While several alternative biomechanical models have been considered in the literature to describe the mass effect induced by brain tumors [10, 1, 160], Hormuth *et al.* follow the same rationale as Jarrett *et al.* [122] in their breast cancer model. Hence, both the single and the two-species model are coupled with quasi-static linear mechanics and their diffusion coefficients are mechanically inhibited through the evaluation of the Von Mises stress. To model the tumor response to concomitant radiotherapy and chemotherapy, Hormuth *et al.* assume that either treatment induces an independent and immediate reduction in the tumor cell species in the model (i.e., they do not explicitly introduce any synergistic mechanism). Hence, the authors propose four alternative formulations of the survival fraction to either treatment: one depending on the local tumor cell density; two depending on the level of perfusion measured through the enhancement ratio; and another that is constant throughout the whole tumor. Then, they select 10 pairs from these four options to represent chemotherapeutic and radiotherapeutic effects in their model selection study.

Hormuth *et al.* initialize, calibrate, and assess the performance of their model alternatives by leveraging longitudinal MRI datasets for each patient (N=9) consisting of two anatomical data types (contrast-enhanced T1-weighted and T2-FLAIR images) and one quantitative MRI data type (DW-MRI). To prepare the imaging dataset for use within the model, the authors perform a rigid intravisit and intervisit registration by leveraging *imregister* in MATLAB. The enhancing and non-enhancing, T2-hyperintense tumor regions are segmented using a semi-automated approach on the anatomic MRI datasets, consisting of sequential thresholding and manual adjustments by experienced radiologists. The brain-skull interface is manually segmented on the T2-FLAIR images. Additionally, Hormuth *et al.* use a k-means clustering algorithm [148] to obtain masks of white and gray matter to define heterogeneous material properties in the brain tissue. The authors estimate the tumor cell density in the single-species model and that of the enhancing fraction of the two-species model from ADC maps using the same approach as in the breast cancer model by Jarrett *et al.* [122]. In the non-enhancing, T2-hyperintense tumor region, since the relationship between imaging properties and tumor cell density is less clear, the authors initialize its value to a constant both for the tumor cell density in the single-species model and that of the non-

enhancing fraction in the two-species model, although they also note that alternative approaches have been proposed in the literature [240, 177]. Hormuth *et al.* employ a fully-explicit finite-difference scheme to solve their models and a Levenberg-Marquardt least-square algorithm to calibrate the relevant patient-specific parameters in each model, similarly to the breast cancer model above [109]. The rest of the parameters are either taken from the literature or fixed by the authors. Additionally, Hormuth *et al.* use the Akaike information criterion (AIC) [3] to select the best model balancing model-data agreement and complexity in terms of number of calibrated parameters.

Hormuth *et al.* carry out their modeling selection study in a cohort of 9 high-grade glioma* patients with unresected or partially resected tumors, whose individual imaging datasets consisted of a baseline MRI study (prior to the onset of chemoradiation) and two to three MRI studies at 1 to 2-month intervals after the conclusion of their chemoradiotherapeutic plan. They found that the best model across all patients was the two-species model, with spatially varying proliferation rates, and both chemotherapeutic and radiotherapeutic effects coupled to an estimate of perfusion obtained *via* the enhancement ratio. Hormuth *et al.* further explore the predictive accuracy of this model by considering two to all the datasets for each patient during calibration, and then forecasting the calibrated model until the date of the remaining datasets (if any). Their results show a good model-data agreement at the voxel level, while at the global level they report higher accuracy in terms of the Dice coefficient and tumor volume error in the enhancing region than in the non-enhancing region. Figure 2.2B shows an example of a model forecast along with the corresponding imaging data at the same date for a high-grade glioma* patient using the computational technology presented in this study. In particular, the authors show a strong agreement between measured and model predicted tumor volume and total tumor cell count within the enhancing region, with Kendall rank correlation coefficients above 0.94 and 0.79, respectively. Thus, Hormuth *et al.* conclude that their methodology is a promising strategy to integrate multimodal imaging data into personalized biomathematical models of high-grade glioma* in order to forecast spatiotemporal changes in tumor growth and response to therapy.

Prostate cancer Benign prostatic hyperplasia (BPH) and prostate cancer are two common pathologies among ageing men [257]. Most new cases of prostate cancer are organ-confined adenocarcinomas, while BPH consists of the progressive enlargement of the central gland of the prostate and usually provokes bothersome urological symptoms [150, 151, 257]. Prostatic tumors originating in larger prostates tend to present more favorable pathological features [90, 27], but the fundamental mechanisms that explain this interaction between BPH and prostate cancer are largely unknown and much debated in the medical community. In [151], Lorenzo *et al.* hypothesize that this phenomenon may be caused by the mechanical inhibition induced by BPH over prostate cancer growth, which the authors explore computationally by leveraging a new patient-specific model accounting for the mechanical interplay between both diseases.

The model proposed by Lorenzo *et al.* in [151] relies on a phase-field formulation of prostate cancer growth, whereby a variable termed phase field identifies and describes the joint spatiotemporal evolution of both healthy and cancerous

tissue [150, 151, 97]. In this study, tumor growth is driven by nutrient-dependent proliferation and apoptosis. The authors consider a generic nutrient that follows reaction-diffusion dynamics. This model also features a reaction-diffusion equation to describe the local production of a key biomarker in the clinical management of prostate cancer: the serum Prostate Specific Antigen (PSA) [150]. The integration of the local PSA field over the prostate volume ultimately yields the usual serum PSA values that physicians would consider in clinical decision-making. To represent the pathological deformation of the prostate due to tumor growth and BPH development, Lorenzo *et al.* follow a similar approach to the previous brain and breast cancer models [122, 112] that also accounts for the observed higher stiffness of the prostate central gland with respect to the surrounding peripheral zone [151]. The volumetric expansion induced by BPH is modeled with a time-dependent pressure term that is only defined within the central gland. Likewise, the tumor mass effect is modeled with another pressure term defined upon the phase field, thereby coupling tumor dynamics with the mechanical deformation of the prostate. To account for the confinement of the prostate within the pelvic region, the authors leverage Winkler-inspired boundary conditions over the external surface of the prostate. Additionally, Lorenzo *et al.* define a mechano-transductive function in the phase-field equation that progressively inhibits prostatic tumor growth as the local mechanical stress field intensifies. To this end, they use an exponentially decaying formulation of the stress level, similarly to the models discussed for breast and brain cancer above [122, 112] which, however, accounts for the surrounding tissue distortion and the usual internal stress state within growing tissue [119, 151].

Lorenzo *et al.* perform the study in [151] over the anatomy of the BPH-enlarged prostate of a patient with a tumor in the peripheral zone, which they extracted from MR imaging data available at the Initiative for Collaborative Computer Vision Benchmarking (I2CVB: i2cvb.github.io) [141]. For each patient with biopsy-confirmed PCa, this public database features a single-visit dataset including: T2-weighted MR images, DCE-MR images, DW-MR images, MR spectroscopic images, ADC maps, and the segmentations of the prostate, its local anatomy (i.e., central gland and peripheral zone), and the tumor delineated by an experienced radiologist [140]. Lorenzo *et al.* construct a volumetric Non-Uniform Rational B-spline (NURBS) mesh of the patient's prostate by leveraging a parametric mapping method [275, 84], whereby they deform the outer surface of a torus solid NURBS model to match with a surface model of the patient's prostate. To this end, Lorenzo *et al.* use 3DSlicer [80] to build a triangulated surface model of the patient's prostate by leveraging the T2-weighted images and the anatomic segmentations obtained from I2CVB, which they posteriorly smooth in Meshlab [53]. The resulting solid NURBS model of the patient's prostate is then refined by using standard knot insertion to ensure high accuracy in model simulations, which rely on isogeometric analysis (IGA) [60, 56]. Finally, the segmentations of the central gland and the patient's tumor are L^2-projected over the prostate mesh to define zone-dependent material properties and set the initial conditions of the tumor phase field. To define the BPH load and the parameter describing the Winkler-inspired boundary conditions, Lorenzo *et al.* run an inverse calculation that aims at deforming the patient's prostate back to a healthy state according to standard anatomical features [257]. This procedure is performed without considering the tumor. As a by-product, this calculation also renders a rough estimate of the mechanical stresses that

BPH had induced in the patient's prostate before the diagnosis of prostate cancer at the MRI date, which is used as a prestress in the simulation study presented in their work [151]. The remainder of the model parameters are fixed from the literature or computationally estimated [150, 151].

Using the biomechanical approach described above, Lorenzo *et al.* qualitatively show that the accumulation of mechanical stress due to prolonged BPH in enlarged prostates hinders the growth of prostatic tumors, which tend to develop more slowly, with limited invasiveness, and maintaining a smaller volume for a longer time. Thus, the mechanism described in [151] would contribute to explaining the favorable pathological features observed in tumors originating in larger prostates [90, 27]. Figure 2.2C shows an example of a forecast of prostatic tumor growth over a patient-specific prostate mesh using the methodology proposed by Lorenzo et al in [151]. Additionally, the mechanism proposed by Lorenzo *et al.* suggests that medical therapies aiming at reducing the volume of the prostate to alleviate BPH symptoms could potentially reduce the mechanical constraint on the tumor, and ultimately favor its development. Indeed, the authors analyze this possibility in a posterior study [152], where they explore the effects on prostate cancer of a type of common BPH drugs known as 5α-reductase inhibitors (e.g., finasteride, dutasteride). These drugs may reduce the prostate volume by approximately 18% to 26% and can also promote apoptosis in the tumor [164, 65, 81, 129]. In [152], Lorenzo *et al.* extend their model to account for these two drug-induced mechanisms by introducing an additional time-dependent pressure term describing prostate shrinkage and by increasing the apoptotic rate in the tumor dynamics equation, respectively. In particular, the new pressure term is parameterized by leveraging population-based observations from two large clinical studies [164, 65]. Lorenzo *et al.* used the same patient data from I2CVB to conduct a simulation study that shows that the maintenance of a mechanical constraint on tumor growth ultimately depends on the long-term competition between the apoptotic boost, which inhibits tumor growth, and the decrease in mechanical stress caused by prostate shrinkage, which favors tumor growth. In particular, their simulations show that tumors experiencing a major stress relaxation from drug-induced prostate shrinkage and only a limited upregulation of apoptosis ultimately exhibit more aggressive dynamics. In [152], the authors further hypothesize that this unfavorable outcome described by their model may contribute to explaining the larger proportion of higher-risk tumors in the treatment arm of two critical clinical trials exploring the use of 5α-reductase inhibitors for chemoprevention of prostate cancer [242, 9], which remains an open medical debate.

Authors	Framework	Location | sub-types	Objective	Nb. patients
Jarrett *et al.* 2020 [122]	Mechanically-constrained reaction-diffusion dynamics to describe tumor growth and neo-adjuvant therapy (NAT) response. Tissue deformation is modeled with linear elasticity.	Breast	Forecast patient's response to NAT and explore treatment personalization	21
Hormuth *et al.* 2021 [112]	40 models evaluated, composed of: mechanically-constrained reaction-diffusion dynamics to describe tumor growth and treatment response, tissue deformation modeled with linear elasticity, one or two tumor cell species, concomitant chemo- and radio-therapy.	Brain | high-grade glioma* multiforme	Forecast tumor evolution after surgery during concomitant chemo- and radio-therapy	9
Lorenzo *et al.* 2019 [151]	Mechanically-constrained phase-field model to describe tumor growth and reaction-diffusion dynamics for a generic nutrient and the prostate-specific antigen. Tissue deformation is modeled with linear elasticity.	Prostate | Concomitant prostate cancer and benign prostate hyperplasia (BPH)	Relationship between BPH and favorable prognosis* of prostate cancer	1

Table 2.2: **Representative studies of mechanically-constrained tumor growth and treatment response studies in the clinical setting.** For further studies and additional details on the underlying modeling framework and computational technologies, the interested reader is referred to [153, 203, 268]

Tumor growth forecasting: key points

•Clinical imaging data provide physical measurements that can be leveraged to define the tumor-bearing organ geometry, initialize a mathematical model, and calibrate its parameters on a patient-specific basis.

•Once calibrated, computer simulations provide personalized forecasts that can be assessed against further clinical imaging data collected at posterior dates.

•A general modeling framework is presented: solid mechanics, with mechanically-inhibited tumor growth, coupled with reaction-diffusion of chemical agents. Clinically-relevant applications of this framework are provided.

•We identify two key challenges: (1) assessing uncertainty in clinical imaging data and model outcomes, and (2) transfer these forecasting technologies to the clinic.

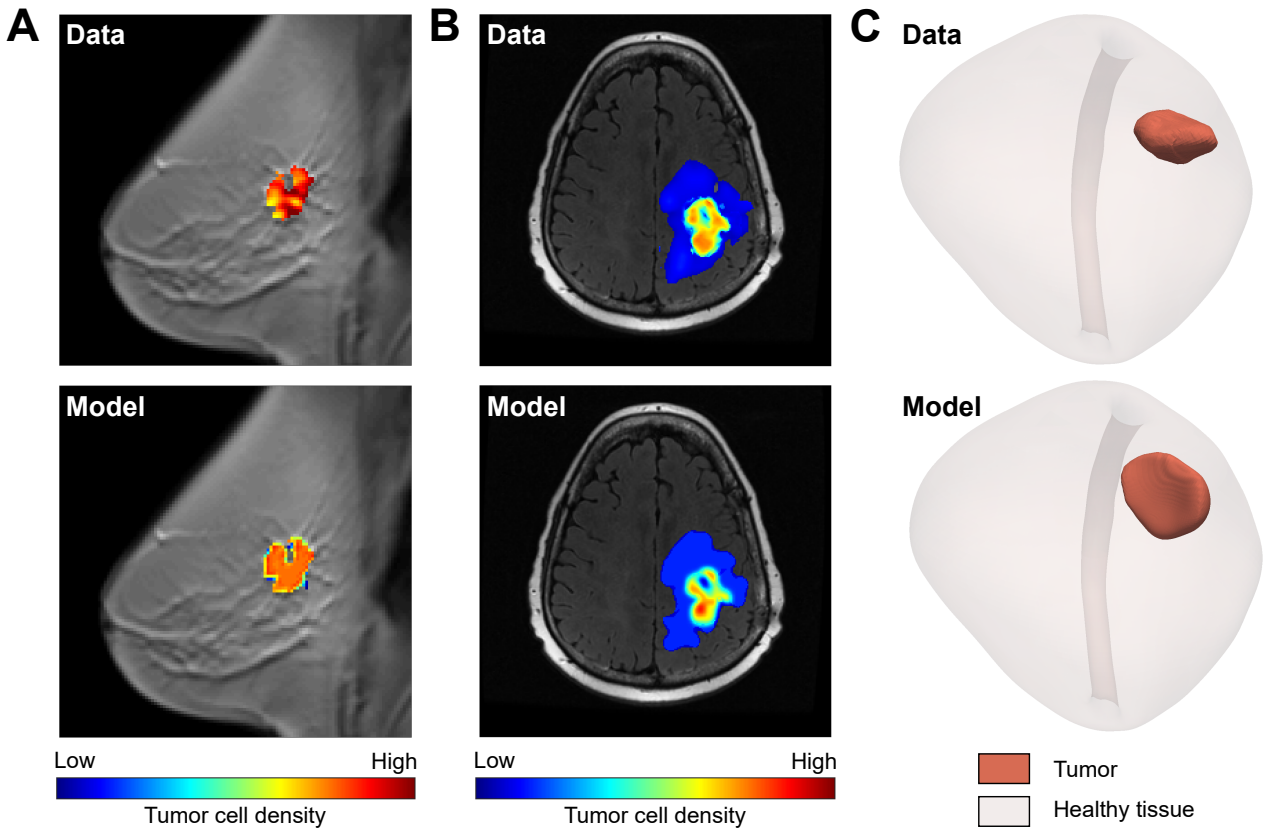

Figure 2.2: **Imaging-informed computational forecasting of tumor growth and treatment response in clinical settings.** Anatomic and quantitative clinical imaging data can be leveraged to initialize and parameterize mechanistic mathematical models of cancer growth and therapeutic response on a patient-specific basis [268, 111, 153]. The personalized model can then be used to run computer simulations to forecast the growth of the patient's tumor and the efficacy of treatments. These simulations can be further validated by comparison with additional imaging data from the patient at a posterior date. **Panel A** illustrates an application of this framework in the setting of NAT of breast cancer by Jarrett *et al* in 2020 [122]. The top figure shows a measurement of tumor cell density obtained from an ADC map calculated from DW-MRI data and plotted within the tumor region of interest identified on DCE-MRI data. The background anatomic image is a contrast-enhanced T1 map of the patient's breast. The bottom figure provides a model forecast of tumor cell density at the same location and time as the MR measurement shown above. **Panel B** illustrates an analogous ADC-based measurement (top) and model forecast (bottom) of tumor cell density at the same date during the post-surgical chemoradiotherapy of a glioblastoma* patient by Hormuth *et al* in 2021 [112]. In this case, the background anatomic data is a T2-FLAIR image of the patient's brain. **Panel C**, top figure shows a three-dimensional rendering of an isogeometric mesh of a patient-specific prostatic anatomy extracted from a T2-weighted MR image along with the L2-projected segmentation of an organ-confined tumor, which was obtained using the methods described in Lorenzo *et al* in 2019 [151]. The bottom figure shows a forecast of the tumor morphology at a later date using the mechanically-constrained model proposed in [151], in which the local mechanical deformation of prostatic tissue induced by concomitant BPH and prostate cancer exerts an inhibitory effect on tumor growth.

2.3 Clinical applications of mechanics in cancer management

Two classes of mechanical effects exposed *in vitro* transverse this review: i) tumor growth inhibition, which can help to design clinically-relevant modeling as shown in the previous section, ii) mechanically-induced phenotype switch *via* integrin signaling, which have been in-depth studied [256, 192, 17, 184] for more than twenty years. In the last years, the understanding of this phenotype switch led to new therapeutic targets. In 2020, it also led to an promising prognosis* tool [19]. We present these results in this section. We should note that, although stroma* mechano-biology constitutes a new reservoir of powerful tools, it is still underrepresented in the modeling community.

Mechanics is not only defined by the building of mathematical problems, it is also the underlying discipline enabling the design of new experimental setups. In particular, fluid mechanics underlies important applications in cancer management. Experimental setups for the isolation of circulating tumor cells are built upon microfluidic devices. The determination of the optimum diameter of a nanocarrier also requires fluid dynamics, as does the normalization of tumor vasculature induced by drugs. These two examples of clinical applications are presented into the fluid dynamics subsection.

Non-thermal electrophysics has already matured and journeyed from pre-clinical to clinical. A well-known application, the irreversible electroporation (IRE) is applied in clinics for fifteen years (see Davalos *el al.* [64]). As the *in vitro* findings date back to 1950, we decide to consider the application of electrophysics from the clinical side only. IRE applies on unresectable tumors and on poor prognosis* location such as the pancreas. We present section 2.3.3 the current developments of IRE, such as its coupling with immunotherapy. To conclude the clinical applications of mechanics in cancer, we present the idea of tumor-treating fields, a recent development in non-thermal electrophysics, the. Tumor-treating fields were approved in 2019 by US Federal Drug Agency as a new treatment for recurrent glioblastoma* multiforme.

2.3.1 Mechano-biology

We present the clinical applications derived from the mechano-biological findings presented in section 2.1.2. For a detailed description of these *in vitro* experiments, the reader will be referred to the section 2.1.2.

In vivo mechano-biology of colorectal cancer Recently, Bauer *et al.* [19] have proven that stroma* mechano-biology and its consequences can be used for the prognosis* of metastasis in colorectal cancer. The cancer-associated fibroblasts* contribute to a stiffer and denser ECM network which surrounds the colorectal cancer[2]. This increasing mechanical stress environment will lead malignant carcinoma* cells to an epithelial* to mesenchymal* transition (EMT), *via* integrin downstream signaling (see section 2.1.2 for a detailed description). Disorganized carcinoma* cells after EMT have a metastatic profile. When the ECM becomes stiffer, the secretion of activin A by intestinal epithelial* cells increases.

[2] *Stricto sensu*, this phenomenon is termed fibrosis. However, in medical vocabulary, it could be reserved for scars and wound healing. More generally, and in the context of clinical oncology, this phenomenon will be rather termed desmoplasia*.

The level of activin A has been measured in 28 control and 28 patients of the Chicago Colorectal Cancer Consortium. It correlates with stage* IV metastatic cancers, the level of activin A being 4-fold as high as in the control group. Additionally, there is no significant difference in level between controls and all pre-metastatic stages* I-III.

For decades, the integrin downstream signaling and its consequences on EMT have already been studied in-depth *in vitro* [192],[17] and with animal model [172], [123]. This direct clinical applications for metastatic prognosis* is one more landmark of the critical importance of the ECM mechano-biology in carcinoma* malignant evolution.

Targeted drugs: focal adhesion* kinase inhibitor The mechanical signaling applied by the ECM is received by cell cytoskeleton through the transmembrane proteins, such as integrin. The cell in return tends to balance these mechanical stimuli by contractility and to maintain the equilibrium. In these conditions, the equilibrium is termed the tensional homeostasis. When the stiffness of ECM increases - hence the corresponding mechanical signaling - the magnitude of the cell mechanical response will increase accordingly.

At the cell surface, this mechanical response is allowed by the clustering of integrin proteins, denoted focal adhesions* (FA). This mechanism is described section 2.1.2. These FA contain multiple mechanosensors, where focal adhesion* kinases (FAKs) play a specific role. FA allow increasing the generated traction force by actomyosin activity at the cell's surface. This instantaneous mechanical response is modified by FAKs. By altering the phenotype* of actomyosin, FAKs provoke a sustained tensional response. This augmented and sustained cellular tension will ultimately lead to enhanced tumor cell growth, survival, and invasion [195]. Lindsey *et al.* described in [145] the consequences of FAKs hyperactivity on well-organized epithelial* tissue. As the cell-matrix adhesions increase in number and intensity, the cell-cell adhesions essential to the organization of epithelial* tissue are lost. These cells then gain the ability to move individually, and this ability is characteristic of carcinoma* after EMT. Considering these mechano-biological findings, the inhibition of FAKs emerge as a potential therapeutic target.

In 2016, Jiang *et al.* [123] design a pre-clinical study in mouse models of FAKs inhibitor in pancreatic ductal carcinoma* (PDAC). This disease has a specific desmoplastic* stroma*, that acts as a barrier to T lymphocytes infiltration. At the tumor cell's level, this abundant and stiffer stroma is sustained by FAKs hyperactivity. Two groups of mouse models are treated, one with a microscopic early stage* PDAC and the other with a palpable late stage*. The prescription of a single-agent FAKs inhibition (VS-4718 in this study) significantly limits the tumor progression and increases responsiveness to immunotherapy PD-1 antagonists. VS-4718 leads to a significant extension of survival in both early and late treatment groups (4 and 8 months respectively). Promising results in animal models then authorize clinical trials with patients.

In 2020, Mohanty *et al.* reviewed in [169] the progress of FAKs inhibitors in clinical trials. Among these inhibitors, only 4 (PF-00562271, GSK2256098, VS-6063, and BI 853520) moved to subsequent development and were tested in clinical trials in solid tumors. These trials demonstrate the cytostatic activity of FAKs inhibitors. In other words, FAKs inhibitors stop the disease progression, without reducing the tumor volume. They extend the progression-free survival of 12 weeks in severe advanced solid tumors, as mesothelioma or PDAC. This extension is not accompanied by a clinical response,

that is to say, the disease remains stable during this extension. The trials also show that the patients response could be correlated with two biomarkers, E-cadherin and merlin. Concerning the E-cadherin relationship with FA, the reader is referred to the section 2.1.2. In these trials, FAKs inhibitors are currently tested in several combinations of chemotherapy and immunotherapy.

2.3.2 Microfluidics of metastasis and tumor vasculature

The interplay between circulating fluids and cancer are numerous and his large topic would require a review by itself. The applications of this field in cancer management in particularly inspiring. Indeed, *in vitro* findings, modeling framework and adaptation to biological cues work together towards clinical applications.

We selected two paradigmatic examples of fluid mechanics application on cancer management. Over the last years, nanoparticle delivery has emerged as an important topic in which biomechanical models can make an important contribution. The seminal review of Jain in 2005 [118] pointed out the critical aspect of the normalization of the tumor blood vessels. The first example is a direct application of this principle: the injection of blocking vascular endothelial growth factor will normalize the poorly perfused tumor vasculature, resulting in an increase in pressure gradient, and in a reduction of the vessels diameter. These coupled phenomena can be advantageously modeled and exploited by fluid mechanics, to optimally design the nanocarriers diameter.
The second example belongs to the experimental field of cancer diagnosis of metastasis: the circulating tumor cells can be filtered or captured by microfluidic designs. Once again, complementary biological and mechanical approaches lead to successful applications. They overcome the sparsity of metastatic cells in blood, as well as heterogeneity.
The physical aspects of fluid mechanics in cancer are reviewed in [134]. From a clinical point of view, fluid mechanics' applications in cancer are reviewed in [86].

Anti-angiogenic therapy and nanoparticles delivery In [44], Chauhan *et al.* study the effect of anti-angiogenic treatment on the delivery of nanoparticles. The drug is DC101 (ImClone System), a blocking vascular endothelial growth factor (VEGF) receptor-2, and two nanoparticles are tested: Abraxane, $10\,\text{nm}$ diameter and Doxil $100\,\text{nm}$ diameter. The experiments are performed on severe combined immunodeficient mice. DC101 and one of the nanoparticles diameter are injected on days 0, 3 and 6 and imaging by intravital microscopy are performed on days 2, 5 and 8 (imaging is performed through a window earlier implanted into the animal by surgery). Images are analysed by a custom code in Matlab, developed in a previous work of Chauhan *et al.* [43]. The experimental results give that DC101 injections decrease vessels diameters and enhanced between 2.7 to 3-fold the transvascular flux for the $10\,\text{nm}$ particles, but with no change for $100\,\text{nm}$ particles.
The mathematical model assumes classic Poiseuille's law for the blood flow, Starling's law for the intra/extra-vascular exchanges and the interstitial fluid flow follows poromechanics Darcy's law. The nanoparticles delivery is modeled by advection inside vessels and by advection-diffusion in extra-vascular space. The mathematical model shows that reducing

vessel wall pore size decreases interstitial fluid pressure in tumors, allowing nanoparticles to enter more easily, but smaller pores associated with better hydrodynamics obstruct the penetration of bigger nanoparticles. The authors of [44] suggest that nanoparticles with diameters smaller than $12\,\text{nm}$ are ideal for cancer therapy. These numerical results emphasize both the significance of the normalization of tumor blood vessels [118] and the efficiency of biomechanical modeling in the nanoparticles delivery challenge.

Microfluidic and circulating tumor cells (CTC) The isolation and characterization of CTC is a key challenge in metastatic cancer management. This can be achieved by the exploitation of biological properties (CTC biomarkers) or physical properties (size, deformation, viscosity). The first difficulty is the sparsity of CTC cells, which represent 0.004% of all cells in metastatic patient blood. Moreover, CTC present a high heterogeneity in biological and physical properties, thus, a microfluidic device solely based on size filtration and isolation could not be relevant as in a single patient CTC sizes vary between 4 and $30\cdot\mu\text{m}$. The review, in [68], reports several successful examples of dual approaches, biological and mechanical, which efficiently capture CTC heterogeneities.

In [175], Nagrath *et al.* present the CTC-chip device. Their approach is based on microposts coated with the antibodies EpCAM, standing for epithelial* cell adhesion molecule. The use of these specific antibodies for the CTC capture is justified by the over-expression of EpCAM by many carcinomas* (lung, colorectal, breast, prostate, among others) and by its absence of expression in haematologic cells. From the mechanical aspect, two parameters are critical for the CTC capture: the flow velocity, which determines the duration of the cell/micropost contact, and the minimization of the shear force, to ensure cell-micropost attachment. Additionally, these two parameters are constrained by a reasonable duration of patient blood analysis. The CTC-chip has been designed by simulation results. These results indicated that an equilateral triangle surface of $970\,\text{mm}^2$, with an architecture of $50\,\mu\text{m}$ microposts separated by a shift of $50\,\mu\text{m}$ every 3 rows, and a flow rate of 1 to $2\,\text{ml}\cdot\text{h}^{-1}$ ensured the best compromise. The CTC-chip successfully identified CTCs in the peripheral blood of patients with metastatic lung, prostate, pancreatic, breast and colon cancer in 115 of 116 (99%) samples.

Three years later, Stott *et al.* in [232] proposed an improved design of the CTC-chip. Adding ridges on the wall of the device creates passive micro-vortex in the flow which notably increase the collision between CTC and EpCAM location. Therefore, the complex CTC-chip architecture could be simplified in superimposed micro-channels with their walls shaped by asymmetrical chevrons. The device is denoted Herringbone-Chip. Its design allows for 93% CTC captures at a flow rate 4-fold higher than CTC-chip. Its high-throughput and easier fabrication make it suitable for clinical use.

These two examples show that the collaboration between biological and mechanical approaches, with a well-designed modeling, lead to successful clinical applications. Experimental design of isolation of metastatic cells or modeling of nanocarriers is of critical importance for the future of cancer management. These are inspiring examples of the involvement of mechanics in cancer.

2.3.3 Non-thermal electrophysics

We conclude this review of the exploration of electrical treatments currently used in clinical management of cancer. The first one targets cell membranes: the irreversible electroporation (IRE). IRE is a non-thermal, minimally invasive technique which provokes tumor cell death by short high-voltage electric pulses. Since 2005 (see Davalos *el al.* [64]), IRE is a well-established treatment for non-resectable tumors. We focus on recent development of this technique on several locally advanced cancers. The second one targets cell mytotic activity: the tumor treating fields (TTF). TTF are the application of intermediate frequency alternating electric fields with low intensity. In 2019, TTF has been approved by the US Federal Drug Agency as a new treatment for recurrent glioblastoma* multiforme [179].

Electroporation The Irreversible Electroporation is a non-thermal ablation technique which uses electric pulses to disrupt cell membrane [13]. Since 2005, more than 50 clinical trials have been applied to pancreatic, prostate, liver and kidney cancer showing that IRE has varying degree of clinical success, and reducing the progression of cancer [13]. Additionally, recent studies in human and mice suggest that IRE increases immune response of tumor-protective CD8+T cells. The success combination of IRE and immunomodulatory therapy (GC-CSF/STING agonist) shows significant improvement of treatment. In Shao *et al.* [223], an *in vitro* study shows that IRE enhances tumor antigen release. In the recent works of Burbach *et al.* [37], the hypothesis that primary treatment with IRE and following treatment with checkpoint immunotherapy increase the effective destruction and promote tumor clearance. In this study, authors also indicate that anti-CTLA-4 is a potential in-situ tumor vaccination strategy which could generate protective tumor-specific CD8+T cells, which play a critical role in host immune response.

In [144], Lin et *et al.* conduct a clinical trial on the combination of IRE and immunotherapy by $V\gamma 9V\delta 2$ cells. 62 patients (32 control) with stage* III PDAC receive IRE therapy and 30 patients receive at least two cycles of $V\gamma 9V\delta 2$ cells infusion. This is the first reported immune treatment of PDAC by γ T cells. Advanced PDAC is characterized by a strong immunosuppressive stroma*, IRE can improve, by its damaging effect, the drug delivery through this stroma*, but also increase tumor cells infiltration. Additionally, IRE provokes systemic change in tumor microenvironment, specifically in tumor immunity [104]. The combination of IRE and immunotherapy shows a significant improvement median survival (14.5 months, control 11). This is a promising strategy for treatment of stage* III PDAC.

Tumor treating fields (TTF) Glioblastoma* is a common brain tumor, which is very aggressive and recurrent. Its 5-year survival rate is still around 5% percent since 2000 [241]. Its standard of care is, if possible, maximum surgical resection followed by 6 one-week cycles a concomitant radiotherapy, temozolomide (TMZ) chemotherapy [233]. The TZM is used for its radio sensitizer effect, and after the 6 cycles, as chemotherapy maintenance for 6 or 12 months. Since 2005, no significance improvement has been made in this standard of care.

TTF [96] brought progress in glioblastoma* survival as shown in the phase III of clinical trial [234]. TTF are an antimitotic treatment, *i.e.* they affect dividing cells by delivering low-intensity alternating electric fields *via* electrodes arrays placed

on the scalp. It is shown in [96] that the intermediate frequency of $200\,$kHz has the stronger effect on glioblastoma* cells. In a phase III clinical trial, 637 patients, after the concomitant radiotherapy TZM treatment, receive TTF-TMZ maintenance or TMZ alone during 28 cycles. The TTF treatment shows a significant influence on progression-free (6.7 months *vs.* 4.0) and survival (20.9 months *vs.* 16.0). This treatment is a notable improvement on a particularly difficult cancer location. Recently, TTF has been approved by the US Federal Drug Agency as a new treatment for recurrent glioblastoma* multiforme [179].

Clinical application: key points

•Stroma* mecano-biology emerges as a promising field for prognosis* tools and new therapeutic targets.

•Fluid mechanics opened new opportunities to experimental design and nanocarriers design, of critical importance in the field.

•Non-thermal electrophysics is a well-established protocol for non-resectable tumors and its recent development led to promising new tools for pancreatic cancer and glioblastoma* multiforme.

2.4 Challenges and perspectives

In 2009, the National Cancer Institute deputy director Anna Barker wrote "we had reached an inflection point where we knew enough about the biology to bring in other fields". In 2012, Jennie Dusheck wrote a letter published in Nature, addressed to biologists and entitled *"Oncology: Getting Physical"* [69]. She pointed out that since the 1950's, age-adjusted cancer mortality rates have declined by only 11% whereas the budget allowed to treatment research have a 25-fold increase. This letter was mainly motivated by the examples given in the 2011 Nature review cancer of Mauro Ferrari *et al. "What does physics have to do with cancer"* [167], who has an important contribution in cancer nanomedicine [114] and cancer biophysical modeling [132, 216].

The years following this 'inflection point' have shown major reviews of cancer mechanical interplay as *"The role of mechanical forces in tumor growth and therapy"* in 2014 by Jain *et al.* [119]. The progress of clinical imaging led to the seminal review by T. Yankeelov *et al. "Clinically relevant modeling of tumor growth and treatment response"* in Science Translational Medicine in 2013 [268]. These studies showed decades of persevering research bringing to light and mechanics were finally allowed to 'make its part' in cancer research. Two examples to illustrate this statement: i) early research on elevated interstitial fluid pressure inside tumors as impediments of drug delivery in 1988 by Jain *et al.* [117] led to nanocarrier design through normalization of tumor vasculature in 2012 [44], ii) early work of Weaver *et al.* in 1997

[256] on integrin-mediated phenotype switch led to a clinical tool for early diagnosis of colorectal cancer with a metastatic prognosis* by Bauer *et al.* in 2020 [19]. Thus, the collaboration between biological and mechanical approaches could be a key for the next step of cancer treatments.

We have seen enormous efforts in the literature to select the best model, agent-based, individual-based, or focusing on partial differential equations, to best reproduce the phenomena of interest for computational oncology. However, the question of verifying whether the problem is solved to a satisfactory accuracy level is mostly neglected in literature. Recent efforts have been expended in the area of quality control and estimation for biomechanics problems, with the first real-time error estimation for surgical simulation proposed by Bui *et al.* in [36]. Additionally, adapting the computational mesh to obtain optimal accuracy in solving a model with minimal computational cost is a key strategy to obtain an efficient and precise implementation of computational oncology problems. Therefore, one of the most challenging problems in computational oncology resides in selecting the right model and identifying the best statistical distribution for each of its parameters (see Rappel *et al.* in [196]).

Personalized medicine has been a challenge for the last decade. Since 2017, numerous articles with promising results are converging within the same modeling framework: i) the coupling of chemical reaction-diffusion equations and multi-physics mechanical equations, ii) the use of rich clinical patient-specific datasets with the robust experience of mechanical engineering. This framework is denoted as imaging-informed mechanical-based modeling. Yet the challenge of developing personalized medicine based on this framework is not achieved, we hope that the clinician will be willing to get acquainted with these promising new tools.

Acknowledgments

G.L. acknowledges funding from the European Union's Horizon 2020 research and innovation program under the Marie Skłodowska-Curie grant agreement No. 838786. D.B. acknowledges funding from the European Union's Horizon 2020 research and innovation programme under MSCA ITN ElectroPros No. 813192. The authors gratefully thank Dr. Angela M. Jarrett, Dr. David A. Hormuth II, and Dr. Thomas E. Yankeelov for providing the subfigures for breast and brain cancer shown in Figure 2.2 of this work.

2.5 Supplementary information

2.5.1 Presentation of the modeling framework

Tumor growth approaches

In general, the tumor growth between t_0 and t may be described by two approaches: the phenomenological approach and the balance law approach. The older and most famous phenomenological approach is the Gompertz law. The formulation comes from the work of Anna Laird in 1964 [135]. This adaptation of the sigmoid function can give good results *in vitro*, but the *in vivo* dynamics can not be properly reproduced. The Gompertz law may be replaced by a more general Logistic law: $\partial_t N = \gamma(x)N(t)\left(1 - \frac{N(t)}{\theta}\right)$ where the growth rate $\gamma(x)$ is spatially resolved. These laws can be replaced or completed by a diffusion law (see the models presented in section 2.2.2), where the tumor is considered as chemical species diffusing in the domain.

The mass conservation approach poses the problem of cancer growth and treatment relying on fundamental physical balances (for instance, see [38, 91]). The mass of the system being conserved, the evolution of the tumor volume will be balanced by the evolution of the other components of the system (fluids, nutrients, and cells). Nevertheless, the mass exchange between the components $\overset{i\to T}{M}$ may be defined by various constitutive equations, physical or phenomenological.

Tumor growth inhibition

We distinguish two main ways to model the tumor growth inhibition: mechanical inhibition through a stress criterion and chemical inhibition through a concentration threshold of a chemical agent.

From the displacement $\mathbf{u}$ and the material parameters, we can deduce the stress tensor $\bar{\bar{\sigma}}$. In figure 2.4, σ is modeled with a linear elastic law. Then, a scalar stress metric, such as the Von Mises stress σ_{VM}, can be compared to an inhibition threshold σ_y. This stress could be compared to an inhibition threshold σ_y (see figure 2.4).

Chemical inhibition of tumor growth may be modeled with various criteria (*e.g.* nutrients, treatment), in figure 2.4, it is oxygen. Oxygen level may be evaluated with a reaction-diffusion equation, as in figure 2.4, or by a heuristic relationship. Then it is compared with the hypoxia* threshold.

Depending on how the inhibition is modeled, dependencies will be added to the tumor growth model. The growth rate γ may become $\gamma(O_2)$, the tumor cells diffusion coefficient D_T may become $D_T(\sigma_{\mathsf{VM}})$ or the mass exchange between the system components $\overset{i\to T}{M}$ may become $\overset{i\to T}{M}(O_2, \sigma_{\mathsf{VM}})$.

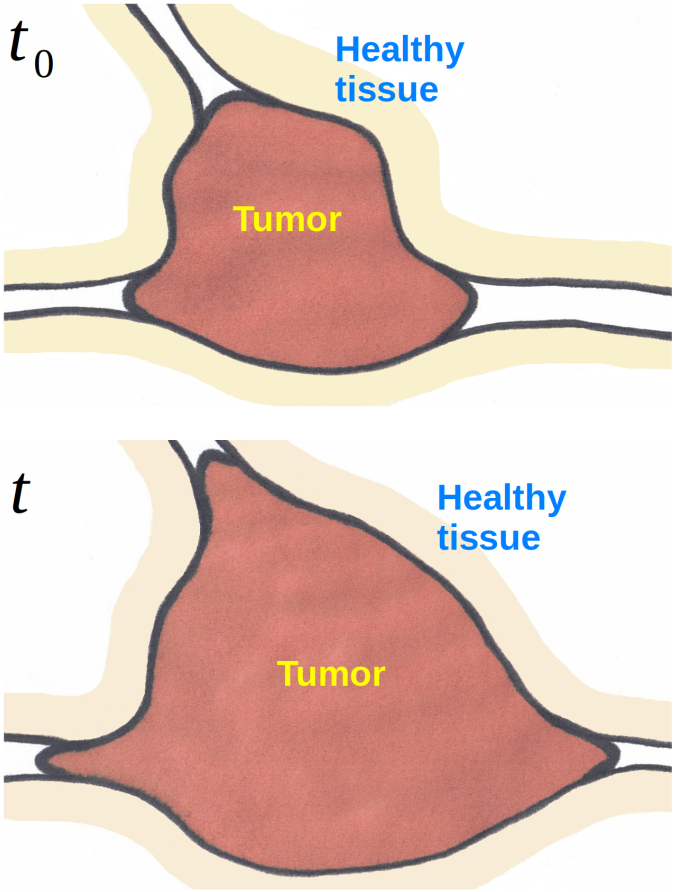

Figure 2.3: **Tumor growth approaches**
Phenomenological:

- Gompertz law:

$$N(t) = N_0 \exp\left[\ln\left(\frac{\theta}{N_0}\right)(1 - \exp(-\gamma t))\right]$$

  t time, $N(t)$ tumor cell density at time t, N_0 tumor cells initial density, θ carrying capacity of the domain, γ growth rate (see [135]).

- Diffusion law: $\partial_t N = \nabla \cdot (D_T \nabla N)$
  D_T the diffusion coefficient of tumor cells.

Mass conservation:

$$\begin{cases} \partial_t(\rho^T V^T) = \sum \overset{i \to T}{M} \\ \sum \partial_t(\rho^i V^i) = -\sum \overset{i \to T}{M} \quad i \neq T \end{cases}$$

V^T tumor volume, i other components of the system (for instance, interstitial fluid, stroma*). $\overset{i \to T}{M}$ mass exchange between phases i and T.

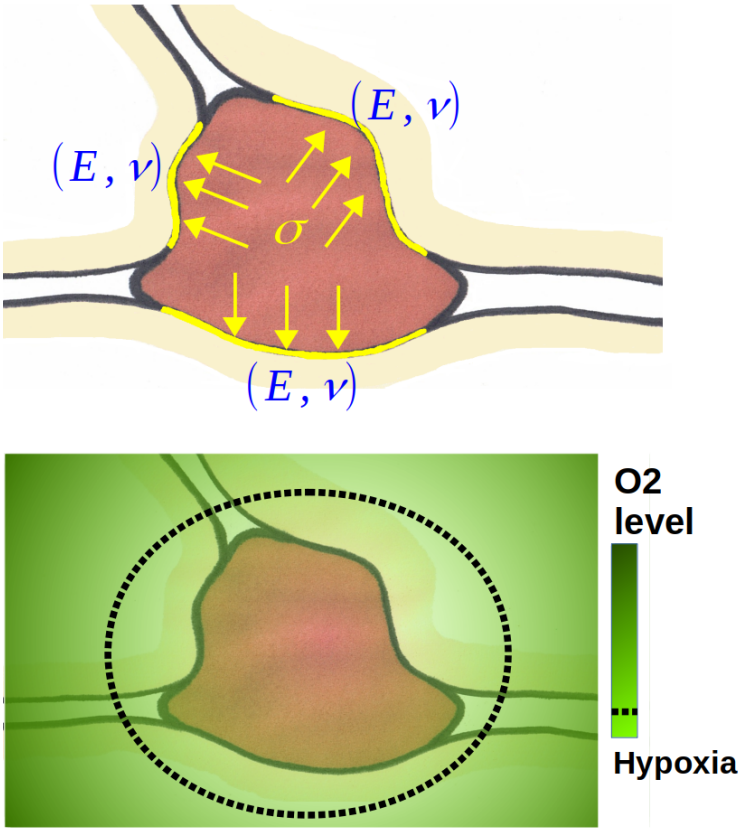

Figure 2.4: **Tumor growth inhibition** may be modeled as:

•Mechanical, with a stress inhibition threshold σ_y.

$\bar{\bar{\sigma}} = \bar{\bar{\bar{\bar{C}}}}(E, \nu) : \epsilon(\mathbf{u})$

$\sigma_{\text{VM}} = \sqrt{\frac{3}{2}(\sigma - \frac{tr(\bar{\bar{\sigma}})}{3}\bar{\bar{\mathbf{I}}})}$

and test if $\sigma_{\text{VM}} \geq \sigma_y$

•Chemical, with a hypoxia* threshold $O_{2\text{crit}}$.

$\partial_t(C) - \nabla \cdot (D_C \nabla(C)) = T_{\text{Source}} - T_{\text{Sink}}$

and test if $C(t) \leq O_{2\text{crit}}$

where D_C is the diffusion coefficient of the evaluated chemical agent, here oxygen.

Specificity of poromechanics

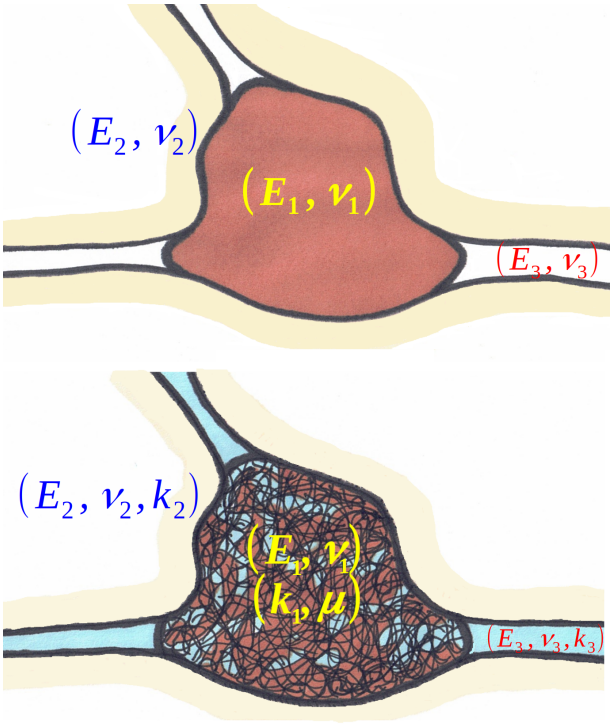

Elastic solid and porous system mechanics.

•An elastic solid is characterized by two material parameters, the Young's modulus E -its stiffness- and the Poisson's ratio ν -its compressibility-. Each elastic solid in the domain has its own tuple (E, ν). The unknown of the system is the displacement field $\mathbf{u}$. The linear momentum balance, in absence of external load, reads:

$\nabla \cdot \sigma = \mathbf{0}$ with

$$\sigma = \frac{E\nu}{(1+\nu)(1-2\nu)}\epsilon(\mathbf{u}) + \frac{E}{2(1+\nu)}tr(\epsilon(\mathbf{u}))\bar{\bar{I}}$$

•A porous system is composed of porous solid(s) with inner fluid(s) passing through. An elastic porous solid is defined by the elastic tuple (E, ν) and its permeability k. The fluid is characterized by its dynamic viscosity μ. The unknowns of the system are the displacement field $\mathbf{u}$ and the fluid pressure p. The system linear momentum balance, in absence of external load, reads:

$\nabla \cdot \sigma^T = \mathbf{0}$ with $\sigma^T = \sigma - p\bar{\bar{I}}$

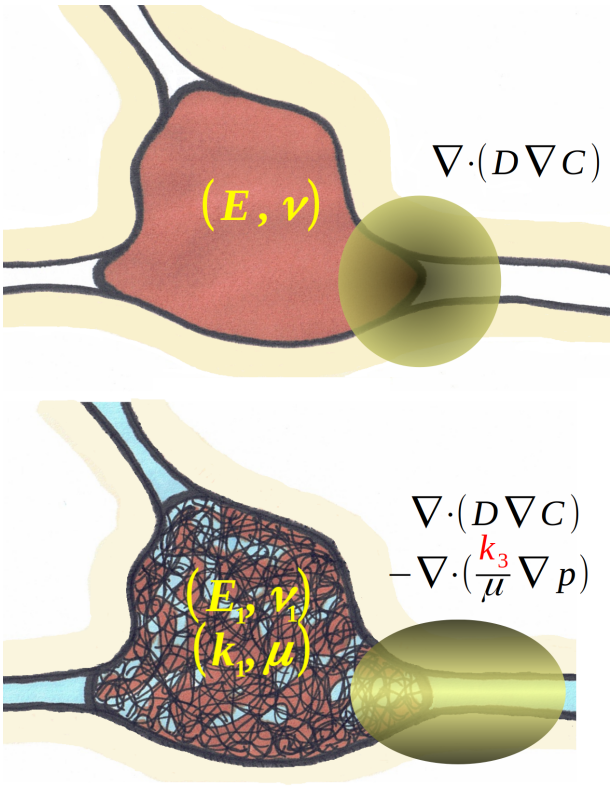

Diffusion of chemical species

•In an elastic solid a diffusive chemical species may be added. Its diffusion will depend only on its diffusion coefficient D. However, this coefficient may be space dependent $D(x)$ and partially coupled to the elastic solid through a stress inhibition threshold $D(\sigma_{\text{VM}})$.

•In a porous medium, diffusive chemical species will also be advected by the inner fluid. A Darcy's term, dependent on both permeability k and dynamic viscosity μ, will be added to the diffusion equation.

2.5.2 Glossary of clinical terms

Adenocarcinoma: From Greek *Adeno* 'gland'. Subtype of carcinoma* which originates or presents the characteristics of a gland.

Apoptosis: From Greek 'falling off'. Programmed cell death. Contrary to necrosis*, this is a highly regulated and controlled process.

Carcinoma: From Greek 'crabe'. Subtype of cancer characterized by abnormal and excessive growth of epithelial* cells.

Desmoplasia: Formation of connective tissue due to proliferation of fibroblasts*.

Epithelial cells: These cells, thanks to their organized cell-cell adhesions, form a thin and continuous layer of packed cells that covers the outer surfaces of the organs. Epithelial cells also constitute the main component of glands.

Etiology: Causes of disease.

Extra-cellular matrix: Non-cellular material secreted by cells into the surrounding medium, which provide cell adhesion and intercellular communication. Depending on the cells, this material is mainly composed of collagen (fibrous structure), elastin (elastic property), fibronectin (cell adhesion) or glycosaminoglycans (shock absorption).

Fibroblast: Mobile cell that produces the extra-cellular matrix* collagen.

Focal adhesion: Sub-cellular structure that serves as the mechanical linkage to the extra-cellular matrix*, *i.e.* cell-matrix adhesion. This mechanical linkage forms by the concentration of integrin proteins (and other signaling proteins) upon fibronectin and other cell-matrix adhesion sites.

Glioma: Brain tumor originating of glial cells, mainly from oligodendrocytes or astrocytes.

Glioblastoma: Stage* IV glioma*. Aggressive and recurrent, characterized by necrotic core and/or micro-vascular abnormal proliferation. Glioblastoma almost exclusively come from astrocytes (rare hybrids may have an oligodendrocytes-astrocytes profile).

Histology: From Greek 'Tissue knowledge'. The study of the microscopic anatomy of tissues. Various processes are involved: light microscopy, cell staining or freezing.

Hypoxia: At the cell's scale, it refers to a state in which oxygen supply is insufficient. If this insufficiency is severe and prolonged, it could lead to necrosis*.

Lymphoma: Cancers of lymphocytes (white blood cells). The common feature of different types of lymphoma is the enlargement and the swelling of lymph nodes.

Mesenchymal cell: Undifferentiated cell, highly mobile, which can form various tissues (muscle, bone, neural tube). Epithelial* cells can lose their organization and return to the state of mesenchymal. This process is termed epithelial to mesenchymal transition (EMT).

Necrosis: From Greek 'death'. External factors, such as infection or trauma, cause cell deregulation leading to death, which provokes an inflammatory response of the surrounding tissue.

Neoadjuvant therapy: Therapy or a group of therapies (radio-, immuno- or chemotherapy) that are delivered before surgery or another primary treatment with curative intent.

Parenchyma: Functional part of an organ, complemented by the stroma*.

Phenotype: Observable characteristics resulting from the interaction of a genotype with its environment.

Prognosis: From Greek 'foreseeing'. Expected development of a disease.

Stage: Staging of cancer: I - local, benign; II invasion of nearby tissue; III lymph node invasion; IV metastatic, recurrent.

Stroma: Structural part of an organ, also termed connective tissue, complemented by the parenchyma*.

2.5.3 List of acronyms

ADC	Apparent diffusion coefficient
BOLD	Blood oxygen level dependent
CE	Contrast enhanced
CFD	Computational fluid dynamics
CNN	Convolutional neural network
CSF	Cerebro-spinal fluid
CT	Computed tomography
CTC	Circulating tumor cell
DCE-MRI	Dynamic contrast enhanced magnetic resonance imaging
DTI	Diffusion tensor imaging
DW-MRI	Diffusion weighted magnetic resonance imaging
ECM	Extra-cellular matrix*
EGF	Epidermal growth factor
EMT	Epithelial* to mesenchymal* transition
F-FDG	^{18}fluor-fluorodeoxyglucose (radio-tracer)
FAKs	Focal adhesion* kinases
FlAIR	Fluid attenuated inversion recovery
GBM	Glioblastoma* multiforme
H&E	Hematoxylin and eosin
HER2	Human epidermal growth factor receptor 2
IRE	Irreversible electroporation
MEC	Mammalian epithelial* cell
MRI	Magnetic resonance imaging
PET	Proton emission tomography
rCVB	Relative cerebral blood volume
TTF	Tumor-treating fields

Chapter 3

In vitro poromechanical modeling of tumor growth

Convention

Font	Mathematical quantity
Italic	scalar s
Bold	vectorial $\mathbf{v}$
$\bar{h}$	h homogenized
$n > 1$ overlines	n^{th} order tensorial, *i.e.* 2^{nd} order $\bar{\bar{T}}$

3.1 Introduction to poromechanics

We present in this section the historical context and basic notion of poromechanics. The provided examples come from the books chapter of Detournay *et al.* in [66], A. Verruijt [253] and Gueguen *et al.* in [100]. The reader may be referred to them for further readings.

The first objects of the mechanics of porous medium are rocks and soil. The physical fact that best summarizes this primary approach, give in [66] is "(i) an increase of pore pressure induces a dilation of the rock, and (ii) compression of the rock causes a rise of pore pressure, if the fluid is prevented from escaping the pore network. These coupled mechanisms bestow an apparent time-dependent character to the mechanical properties." This phenomenon was first exploited by the engineer Darcy in 1857 to build fountains. The study of poromechanics was first motivated by civil engineering problems, such as the progressive settlement of the soil under buildings, termed as consolidation. Terzaghi was the first in 1923 to formulate a theory of poromechanics, based on the consolidation problem. However, his one-dimension theory relied on strong hypotheses which impeded further generalization. It is Biot in 1941 who first exposed a general theory consistent

with the physics of porous medium.

We introduce vocabulary and elements of notation which will be used thereafter in the manuscript. The porosity ε is the ratio of the pore volume to the total porous medium volume. Its complement, the solid scaffold, is noted ε^s. The drained or undrained conditions refer to the asymptotic cases of poromechanics. If the fluid can freely flow outside the solid scaffold, this problem is solved under drained condition. If the solid scaffold boundary is impervious, this condition is termed as undrained. The strain ϵ denotes a relative deformation of the porous body, respectively of an initial state.

We can now present a very important concept of Biot's theory: the effective stress. It is introduced, as prescribed in [100], by the close concept of effective pressure. Let a homogeneous porous medium, composed of a solid scaffold and one fluid phase, in undrained condition. To reduce the complexity, we consider a one-dimensional case. Let P and p, two pressures with $P > p$, and let K_s the bulk modulus of the solid scaffold and K the bulk modulus of the entire porous medium. If the external boundary of the medium is subjected to the compressive pressure $P - p$, and there is no pressure in the pore, then the strain of the porous medium will be equal to:

$$\epsilon = -\frac{P - p}{K}$$

If the external boundary of the medium is subjected to the compressive pressure p, and there is an inner pressure also equal to p in the pore, then the strain of the porous medium will be only supported by the solid scaffold, then:

$$\epsilon = -\frac{p}{K_s}$$

Finally, if we superimpose these two linear cases, we obtain the case of a porous medium subjected to an external pressure P and with an inner pressure p in the pore. The corresponding strain is equal to:

$$\epsilon = -\frac{P - \alpha p}{K} \qquad \alpha = 1 - \frac{K}{K_s}$$

α is denoted the Biot's coefficient[1] and $P - \alpha p$ the effective pressure. In the manuscript, we hypothesize that the solid scaffold is incompressible. Therefore, the Biot's coefficient will always be equal to 1.

In the manuscript, we model microscopic phenomena at the macroscopic scale. Thus, we need to introduce a last notion: the representative elementary volume (REV). We chose the description of [100] for this notion. The continuum mechanics hypothesises that "[...] all defined mechanical quantities are averaged over spatial and temporal scales that are

[1] In the literature, the Biot's coefficient is noted b. Unfortunately, in this multidisciplinary manuscript, this letter had too many confusing uses.

large compared with those of the microscale process, but small compared with those of the investigated phenomenon." The REV is in the middle of both scales. From a macroscopic point of view, the REV appears as a macroscopic point, where all the phases, solid and fluid, are superimposed. Inside the REV, the microscopic geometry can be described. In the manuscript, the volume of a REV may be approximated by a sphere between $5\,\mu$m and $30\,\mu$m. The physical quantities that result of the homogenization of microscopic processes are noted with an over-line $\bar{h}$.

3.2 Article

This work was published in 2021 in the PLOS One review, see Urcun *et al.* [247].

Contribution (CRediT author statement)

Conceptualization, Methodology, Software, Validation, Investigation, Writing – original draft

Digital twinning of Cellular Capsule Technology: emerging outcomes from the perspective of porous media mechanics

Urcun Stéphane[1,2,3] ¶, Rohan Pierre-Yves[1] ¶, Skalli Wafa[1], Nassoy Pierre[4], Bordas Stéphane P.A.[2], Sciumè Giuseppe[3*]

1 Institut de Biomécanique Humaine Georges Charpak, Arts et Metiers Institute of Technology, Paris, France

2 Institute for Computational Engineering Sciences, Department of Engineering Sciences, Faculté des Sciences de la Technologie et de Médecine, Université du Luxembourg, Campus Belval, Luxembourg

3 Institut de Mécanique et d'Ingénierie, Université de Bordeaux, Talence, France

4 Institut d'Optique Graduate School, CNRS UMR 5298, Talence, France

* giuseppe.sciume@u-bordeaux.fr

Abstract

Spheroids encapsulated within alginate capsules are emerging as suitable *in vitro* tools to investigate the impact of mechanical forces on tumor growth since the internal tumor pressure can be retrieved from the deformation of the capsule. Here we focus on the particular case of Cellular Capsule Technology (CCT).

We show in this contribution that a modeling approach accounting for the triphasic nature of the spheroid (extracellular matrix, tumor cells and interstitial fluid) offers a new perspective of analysis revealing that the pressure retrieved experimentally cannot be interpreted as a direct picture of the pressure sustained by the tumor cells and, as such, cannot therefore be used to quantify the critical pressure which induces stress-induced phenotype switch in tumor cells.

The proposed multiphase reactive poro-mechanical model was cross-validated. Parameter sensitivity analyses on the digital twin revealed that the main parameters determining the encapsulated growth configuration are different from those driving growth in free condition, confirming that radically different phenomena are at play. Results reported in this contribution support the idea that multiphase reactive poro-mechanics is an exceptional theoretical framework to attain an in-depth understanding of CCT experiments, to confirm their hypotheses and to further improve their design.

3.2.1 Introduction

As a tumor grows, it deforms the surrounding living tissues, which, in turn, produce pressure on the growing tumor and causes strains and associated stresses. Mechano-biology focuses on these mechanical forces and their interplay with biological processes which has been extensively studied experimentally [107, 192, 48]. Within this context, current mathematical models of tumor growth are becoming more and more reliable, complement experiments and are useful tools for understanding, explaining and building upon these experimental findings [119, 235, 88].

This article focuses on the Cellular Capsule Technology (CCT), an experimental protocol developed by some of the authors in [4] where multi-cellular tumor spheroids (MCTS) were cultured within spherical porous alginate capsules. The latter, after confluence (*i.e.* when the MCTS comes in contact with the inner wall), work as mechanosensors i.e. from their deformation, one can retrieve the stress state within the MCTS. The interaction pressure between the MCTS and the capsule, coming from the basic action-reaction principle, is a capital information since, as envisioned in [4], it could enable the prediction of stress-induced phenotype alterations to characterize cell invasiveness. To this aim, it is essential to quantify the critical pressure which induces the phenotype switch. Notably, it is also relevant to quantify the characteristic time of this process since one can infer that a relatively high pressure sustained by cell during a relatively short time does not lead to phenotype modifications.

Using the measured interaction pressure as a direct discriminant to predict the occurrence of the phenotype switch is very attractive also due to the simplicity of the concept. However, as hypothesized in this paper, directly linking the interaction pressure and the phenotype switch could be a simplistic shortcut since behind the promising practical simplicity of the MCTS-capsule concept, there is a behavior which is not trivially explainable with basic physical concepts. Indeed, the interaction pressure is a quite overall consequence encompassing several mechanisms at a lower level of description. The mechanics of porous media, on which is founded the proposed digital twin of the CCT experiment proposed in this contribution, has emerged as an excellent paradigm to model and possibly reveal these mechanisms offering a new perspective from which one can better interpret and exploit results of the CCT.

The internal structure of a tumor is typically very heterogeneous. Hence, instead of analyzing the system with a homogeneous modeling framework - which is the only option to exploit available data and produce clinically-relevant tumor forecasts (e.g., see [268]), in this contribution the MCTS is modeled as a multiphase continuum consisting of tumor cells, interstitial fluid and an extracellular matrix. This is possible thanks to the richness of experimental data provided by CCT. Mathematical modeling enables retrieving of the stress of each phase from the Biot's effective stress principle and the

adopted multiphase formulation. The model is founded on the rigorous framework provided by the Thermodynamically Constrained Averaging Theory (TCAT) of [99].

To guarantee the scientific relevance of numerical results, the reliability of the model was evaluated using a crossing validation methodology. This has allowed a step-by-step customization of the mathematical model, obtaining a mechanistic formulation which remains predictive also when the experimental conditions of CCT experiment are modified. Systematic sensitivity analyses have been helpful for the analysis and interpretation of results, allowing for quantification of the relative relevance of mechanisms underlying tumor growth phenomenology.

The effective digital twinning of the MCTS-capsule system and emerging biophysical outcomes from the perspective of multiphase porous media mechanics constitute together the novelty of this work. Differently from existing modeling approaches, which are often phenomenological and either too simplistic or too complex that their utility is very weak, the proposed modeling approach is mechanistic and contains the suitable degree of complexity to be representative such a kind of experiment.

3.2.2 Methods and Model

CCT offers a framework to quantitatively assess the influence of mechanical stresses and its coupling with other biophysical factors impacting tumor cells proliferation and metabolism. Input data for the mathematical model can be retrieved from the CCT experimental conditions; furthermore, numerical results in terms of pressure and displacement can be compared with those measured experimentally. This motivated the selection of CCT as reference experiments.

For the sake of clarity, the experimental observations reported by [4] together with some additional data provided by the authors are briefly summarized in the following subsection. The mathematical model and the *in silico* reproduction process are then presented.

Encapsulated MCTS: experimental procedure and observed phenomenology

MCTS cultures have been developed to overcome the limitations of 2D cultures which, inherently, lead to artifacts in cellular behaviors [62], and investigate biophysical aspects. They involve integrin-mediated adhesion, cell differentiation, or drug penetration as a readout for efficient delivery of active species, for which the 3D architecture of the tumor cell aggregate is suspected of having a significant contribution.

MCTS are generally formed and cultured in aqueous medium that we will refer to as "free conditions". Recently, Alessandri et al. [4] developed a microfluidic technique, namely the CCT, to produce confined MCTS cultures, and they demonstrated that confinement-induced mechanical forces inhibit tumor growth as previously shown[107] but may also trigger a switch towards an invasive phenotype of the tumor cells, with a mechanism that differs from the one mediated by matrix rigidity-sensing [192]. The CCT allows the encapsulation and growth of cells inside permeable, elastic, hollow hydrogel microspheres for the production of size-controlled MCTS. The hydrogel is made of calcium alginate whose pore size of about 20 nm

provides a permeability that permits free flow of nutrients and oxygen and ensures favorable conditions for cell proliferation. All experimental details and useful references can be found in [4], [243]. Briefly, alginate spherical capsules are generated by co-extrusion using a 3D printed device composed of 3 co-axial channels (see figure 3.1.A): the outermost channel contains the alginate solution; the innermost capillary contains the cells in suspension; the intermediate channel contains an inert (sorbitol) solution that creates a barrier against calcium diffusion from the cell suspension to the alginate solution and subsequent plugging of the device. At flow rates in the 30-45 mL/h range for each channel, a composite liquid jet exits the nozzle and gets fragmented into composite droplets (of radius of the order of the diameter of the nozzle) due to the Rayleigh-Plateau instability. Composite droplets fall into a calcium bath. Since alginate crosslinks almost instantaneously in the presence of divalent ions, hydrogel shells encapsulating cells are readily formed. Then, cellular capsules are washed and transferred to a culture medium and placed in an incubator for temperature and atmosphere control. The capsule therefore serves as a micro-compartment for 3D cell culture.

In the present work, we used CT26 cell lines which are derived from mouse colon carcinoma. During the early stages, cells aggregate with each other. Upon proliferation, the MCTS first grows freely and increases the fraction of the capsule volume occupied by cells until the capsule is filled. By analogy with 2D cell monolayers in a Petri dish, this stage is named confluence. From then on, the MCTS interacts with the alginate shell and deforms it. Conversely, the dilated capsule exerts back a confinement pressure due to action-reaction principle. In this respect, the post-confluent growing MCTS can be regarded as a tumor model that grows against the surrounding tissues and organs. While necrosis at the core of freely growing MCTS due to nutrient diffusion limitation is well known, once the radius of the MCTS exceeds $\sim$ 250-300 µm, similar necrosis can be observed in this experiment, suggesting that both confinement pressure and non-optimal oxygenation due to increased cell density cause these important measurable heterogeneities along the spheroid radius. In order to use the capsules as stress sensors, we need to characterize the material (Young's modulus E_{alg}) and morphological (shell thickness, inner and outer radii) properties. First, the dilatation of the alginate capsule was shown to exhibit an elastic deformation with negligible plasticity and no hysteresis. Young's modulus was measured by atomic force microscopy indentation and osmotic swelling and has been found to be equal to $E_{\mathsf{alg}} = 68 \pm 21$kPa [4]. Second, and quite remarkably, i) the size of the capsules is set by the size of the nozzle, indicating that different capsule sizes can be obtained by fabricating another microfluidic chip; ii) the thickness of the shell can be tuned with a given chip by varying the ratio between the flow rates in the different channels. For instance, increasing the inner flow rate of the cell suspension with respect to the sum of all flow rates will make the shell thinner. On the basis of these measured parameters, capsules can truly be used as a biophysical dynamometer by using a relation that yields the variation of the inner pressure from the measurement of the capsule radial deformation.

To do so, we used time lapse phase-contrast video-microscopy, which is minimally invasive in terms of photo-toxicity and thus allows monitoring MCTS growth over several days (up to about a week). While MCTS are clearly visible because of the strong light absorption by living tissues, the alginate shell, which is made of 98% water, is fainter. Images were thus analyzed using a custom-made, gradient-based edge detection algorithm that allows tracking simultaneously R_{MCTS} and

R_{out}. At time $t = 0$, R_{in} was measured manually and did not vary as long as confluence was not reached. In these pre-confluent stages, for all capsule thicknesses, the growth rate of the CT26 spheroid was not significantly different from the one derived from freely growing conditions, indicating that access to nutrients is not compromised by the presence of the alginate shell, whatever its thickness. When confluence was reached (i.e. when R_{MCTS}=R_{in}), simultaneous monitoring of R_{MCTS} and R_{out} allowed computing the variation of the shell thickness, b, which was averaged over the capsule perimeter. After confluence, the behavior strongly deviated from that of the free MCTS case. Qualitatively, the same phenomenology was observed for all capsule thicknesses. However, capsule thickness appeard to be a significant determinant of MCTS confined growth when quantitative analysis was performed. Finally, we also reported radial distributions of cell nuclei, dead cells and proliferative cells. These data were obtained i) by fixing the samples at different time points, typically before and after confluence, following standard protocols, then ii) by embedding them in a resin and freezing for cryosection. Immunostaining for nucleus (DAPI) and cell proliferation (KI-67) was performed using two types of fluorophores. Confocal images were then analyzed using standard ImageJ routines for particle detection. To detect dead cells, we exploited the fact that nuclei of dead cells are smaller and brighter (when DAPI-stained) than the ones of living cells. We thus applied additional threshold criteria for brightness and size.

The pressure exerted by the MCTS was calculated using the formalism of thick-walled internally pressurized spherical vessels, and thus could be compared to the stress of each phase from the Biot's effective stress principle of the multiphase system. Assuming that the alginate gel is isotropic and incompressible the radial displacement of the inner wall, $u(R_{\text{in}})$, reads

$$u(R_{\text{in}}) = \frac{3}{4}\frac{P_{\text{conf}}}{E}\frac{R_{\text{in}}}{1-(R_{\text{in}}/R_{\text{out}})^3} \tag{3.1}$$

where P_{conf} is the internal pressure, E is the Young's modulus, and R_{in} and R_{out} are the inner and outer radii of the capsule, respectively. Alginate incompressibility also implies volume conservation of the shell. This gives the following constraint equation

$$R^3_{\text{out}}(t) - R^3_{\text{in}}(t) = R^3_{\text{out}}(0) - R^3_{\text{in}}(0) = \delta(R^3_0) \tag{3.2}$$

Using this equation, the two time variables $R_{\text{in}}(t)$ and $R_{\text{out}}(t)$ can be separated and pressure, $P(t)$, written as a function of $R_{\text{in}}(t)$ only

$$P_{\text{conf}}(t) = \frac{4}{3}E\left[1 - \frac{1}{1+\delta(R^3_0)/R^3_{\text{in}}(t)}\right]\frac{u(R_{\text{in}}(t))}{R_{\text{in}}(t)} \tag{3.3}$$

Experimental input data

First, we considered the denoted *training dataset*:

- for the free MCTS, denoted FG0, the volume was monitored over a time span of 8 days (Fig.3.1B) ;
- for the encapsulated MCTS, denoted CCT0, the radial displacement of the capsule (inner radius $R = 100\,\mu$m and thickness $h = 34\,\mu$m) was monitored for 8 days (Fig.3.1C).

The reliability of the mathematical model was then tested with a *validation dataset* (Fig. 3.1D):

- Two thick capsules, denoted CCT1 ($R = 91\,\mu$m, $h = 30\,\mu$m) and CCT2 ($R = 116\,\mu$m, $h = 38\,\mu$m);
- Two thin capsules, denoted CCT3 ($R = 98\,\mu$m, $h = 9\,\mu$m) and CCT4 ($R = 102\,\mu$m, $h = 9\,\mu$m);

Sparse experimental data have been used to qualitatively measure the model emerging outcomes: the measurements of cell states (quiescent, proliferative, necrotic) of a $R = 50\,\mu$m free MCTS denoted FGS (Fig. 3.1.E) and a small thick capsule, denoted CCTS ($R = 50\,\mu$m, $b = 12\,\mu$m), 26 hours after confluence (Fig. 3.1.F). Concerning the stiffness of the alginate, E_{alg}, a range $E_{\text{alg}} = 68 \pm 21$kPa is provided.

The mathematical model: a physics-based description of the MCTS-capsule system

Our understanding of the physics and mathematical modeling in oncology has made significant progress owing to our improved ability to measure physical quantities associated with the development and growth of cancer. Hence, health research centers have been collaborating with engineers, mathematicians and physicists to introduce mechano-biology within clinical practice. In [151], the growth inhibition by mechanical stress has been used to reproduce patient specific prostate cancer evolution. This approach can be supplemented by biochemical and genetic approaches, for the prediction of surgical volume for breast cancer [71], or the diffusion of chemical agent in pancreatic cancer [132]. For several years, robust clinical oriented modeling frameworks have emerged (see the seminal article of [268]) wherein multi-parametric MRI patient sets have been processed to initiate patient specific modeling conditions [110]. Recent developments in [111] lead to a deep integration of mathematical oncology in the clinical process, from pre-clinical cell-line growth used for model pre-calibration to multi-parametric MRI for patient specific calibration.

In physics-based modeling, three approaches are currently used to model cancer: discrete, continuum and hybrid (the reader is referred to more detailed descriptions in the work of [155]). Among continuum models, poromechanical ones (e.g., see [214, 216, 162, 88]) emerge today as valid approaches to model the interplay between biomechanical and biochemical phenomena. As extensively reported in the literature, appropriate elementary models for describing the response of tumour tissue to mechanical and environmental cues will depend on its timescale. At very short time scales (seconds to minutes), tumour cell response is dominated by the elastic response of the cytoskeleton giving tumours a solid-like behavior. For times much longer than a second on the other hand, the response of the cytoplasm to solicitations is essentially viscous and tumour tissue undergoes cellular reorganizations, which lead to large persistent deformations easily represented by a fluid-like viscoelastic model. In this contribution, tumour tissue is modeled neither as a fluid, nor as a solid, but as a multiphasic continuum consisting of a solid matrix (ECM) filled by Newtonian fluid phases.

The application of physics-based models is continuously growing with, for example, *in vivo* modeling reproducing the vascular behavior and experimental validation using histological animal and human samples [235], hybridization of poromechanics and cell population dynamics to mimic the effect of *in vivo* micro-environment [88] or more classic pre-clinical *in vitro* tumor growth [162].

In this paper the multiphase reactive poro-mechanical model of [216] is here further developed and customized for digital twinning of CCT in order to reproduce numerically the experiment of [4] gaining additional information not yet measurable *in vitro*.

Our approach considers the tumor tissue as a reactive porous multiphase system: tissue extra-cellular matrix constitutes the solid scaffold while interstitial fluid (IF) and tumor cells (TC) are modeled as fluid phases. Hence, the mathematical model is governed by momentum and mass conservation equations of phases and species constituting the MCTS-capsule system. Once the capsule is formed, three different spatial domains can be defined (Fig. 3.2.A): the intra-capsular domain where the tumor cells phase (t), the medium/interstitial fluid phase (l) and the extra cellular matrix phase (s) coexist; the alginate shell domain, where a solid scaffold phase (s) and the medium fluid phase (l) coexist; and the extra capsular domain where the only medium fluid phase (l) exists. In these three domains, strains are calculated according to the theory of poro-elasticity which always assumes the presence of a certain solid phase volume fraction constituting the porous/-fibrous medium. Therefore, a certain proportion of the solid phase must always be present even in the extra-capsular domain where it does not exist. Despite this unrealistic condition enforced by the theoretical framework, the reliability of the model is only weakly affected, because the stiffness of this fictitious solid phase is two orders of magnitude lower than that of the alginate solid scaffold (Fig.3.2.A). A unique physical model is defined for the three domains, with some penalty parameters (*e.g.*, a low intrinsic permeability in the alginate domain) to avoid cell infiltration in the alginate shell. Oxygen advection-diffusion within the medium/interstitial fluid phase is considered. Oxygen acts as the limiting nutrient of TC with prolonged hypoxia leading to the cell necrosis.

The physical model consists of five governing equations:

- the solid scaffold s mass conservation
- the tumor cell phase t mass conservation
- the medium/liquid phase l mass conservation
- the advection-diffusion equation of oxygen in the medium/liquid phase l
- the momentum conservation equation of the multiphase system.

We have four primary variables: three are scalar and one vectorial.

- p^l the pressure of the medium/interstitial fluid
- p^{tl} the pressure difference between the cell phase t and the medium/interstitial fluid l
- $\omega^{\bar{n}l}$ the mass fraction of oxygen
- $\mathbf{u}^s$ the displacement of the solid scaffold.

We also have two internal variables: the porosity ε and the TC necrotic mass fraction ω^{Nt}. The evolution of porosity is calculated from the mass conservation equation of the solid phase while the mass fraction of necrotic cells is updated according to the tissue oxygenation in the TC phase (see [214]). We introduce two kinds of closure relationships for the system: mechanical and mechano-biological. Details about the derivation of the governing equations and these constitutive relationships are provided in the following sub-paragraphs.

The multiphase system

Three phases constitute the multiphase system namely: the solid scaffold s, the medium/interstitial fluid l and the tumor cells phase t. Hence, at each point in the domain, the following constraint must be respected

$$\varepsilon^s + \varepsilon^t + \varepsilon^l = 1, \tag{3.4}$$

where ε^α is the volume fraction of phase α. Defining the porosity ε as

$$\varepsilon = 1 - \varepsilon^s, \tag{3.5}$$

Equation 3.4 can also be expressed in terms of the saturation degree of fluid phase, $S^f = \varepsilon^f/\varepsilon$ (with $f = t, l$)

$$S^t + S^l = 1. \tag{3.6}$$

Mass conservation equations

We express the mass conservation equation for each phase. We use a material description for the motion of the solid phase and a spatial description for the fluid phases, whose reference space is that occupied by the solid scaffold. As the solid is deformable, this reference space is not fixed in time but evolves according to the displacement of the solid phase. For this reason we express mass conservation equations for each phase and species in their material form with respect to the solid scaffold velocity. Mass conservation equations of solid, cell and interstitial fluid phases read:

$$\frac{D^s}{Dt}\left(\rho^s \varepsilon^s\right) + \rho^s \varepsilon^s \nabla \cdot \mathbf{v}^{\bar{s}} = 0, \tag{3.7}$$

$$\frac{D^s}{Dt}\left(\rho^t \varepsilon S^t\right) + \nabla \cdot \left(\rho^t \varepsilon S^t \mathbf{v}^{\bar{ts}}\right) + \rho^t \varepsilon S^t \nabla \cdot \mathbf{v}^{\bar{s}} = \sum_{i \in l} \overset{i \to t}{M}, \tag{3.8}$$

$$\frac{D^s}{Dt}\left(\rho^l \varepsilon S^l\right) + \nabla \cdot \left(\rho^l \varepsilon S^l \mathbf{v}^{\bar{ls}}\right) + \rho^l \varepsilon S^l \nabla \cdot \mathbf{v}^{\bar{s}} = -\sum_{i \in l} \overset{i \to t}{M}, \tag{3.9}$$

where $\frac{D^s}{Dt}$ is the material time derivative with respect to the solid phase, ρ^α is the density of phase α, $\mathbf{v}^{\bar{s}}$ is the velocity vector of the solid phase, $\sum_{i\in l} \overset{i\to t}{M}$ is the total mass exchange (water, oxygen and other nutrients) from the interstitial fluid to the tumor due to cell growth and metabolism, $\mathbf{v}^{\bar{ts}}$ is the relative velocity of cells and $\mathbf{v}^{\bar{ls}}$ is relative velocity of the interstitial fluid with respect to the solid phase.

The tumor cell phase is a mixture of living (LTC) and necrotic tumor cells (NTC), with mass fraction $\omega^{\bar{L}t}$ and $\omega^{\bar{N}t}$, respectively. The following constraint applies

$$\omega^{\bar{L}t} + \omega^{\bar{N}t} = 1. \tag{3.10}$$

Mass conservation equations for each fraction, assuming that there is no diffusion of both necrotic and living cells, read

$$\frac{D^s}{Dt}\left(\rho^t \omega^{\bar{L}t} \varepsilon S^t\right) + \nabla\cdot(\rho^t \omega^{\bar{L}t} \varepsilon S^t \mathbf{v}^{\bar{ts}}) + \rho^t \omega^{\bar{L}t} \varepsilon S^t \nabla\cdot\mathbf{v}^{\bar{s}} = \sum_{i\in l} \overset{i\to t}{M} - \varepsilon^t r^{Nt}, \tag{3.11}$$

$$\frac{D^s}{Dt}\left(\rho^t \omega^{\bar{N}t} \varepsilon S^t\right) + \nabla\cdot(\rho^t \omega^{\bar{N}t} \varepsilon S^t \mathbf{v}^{\bar{ts}}) + \rho^t \omega^{\bar{N}t} \varepsilon S^t \nabla\cdot\mathbf{v}^{\bar{s}} = \varepsilon^t r^{Nt}, \tag{3.12}$$

where $\varepsilon^t r^{Nt}$ is the death rate of tumor cells. Note that only one of Eqs 3.11-3.12 is independent: actually, one can be obtained subtracting the other from Eq. 3.8 and accounting for the constraint Eq. 3.10.

Oxygen is the only nutrient which we consider explicitly. Another mass balance equation is introduced which governs the advection-diffusion of oxygen, n, within the interstitial fluid

$$\frac{D^s}{Dt}\left(\rho^l \omega^{\bar{nl}} \varepsilon S^l\right) + \nabla\cdot(\rho^l \omega^{\bar{nl}} \varepsilon S^l \mathbf{v}^{\bar{ls}}) + \nabla\cdot(\rho^l \omega^{\bar{nl}} \varepsilon S^l \mathbf{u}^{\bar{nl}}) + \rho^l \omega^{\bar{nl}} \varepsilon S^l \nabla\cdot\mathbf{v}^{\bar{s}} = -\overset{nl\to t}{M} \tag{3.13}$$

where $\mathbf{u}^{\bar{nl}}$ is the diffusive velocity of oxygen in the interstitial fluid and $\overset{nl\to t}{M}$ the oxygen consumed by tumor cells due to their metabolism and proliferation rate.

Momentum conservation equations

We neglect here the effect of gravitational body forces as their contribution is negligible compared to that of other forces. Furthermore, as we assume quasi-static processes and small difference in density between cells and aqueous solutions, inertial forces and the force due to mass exchange can also be neglected. These assumptions simplify the general form of the linear momentum balance equation given in [99] which becomes

$$\nabla\cdot(\varepsilon^\alpha \mathbf{t}^{\bar{\bar{\alpha}}}) + \sum_{K\in\mathfrak{J}_{c\alpha}} \overset{K\to\alpha}{\mathbf{T}} = \mathbf{0} \quad (\alpha = s,t,l), \tag{3.14}$$

where $\mathbf{t}^{\bar{\bar{\alpha}}}$ is the stress tensor of phase α, $\mathfrak{J}_{c\alpha}$ is the set phases connected to α and $\overset{K\to\alpha}{\mathbf{T}}$ is the interaction force between phase α and the adjacent phases. Summing Eq. 3.14 over all phases gives the momentum equation of the whole multiphase

system as

$$\nabla \cdot \mathbf{t}^{\bar{\bar{T}}} = \mathbf{0}, \tag{3.15}$$

where $\mathbf{t}^{\bar{\bar{T}}}$ is the total Cauchy stress tensor acting on the multiphase system.

Assuming that for relatively slow flow, the stress tensor for a fluid phase,f, can be properly approximated as

$$\mathbf{t}^{\bar{\bar{f}}} = -p^f \mathbf{1} \quad (f = t, l) \tag{3.16}$$

where p^f is the averaged fluid pressure and $\mathbf{1}$ the unit tensor, Eq. 3.14 which apply for a generic phase α (solid or fluid) can be expressed in an alternative form for fluid phases as [214]

$$\varepsilon^f \nabla p^f + \mathbf{R}^f \cdot (\mathbf{v}^{\bar{f}} - \mathbf{v}^{\bar{s}}) = \mathbf{0} \quad (f = t, l) \tag{3.17}$$

where $\mathbf{R}^f$ is a symmetric second-order resistance tensor accounting for interaction between the fluid phase and the solid phase, s. Eq. 3.17 can be rewritten as

$$-\mathbf{K}^f \cdot \nabla p^f = \varepsilon^f (\mathbf{v}^{\bar{f}} - \mathbf{v}^{\bar{s}}) \quad (f = t, l), \tag{3.18}$$

where $\mathbf{K}^f = (\varepsilon^f)^2 (\mathbf{R}^f)^{-1}$ is called the hydraulic conductivity. The hydraulic conductivity depends on the dynamic viscosity of the flowing fluid, μ^f, on the intrinsic permeability of the porous scaffold, k, and on the fluid saturation degree, S^f, via a relative permeability function $k^f_{\mathsf{rel}}(S^f) = (S^f)^A$ (A depending on the fluid characteristics, see [215, 219]). As customary in biphasic flow problems we set here $\mathbf{K}^f = k \frac{k^f_{\mathsf{rel}}(S^f)}{\mu^f} \mathbf{1}$. Hence, the governing linear momentum conservation equations for tumor cells and interstitial fluid read respectively

$$-k \frac{k^t_{\mathsf{rel}}(S^t)}{\mu^t} \nabla p^t = \varepsilon^t (\mathbf{v}^{\bar{t}} - \mathbf{v}^{\bar{s}}), \tag{3.19}$$

$$-k \frac{k^l_{\mathsf{rel}}(S^l)}{\mu^l} \nabla p^l = \varepsilon^l (\mathbf{v}^{\bar{l}} - \mathbf{v}^{\bar{s}}), \tag{3.20}$$

Effective stress principle

We assume here that all phases are incompressible. However, the overall multiphase system is not incompressible, because of the presence of porosity that evolves according to the scaffold deformation. As all phases are incompressible, their densities ρ^α (with $\alpha = s, t, l$) are constant and the Biot's coefficient is equal to 1. With these premises, the total Cauchy stress tensor appearing in Eq. 3.15 is related to the Biot's effective stress as follows

$$\mathbf{t}^{\bar{\bar{E}}} = \mathbf{t}^{\bar{\bar{T}}} + p^s \mathbf{1}, \tag{3.21}$$

where $p^s = S^t p^t + S^l p^l$ is the so-called solid pressure, describing the interaction between the two fluids and the solid scaffold.

The chosen closure relationship for the effective stress $\mathbf{t}^{\bar{\bar{E}}}$ is linear elastic:

$$\mathbf{t}^{\bar{\bar{E}}} = \bar{\bar{\bar{C}}} : \epsilon(\mathbf{u}^{\bar{s}}), \tag{3.22}$$

with $\epsilon(u^s) = \frac{1}{2}(\nabla \mathbf{u}^{\bar{s}} + (\nabla \mathbf{u}^{\bar{s}})^T)$ and $\bar{\bar{\bar{C}}}(\lambda, \mu)$ the fourth order elasticity tensor,

reduced in Voigt notation: $\begin{pmatrix} \lambda+2\mu & \lambda & \lambda & 0 & 0 & 0 \\ \lambda & \lambda+2\mu & \lambda & 0 & 0 & 0 \\ \lambda & \lambda & \lambda+2\mu & 0 & 0 & 0 \\ 0 & 0 & 0 & \mu & 0 & 0 \\ 0 & 0 & 0 & 0 & \mu & 0 \\ 0 & 0 & 0 & 0 & 0 & \mu \end{pmatrix}$

with the Lamé constant $\lambda = \dfrac{E\nu}{(1+\nu)(1-2\nu)}$ and $\mu = \dfrac{E}{2(1+\nu)}$.

E is the Young modulus of the solid scaffold and ν its Poisson ratio.

Pressure-saturation relationship

The experimental measurement of cells density inside the capsule revealed a strong dependency to necrotic fraction $\omega^{\bar{N}t}$. Hence, the pressure-saturation closure relationship has been improved with respect to that proposed in [216], to be more physically relevant and adapted to confinement situation

$$S^t = \frac{2}{\pi} \arctan\left(\frac{p^{tl}}{(1-\omega^{\bar{N}t})a}\right), \tag{3.23}$$

with p^{tl} pressure difference between tumor and interstitial fluid (i.e. $p^{tl} = p^t - p^l$). The saturation is directly linked to the partial pressure of the phase and a constant parameter a, which accounts for the effect of cell surface tension and of the refinement of the porous network (see [219] for the biophysical justification of the proposed equation). Its influence is offset by the necrotic fraction of tumor cells, $\omega^{\bar{N}t}$ (see Fig. 3.3), which allows us modeling necrotic areas of very high cell density according to experimental evidence.

Nutrient diffusion

The tumor cells growth, metabolism and necrosis are regulated by a variety of nutrient species and intracellular signalling. However, without losing generality, in the present model one single nutrient is considered: oxygen. The case of multiple

species can be easily obtained as a straightforward extension of the current formulation. The Fick's law, adapted to a porous medium, was adopted to model diffusive flow of oxygen Eq.3.13:

$$\omega^{\bar{nl}}\mathbf{u}^{\bar{nl}} = -D^{nl}\nabla\omega^{nl} \tag{3.24}$$

where D^{nl} the diffusion coefficient for oxygen in the interstitial fluid is defined by the constitutive equation from [215]

$$D^{nl} = D_0^{nl}(\varepsilon S^l)^{\delta}, \tag{3.25}$$

the exponent δ it set equal to 2 to account for the tortuosity of cell-cell interstitium where oxygen diffuse ([216], [162], [211]).

Tumor cells growth, metabolism and necrosis

Tumor cell growth is related to the exchange of nutrients between the IF and the living fraction of the tumor. The total mass exchange from IF to the tumor cell phase is defined as

$$\sum_{i\in l}^{i\to t} \dot{M} = \gamma_g^t \mathcal{H}(\omega^{\bar{nl}})\left(1-\mathcal{H}_p(p^t)\right)\left(1-\omega^{\bar{N}t}\right)\varepsilon S^t, \tag{3.26}$$

Note that $\left(1-\omega^{\bar{N}t}\right)\varepsilon S^t$ is the living fraction of the tumor. γ_g^t is the tumor growth rate parameter, cell-line dependent. $\mathcal{H}$ and $\mathcal{H}_p$ are regularized step functions varying between 0 and 1, with two threshold parameters σ_1, σ_2, that is to say $\mathcal{H} = \mathcal{H}(\sigma, \sigma_1, \sigma_2)$. When the variable σ is greater than σ_2, $\mathcal{H}$ is equal to 1, it decreases progressively when the variable is between σ_1 and σ_2 and is equal to zero when the variable is lower than σ_1. $\mathcal{H}$ represents the growth dependency to oxygen:

$$\mathcal{H}(\omega^{\bar{nl}}, \omega_{\text{crit}}, \omega_{\text{env}}) = \begin{cases} 0 \quad \text{if} \quad \omega^{\bar{nl}} \leq \omega_{\text{crit}} \\ \\ \dfrac{1}{2} - \dfrac{1}{2}\cos\pi\dfrac{\omega^{\bar{nl}} - \omega_{\text{crit}}}{\omega_{\text{env}} - \omega_{\text{crit}}} \quad \text{if} \quad \omega_{\text{crit}} \leq \omega^{\bar{nl}} \leq \omega_{\text{env}} \\ \\ 1 \quad \text{if} \quad \omega^{\bar{nl}} \geq \omega_{\text{env}} \end{cases} \tag{3.27}$$

ω_{env}, the optimal oxygen mass fraction, is set to $4.2 * 10^{-6}$ which corresponds, according to Henry's law, to 90mmHg, the usual oxygen mass fraction in arteries (see [188]). ω_{crit}, the hypoxia threshold, is cell-line dependent, for tumor cells, it has been set to a very low value: 10^{-6} (≈ 20mmHg, for common human tissue cells, hypoxic level is defined between 10 and 20mmHg [128]) The function $\mathcal{H}(\omega^{\bar{nl}}, \omega_{\text{crit}}, \omega_{\text{env}})$ is plotted Fig. 3.4A.

Function $(1-\mathcal{H}_p)$ represents the dependency on pressure:

$$\mathcal{H}_p(p^t, p_1, p_{\text{crit}}) = \begin{cases} 0 \quad \text{if} \quad p^t \leq p_1 \\ \sqrt{\dfrac{p^t - p_1}{p_{\text{crit}} - p_1}} \quad \text{if} \quad p_1 \leq p^t \leq p_{\text{crit}} \\ 1 \quad \text{if} \quad p^t \geq p_{\text{crit}} \end{cases} \tag{3.28}$$

An example of the function $\mathcal{H}_p(p^t, p_1, p_{\text{crit}})$ is plotted Fig. 3.4B, we have set p_{crit} to 6 kPa as initial guess (in [107], they found a inhibitory pressure at 10 kPa) and p_1, the pressure threshold when the inhibitory process starts, at 2 kPa.
As tumor grows, nutrients are taken up from the IF so that the sink term in Eq.3.13 takes the following form:

$$\overset{nl\to t}{M} = \left[\gamma_g^{nl}\mathcal{H}(\omega^{\bar{nl}})\left(1-\mathcal{H}_p(p^t)\right) + \gamma_0^{nl}\tilde{\mathcal{H}}\right](1-\omega^{\bar{N}t})\varepsilon S^t, \tag{3.29}$$

Nutrient consumption from IF is due to two contributions: the growth of the tumor cells, as given by the first term within the square brackets in Eq.3.29, the metabolism of the healthy cells, as presented in the second term. Thus, γ_g^{nl} is related to the cell proliferation, as discussed above; whereas the coefficient γ_0^{nl} relates to the cell metabolism. $\tilde{\mathcal{H}}$ is an adaptation of the previous step functions for the cell metabolism:

$$\tilde{\mathcal{H}}(\omega^{\bar{nl}}) = \begin{cases} 1 \quad \text{if} \quad \omega^{\bar{nl}} \geq \omega_{\text{crit}} \\ \dfrac{1}{2} - \dfrac{1}{2}\cos\pi\dfrac{\omega^{\bar{nl}}}{\omega_{\text{crit}}} \quad \text{else} \end{cases} \tag{3.30}$$

The model does not discriminate between proliferating and quiescent cells, but the growth is subject to $\mathcal{H}(\omega^{\bar{nl}}, \omega_{\text{crit}}, \omega_{\text{env}})$. To make possible the comparison with the experimental proliferative cell quantities (see Fig. 3.9), the following relationship has been set:

$$\omega^t_{\text{grow}} = \begin{cases} 0 \quad \text{if} \quad \omega^{\bar{nl}} \leq \omega_{\text{crit}} \\ S^t\dfrac{\omega^{\bar{nl}}}{\omega_{\text{env}}} \quad \text{else} \end{cases} \tag{3.31}$$

$\tilde{\mathcal{H}}$ is also used in the definition of hypoxic necrosis rate which reads

$$\varepsilon S^t r^{Nt} = \gamma^{Nt}(1-\tilde{\mathcal{H}}(\omega^{\bar{nl}}))(1-\omega^{\bar{N}t})\varepsilon S^t, \tag{3.32}$$

where $\gamma^{Nt} = 0.01$ is the necrotic growth rate. As the experimental data on necrosis were too sparse for this parameter identification (only a few stained-cell imaging), we have kept its generic value.

Initial parameter settings

As prescribed in [26], aiming for biological or clinical relevancy demands to investigate the choice of the initial values for each of the parameters. Some parameters are of physical nature (the IF dynamic viscosity, the oxygen mass fraction inside cell cultures), they can be, sometimes with enormous efforts, measured (or at least their values will be compared to the physical soundness). Others parameters belong more specifically to bio-poromechanical models in the mathematical oncology fields. Some of them have quite a theoretical nature (*e.g.*, the 'permeability' of the ECM) while others have been experimentally measured at the cellular level (*e.g.*, the oxygen consumption rate of EMT6/Ro cell line in [40]). For these parameters, we have taken values that previous numerical studies ([50], [216], [162], [211]) have used for MCTS cultured with other cell lines (human glioblastoma multiforme and human malignant melanocytes), averaged these values, denoted '*generic*', and used them as initial guess for identification of parameters of our CT26 cell line based MCTS.
When experimental data did not provide any relevant information on a parameter (*e.g.* for ECM stiffness and permeability), we chose to fix them at their generic value. The following parameters have a non negligible influence on the model outputs, and the closure relationships they belong to are explained in detail in the mathematical model section: γ_g^t the TC growth rate (Eq.3.26), γ_g^{nl} and γ_0^{nl} the oxygen consumption rate due to growth and quiescent metabolism respectively (Eq.3.29), a the parameter tuning the joint impact of the ECM thinness and cell surface tension (Eq.3.23) and μ_t the TC dynamic viscosity, presented in Eq.3.19. Two other parameters, p_1 and p_{crit}, are introduced in this modeling. They represent thresholds which govern the inhibition of the proliferation (Eq.3.28) of cancer cells. The initial guess of p_{crit} have been chosen according to the work of [107] and [192], and the initial guess of p_1 has been set by observation of the experimental data.

In silico reproduction process

From the computational point of view, we aimed to a light and adaptable process: free, open source and compatible with any 2D or 3D geometry. For the model validation, we followed the convention of mathematical oncology proposed in [26]: two distinct sets of data for optimization and validation, the parameters set being fixed before validation. To measure the quality of the fits, we followed the prescription of [22]: the root mean square error (RMSE) relative to a reference, specified each time. The error on the numerical quantity ξ_{num} relative to a reference ξ_{ex}, evaluated at n points is computed as:

$$RMSE(\xi_{\text{num}}, \xi_{\text{ex}}, n) = \sqrt{\frac{1}{n}\sum_{k=1}^{n}\left(\frac{\xi_{\text{ex}}(k) - \xi_{\text{num}}(k)}{\xi_{\text{ex}}(k)}\right)^2} \tag{3.33}$$

Computational framework We implemented the above model in Python and C++ within the FEniCS framework [7], with an incremental monolithic resolution of the mixed finite element (FE) formulation. The simulations have been run with composite Taylor-Hood element $P_3(\mathbb{R}^2)$, $[P_2(\mathbb{R})]^3$ (one vectorial and three scalar unknowns), a mesh element size of $dh = 5\,\mu$m and an implicit Euler scheme with $dt = 1200\,$s. All the details and analytical verification of the FE formulation can be found in Supporting information: solution's sensitivity on the ROI size. All the codes used in this article, analytical verification, integration along the inner radius of the radius, free growth and confined growth, are available on Github, at `https://github.com/StephaneUrcun/MCTS_mechanics`

Initial and boundary conditions The Fig. 3.2 shows the two modeled configurations of MCTS (the free on the left and the confined on the right). Each mesh is half of a sphere because we also exploit symmetry with respect to a diametrical plane. For the three scalar variables, we prescribed Dirichlet boundary conditions along the outer radius of the domain $p^l = 0$, $p^{tl} = 0$ and $\omega^{\bar{nl}} = 4.2 \cdot 10^{-6}$ (which corresponds, according to Henry's law, to 90 mmHg, the usual oxygen mass fraction in arteries, see [188]) and no flux condition at $r = 0$ and $z = 0$. For the ECM displacement field $\mathbf{u}^s$, slip conditions $u_r^s = 0|_{r=0}$ and $u_z^s = 0|_{z=0}$ are used, and Dirichlet conditions $\mathbf{u}^s = \mathbf{0}$ at the outer radius of the domain (see Fig. 3.2).

Local sensitivity analysis We performed a local sensitivity analysis to estimate Sobol sensitivity indices on the FG0 and CCT0 training datasets to assess the sensitivity of the FE solution to the input parameters, both on the free and encapsulated MCTS. Further details of the process can be found in Variance-based local sensitivity analysis.
First, we designed two cost functions, for FG0 and CCT0. The free growth cost function, J_{free}, compares the experimental aggregate volume V_{exp} and the simulated volume from day one to day four.

$$J_{\text{free}} = \sum_{i=1}^{4} \left(V_{\text{exp}}(D_i) - \int_{\Omega} \varepsilon_i S_i^t \, dx \right)^2 \tag{3.34}$$

The cost function for CCT0, J_{conf}, compares two experimental quantities, the displacement of the internal radius $\mathbf{u}(R_{\text{in}})$ and the internal pressure calculated in Eq.3.3, with the corresponding model outputs $\mathbf{u}^s$ and p^s, one day after confluence.

$$J_{\text{conf}} = \int_{\partial_{\text{Caps}}} < \mathbf{u}(R_{\text{in}}) - \mathbf{u}^s > \, ds + \int_{\partial_{\text{Caps}}} (P_{\text{conf}} - p^s)^2 \, ds \tag{3.35}$$

where $\partial_{\text{Capsule}}$ means along the inner radius of the capsule.
The results of the two configurations, with the parameters at their initial values used for the sensitivity analysis can be found Fig.3.14 Variance-based local sensitivity analysis.
Secondly, the 7 parameters (μ_t, a, γ_g^t, γ_g^{nl}, γ_0^{nl}, p_1, p_{crit}) were disturbed one at a time respectively to a $[-10, -5, -2, -1, +1, +2, +5, +$ grid. The variations of J_{free} and J_{conf} were interpolated by a linear model, which constitute first-order Sobol indices. The influence of the i^{th} parameter was deduced from the slope θ_i of the linear fit. The Sobol index S_i was calculated as follows:

$$S_i = \frac{\theta_i^2}{\sum_i \theta_i^2} \tag{3.36}$$

Finally, the 21 parameters tuples were evaluated at the 2 extreme values of the grid, $[-10, +10]\%$, for each configuration. The variations of J_{free} and J_{conf} were interpolated by a second-order polynomial model. This allowed computing two types of Sobol indices: S_i for the influence of the parameter i and S_{ij} for the influence of each couple (i, j) of parameters.

$$S_i = \frac{\theta_i^2}{\sum_i \theta_i^2 + \sum_{ij, i>j} \theta_{ij}^2} \quad \text{and} \quad S_{ij} = \frac{\theta_{ij}^2}{\sum_i \theta_i^2 + \sum_{ij, i>j} \theta_{ij}^2} \tag{3.37}$$

Parameter identification and model validation For both configurations, the optimization procedure was based on sensitivity profiles, that is to say, we identified the set of parameters that gathered at least 90% of the variance of the solution. Then, the selected parameters were identified by a Nelder-Mead simplex algorithm (in the Python library SciPy, method minimize, option Nelder-Mead). In one hand, this algorithm has the advantage of not requiring the computation of the system gradient to the parameters, and, on the other hand, generally converges to a local minimum. To avoid this phenomenon, a large range of initial guess was tested: $[-20, +20]\%$ around the *generic* values for μ_t, a, γ_g^t, γ_g^{nl} and γ_0^{nl} and $[-50, +50]\%$ around the initial guess of p_1 and p_{crit}, as we have not previous literature values. All the parameters having a physical meaning, their values were bound to the physical and physiological values reported in the literature, and we choose not to extend this range. In the CCT0 configuration, considered as the representative case by the team of [4], the parameters of the MCTS cell-line were identified with the mean experimental value of the alginate stiffness: $E_{\text{alg}} = 68\,\text{kPa}$; it is important to note that this study is not aiming to identify the stiffness of this biomaterial.

To evaluate the reliability of the identified parameters, an author of this article and member of the team of [4] have jointly provided unpublished experimental results of encapsulated MCTS, CCT1 to 4 and CCTS, namely the validation dataset. As their alginate stiffness is not known (the Young's modulus of the alginate is estimated to be $E_{\text{alg}} = 68 \pm 21\,\text{kPa}$), two simulations were run for each capsule with the extreme values of E_{alg}. This provided the range of modeling possibilities of the identified parameters (Fig 3.6, grey range), for each capsule an indicative fit is proposed with a value of E_{alg} which minimize the RMSE.

3.2.3 Results

Based on a detailed sensitivity study, the identified set of parameters was tested and cross-validated on unpublished experimental results (Fig. 3.1.C-E) provided by the same team of [4]. Numerical simulation also provides a wide output of qualitative results which are presented and interpreted. At the end of the section, we show that the model outputs allow predicting, with a reasonably good accuracy, experimental TC saturation and its necrotic fraction, despite these quantities have not been used for the model optimization.

Sensitivity analysis

Fig. 3.5 shows the results of first-order and second-order interaction analyses, for the free and encapsulated configurations respectively. Clearly distinct profiles were obtained.

In the free growth control group FG0, the governing parameter is γ_g^t the tumor cells growth rate (first-order index, $S_{\gamma_g^t} = 81\%$, with interactions $S_{\gamma_g^t} = 66.4\%$). In decreasing order of magnitude, we observed that two parameters are not negligible: γ_0^{nl} the oxygen consumption due to metabolism (first-order index 7.45%, with interactions 6.10%) and a, the parameter determining the joint impact of the ECM thinness and cell surface tension (first-order index 6.25%, with interactions 5.11%). The important difference between the 2 Sobol indices of γ_g^t is explained by the only non negligible interaction between two parameters: γ_g^t and a ($S_{(a,\gamma_g^t)} = 14.5\%$, see Fig. 3.5, right). This important interaction is indicative of the significant roles that ECM properties and cell-cell adhesion have on proliferative-migration behavior (this is widely described in literature, see for instance [192]) and that our modeling approach can reproduce mechanistically how these properties impact the overall observed phenomenology of tumor growth. Thus, these two parameters are not independent and should be identified together.

For all parameter perturbations in the first-order and second-order interaction analyses, the pressure of the TC phase $p^t = p^l + p^{tl}$ was less than 1 KPa, thus the first threshold of growth inhibitory due to pressure p_1 was never reached and, *a fortiori*, the critical threshold of total inhibition p_{crit}. Thus, the sensitivity of the FE solution to p_1 and p_{crit} was 0. The 3 parameters γ_g^t, a and γ_0^{nl} has therefore been optimized for the free configuration.

For the encapsulated configuration CCT0, the governing parameter is the critical inhibitory pressure p_{crit} (first-order $S_{p_{\text{crit}}} = 73.5\%$, with interaction 70.9%). γ_g^t, a and γ_0^{nl} has already been identified for the free configuration, the only non negligible parameter remaining is p_1 (first-order index $S_{p_1} = 3.4\%$, with interaction 3.3%). The difference between Sobol indices of first-order and interactions is weak. Indeed, the 21 parameters tuples capture only 3.6% of the solution variance. Thus, in the encapsulated configuration the parameters can be considered non-correlated and be identified separately.

Such results allow us highlighting that, in the encapsulated configuration CCT0, the mechanical constraint is the phenomenon that determines the overall growth phenomenology provided by the mathematical model.

Calibration

The three governing parameters $\gamma_g^t, \gamma_0^{nl}, a$ for the free MCTS configuration were identified using the Nelder-Mead simplex algorithm and fitted to the experimental data with a $RMSE = 0.031$. To be physically relevant, the same parameters set should be shared by the two configurations. These three parameters being calibrated, we consider they describe a limited part of the mechano-biological states and they are thereafter fixed and injected in the encapsulated configuration. Its two remaining parameters p_1, p_{crit} (74% of the variance) were identified using the same algorithm. We fitted the experimental data of the encapsulation with a $RMSE = 0.124$. Fig. 3.6A shows the two configurations fitted with the following set of parameters: $\gamma_g^t = 3.33 \cdot 10^{-2}$kg/(m^3.s), $\gamma_0^{nl} = 6.65 \cdot 10^{-4}$kg/(m^3.s), $a = 890$ Pa, $p_1 = 1432$ Pa, $p_{\text{crit}} = 5944$ Pa (see

Table 3.1). This set is cell-line specific, only relevant for CT26 mouse colon carcinoma.

Validation

Unpublished experimental results of encapsulated MCTS, both thick and thin, have been used as validation dataset (Fig. 3.1D). Each capsule had its own radius R and thickness h and two simulations have been run with the extreme experimental values of the alginate stiffness ($E_{\text{alg}} = 47$ kPa and $E_{\text{alg}} = 89$ kPa).

Fig. 3.6A right shows the range of modeling possibilities of the identified parameters on the training data CCT0, respectively to the alginate stiffness range. The parameters set was identified with the mean stiffness value ($E_{\text{alg}} = 68$ kPa).

Fig. 3.6B shows that the modeling range on two thick capsules, CCT1 and CCT2, is in accordance with the experimental results. Two fits with an alginate stiffness at $E_{\text{alg}} = 52.5$ kPa and $E_{\text{alg}} = 70$ kPa respectively are proposed.

The Fig. 3.6C shows results relative to two thin capsules, CCT3 and CCT4. The dynamic is properly reproduced by the model for both capsules which are importantly deformed (the strain is of 16% for the left one and 20% for the right one). Despite in the right case CCT4 where the model shows some limitations, because the proposed fit is at the minimum of the experimental stiffness value $E_{\text{alg}} = 47$ kPa, the presented cross-validation demonstrates that this mechanistic mathematical model can adapt to different geometries and thickness without losing its relevance. Focusing on the left graphs in figures B and C we can note that, with the same parameters set and almost the same alginate stiffness (B Left, $E_{\text{alg}} = 52.5$ kPa and C Left, $E_{\text{alg}} = 54$ kPa), the model reproduces experimental strain of 8% and 16% respectively. The difference between the two strains is induced by the geometrical effect due to the capsule thickness, which impacts on the evolution of internal stresses, cell growth and oxygen consumption.

Qualitative results and emerging outcomes

In addition to overall quantitative results, Fig. 3.7 and Fig. 3.8 provide details on the physical phenomena occurring during growth (from confluence to 85 hours after confluence) of a MTCS encapsulated in a thick capsule with the same geometry than CCT0. These figures quickly allow understanding the importance of physics-based modeling, as it provides qualitative information that could be used to interpret the experimental process as a whole and to better understand the tumor growth process. Fig. 3.7 shows contours of oxygen, necrotic fraction, IF pressure, ECM displacement, TC pressure and TC saturation at confluence and 85 hours after. To gain information about the dynamics of these quantities, Fig. 3.8 shows them probed along the radius at confluence, 85 hours after, and at two intermediate times (28 and 56 hours).

Fig. 3.8A and B show the interplay between oxygen consumption and necrosis. Indeed as mentioned in the experiments, 85 hours after confluence, the viable space remaining for TC is a $20\,\mu$m thick rim. This is explicit in Fig. 3.7, upper right circle, NT quarter. The comparison of Fig. 3.8F and B shows a relation between the saturation of TC and their necrotic fraction. This is a basic experimental fact that, when the cells bodies collapse in a necrotic core, the aggregate density increases accordingly. Fig. 3.8D and E allow 'visualizing' the overall dynamics of the process: the capsule displacement

strongly increases after confluence due to the contact with tumor cells whose pressure rises from 1.15 kPa at confluence to almost 4 kPa, 85h after confluence. Beyond 85h and until eight days after confluence, it was observed that the tumor cells pressure $p^t < p_{\text{crit}}$. This is in accordance with the experiment as recorded in [4] where it was reported that the MCTS continued to grow twelve days after confluence, even very slowly.

The tumor cells pressure p^t does not determine directly the capsule deformation, which is more directly driven by the solid pressure, p^s (see definition Eq.3.21). The pressure p^s is more representative of the average internal pressure P_{conf} obtained experimentally by inverse analysis (see Eq.3.3). At the confluence time, p^s is importantly lower than the pressure in the tumor cell phase since at that time the MCTS also consists of 40% of IF. After confluence the saturation of tumor cells increases progressively, so p^s, becomes closer to the pressure sustained by the cells. To allow the numerical comparison, we designed a mesh with a subdomain along the internal radius of the capsule to integrate the numerical quantities with FEniCS. Fig 3.10 shows the comparison between p^s, p^t and the P_{conf}.
In the presented physics-based approach, mass conservation is prescribed, so the growing MCTS, which increases in density and size, results in a decrease in interstitial fluid mass. This result, which cannot be measured experimentally, is shown in Fig. 3.8 where a sucking phenomenon due to IF absorption by growing TC can be observed. The Fig. 3.8C shows that after confluence the interstitial fluid pressure becomes positive during a while (see plot relative to 28h). Indeed, after confluence the initial gradient of IF pressure (green line in Fig. 3.8C) reverses since cells in the proliferative peripheral areas move toward the core so IF has to go in the opposite direction, as imposed physically by mass conservation. After 2 days of quick growth, experimentally and numerically, the MTCS reaches a state of linear and slow evolution and from that point onward, the IF flux will not qualitatively change.

To further analyze the reliability of the mathematical model we also exploit additional data of cell states inside MCTS presented in [4]. More specifically, we reproduced numerically a CT26-MCTS growing in free conditions and the capsule CCTS. Fig. 3.9A and Fig. 3.9B present experimental cell densities (total, proliferative and necrotic, plain lines) at $50\,\mu$m radius for the free MCTS and 26h after confluence for CCTS. These experimental results are qualitatively compared with the numerical simulations (Fig. 3.9A and Fig. 3.9B for the free and confined cases respectively, dotted lines). Both configurations show a reasonable agreement with the experimental results, knowing that none of these quantities have been used for the parameters identification and are very far of the conditions of calibration. This is a supplementary argument that showcases the adaptability of this physical based modeling. The accuracy of the results Fig. 3.9A and B have been quantified by RMSE ($2.5\,\mu$m sampling on experimental data) in Table 3.2. We used the data available in the free MCTS (FGS), to normalize S^t by the experimental nuclei density at $r = 0$. Unfortunately, in this work, we did not have access to a large sample size to evaluate our numerical assumptions against experimental data.

On the experimental estimation of the tumor cell pressure

As explained in the work of Alessandri et al. [4], the pressure in the tumor cell phase is directly related to the confinement pressure arising from the interaction between the capsule and the MCTS calculated with equation 3.3. However, from the perspective of porous media mechanics, this confinement pressure essentially corresponds to the total Cauchy stress tensor and not to the pressure in the tumor cell phase. Actually, in the post-confluence stage, the rise of cell pressure induces the deformation of the alginate shell but also the deformation of the extracellular matrix (constituting the solid scaffold of the MCTS). Thanks to spherical symmetry of the problem, it is easy to derive an equation which allows us calculating the 'experimental' solid pressure, p^s, from the confinement pressure (calculted with equation 3.3) and the stiffness of the ECM (here assumed equal to 1kPa). From the effective stress principle and accounting for assumed elastic constitutive behavior, the solid pressure can be estimated with the following equation

$$p^s = P_{\text{conf}}(t) + 3K_T \frac{u(R_{\text{in}}(t))}{R_{\text{in}}(t)} \tag{3.38}$$

with K_T Bulk's modulus of the ECM scaffold.

From the solid pressure, the tumor cell pressure could be estimated by means of an experimental evaluation of the tumor cell saturation degree. The experimental confinement stress evaluated with equation 3.3 and the solid pressure evaluated with equation 3.38 are depicted in figure 3.10 for CCT0. In figure 3.10, numerical results for the temporal evolution of σ_{rr}, p^s and p^t within the MCTS (proximity of the alginate shell) are also reported. It can be observed that the final tumor cell pressure is almost 20% higher than the magnitude of the computed radial stress. This difference is however strictly related to the Bulk's modulus of the ECM scaffold for which may also vary during the experiment due to the production of extracellular matrix by tumor cells. The mechanical properties of the ECM have not been investigated in this study, thus these results are theoretically interesting but only have a qualitative value.

A deviation of the solid pressure and the radial stress from respective experimentally-derived values can be observed in the figure. The reason is that equation 3.3 has been derived assuming a non compressible alginate while in our calculation we assumed a Poisson ratio $\nu = 0.4$. When strain becomes relatively large in the numerical case the reduction of the thickness due to geometrical non-linearity is smaller than that of the assumed non compressible case, so the alginate shell is more rigid and consequently the pressure is higher.

3.2.4 Discussion

We showed, in this paper, the *in silico* reproduction of MCTS growth experiments in various physical conditions: free and encapsulated within alginate shells of different sizes and thicknesses. Thanks to a robust validation protocol, variance-based sensitivity analysis, distinct training and validation datasets, all these physical conditions have been successfully simulated by means of a bio-chemo-poromechanical mathematical model. It is important to notice that only one set of parameters, identified on a training dataset (reported in Fig. 3.1B and C), has been used for all the numerical simulations performed.

In the frame of the parameter identification process, a local second-order sensitivity analysis has revealed that the parameters of the model become almost independent under confinement (see Fig. 3.5D) within a range of $\pm 10\%$ around the usual literature values. Results of sensitivity analyses also demonstrate that, if the tumor is free to grow, the only influential parameters are the proliferation and the oxygen consumption rates. Conversely, when the tumor growth is constrained by the presence of the alginate capsule, the value of the critical pressure beyond which mechanical stresses inhibit its growth is the main driver. The mathematical model remains reliable even when the growth conditions of the MCTS are modified. This is an advancement with respect of other numerical studies based on poromechanics which are quite qualitative [211] or solely connected with a reference experimental setup [162].

However, this advancement is only a first step to a more robust *in vitro*/*in silico* process. From experimental side, a wider set would raise the confidence on the calibration of the parameters and the validation of the model; repeating this experimental protocol on other standardized cancer cell-lines (glioma, breast cancer, prostate cancer, to name a few) would allow enlarging the understanding if this mechano-biological framework and its digital twinning. From the numerical side, if a detailed but local sensitivity analysis accelerate the calibration process, its relevance concerns only a part of the parameters' space, and only these experimental data. Attempt of global sensitivity without a data bias, or extent these local analyses to other cell-line would be a desirable next step.

The mathematical model is the digital twin MCTS-capsule system since it takes into account mechanistically its real multiphase nature; hence, the numerical results add new dimensions to the Cellular Capsule Technology. In particular, it is shown that the pressure estimated experimentally is illustrative of the evolution of the solid pressure, p^s, (in the sense of porous media mechanics, see Eq.3.21) and not of the pressure sustained by the cells, p^t. The pressure p^t is always higher than p^s especially during the first phase after confluence (when the MTCS still contains an important volume fraction of IF). This fact is the direct consequence of the fact that each phase of the MCTS (*i.e.*, the ECM, the IF and the TC) has its own stress tensor and that the pressure obtained experimentally by inverse analysis is an average pressure (see Fig. 3.10). The multiphase approach also reveals other behaviors not measurable experimentally. We observe for instance that after confluence there is a suction of IF from the extra-capsular domain and that cells move from the proliferating rim towards the core of the MCTS where they become necrotic.

Although these emerging results are inspiring, several physical phenomena are not represented and could lead to valuable insight from the experimental and modeling point of view. The mechanical stress can be the primer of cell necrosis [48] and the CCT experimental framework would be a interesting framework to measure this mechano-biological interplay. The phenotype switch of tumor cells under homeostatic pressure studied in [192] could be modeled and revealed by a alternating CCT growth and free growth on the same aggregate. In this specific study, we hold a line which we wanted simple, by limiting the number the modeled physical phenomena, light, our code can be run on a eight-core processor, and easily adaptable to any geometry and cell-line.

In 2020, mathematical modeling in oncology begins to enter a stage of maturity; today mathematical models of tumor growth tend to clinical applications and therefore must be really predictive and funded on measurable or at least quan-

tifiable parameters having, as much as possible, a sound physical meaning. This motivated this paper which presents not only a mechanistic bio-chemo-poromechanical model but also a *modus procedendi* to achieve a suitable predicative potential and, with intercession of sensitivity analysis, to quantify relative relevance of mechanisms underlying tumor growth phenomenology.

Acknowledgments

The results presented in this paper were carried out using the HPC facilities of the University of Luxembourg [251] (see `https://hpc.uni.lu`).

3.2.5 Supporting information

Appendix A. Computational framework The model has been coded in Python and C++ in the open-source FEniCS framework [7] with an incremental monolithic resolution of the mixed finite element (FE) formulation. The monolithic resolution allows us reducing substantially the computational time compared with staggered resolution methods usually adopted (*e.g.*, see [216]). Whereas spherical symmetry is assumed in experimental results, we have chosen cylindrical symmetry to preserve the generality and the adaptability of the FE mesh and formulation. Even if the computational time is more important, it remains reasonable: 3 hours in a single core of an average laptop ; 1D spherical formulation would have forced us to quit classical FE formulation or to design, for each case, a specific finite difference formulation.
An updated lagrangian approach has been adopted to account for geometrical nonlinearities, the incremental resolution allows us updating primary variables as follows:

$$\mathbf{X}_{n+1} = \mathbf{X}_n + \delta\mathbf{X} \tag{3.39}$$

with $\delta\mathbf{X}$ the vector of unknowns

$$\delta\mathbf{X} = \begin{pmatrix} \delta u_r^s \\ \delta u_z^s \\ \delta p^l \\ \delta p^{tl} \\ \delta \omega^{\bar{nl}} \end{pmatrix}$$

After each time step, the space $\mathcal{X}^s \in \mathbb{R}^2$ is updated:

$$\mathcal{X}_{n+1}^s = \mathcal{X}_n^s + \delta\mathbf{u}^s$$

Choice of the element

For all mixed FE problem with vectorial and scalar coupled unknowns, the chosen finite element should verify the inf-sup condition, that is to say, should preserve the coercivity of the bilinear form (see [25] p.223-230). A simple choice is the Taylor-Hood element, with a Lagrange element of order $k \geq 1$ for the scalar unknowns and order $k+1$ for the vectorial one. However, modelling an encapsulated tumor growth implies a very sharp gradient at the capsule inner radius for the pressure difference p^{tl}, between l and t phases. The linear approximation of the Lagrange element of order 1 could not describe it, except at the cost of an extremely refined mesh at the interface, and the error could provoke *numerical infiltration* of tumor cells in the alginate capsule (see Fig. 3.11). To avoid this phenomenon, the composite Taylor-Hood element has been set to a higher order, precisely the mixed FE formulation in FEniCS uses the composite Taylor-Hood element $P_3(\mathbb{R}^2), [P_2(\mathbb{R})]^3$. The demonstration of Lax-Milgram theorem for this type of mixed problem could be found in the *Encyclopedia of Computational Mechanics*, Vol.1, p.149-202 [231].

Choice of mesh element size

The mixed FE problem has been computed on 5 different meshes, with uniform element sizes $dh = 50, 20, 10, 5$ and $2.5\,\mu$m. To measure the FE solution degradation the primary variable $\omega^{\bar{nl}}$, the oxygen mass fraction, has been monitored at the spheroid center for 4 days (see Fig Fig. 3.12) . The thinner mesh of element size $dh = 2.5\,\mu$m has been used as a reference for the RMSE. Despite an important increase of the computation time, the mesh element size of $dh = 5\,\mu$m has been chosen to restrict the relative degradation of the FE solution to $RMSE = 0.01$ (see Table 3.3).

Verification of the FE formulation with an analytical solution

If this system is considered with a single-phase flow into a porous medium under a constant load with the right boundary conditions, one obtains the problem as known as Terzaghi's consolidation, which has an analytical solution [253]. The system, under a constant load $\mathbf{T}$, is reduced to two primary variables the displacement of the solid scaffold $\mathbf{u}^s$ and the pressure of the single phase fluid p^l:

$$\begin{cases} \nabla.\mathbf{v}^s - \nabla.\left[\dfrac{k}{\mu}\nabla p^l\right] = 0 \text{ on } \Omega \\ \\ \nabla.\bar{\bar{t}}_t = 0 \text{ on } \Omega \\ \\ \nabla.\bar{\bar{t}}_t = -\mathbf{T} \text{ on } \Gamma_s \end{cases} \tag{3.40}$$

$$\text{with } \mathbf{T} = \begin{pmatrix} 0 \\ p_0 \end{pmatrix}$$

The fluid is free to escape only at the loaded boundary, this boundary condition is known as drained condition. The analytical solution of this problem is:

$$p^l(y,t) = p_0 \frac{4}{\pi} \sum_{k=1}^{\infty} \frac{(-1)^{k-1}}{2k-1} \cos\left((2k-1)\frac{\pi}{2}\frac{y}{L}\right) \exp\left((2k-1)^2 \frac{\pi^2}{4}\bar{t}\right) \tag{3.41}$$

With the characteristic time of the consolidation $\bar{t}$, equal to $\frac{c_v t}{L^2}$, L sets to $100\,\mu$m and c_v, the consolidation coefficient:

$$c_v = \frac{k}{\mu_l}(\lambda + 2\mu)$$

where λ and μ are Lamé constants of the solid scaffold, k is its intrinsic permeability and μ_l the fluid dynamic viscosity. The addition of the RMSE of the 4 samples at $\bar{t} = 0.01, 0.1, 0.5, 1$ (see Fig. 3.15) with the analytical solution as reference gives $\sum RMSE = 0.0028$. The surface error for different element sizes dh and time steps dt is in Fig. 3.15(right).

Appendix B. Sensitivity analysis For the sensitivity analysis, the experimental input data were:

- for the free MCTS, the volume monitored over a time span from day 1 to day 4. These data are denoted $Y_{\text{free}}^{\text{exp}}$
- for the encapsulated MCTS CCT0 the capsule radial displacement one day after confluence and the corresponding analytical pressure (i.e. incompressible elastic membrane). We chose the capsule of inner radius $= 100\,\mu$m and thickness $= 34\,\mu$m, presented as the reference case in [4]. These data are denoted $Y_{\text{conf}}^{\text{exp}}$.

We performed a variance-based sensitivity study of the FE solution on the parameters, both on the free and encapsulated MCTS, as follows:

- A first-order analysis, the 7 parameters are disturbed one at a time respectively to an 8-points grid.
- Interaction analysis, the 21 parameters tuples are evaluated at the 2 extreme points of the grid.

All the results were interpreted with a polynomial model in order to quantify their weights in the FE solution variance, referred to as Sobol indices.

First-order analysis

Each parameter is disturbed one at a time respectively to this grid $[-10, -5, -2, -1, +1, +2, +5, +10]\%$, giving the corresponding $\tilde{J}_{\text{free}}$ and $\tilde{J}_{\text{conf}}$. The relative variations of the cost functions were calculated as follows:

$$\text{Var}_{\text{free}} = \frac{\tilde{J}_{\text{free}} - J0_{\text{free}}}{J0_{\text{free}}} \quad \text{and} \quad \text{Var}_{\text{conf}} = \frac{\tilde{J}_{\text{conf}} - J0_{\text{conf}}}{J0_{\text{conf}}} \tag{3.42}$$

where $J0_{\text{free}}$ and $J0_{\text{conf}}$ are the costs with the parameters at their generic values. In order to quantify the impact of each parameter, the following linear model was set:

$$\text{Var} = 1 + \sum_i \theta_i \alpha_i \tag{3.43}$$

where α_i is an auxiliary parameter $\in [-1, +1]$ representing the perturbations of the i^{th} parameter along the grid and θ_i the slope of the variation.

In a first-order analysis, the influence of the i^{th} parameter is given by the Sobol indices:

$$S_i = \frac{\theta_i^2}{\sum_i \theta_i^2} \tag{3.44}$$

The results for the free and encapsulated configurations are reported in Tables 3.4 and 3.5.

Interaction analysis

As the independence of physical phenomenons involved in encapsulated configuration is one our major modeling assessment, the interaction between parameters has also been studied. The 21 tuples have been evaluated at the 2 extreme values of the grid for each configuration. The corresponding polynomial model becomes:

$$\text{Var} = 1 + \sum_i \theta_i \alpha_i + \sum_{ij, i>j} \theta_{ij} \alpha_i \alpha_j \tag{3.45}$$

with the respective Sobol indices:

$$S_i = \frac{\theta_i^2}{\sum_i \theta_i^2 + \sum_{ij,i>j} \theta_{ij}^2} \quad \text{and} \quad S_{ij} = \frac{\theta_{ij}^2}{\sum_i \theta_i^2 + \sum_{ij,i>j} \theta_{ij}^2} \tag{3.46}$$

The results for the free and encapsulated configurations are reported in Tables 3.6 and 3.7.

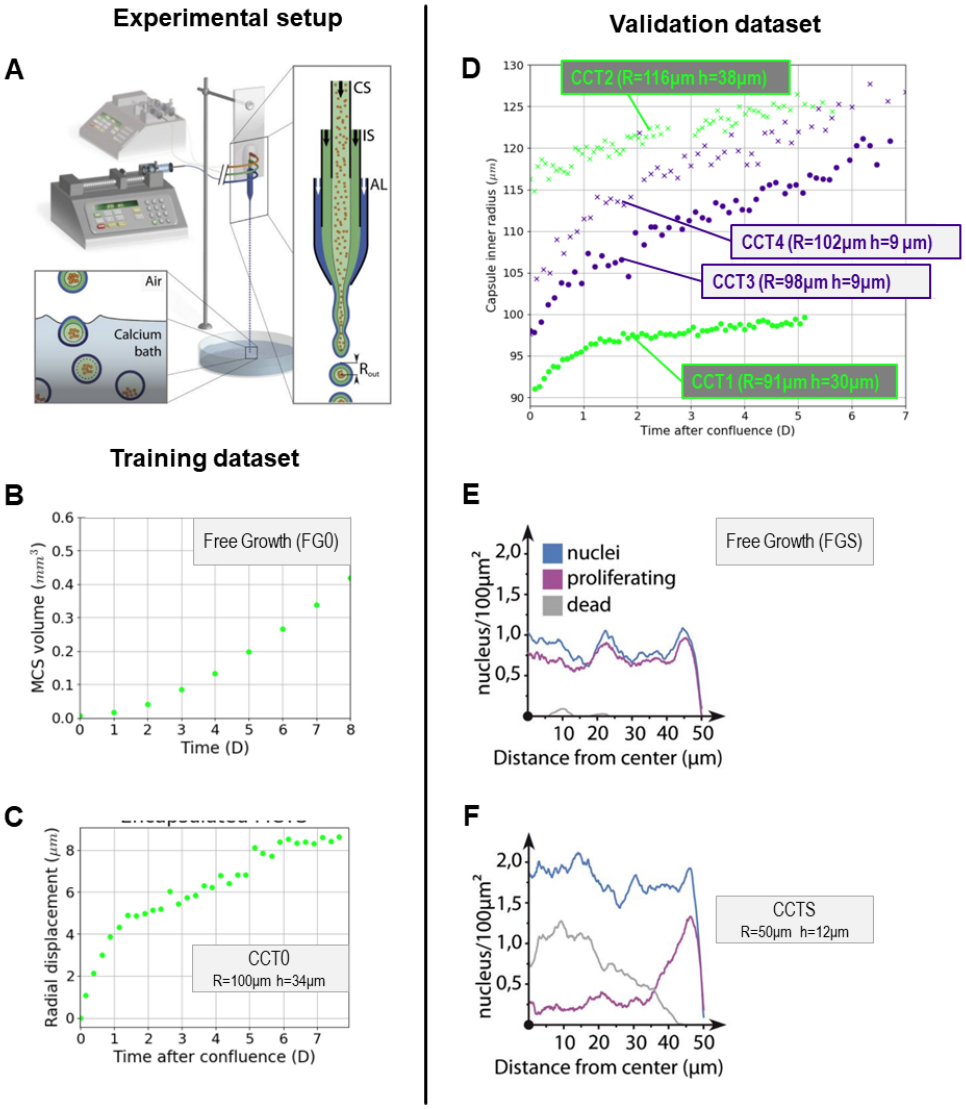

Figure 3.1: **CCT experimental setup and data.** **A** CCT microfluidic co-extrusion device; the enlarged view of the chip shows the three-way configuration, with cell suspension (CS), intermediate solution (IS), and alginate solution (AL), respectively, flowing into the coaligned capillaries. **B**-**C** Experimental training data: **B** free growth MCTS control group (FG0), the volume is monitored over a time span of 8 days; **C** encapsulated MCTS, the radial displacement of the capsule (CCT0) is monitored over a time span of 8 days. **D** Validation dataset: two capsules, denoted as thick CCT1 and CCT2; two capsules, denoted as thin CCT3 and CCT4. Their strains are monitored over a time span of 5 to 7 days.
E-**F** Experimental quantification of cell nuclei (blue), proliferating cells (purple),and dead cells (gray) along the radius for small free (FGS), **E**, and small confined (CCTS), **F**, spheroids [4].

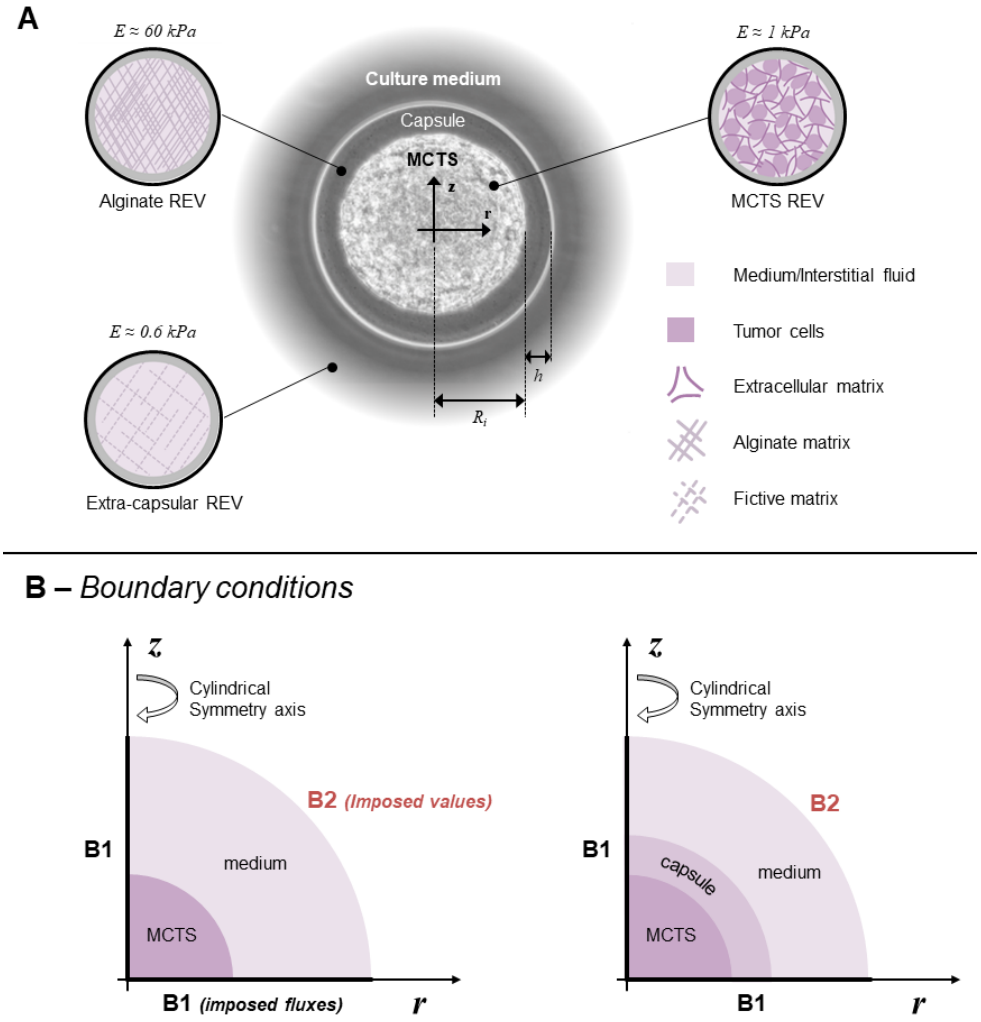

Figure 3.2: **The capsule model. A** Geometrical description of the capsule and assumed representative elementary volumes (REV): Three spatial domains modeled within the same mathematical framework: MCTS REV (consisting of tumor cells, interstitial fluid (IF) and extracellular matrix), the alginate shell (only IF phase within a solid scaffold of Young Modulus $E_{\text{alg}} = 60\text{kPa}$) and extra-capsular domain (only IF phase within a fictive solid scaffold of Young Modulus $E_{\text{fict}} = 0.6\text{kPa}$) enforced by the theoretical framework. **B** Computational boundary condition for the free (left) and confined (right) MCTS. At the bondary B1 symmetry conditions of no-normal flow/displacement are assumed while Dirichlet boundary conditions (e.g., prescribed oxygen concentration) are assumed at the boundary B2

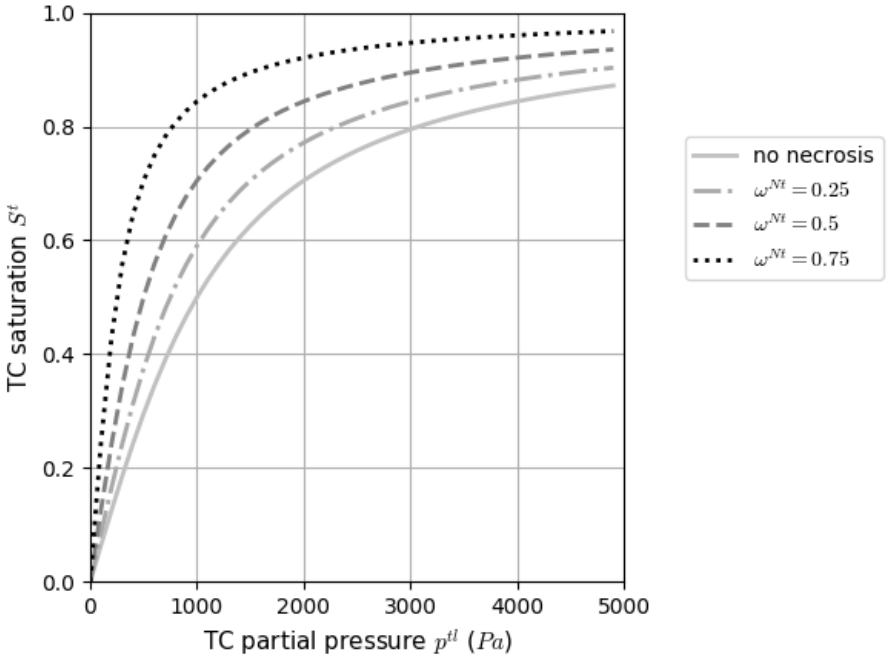

Figure 3.3: **Constitutive relationship between tumor cell partial pressure and saturation.** Tumor cell phase saturation S^t, with the parameter a (fixed to 1kPa in the figure), evolving with the necrotic fraction of the phase $\omega^{\bar{N}t}$

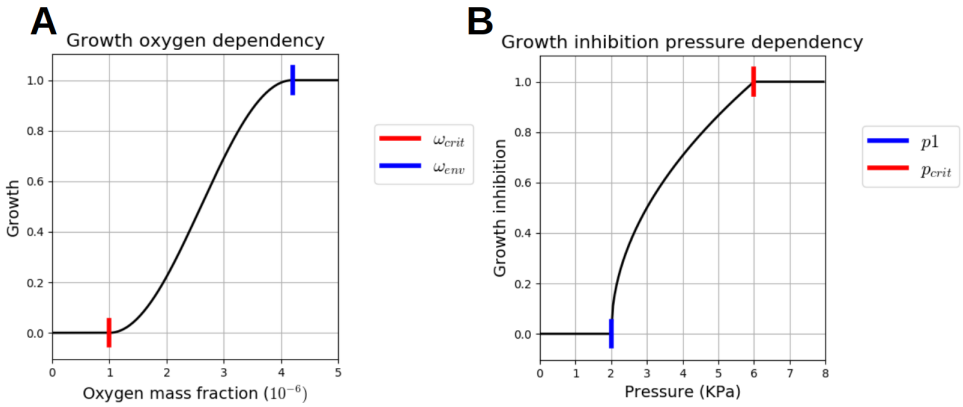

Figure 3.4: **Two mechano-biological laws A** $\mathcal{H}(\omega^{\bar{nl}}, \omega_{\text{env}}, \omega_{\text{crit}})$. The TC growth and nutrient consumption are dependent to the oxygen mass fraction $\omega^{\bar{nl}}$. If it is lower than ω_{crit}, the TC growth is stopped and the nutrient consumption is reduced to the metabolism needs only. If it is greater or equal to ω_{env}, the growth and the nutrient consumption are maximum. **B** $\mathcal{H}_p(p^t, p_{\text{crit}}, p_1)$. The TC growth and nutrient consumption are dependent to the TC pressure. If it is greater than p_1, the 2 processes begin to be strongly affected and if the TC pressure reaches p_{crit}, they are totally stopped.

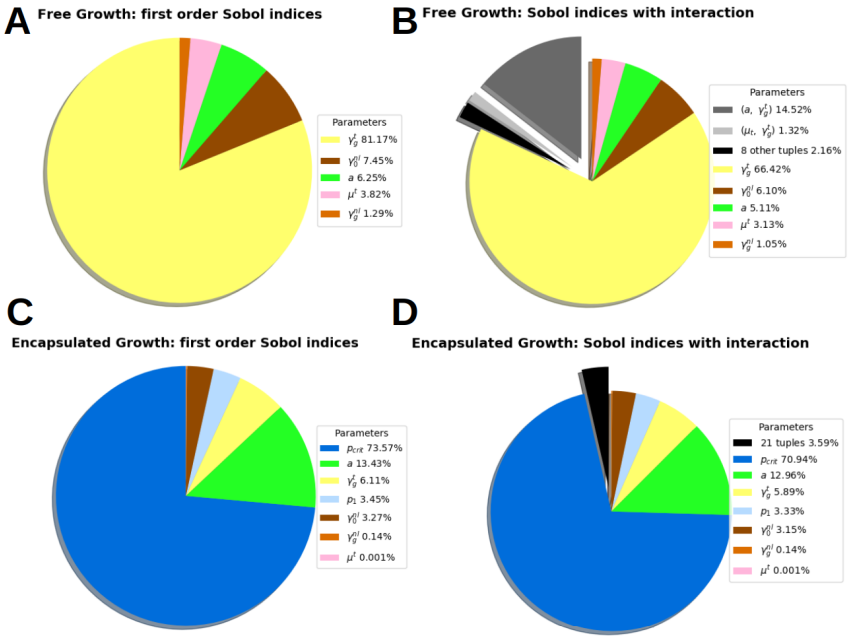

Figure 3.5: **Sobol indices of the solution sensitivity.** Sobol indices of the solution sensitivity on 7 parameters: μ_t the TC dynamic viscosity, the parameter a accounting for the joint impact of the ECM thinness and cell surface tension, γ_g^t the TC growth rate, γ_g^{nl} and γ_0^{nl} the oxygen consumption rate due to growth and quiescent metabolism respectively, p_1 and p_{crit}, two thresholds which govern the pressure-induced inhibition of the TC proliferation. Free MCTS configuration (top row). **A First-order analysis**: Only 5 parameters remain, the governing parameter is γ_g^t, the tumor cells growth rate, the sensitivity of the solution on the pressure parameters, p_1 and p_{crit}, is 0. **B Interaction**: among 10 parameters tuples, one is significant (a, γ_g^t) accounting for 14.5% of the solution variance. Thus, these two parameters are not independent and should identified together. The total variance of the solution shows that, considering all the interactions, the influence of each parameter alone is not qualitatively changed: γ_g^t from 81.1% to 66.4%, γ_0^{nl} from 7.4% to 6.1%, a from 6.2% to 5.1%. Encapsulated MCTS configuration (bottom row). **C First-order analysis**: the governing parameter is p_{crit} the inhibitory pressure of tumor cells growth (73.5% of the solution variance). **D Interaction**: the sum of 21 parameters tuples represents 3.6% of the solution variance (the detail of 21 tuples can be found in Variance-based local sensitivity analysis, table 3.7).

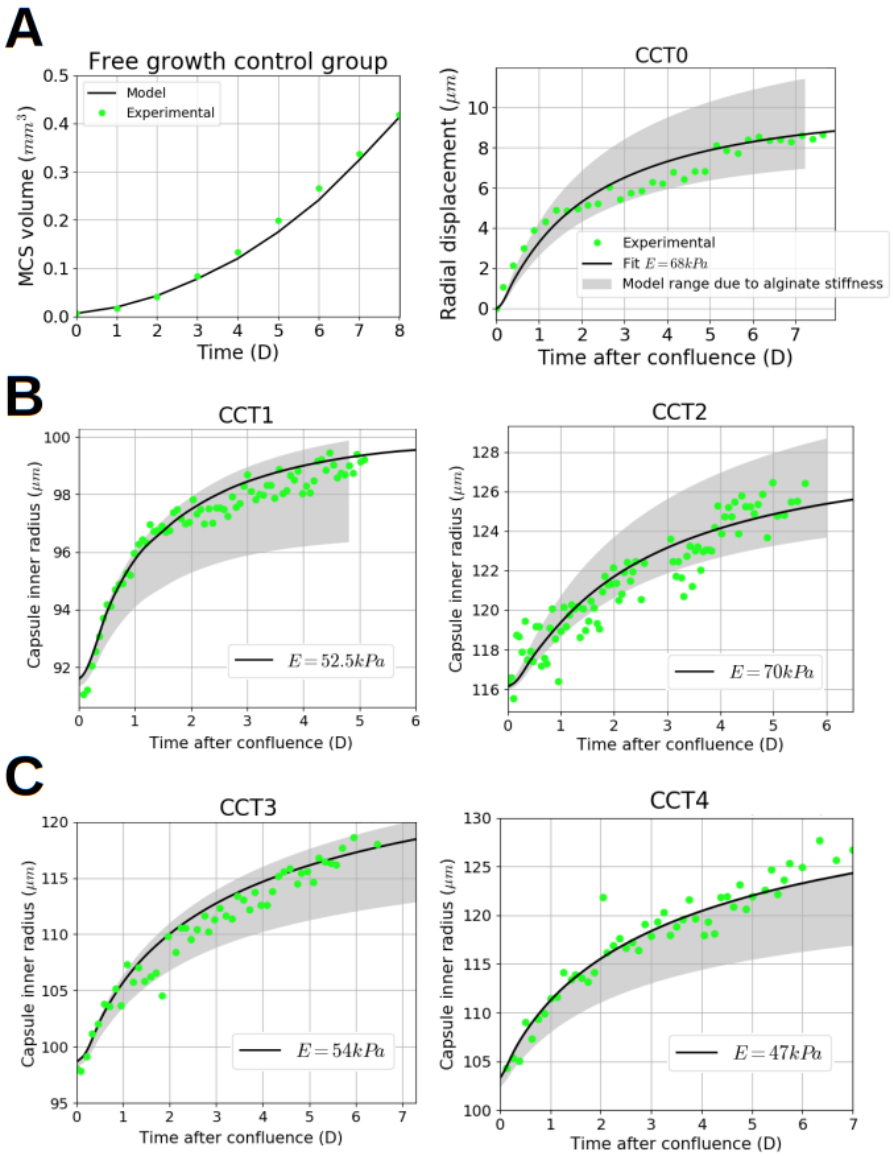

Figure 3.6: **Validation of the calibrated parameters.** Alginate Young's modulus was estimated in [4] as $E_{\text{alg}} = 68 \pm 21$ kPa. Simulations with the extreme values of E_{alg} give the range of possibilities of the optimized set predicted with the model. Experimental results, green dotted ; Numerical results with the optimized parameters set, black; Modeling range, grey filled. **A**. Left, free MCTS control group, Time (Day) versus MCTS volume (mm^3), the model fits the experimental data with a $RMSE = 0.031$. Right, CCT0. The fit uses the mean experimental value of the alginate stiffness $E_{\text{alg}} = 68$ kPa. The model fits the experimental data with a $RMSE = 0.124$. **B** Validation of the identified parameters on 2 thick capsules, CCT1 and CCT2. Time (Day) versus Capsule radius (μm). The experimental points are in the modeling range. Both capsule fit with $E_{\text{alg}} = 52.5$ kPa and $E_{\text{alg}} = 70$ kPa respectively. **C** Validation of the identified parameters on 2 thin capsules, CCT3 and CCT4.. Time (Day) versus Capsule radius (μm). Left, one capsule is fitted with $E_{\text{alg}} = 54$ kPa ; right, an important part the experimental points are outside of the modeling range.

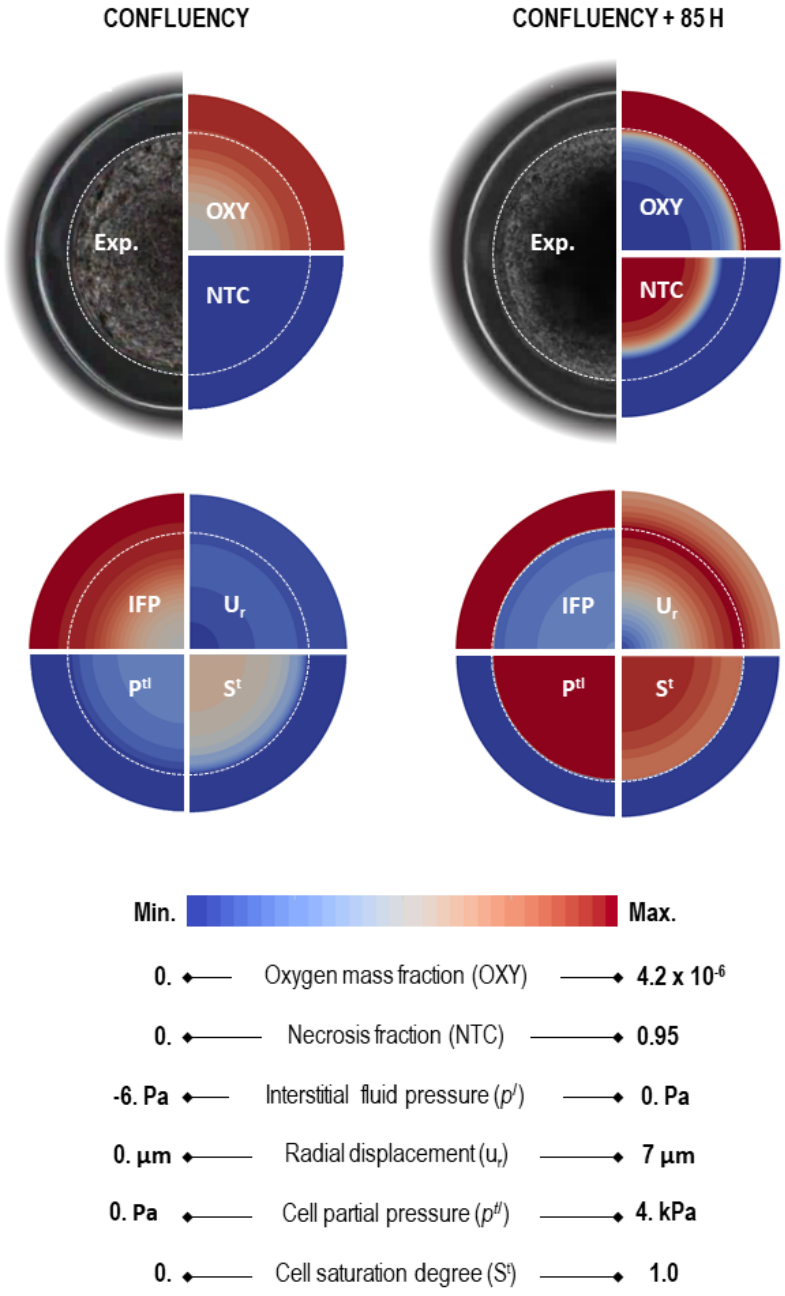

Figure 3.7: **Experimental microscopy image augmented by qualitative numerical results.** 6 physical quantities from numerical results of the mathematical model on CCT0: oxygen, necrotic tumor cells, interstitial fluid pressure, radial displacement, the pressure difference between the phases l and t and tumor cells saturation. Left, at confluence. Right, 85 hours after confluence.

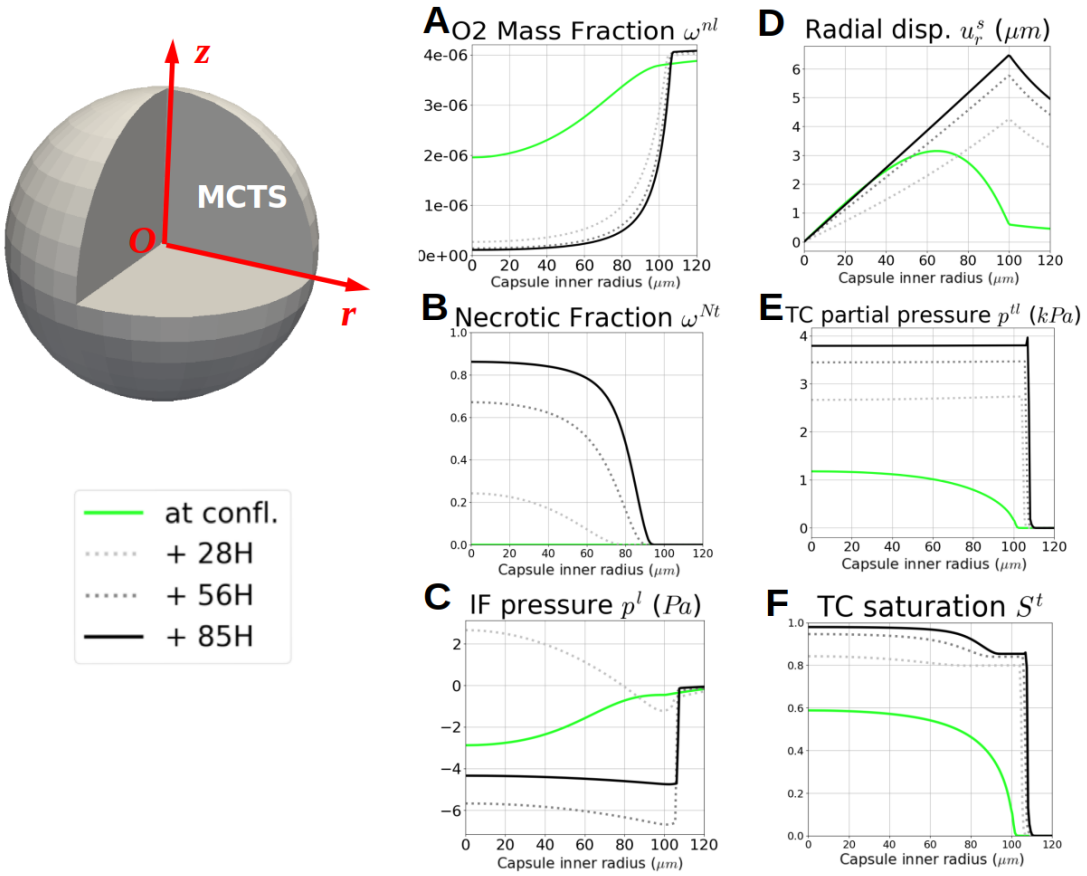

Figure 3.8: **Qualitative numerical results of CCT0 probed along the $r = z$ line.** Quantities probed at confluence, 85 hours after, and two intermediate times (28 and 56 hours): **A** oxygen, **B** necrotic fraction, **C** IF pressure, **D** ECM displacement, **E** TC pressure and **F** TC saturation. **A** and **B**: as mentioned in the experiments, 85 hours after confluence the viable space remaining for TC is a $20\,\mu$m thick rim. **C**: after confluence, IF is absorbed by growing TC, provoking a sucking phenomenon, as the cells activity decrease at the MCTS inner core, IF accumulates and its pressure becomes positive. As described in [4], after 2 days of quick growth, the MTCS reaches a state of linear and slow evolution. **D** and **E**: the capsule displacement is driven by TC pressure with the same overall dynamic. **E**, **F** and **B**: relation between the saturation of TC and their necrotic fraction, the TC aggregate density increases with necrotic core.

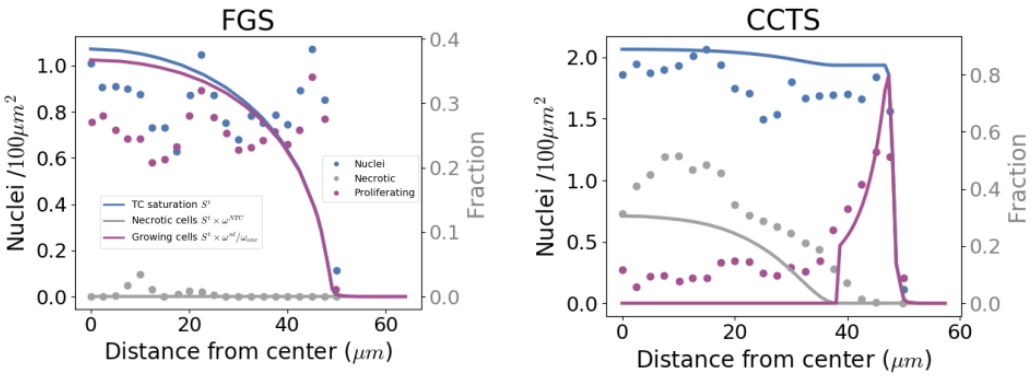

Figure 3.9: **Qualitative comparisons of proliferative and dead cells.** Quantification of proliferating and dead cells radial densities for free growth and CCTS: *in vitro-in silico* results. Experimental quantification of cell nuclei (blue), proliferating cells (purple),and dead cells (gray) along the spheroid radius ($2.5\,\mu$ m sampling). Numerical quantities: TC Saturation S^t, blue dotted; Necrotic saturation of TC $\omega^{Nt}S^t$, gray dotted; Growing TC fraction $\omega^t{}_{\text{grow}}$ (see Eq.3.31), purple dotted. **A**, FGS. **B**, CCTS, **B**, growth (from [4]). TC saturation almost doubles between the two configurations, in encapsulation, necrotic fraction occupy almost half of the TC phase and only a thin rim of the MTCS is viable. CCTS is very far of the conditions of parameters calibration, nevertheless *in vitro-in silico* comparison shows a reasonably good agreement, which is quantified Table 3.2.

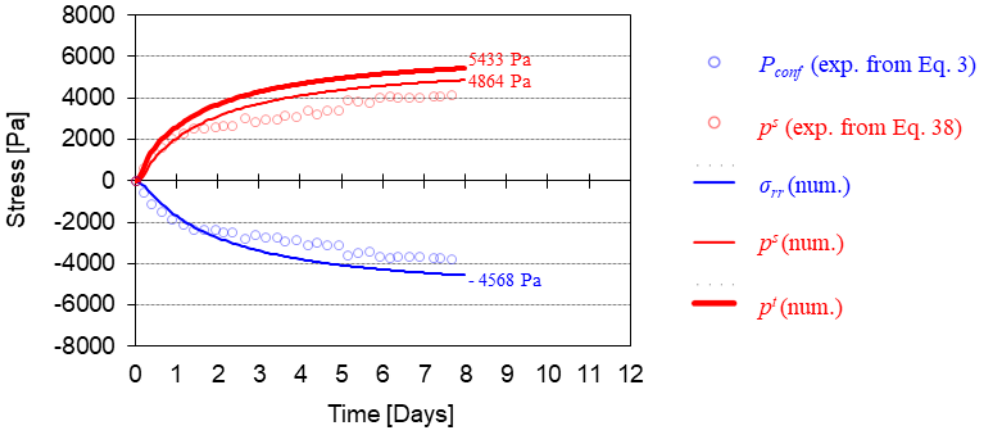

Figure 3.10: **Comparison between numerical stress/pressures and the ones retrieved from the experimental results of CCT0.** Blue circles are the confinement pressure obtained experimentally by inverse analysis with equation 3.3; red circles is the solid pressure, p^s, obtained from the measured displacement using equation 3.38; solid lines are σ_{rr}, p^s and p^t obtained numerically.

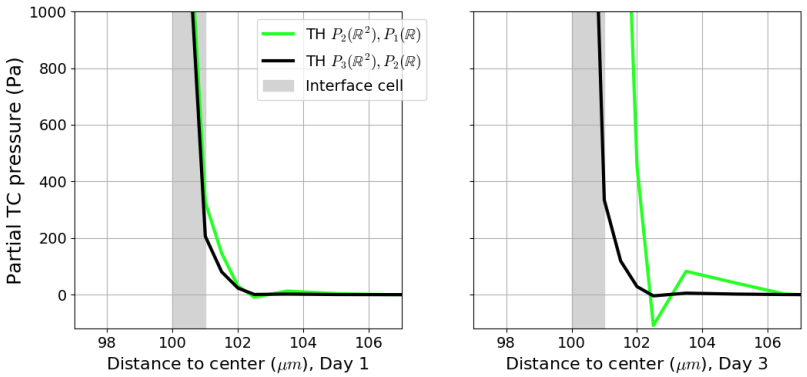

Figure 3.11: **Choice of the element.** Composite Taylor-Hood $P_2(\mathbb{R}^2), [P_1(\mathbb{R})]^3$, green ; composite Taylor-Hood $P_3(\mathbb{R}^2), [P_2(\mathbb{R})]^3$, black. The linear approximation $P_1(\mathbb{R})$ of the pressure difference between l and t phases at the capsule interface (Interface element shared, green) is poor (Left, Day 1) and provoke numerical infiltration of tumor cells into the alginate capsule (Right, Day 3). The quadratic approximation $P_2(\mathbb{R})$ (Interface element shared, black) does not provoke numerical infiltration.

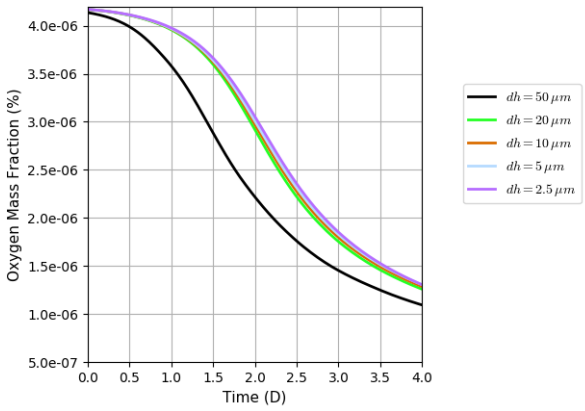

Figure 3.12: **Sensitivity of the solution related to mesh refinement.** The numerical oxygen mass fraction, $\omega^{\bar{n}l}$, at the center of the spheroid has been monitored during six days for five different mesh finite element sizes dh. ($dh = 50\,\mu$m, black ; $dh = 20\,\mu$m, green ; $dh = 10\,\mu$m, brown; $dh = 5\,\mu$m, light blue ; $dh = 2.5\,\mu$m, purple)

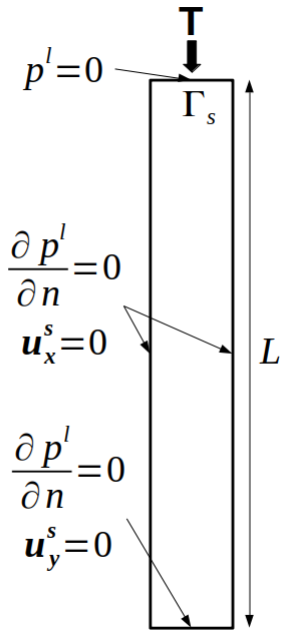

Figure 3.13: **Boundary conditions of the Terzaghi's problem.** The load is applied at the top face, where the fluid is free to espace, say under drained condition. The five remaining faces are under slip condition for the displacement $\mathbf{u}^s$ and no flux condition for the fluid pressure p^l.

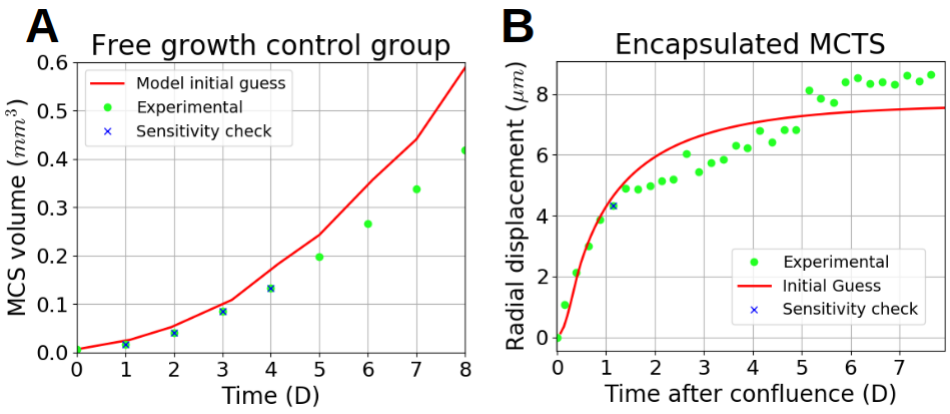

Figure 3.14: **Results with the 7 parameters at their initial values.** $\gamma_g^t = 4.10^{-2}$, $\gamma_0^{nl} = 6.10^{-4}$, $a = 800$, $p_1 = 1800$, $p_{\text{crit}} = 4000$ (see Table 3.1). Experimental, green dot ; Model, red ; Sensitivity evaluation, blue x. Left: FG0 ; Right: CCT0

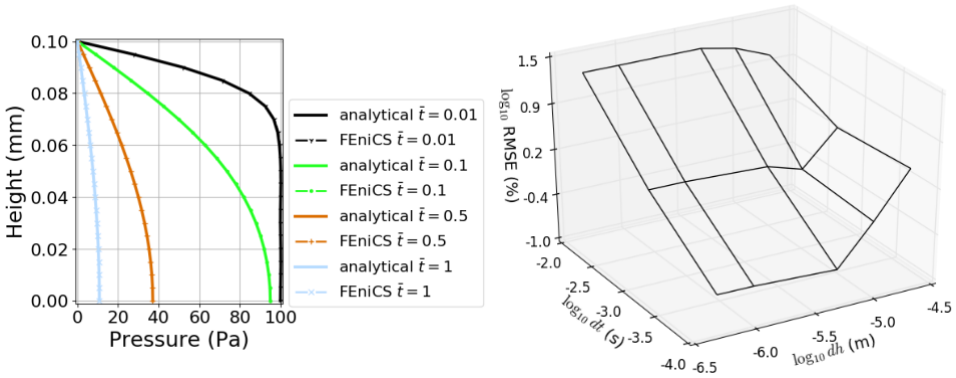

Figure 3.15: **Comparison between analytical solution and numerical result.** Left: qualitative comparison between analytical solution of Terzaghi's problem and FEniCS computation. (4 comparisons at characteristic time of consolidation $\bar{t} = 0.01, 0.1, 0.5, 1$). Right: quantitative comparison, error surface between Terzaghi's analytical solution and FEniCS computation. (x axis: $\log_{10}$ of element size dh ; y axis: $\log_{10}$ of dt ; z axis: $\log_{10}$ of RMSE). The minimum RMSE$= 0.0028$ is reached at $dh = 5\,\mu$m, $dt = 1e^{-4}$

Parameter	Symb.	Generic	Unit	Optimized
ECM network thinness	a	800	Pa	890
Dynamic viscosity of TC	μ_t	36	Pa.s	negligible
TC growth rate	γ_g^t	$4 \cdot 10^{-2}$	kg/(m^3.s)	$3.33 \cdot 10^{-2}$
TC growth O_2 consump.	γ_g^{nl}	$4 \cdot 10^{-4}$	kg/(m^3.s)	negligible
TC metabolism O_2 consump.	γ_0^{nl}	$6 \cdot 10^{-4}$	kg/(m^3.s)	$6.65 \cdot 10^{-4}$
Start TC growth inhibitory	p_1	1800	Pa	1432
Stop TC growth	p_{crit}	4000	Pa	5944

Table 3.1: **Parameters for the CT26 cell line. Source of the generic values: [50], [216], [162], [211]**.

in vitro-in silico results	RMSE control group	RMSE CCTS
nuclei/S^t	0.317	0.486
proliferative/$\omega^t{}_{\text{grow}} S^t$	0.303	0.327
necrotic/$\omega^{Nt} S^t$	0.026	0.238

Table 3.2: **Quantitative comparison between in vitro-in silico results, for FGS radius and CCTS.**

	$dh = 50\,\mu$m	$dh = 20\,\mu$m	$dh = 10\,\mu$m	$dh = 5\,\mu$m
$RMSE(dh, 2.5\,\mu\text{m}, 400/dh)$	0.182	0.032	0.019	0.010

Table 3.3: **Relative degradation of the solution due to mesh element size.** Measured by root mean square, the reference being the thinner mesh with a mesh element size of $dh = 2.5\,\mu$m.

Parameter	θ	$S_i(\%)$
a	0.2554	6.25
μ_t	-0.1998	3.82
γ_g^t	0.9205	81.17
γ_g^{nl}	-0.1161	1.29
γ_0^{nl}	-0.2790	7.45
p_1	0	0
p_{crit}	0	0

Table 3.4: **Sobol indices of the first-order sensitivity analysis of the FG0 configuration.**

Parameter	θ	$S_i(\%)$
a	$0,0550$	13.43
μ_t	$-0,0006$	0.001
γ_g^t	$0,0371$	6.11
γ_g^{nl}	$-0,0056$	0.14
γ_0^{nl}	$-0,0271$	3.27
p_1	$0,0279$	3.45
p_{crit}	$0,1288$	73.57

Table 3.5: **Sobol indices of the first-order sensitivity analysis of the encapsulated growth configuration CCT0.**

Parameter	$S_i(\%)$
a	5.11
μ_t	3.13
γ_g^t	66.42
γ_g^{nl}	1.05
γ_0^{nl}	6.10
p_1	0
p_{crit}	0
Parameter tuples	$S_{ij}(\%)$
$(a,\ \mu_t)$	0.06
$(a,\ \gamma_g^t)$	14.52
$(a,\ \gamma_g^{nl})$	0.02
$(a,\ \gamma_0^{nl})$	1.10^{-4}
$(\mu_t,\ \gamma_g^t)$	1.32
$(\mu_t,\ \gamma_g^{nl})$	0.06
$(\mu_t,\ \gamma_0^{nl})$	0.38
$(\gamma_g^t,\ \gamma_g^{nl})$	1.20
$(\gamma_g^t,\ \gamma_0^{nl})$	0.21
$(\gamma_g^{nl},\ \gamma_0^{nl})$	0.37

Table 3.6: **Sobol indices of the interaction sensitivity analysis of the FG0 configuration.**

Parameter	$S_i(\%)$
a	12.96
μ_t	0.001
γ_g^t	5.89
γ_g^{nl}	0.13
γ_0^{nl}	3.15
p_1	3.33
p_{crit}	70.94
Parameter tuples	$S_{ij}(\%)$
$(a,\ \mu_t)$	0.01
$(a,\ \gamma_g^t)$	0.003
$(a,\ \gamma_g^{nl})$	0.01
$(a,\ \gamma_0^{nl})$	0.02
$(a,\ p_1)$	0.009
$(a,\ p_{\text{crit}})$	0.02
$(\mu_t,\ \gamma_g^t)$	0.02
$(\mu_t,\ \gamma_g^{nl})$	5.10^{-6}
$(\mu_t,\ \gamma_0^{nl})$	0.007
$(\mu_t,\ p_1)$	0.003
$(\mu_t,\ p_{\text{crit}})$	0.7
$(\gamma_g^t,\ \gamma_g^{nl})$	0.02
$(\gamma_g^t,\ \gamma_0^{nl})$	0.01
$(\gamma_g^t,\ p_1)$	5.10^{-4}
$(\gamma_g^t,\ p_{\text{crit}})$	0.08
$(\gamma_g^{nl},\ \gamma_0^{nl})$	0.01
$(\gamma_g^{nl},\ p_1)$	0.002
$(\gamma_g^{nl},\ p_{\text{crit}})$	0.87
$(\gamma_0^{nl},\ p_1)$	0.01
$(\gamma_0^{nl},\ p_{\text{crit}})$	1.30
$(p_1,\ p_{\text{crit}})$	0.42

Table 3.7: **Sobol indices of the interaction sensitivity analysis of the encapsulated growth configuration CCT0.**

Chapter 4

Ex vivo cortex tissue poromechanical modeling

Describing the mechanical behavior of the brain tissue as a holistic manner is a task of an overwhelming difficulty. The brain organ possesses three fluid networks - cerebro-spinal fluid, blood and interstitial fluid -, impervious membranes as dura mater, highly diffusive fibers with white matter tracts [120], and a strong spatial heterogeneity of its mechanical properties. This heterogeneity can be divided into four main regions: cortex, corona radiata, basal ganglia and corpus callosum [31]. As glioma more commonly appears in the cortex, we decided to focus on this specific location. Forte *et al.* in [87] deeply studied the effects of temperature and dehydration in the brain tissue, underlying their strong influence. For instance, all other conditions remaining equal, temperatures of $24°$C and $37°$C will lead to a tissue stiffness 40% lower. Therefore, in this chapter, our modeling will only focus on cortex tissue, at constant temperature and humidity.

4.1 Article

Contribution (CRediT author statement)

Conceptualization, Methodology, Software, Validation, Investigation, Writing – original draft, Visualization

Cortex tissue relaxation and slow to medium load rates dependency can be captured by a two-phase flow poroelastic model

Urcun Stéphane[1,2,3], Rohan Pierre-Yves[1], Sciumè Giuseppe[3], Bordas Stéphane P.A.[2*],

1 Institut de Biomécanique Humaine Georges Charpak, Arts et Metiers Institute of Technology, Paris, France

2 Institute for Computational Engineering Sciences, Department of Engineering Sciences, Faculté des Sciences de la Technologie et de Médecine, Université du Luxembourg, Campus Belval, Luxembourg

3 Institut de Mécanique et d'Ingénierie, Université de Bordeaux, Talence, France

* stephane.bordas@alum.northwestern.edu

Abstract

This paper investigates the complex time-dependent behavior of cortex tissue, under adiabatic condition, using a two-phase flow poroelastic model. Motivated by experiments and Biot's consolidation theory, we tackle time-dependent uniaxial loading, confined and unconfined, with various geometries and loading rates from $1\,\mu$m/s to $100\,\mu$m/s. The cortex tissue is modeled as the porous solid saturated by two immiscible fluids, with dynamic viscosities separated by four orders, resulting in two different characteristic times. These are respectively associated to interstitial fluid and glial cells. The partial differential equations system is discretised in space by the finite element method and in time by Euler-implicit scheme. The solution is computed using a monolithic scheme within the open-source computational framework FEniCS. The parameters calibration is based on Sobol sensitivity analysis, which divides them into two groups: the tissue specific group, whose parameters represent general properties, and sample specific group, whose parameters have greater variations. Our results show that the experimental curves can be reproduced without the need to resort to viscous solid effects, by adding an additional fluid phase. Through this process, we aim to present multiphase poromechanics as a promising way to a unified brain tissue modeling framework in a variety of settings.

4.2 Introduction

The biomechanical characterization of human brain tissue and the development of appropriate mechanical models is crucial to provide realistic computational predictions. These predictions can assist in understanding the mechanical environment involved in neurodevelopment and neurological disorders [30, 221], in simulating traumatic brain injury, to investigate the mechanical pathogenesis of head trauma [18] and in studying head injuries and developing protection systems [205]. Mathematical modeling is also the key to devising brain surgery simulation for training, assistance and guidance [35, 36].

From an experimental perspective, several sophisticated mechanical tests have been proposed and conducted both on human and animal brain tissue in the past decades (see [34] for a complete review). These have consistently shown that brain tissue is non-linear, asymmetric in tension-compression and sensitive to loading rates. Moreover, grey and white matter, when they are isolated, exhibit different stiffness and brain tissue can be separated into four regions, with their own mechanical profile: cortex, corona radiata, basal ganglia and corpus callosum. It has been shown that the mechanical response of brain tissue is sensitive to the time scale and the characteristic length of loading. This has been attributed by

several authors to the ultra-soft, gel-like nature of brain tissue, which implies that effects on very small length and time scales may hold an important impact on the overall mechanical behavior [34].

To capture the mechanical response of brain tissue, several constitutive models have been proposed based on the type and range of the strain rates associated with pathological and normal conditions. In particular, extensive research has been conducted for brain matter experiencing compression at quasi-static loading [197, 42]. These studies have shaped our understanding of the hyperelastic time-independent response of human brain tissue. However, its time-dependent behavior at finite strains and under various loading conditions remains insufficiently understood.

Visco-elastic models [158, 32, 33, 181] are typically chosen to reproduce the time-dependent, hysteresis, preconditioning softening (regarding this topic, see the review [34] section 3.5) as well as the stress relaxation observed in experiments. The coupling of large deformation (usually hyper-elastic) and visco-elasticity has allowed to accurately capture various deformation types in a large range of strain. These have been employed to predict the essential features of brain tissue: non-linearity, hysteresis, and tension–compression asymmetry. Yet, most models developed to date have been tailored to reproduce particular loading scenarios or for specific applications. We conclude that this specific kind of models, that could be denoted as phenomenological, do not contain the required components to be transferable from one type of experimental conditions to another. Our aim is to alleviate these deficiencies, so that models developed for one patient can be used for another patient, and to make this possible for the most varied types of boundary and environmental conditions. We propose in this paper a particular multi-phase poro-elastic model. We show that this model, once calibrated on a certain set of experiments, can also reproduce the behaviour of brain tissue observed in completely different loading conditions. We therefore hypothesise that such a model could be a sound starting point for a generic mechanical model of the brain. In the supporting information, the interested reader may also find the indication that, for a viscoelastic model, to mimic the behavior of a porous material, the parameters must be adjusted according to the specimen size.

Several studies [89, 49, 102], based on a series of consolidation tests, suggested that extracellular fluid flow dominates the apparent viscoelastic properties of brain tissue. Based on mixture theory, poroelasticity has been extensively used to model brain tissue [138, 136, 73, 83, 70]. Porous media mechanics, [23], which describe the mechanical behavior of a porous solid containing viscous fluid, are compatible with processes which involve low-strain-rate deformations of the brain, such as edema, hydrocephalus, hemorrhage [174, 189] and infusion [228, 143]. However, single phase flow poromechanics show limitation to render the highly non-linear behavior of the brain tissue.

Franceschini et al. (2006) [89] conclude that consolidation (deformation of the solid matrix due to pore fluid flow and its drainage from the interstitial space) is the leading mechanism in quasi-static deformation of brain tissue. To achieve complete adherence between their experimental data and their theoretical formulations, they conclude that the addition of a viscous component to the rheological model is necessary.

This last point remains a matter of debate. Budday *et al.* [34] hypothesised that brain tissue rheology is characterized by at least two different timescales, which are attributed to viscous and porous effects, respectively. The viscous response can be related to the intracellular interactions within the network of cells forming the solid phase of the tissue, while the

porous medium behavior is associated with the interaction between the solid and fluid phase. In a recent study, Comellas *et al.* [59] explored in details the interplay between single phase poro-elasticity and finite visco-elasticity. Their model is capable of accurately reproducing consolidation, shear stress and cycle loading tests. However, the respective influence of porous and viscous components are strongly dependent on the parameters calibration, which could impede the physical interpretation of the results.

Unlike conventional approaches that combine viscoelastic and poroelastic behaviors into a single framework [115], we hypothesize in this article that a two-phase flow poroelasticity can also capture the stress relaxation and the sensitivity of a set of selected load rates. The two fluid phases, with their respective dynamic viscosities, allow for reproducing the two different time scales. As a first step, we limited our study on the cortex region of the brain, which is known to be soft and isotropic [34]. We first reproduce the experimental results of Franceschini *et al.* [89] without the use of a viscoelastic solid and, with the same model, we reproduce the experimental set of Budday *et al.* [31] composed of various indenters, load rates and stress relaxation.

4.3 Experimental data

Consolidation tests

The consolidation test (an uniaxial strain under free drainage conditions) is crucial for poromechanical modeling, as this strain can not be reproduced by an elastic law and is not adapted to viscoelastic models [89]. In this contribution we chose to reproduce the experiment of Franceschini conducted on N=12 specimens. The experimental procedure is briefly reported here. For more details the interested reader could refer to [89].

Twelve human parietal lobe cylindrical samples of 30 mm diameter and 5 to 8 mm height are harvested, within 12h after death, and placed into a consolidometer specifically designed for the tests, shown in Fig. 4.1A. The top and bottom of the samples are under free drainage conditions, using a filter paper against a porous brass employed in geotechnical consolidometer.

We identify three different profiles on the twelve samples, where the same initial load (6 Newton) will lead deformation from 3.5% to 6.5%. We retrieve the same three profiles on the 3 Newton load series. As a consequence, we select six samples from [89] for this study, one of each profile for the 3 and 6 Newton one step loads. We adopt the following nomenclature for the samples: XN for X Newton load series, followed by the figure index and letter of [89], *e.g.* 3N C2 a.

Indentation tests

Due to the difficulties in producing consistent samples, and due to the alterations to the micro-structural arrangement during the sample preparation, it has been reported that stiffness values using confined compression creep and stress relaxation tests are often not reproducible and may vary by an order of magnitude or more. Indentation has been shown to provide a robust, reliable, and repeatable method to quantify the mechanical properties in situ without altering the local

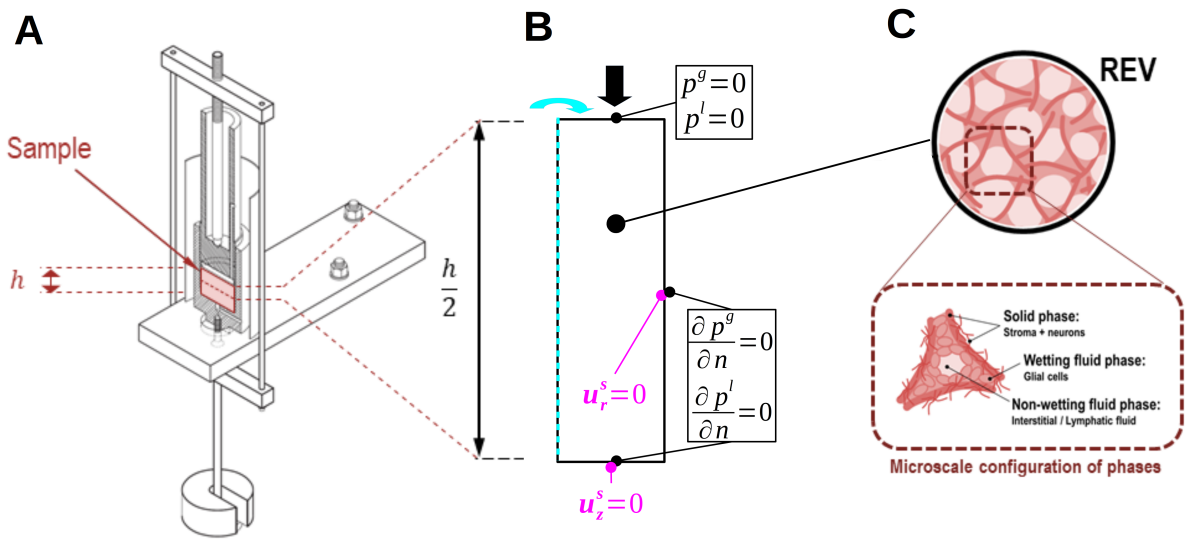

Figure 4.1: **Consolidation tests on ex vivo human cortex [89].** **A** Experimental design of consolidometer of Franceschini *et al.* [89] (reproduced with the authorisation of the authors). **B** Boundary conditions of the physical problem: the fluids are free to escape to loaded boundary (drained condition), the other boundaries are impervious; except at the loaded boundary, the displacement of the solid scaffold is allowed only on the tangential direction (slip condition). **C** Representative elementary volume (REV) with the phase components of the model framework.

micro-architectural arrangement.

Four indentation tests on *ex vivo* bovine grey matter, within 6 hours after death, are reproduced. These are subsets of the long range indentation type, on $N = 192$ samples, described in [31]. Before any test, all samples are subjected to a $100\,\mu$m indentation depth to stabilize the material response and ensure parallelism. The experimental design is shown in Fig. 4.2 A and the characteristics of the tests can be found in Table 4.1. Budday *et al.* present indentation tests with loading rates between $1\,\mu$m/s and $100\,\mu$m/s, for reason of brevity, we choose to reproduce these extreme values without the intermediate $10\,\mu$m/s and $20\,\mu$m/s. In [31], Budday *et al.* present mean experimental curves for each test and indicate 21% of standard deviation in the set of samples.

Characteristics	Test 1	Test 2	Test 3	Test 4
Indentation depth μm	300	300	300	100
Load rate μm/s	5	5	1	100
Indenter $\oslash$ mm	1	0.75	0.75	1.5
Unloading of $300\,\mu$m	Yes	Yes	Yes	No
Holding of $600\,$s	No	No	No	Yes

Table 4.1: **Characteristics of the indentation tests on ex vivo bovine cortex [31].** Test 1, 2 and 3 belong to long range indentation tests, Test 4 is a relaxation test.

4.4 Mathematical Modelling

The descriptions of cortex tissue as a porous medium can take several forms: a solid scaffold saturated by a fluid (Hakim *et al.* [101] in 1976), a visco-elastic scaffold saturated by a fluid [89], an elastic scaffold separated into two compartments,

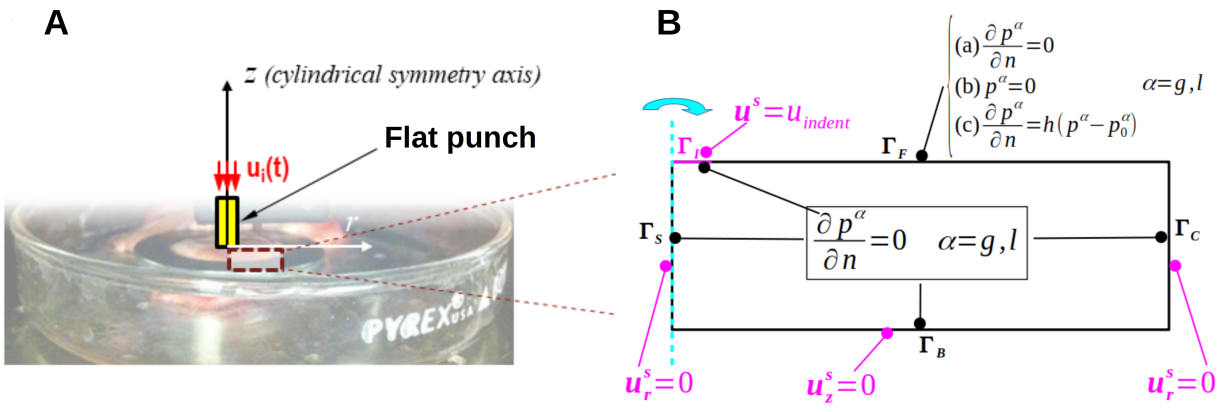

Figure 4.2: **Indentation test on ex vivo bovine cortex [31]. A** Experimental design of indentation tests of Budday *et al.* [31] (reproduced with the authorisation of the authors). The sample is considered under cylindrical symmetry hypothesis, $\mathbf{u}_i(t)$ is displacement prescribed by the indenter on the sample surface. **B** Boundary conditions of the physical problem in cylindrical axis symmetry. Boundaries are denoted Γ_S the axis of symmetry, Γ_B and Γ_C the slip boundaries prescribed in the experimental design, Γ_I the indented surface and Γ_F the free surface, where three different boundary conditions are tested.

vascular and extra-vascular, each saturated by a different fluid [73], among others. In this study, we focus on *ex vivo* material, so the vascular activity will be neglected and the vascular network will be considered a part of the solid scaffold. Within the parenchyma, we distinguish two fluid phases: glial g phase, for which we prescribed a dynamic viscosity close to gel-like, and interstitial/lymphatic l phase, with a prescribed dynamic viscosity one order higher than water. A summary of the representative elementary volume is shown in Fig. 4.1C. This specific description of cortex tissue by two immiscible fluids within a porous solid has no experimental equivalent. Therefore, we present the quantitative information to set the initial guess of the parameters from several sources in the experimental literature.

Governing equations

A porous medium consists in a solid scaffold, that is to say all the material that act as structural solids in the porous medium. Its volume fraction is denoted ε^s. The porosity is the volume fraction saturated by the fluids, denoted ε, and

$$\varepsilon^s + \varepsilon = 1 \tag{4.1}$$

We distinguish, in this contribution, the glial phase g from the remaining fluid phase l. These two phases are assumed to be immiscible fluids with their respective saturation S^l and S^g and

$$S^l + S^g = 1 \tag{4.2}$$

The volume occupied by the liquid phase and by the glial phase are respectively denoted εS^l and εS^g.

The mass balance of the porous solid reads:

$$\frac{\mathrm{D}^s}{\mathrm{D}t}\left(\rho^s\varepsilon^s\right)+\rho^s\varepsilon^s\nabla\cdot\mathbf{v}^{\overline{s}}=0 \tag{4.3}$$

- with $\frac{\mathrm{D}^s}{\mathrm{D}t}\left(\rho^s\varepsilon^s\right)$ the evolution of the solid scaffold mass
- and $\rho^s\varepsilon^s\nabla\cdot\mathbf{v}^{\overline{s}}$ its flux term.

The mass balance of the fluids phases reads:

$$\frac{\mathrm{D}^s}{\mathrm{D}t}\left(\rho^g\varepsilon S^g\right)+\nabla\cdot\left(\rho^g\varepsilon S^g\mathbf{v}^{\overline{gs}}\right)+\rho^g\varepsilon S^g\nabla\cdot\mathbf{v}^{\overline{s}}=0 \tag{4.4}$$

$$\frac{\mathrm{D}^s}{\mathrm{D}t}\left(\rho^l\varepsilon S^l\right)+\nabla\cdot\left(\rho^l\varepsilon S^l\mathbf{v}^{\overline{ls}}\right)+\rho^l\varepsilon S^l\nabla\cdot\mathbf{v}^{\overline{s}}=0 \tag{4.5}$$

- with $\frac{\mathrm{D}^s}{\mathrm{D}t}\left(\rho^\alpha\varepsilon S^\alpha\right)$ the evolution of the fluid phase α
- $\nabla\cdot\left(\rho^\alpha\varepsilon S^\alpha\mathbf{v}^{\overline{\alpha s}}\right)$ the flux term of the phase α where $\mathbf{v}^{\overline{\alpha\mathbf{s}}}$ is the phase α velocity relatively to the solid: $\mathbf{v}^{\overline{\alpha\mathbf{s}}}=\mathbf{v}^{\overline{\alpha}}-\mathbf{v}^{\overline{\mathbf{s}}}$
- and $\rho^\alpha\varepsilon S^\alpha\nabla\cdot\mathbf{v}^{\overline{s}}$ the contribution of the solid deformation to the mass conservation of the phase $\alpha=l,g$

Constitutive relationships

The glial phase will be denoted as the wetting phase, that is to say, the phase that preferentially covers the solid scaffold. Therefore, it is the one that sustains the mechanical load before transmitting it to the non-wetting phase, namely the liquid phase. The pressure relationship with the phases saturation is justified by the simplified entropy inequality of the thermodynamically constrained averaging theory (TCAT) [99]. At the microscale equilibrium, it is assumed that the evolution of the interface surface is negligible compared to the evolution of the fluid saturation, therefore the interfacial tension between the phases is directly linked to the pressure difference (see [220]). This implies a pressure jump between the wetting phase g and the non-wetting phase l, whose saturation S^l depends on the pressure jump $p^{lg}=p^l-p^g$ (see Eq.4.6).

From [220], the expression of the liquid phase saturation, dependent on the difference of the phases pressure, is adapted from the heuristic formulation of van Genuchten [250]:

$$S^l=\frac{2}{\pi}\mathsf{arctan}\left(\frac{p^{lg}}{a}\right) \tag{4.6}$$

with the theoretical parameter a, which represents the intensity of the interplay between the solid scaffold and the non-wetting phase. Its range commonly taken is $[500;800]$ (see [216], [218], [162], [211]).

The solid scaffold has its intrinsic permeability k^s_{int} and follows linear elasticity (Young modulus E, Poisson's ratio ν):

$$\bar{\bar{\sigma}}_{\text{eff}} = \lambda tr(\bar{\bar{\epsilon}})\mathbb{I} + 2\mu\bar{\bar{\epsilon}} \tag{4.7}$$

with $\mathbb{I}$ the identity tensor, $\bar{\bar{\epsilon}}(\mathbf{u}^s) = \frac{1}{2}(\nabla\mathbf{u}^s + (\nabla\mathbf{u}^s)^T)$ the linearised strain tensor, and the Lamé constants $\lambda = \frac{E\nu}{(1+\nu)(1-2\nu)}$ and $\mu = \frac{E}{2(1+\nu)}$.

The two fluid phases have their own relative permeabilities:

$$k^l_{\text{rel}} = (S^l)^{A_l} \qquad k^g_{\text{rel}} = (S^g)^{B_g} \tag{4.8}$$

with A_l and B_g to be calibrated.

The interaction between fluid phases and the solid scaffold are modeled by a generalized Darcy's flow, deduced from the linear momentum conservation of fluid phases:

$$-\frac{k^\alpha_{\text{rel}} k^s_{\text{int}}}{\mu^\alpha}\nabla p^\alpha = \varepsilon S^\alpha(\mathbf{v}^{\alpha\bar{s}}) \qquad \alpha = g, l \tag{4.9}$$

where k^s_{int} is the intrinsic permeability of the solid scaffold, μ^α, k^α_{rel} and p^α are respectively the dynamic viscosity, relative permeability and the pressure of each fluid phase $\alpha = l, g$.

Final system of governing equations

The physical system is governed by the mass conservation of each phase and by linear momentum conservation of the overall system. The primary unknowns of the model are the solid scaffold displacement $\mathbf{u}^s$, the glial phase pressure p^g and the liquid phase pressure difference p^{lg}.
Eqs.4.3-4.5 are treated as follows:

- Eq.4.3 is injected into Eqs.4.4-4.5 thanks to the constraint Eq.4.1
- the difference of order between the mechanical constrains and the compressibility of the components allows us to neglect the variation of their density, therefore ρ^α is considered constant $\alpha = s, g, l$. We also assume that the component have the same density $\rho^s = \rho^g = \rho^l$
- the evolution of the glial volume fraction $\varepsilon\frac{D^s S^l}{Dt}$ is expressed with respect to the constraint Eq.4.2. Its evolution depends on the interstitial fluid pressure $S^l(p^{lg})$, see the constitutive relationship Eq.4.6

We obtain the following system:

$$\begin{cases} -\varepsilon \frac{dS^l}{dp^{lg}} \frac{D^s p^{lg}}{Dt} - \nabla \cdot \left[\frac{k^g_{\text{rel}} k^s_{\text{int}}}{\mu^g} \nabla p^g \right] + S^g \nabla \cdot \mathbf{v}^s = 0 \\ \\ \varepsilon \frac{dS^l}{dp^{lg}} \frac{D^s p^{lg}}{Dt} - \nabla \cdot \left[\frac{k^l_{\text{rel}} k^s_{\text{int}}}{\mu^l} \nabla (p^g + p^{lg}) \right] + S^l \nabla \cdot \mathbf{v}^s = 0 \end{cases} \tag{4.10}$$

The governing equations are completed with the momentum balance of the system:

$$\nabla \cdot \sigma_T = \mathbf{0} \qquad \text{with} \qquad \sigma_T = \sigma_{\text{eff}} - \beta p^s \tag{4.11}$$

where σ_{eff}, the effective stress described Eq.4.7, represents the solid contribution to the mechanical stress. β is the Biot's coefficient, set to 1 thanks to the hypothesis of the phases incompressibility. $p^s = S^t p^t + S^l p^l$, denoted the solid pressure, represents the fluids' contribution to the mechanical stress.

Assumption on the porous medium components and parameters motivated by literature

The stiffness of the cortex has been intensively studied ([226, 127, 29], among many others). It both depends on the chosen modeling framework and the sample composition, so the values of the Young's modulus E can widely vary. In time-independent modeling, as linear elastic or hyperelastic, using linear elastic law leads to scatter values Young's modulus E, from $2.5\,$kPa [262] to $8\,$kPa [226]. Non-linear hyperelastic modeling has more homogeneous values, with E between $1.1\,$kPa [127] and $3\,$kPa [29]. In the reproduced experimental study [31], the authors found by contact theory $E = 1.389 \pm 0.289\,$kPa. Conversely, the values of Poisson's ratio ν are quite consensual in the literature, as the material is constantly described as nearly incompressible, with values varying between 0.495 [226] and 0.45 [212].

In Barnes *et al.* [17], the extra-cellular matrix (ECM) volume fraction is estimated to be 20%. In Lei *et al.* [139], the volume fraction of the interstitial fluid (IF), added to the ECM, is estimated to be between 15% and 20%. From Bender and Klose [20], the IF fraction, strictly limited to the parenchyma, is estimated to be between 5% and 10%, and the vascular system (in [139]) between 3% and 5%. Finally, the distribution indicated by Azevedo *et al.* in [14] for the cerebral cortex gives 20% neuron, 80% non-neuron with $\pm 2\%$ of uncertainty.

We define the solid scaffold as the sum of the stroma cells (membrane, epithelial and endothelial cells), the ECM, the vascular system - because blood circulation is not considered in *ex vivo* testing - and the neurons (bodies and axons). Based on the estimation provided above, we obtain the following range of values for the solid scaffold fraction: the minimum at $(0.15 - 0.1) + 0.03 + 0.18 = 0.24$ and the maximum at $0.2 + 0.1 + 0.05 + 0.22 = 0.57$. Its complement, the porosity ε, is within the range $0.43 \leq \varepsilon \leq 0.76$.

As written in [20], the IF volume fraction estimated to $0.05 \leq \varepsilon S^l \leq 0.1$. With the estimated range of porosity ε, we obtain for the liquid phase saturation: $0.065 \leq S^l \leq 0.232$; and its complement, the glial phase saturation: $0.828 \leq S^g \leq 0.935$.

As initial range of values for the liquid phase dynamic viscosity μ_l, we keep different estimation provided in [230] for cerebral fluid, between $0.7 \cdot 10^{-3}$ Pa·s and $1 \cdot 10^{-3}$ Pa·s. For the rheology of the glial phase, as we do not have experimental data, we choose a value close to literature used for generic cells (see [216] and [211]) $\mu_g \approx 30\,\text{Pa} \cdot \text{s}$.

Regarding the intrinsic permeability k^s_{int} of the solid scaffold, there is still a large knowledge gap. The important difficulty to design experiment on living tissue and the preferential use of single phase solid mechanics rather than poromechanics are probably partly responsible for this problem. In 2021, Sowinski *et al.* [230] reported ranges of values for hydraulic conductivity K, using *in silico* magnetic resonance elastography. They reported hydraulic conductivity values from $2 \cdot 10^{-11}\,\text{ms}^{-1}$ to $2 \cdot 10^{-10}\,\text{ms}^{-1}$. Same year, Jamal *et al.* in [120], reported range of values for the intrinsic permeability k^s_{int}, by *ex vivo* perfusion experiment. They reported a k^s_{int} mean value of $10^{-16}\,\text{m}^2$, with a strong influence of tissue anisotropy, from $2 \cdot 10^{-17}\,\text{m}^2$ to $3.2 \cdot 10^{-15}\,\text{m}^2$, with one order of magnitude difference if perfusion is parallel or perpendicular to the white matter fibers.
Retrieve intrinsic permeability k^s_{int} from hydraulic conductivity K is not straightforward. If the ratio $\frac{k^s_{\text{int}}}{\mu}$ is common to the different equivalence, the size of the sample, its density and difference of pressure could be at play. Applying the ratio on hydraulic conductivity, a dynamic viscosity μ with the order of $1 \cdot 10^{-3}\,\text{Pa} \cdot \text{s}$ will lead to an intrinsic permeability k^s_{int} between $2 \cdot 10^{-14}\,\text{m}^2$ and $2 \cdot 10^{-13}\,\text{m}^2$, which is two orders higher than [120]. In [230], Sowinski *et al.* hypothesise that *in vitro* experiments tend to lead to smaller values, due to pore collapse in sampled tissue. In [120], Jamal *et al.* claim that these microstructural changes become significant after 6h post-mortem, hence they perform their experiments within these 6h. As we do not have sufficient information, we have no other choice to keep this large range, from 10^{-17} to 10^{-13}, as acceptable values of k^s_{int}.

4.5 Computational framework

Using the FEniCS python libraries, the solution of the problem has been done with the finite element method, with a monolithic solution process. Boundary conditions for the consolidation tests are shown in Fig.4.1B and for the indentation tests in Fig.4.2B. The computations have been run on a mesh of 4×20 elements for consolidation tests and 98×60 for indentation tests, both are cylindrical axis symmetric representation of the sample. The same computations have been run with meshes with three levels of refinement, with the same results.
The boundaries of the consolidation tests are shown in Fig.4.1B. The fluids are free to escape to loaded boundary (drained condition) and the other boundaries are impervious. For the solid scaffold, except at the loaded boundary, its displacement is allowed only on the tangential direction (slip condition). The boundaries of the indentation tests are shown in Fig.4.2B. Its boundary conditions are denoted by Γ_S the axis of symmetry, by Γ_B and Γ_C the slip boundaries prescribed in the

experimental design. Γ_I is the indented surface, where the fluid is assumed under impervious condition and Γ_F the free surface.

All the codes used for computation are available on Github, at `https://github.com/StephaneUrcun/BrainTissue`

Local sensitivity analysis and parameters calibration

As an initial guess, we first set all the parameters within their ranges given in section 4.4 paragraph '*Assumption motivated by literature*'. Seven are denoted *tissue specific*, because they are general properties, more likely to be shared by all samples: the porosity ε, the Poisson's ratio ν, the dynamic viscosity of the two fluid phases μ_l, μ_g, their corresponding tortuosity exponent A_l, B_g and a, the referenced pressure of the cell-ECM interplay. Young's Modulus E and intrinsic permeability k^s_{int}, which have the wider ranges, and the initial liquid phase saturation S^l_0 are denoted *sample specific* (S^l_0 varies for each sample, but within the prescribed physiological range, see section 4.4 paragraph *Assumption motivated by literature*).

We perform a variance-based local sensitivity analysis on the parameters at their initial guess value $\pm 10\%$, described 4.8. We perform first order sensitivity analysis (the parameters are modified one at a time) as well as second order analysis (the 45 parameters tuples are tested to quantify parameters correlation). The parameters are strongly inter-dependent, the 45 tuples gather 87.3% of the variance, the parameters can not be calibrated separately. The weights of the parameter tuples confirm the idea of two parameters subsets: the 21 tuples of tissue specific parameters gather 49.6%, where the 21 tuples of tissue *v.s.* sample specific parameters gather only 35.6%, see Fig.4.3A, the 3 tuples of sample specific parameter are less correlated, they weigh only for 2.1%. The results of the first order are in Fig.4.3B and the details of the Sobol indices can be found in 4.8.

The calibration process has been performed on all samples of the consolidation tests and on the mean curve of Test 1 of the indentation tests. It consists in a Newton algorithm on the 7 tissue specific parameters, the sample specific parameters being fixed. Once the algorithm gives no improvement (RMSE improvement below 10^{-4}), we perform, for each sample separately for the consolidation tests and for indentation Test 1, the calibration of the sample specific parameters E, k^s_{int} and S^l_0.

Measure of error

The error between numerical results y^{num} and experiments data y^{exp}, evaluated at n points, is measured in percentage by the relative root mean square error (RMSE):

$$RMSE = \sqrt{\sum_{i=1}^{n} \left(\frac{y_i^{\text{exp}} - y_i^{\text{num}}}{y_i^{\text{exp}}} \right)^2} \tag{4.12}$$

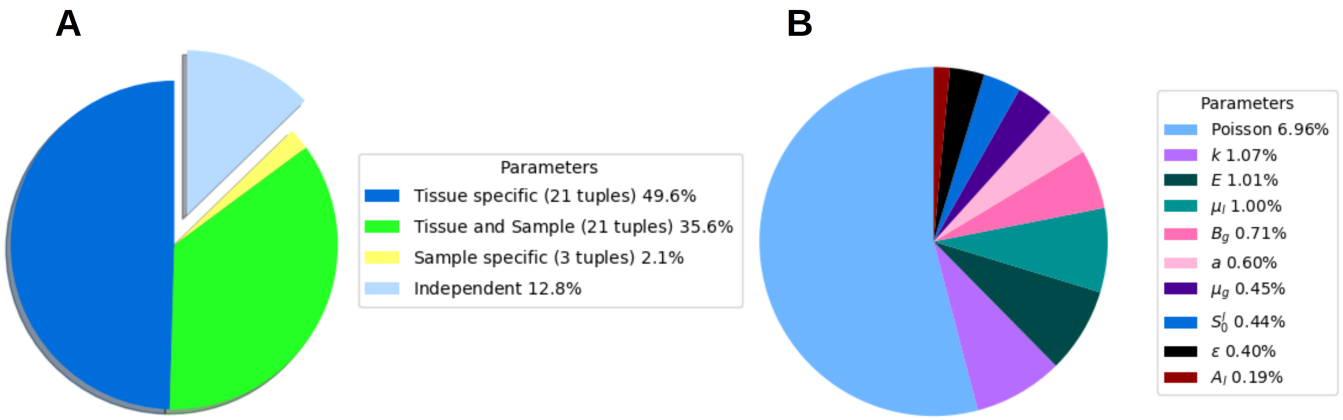

Figure 4.3: **Results of the second-order sensitivity analysis.** **A** The parameters interaction gathers 87.1% of the solution variance, *i.e.* the parameters are strongly correlated. The 21 tuples of tissue specific parameters weight for 49.6%, the 21 tuples of tissue/sample interaction weight for 35.6%, the 3 tuples of sample specific parameter are less correlated, they weight only for 2.1%. **B** Details of the weight of parameter independent sensitivity. The Poisson's ratio ν sensitivity largely dominates the other parameters.

4.6 Results

The working hypothesis of this contribution is that the time-dependent properties of cortex tissue can be modeled using a two-phase flow poroelasticity framework. This hypothesis is tested in this section to reproduce the experimental results of the consolidation tests in [89] and the unconfined indentation tests in [31]. To emphasise the limit of visco-elasticity compared to poro-elasticity, a 1D confined compression test with an available analytical solution is reproduced and discussed in 4.8.

Consolidation tests

The mechanical response of the six samples is generated using parameters shown in Table 4.2. All the samples share the same *tissue specific* parameters set. Fig. 4.4A, B shows the results of the model for the 3 Newton and 6 Newton load series respectively. We obtain accurate results for the 6 samples with an error ranged from 1.1 to 5.6%. These results are obtained by calibrating three parameters, the Young's modulus E, the intrinsic permeability k^s_{int}, and the initial saturation of liquid phase S^l_0 within the physiological range $6.5-17.2\%$ (with one exception sample 3N C2 d at 5.9%). All the details are referenced in Table 4.2.

Indentation tests

The four indentation tests have been reproduced using the same mathematical modeling (section 4.4) and computational framework (section 4.5) than the consolidation tests. However, these indentation tests are not specifically adapted to poromechanical modeling, so that the nature of the free surface of the sample Γ_F (see Fig.4.2B) is not clearly prescribed from the fluids point of view. If the cortex slice cut follows a membrane, it leads to an impervious boundary as eq.4.13(a).

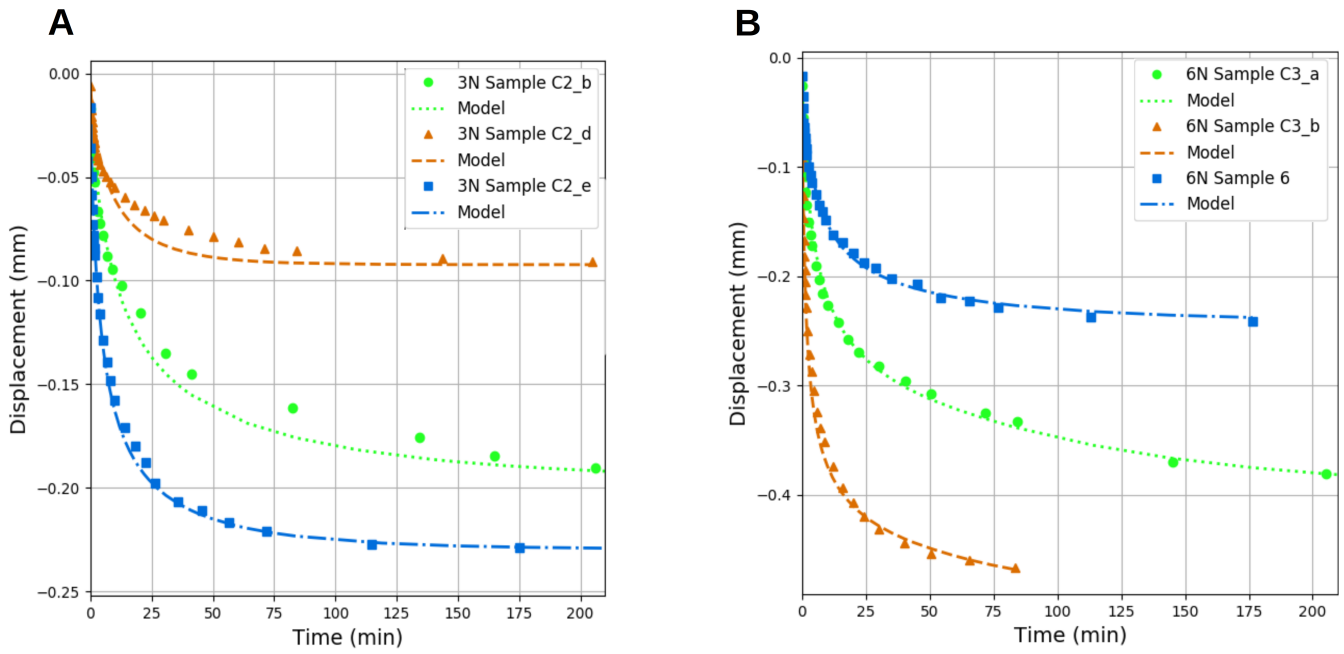

Figure 4.4: **Numerical reproduction of Franceschini et al. consolidation tests on ex vivo human cortex [89].** Time (minutes) *vs.* Displacement (mm). **A** 3 Newton load series. Sample 3N C2 b (experimental green circle; numerical green dotted) is reproduced with 0.056 RMSE (see Eq.4.12); Sample 3N C2 d (experimental orange triangle; numerical orange dotted) with 0.036 RMSE; Sample 3N C2 e (experimental blue square; numerical blue dotted) with 0.016 RMSE. **B** 6 Newton load series. Sample 6N C3 a (experimental green circle; numerical green dotted) is reproduced with 0.011 RMSE; Sample 6N C3 b (experimental orange triangle; numerical orange dotted) with 0.017 RMSE; Sample 6N 6 (experimental blue square; numerical blue dotted) with 0.015 RMSE.

In the case of a proper fluid drainage, this leads to a homogeneous Dirichlet condition, eq.4.13(b). The intermediate case leads to a semi-pervious boundary. To our knowledge, no investigation has been done on the passive drainage of the free surface for *ex vivo* cortex tissue testing, then we adopt a convective condition, usual in mass transfer through boundaries in poromechanics [93] eq.4.13(c).

$$\frac{\partial p^\alpha}{\partial n} = 0 \quad \text{on } \Gamma_F \quad \alpha = g, l \tag{4.13a}$$

$$p^\alpha = 0 \quad \text{on } \Gamma_F \quad \alpha = g, l \tag{4.13b}$$

$$\frac{\partial p^\alpha}{\partial n} = h(p^\alpha - p_0^\alpha) \quad \text{on } \Gamma_F \quad \alpha = g, l \tag{4.13c}$$

Our investigation shows that a semi-pervious boundary on the sample free surface gives slightly better results than an impervious boundary for the indenter surface response evaluated in this article. With the same parameters, the influence of different boundary conditions on the free surface are shown in Fig. 4.5. For the sake of simplicity, we choose an impervious boundary condition on the free surface.

We identify the parameters of [31] with only one test, the 1 millimeter diameter long range indentation on grey matter,

Sample	E (Pa)	k^s_{int} (m^2)	Sl_0	**RMSE**
3N C2 b	4130	$2.2e^{-13}$	0.075	0.056
3N C2 d	9300	$2.1e^{-13}$	0.059	0.036
3N C2 e	3740	$4.7e^{-13}$	0.100	0.016
6N C3 a	4330	$2.9e^{-13}$	0.114	0.011
6N C3 b	3500	$6.1e^{-13}$	0.169	0.017
6N 6	7100	$2.1e^{-13}$	0.094	0.015

Shared parameters	Sl_0	ε	ν	μ_l (Pa · s)	A_l	μ_g (Pa · s)	B_g	a
(tissue specific)	[0.065;0.232]	0.6	0.49	$8e^{-3}$	1	35	2	800

Table 4.2: **Model parameters calibrated of the consolidation tests on ex vivo human cortex [89].** Seven parameters, ε, ν, μ_l (Pa · s), A_l, μ_g (Pa · s), B_g and a (Pa) denoted *tissue specific*, are common to all samples. Three parameters, E (Pa), k^s_{int} (m^2) and S^l_0, within the prescribed range $[0.065; 0.232]$, are calibrated specifically for each sample. Only one sample, 3N C2 d, is slightly below S^l_0 prescribed range.

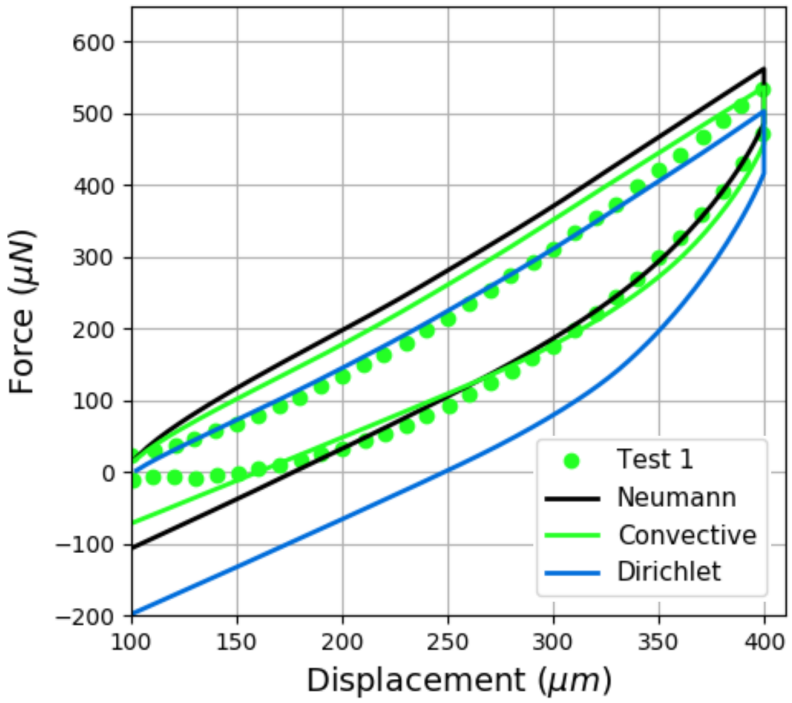

Figure 4.5: **Influence of the free surface boundary condition on the indenter surface response.** Shared parameter set: $E = 730$ Pa, $k^s_{\text{int}} = 3 \cdot 10^{-3}$ m^2, $S^l_0 = 0.063$, $\varepsilon = 0.6$, $\nu = 0.49$, $\mu_l = 3 \cdot 10^{-3}$ Pa · s, $A_l = 1$, $\mu_g = 30$ Pa · s and $B_g = 2$. Experimental (gree dotted); Neumann (black) impervious condition eq.4.13(a); Dirichlet (blue) drained condition eq.4.13(b); Convective (green), with the additional parameter $h = 10^{-4}$, eq.4.13(c) semi-pervious condition.

denoted Test 1 in this article. Then, we validate these parameters on the other tests. The parameters of Test 1 are identified by the same process than consolidation tests, see section 4.5.

The resulting parameters of Test 1 (12.7% RMSE) are validated on Test 2, 3 and 4, see Fig.4.6. It shows that the calibrated parameters lose accuracy but remain capable of reproducing the different tests. The change in the indenter diameter Test 2 slightly increases the error (13.5% RMSE). The results degradation is more significant when loading rates change in Test 3 (16.7% RMSE) or for the relaxation Test 4 (18.3% RMSE). Test 4 has been calibrated independently (10.3% RMSE), see Fig. 4.7, giving a different profile with E almost twice higher, see Table 4.3. The calibrated parameters of Test 1

give a value of S_0^l below the prescribed physiological range ($< 6.5\%$), whereas the calibrated S_0^l of Test 4 is closer to the physiological range (see Table 4.3).

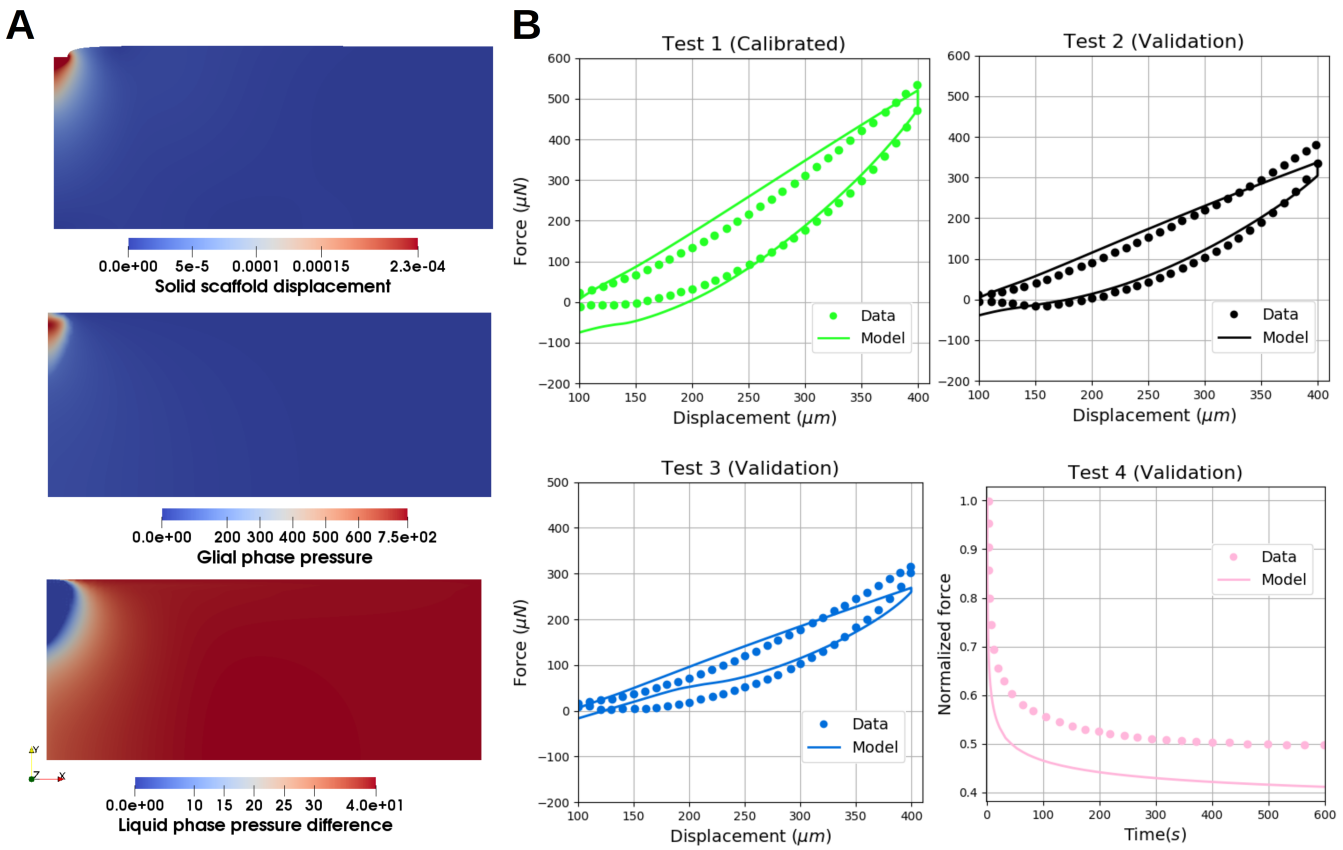

Figure 4.6: **Indentation tests on ex vivo bovine cortex [31]: validation of the calibrated parameters on Test 1. A** Example of the simulation results on Test 1. At $230\,\mu$m indentation depth, the glial pressure raised to $780\,$Pa and flush out the liquid phase (*i.e.* $0\,$Pa of pressure difference p^{lg} in this area). Note that the liquid phase is subjected to a pressure p^l of a few hundreds of Pascal at the indenter zone and only $40\,$Pa at the sample boundaries. **B** Test 1, experimental (green dotted), numerical (green plain line), RMSE$= 12.7\%$; Test 2, experimental (black dotted), numerical (black plain line), RMSE$= 13.5\%$; Test 3, experimental (blue dotted), numerical (blue plain line), RMSE$= 16.7\%$; Test 4, experimental (pink dotted), numerical (pink plain line), RMSE$= 18.3\%$.

4.7 Discussion

The strong time-dependent mechanical behavior of the cortex is generally attributed to both the intrinsic viscoelasticity of the solid phase and fluid flow-induced poroelasticity but the relative contributions of the two are unclear. Conventional approaches combine viscoelastic and poroelastic behaviors into a single framework to be able to reproduce experimental data [89, 115].

In this contribution we propose to implement a two-phase flow poroelastic model of the cortex to capture the consolidation, the relaxation and the sensitivity of a set of selected load rates and investigate the dissipation mechanisms. Two

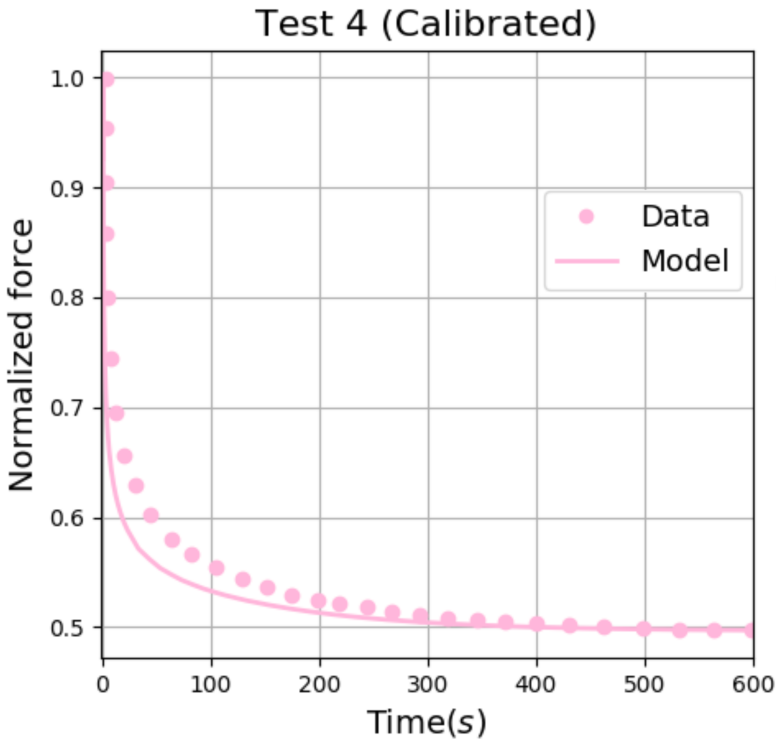

Figure 4.7: **Indentation tests on ex vivo bovine cortex [31]: calibration of the parameters of Test 4.** Experimental (pink dotted), numerical (pink plain line), RMSE$= 10.3\%$.

sets of experiments are reproduced: the consolidation test of [89] and the unconfined indentation test of [31]. Our results show that the experimental curves can be reproduced without the need to resort to viscous effects, by adding an additional fluid phase.

First, we note that we examine in this paper two mechanical tests which are considerably different. For the consolidation test a load as high as 6 Newton is applied on the delicate structure of the cortex, which corresponds to a pressure of 8440Pa. In the indentation test, the load is approximately 0.6 mN (that is 4 orders of magnitude smaller), corresponding to a 20Pa pressure. The two tests are therefore very dissimilar in the way the sample is loaded, deformed and, possibly, damaged.

We estimate material parameters associated with the models we develop. We then compare those parameters with those published in the literature. We consider those parameters through the lens of the PhD thesis of Fanny Morin [170] (Chapter 6). Within this scope, we focus on rheological parameters extracted from confined/unconfined experiments on human/animal grey matter.

The stiffness values (Young's modulus) reported in the literature, computed by considering grey matter as a monolithic solid, are widely scattered (1.1 to $8\,$kPa). In the unconfined indentation case, these stiffness values are much higher than those we obtain (0.6-1.2kPa). This observation is explained by the fact that the stiffness we "measure" consists in both a

Sample	E (Pa)	k^s_{int} (m^2)	Sl_0	**RMSE**
Test 1 (C)	605	$2.8e^{-12}$	0.027	0.127
Test 2 (V)	605	$2.8e^{-12}$	0.027	0.135
Test 3 (V)	605	$2.8e^{-12}$	0.027	0.167
Test 4 (V)	605	$2.8e^{-12}$	0.027	0.183
Test 4 (C)	1100	$4.2e^{-12}$	0.047	0.099

Shared parameters	Sl_0	ε	ν	μ_l (Pa · s)	A_l	μ_g (Pa · s)	B_g	a
(tissue specific)	$[0.065;0.232]$	0.5	0.47	3^{-3}	1	30	1	400

Table 4.3: **Parameters for indentation tests on ex vivo bovin cortex.** Validation (V) on Test 2, 3 and 4 of the calibrated (C) parameters of the Test 1. Specific calibration (C) of the Test 4. Seven parameters, ε, ν, μ_l (Pa · s), A_l, μ_g (Pa · s), B_g and a (Pa) denoted *tissue specific*, are common to all samples.

solid component and a fluid component, thereby decreasing the effective stiffness contribution of the solid phase Young's modulus. The values we obtain for E in the confined consolidation tests are six times as high as those obtained in the unconfined indentation case ($E = 5.35 \pm 2.12$ kPa). This could seem surprising. The possibility of different stiffness between humain and animal - simian, bovine and porcine - brain have led to contradictory results (see [193] and [207]). We looked for a possible explanation for this stiffness discrepancy within environmental conditions such as: sample preservation, hydration and temperature. The loss of hydration and temperature have cumulative effects. All other conditions remaining equal, temperatures of $24°$C and $37°$C will lead to a stiffness 40% lower, but the same variation with dehydration will lead to a stiffness 5 fold higher (see Forte *et al.* [87] for a detailed study on this topic). However, according to the ranges given in [87], the confined consolidation and unconfined indentation tests were made in sufficiently close environmental conditions to rule out this hypothesis.

We therefore hypothesise that, during confined consolidation, pore locking may take place, leading to the creation of fluid "pockets" within the structure. This incomplete consolidation results in an effective stiffening of the sample and thereby in an increase of the apparent Young's modulus.
Regarding the Poisson's values, they correspond to the literature consensus with $\nu = 0.47$ in the unconfined case, and $\nu = 0.49$ in the confined case.

In the confined case, we obtain one order of magnitude smaller permeabilities than in the unconfined case. The intrinsic permeabilities we evaluate, amended by their respective relative permeabilities, are however within the experimental range provided in the literature. Such decrease in permeability can be caused by the pore locking phenomenon described above. Moreover, the consolidation tests were performed within 12 hours, as opposed to 6 hours for the indentation tests. This time delay could lead to significant changes in the microstructure [120], which also alters the permeability.

The review of Budday *et al.* [34] pointed out the promising coupling of poro-viscoelasticity, as it takes account of both the interplay between interstitial fluid and stroma and the time-dependent response of cellular phase. The model proposed by Franceschini *et al.* in [89] along with their experiments is an example of this coupling. We show in this article that a

one-phase flow coupled with a viscoelastic solid, in the reproduced loading scenarii, can be replaced by a two-phase flow with an elastic solid. The two different dynamic viscosities ($\mu_l = 5.5 \pm 2.5\,10^{-3}$ Pa $\cdot$ s and $\mu_c = 32.5 \pm 2.5$ Pa $\cdot$ s) give two different characteristic times. They are comparable to the two-terms Prony series proposed in the viscoelastic parameter identification of human brain tissue of Budday *et al.* in [32] characterised by $\tau_1 = 0.18$ s and $\tau_1 = 63.5$ s. Moreover, our parameters are not dependent on the geometry, as shown in the 4.8. The fact that the tissue characteristics are build upon experimental findings offers a reliable way for a tissue specific pre-calibration. The sample calibration is only done on three parameters, which is equivalent, in computational cost, to the classic hyperelastic models (Yeoh [269], Ogden [185]).

Even if we endeavour to build our model on experimental matter, we are aware of its limits. A solid scaffold described as the sum of the stroma, the vascular network and the ECM is obviously non-linear. We have not included dependency between permeability and porosity in our model (the interested reader could find a presentation in [165]), whereas in confined deformation with an incompressibility hypothesis, the main part of the deformation is absorbed by the pores. Adding this relation would lead to closer values of intrinsic permeability k^s_{int} between indentation and consolidation, and partially suppress the artificial stiffness of consolidation parameters, by increasing the fluids supported stress. We can also point out that the total stress relationship we used, along with a Biot coefficient equal to 1 is a strong hypothesis. The incompressibility of the fluids is not to be questioned. Yet, micro-structural changes due to post-mortem experiments or mechanical damage may increase solid scaffold compressibility. Only three load rates are reproduced in this paper ($1\,\mu$m/s, $5\,\mu$m/s and $100\,\mu$m/s), a large panel still remains to explore. Likewise, our model response on various loading scenarii - tension or shear - or experimental condition - such as temperature dependency - remains open. As a consequence, our results are only relevant at room temperature under humidity control.

The results in this paper indicate that multi-phase models could be a strong basis for the description of biological tissue such as the brain, *ex vivo* and *in vivo*, as some advanced models can reproduced interplay of vessels and tissue [217, 73]. We hope this contribution will encourage the community to develop new experimental techniques which are compatible with poro-mechanical models. More specifically, the enforcement of boundary conditions on free surfaces could help the modeling of different drainage conditions.

Beyond experimental setups, another open challenge lies in the ability of models to be transferred from one observational/experimental situation to another. For this work to have impact in a clinical setting, methods must be developed to transfer parameters and models from one set of patients to another. We believe that a quantitative approach to this would be to develop robust model selection approaches from experimental or clinical data [273].

Acknowledgments

The results presented in this paper were carried out using the HPC facilities of the University of Luxembourg [251] (see https://hpc.uni.lu).

4.8 Supporting information

Viscoelastic modeling limitation on consolidation test reproduction

Let us consider two reference models: a one solid-one fluid poroelastic model and a rheological viscoelastic model constituted by a Kelvin-Voigt chain; and use these two models to simulate a 1D confined compression test. In this test the tissue is constrained in a cylindrical chamber and compressed at the top surface with a constant pressure P_0. The specimen is fully sealed with the exception of the top and the bottom surface where a porous membrane allows drainage of the inside fluid during the test. The geometry and boundary conditions of the test are represented in Fig. 4.4A. The simplicity of the two considered models jointed with the simplicity of the considered test allows to derive the analytical solution for both modeling approaches (see [253] for the poromechanical model). For the one-fluid one-solid poroelastic model:

$$\begin{aligned} &p_z(z,t) = \\ &P_0 \frac{4}{\pi} \sum_{k=1}^{\infty} \frac{(-1)^{k-1}}{2k-1} \cos\left((2k-1)\frac{\pi}{2}\frac{z}{L}\right) \exp\left((2k-1)^2 \frac{\pi^2}{4}\frac{c_v t}{h^2}\right) \end{aligned} \tag{4.14}$$

with the consolidation coefficient under the hypothesis of phases incompressibility:

$$c_v = \frac{kM}{\mu} \tag{4.15}$$

with M the longitudinal modulus:

$$M = \frac{E(1-\nu)}{(1+\nu)(1-2\nu)} \tag{4.16}$$

E the Young's modulus and ν the Poisson's ratio.

For the viscoelastic Kelvin-Voigt chain:

$$u_z(z,t) = \frac{P_0 z}{M}\left[1 - \exp\left(-\frac{Et}{\eta}\right)\right] \tag{4.17}$$

We see that the poroelastic model is governed by the parameters E, ν and the ratio $\frac{k}{\mu}$ and the viscoelastic model by E, ν and η. However, the analytical solution of the porous model contains h, the sample height, which strongly influence the consolidation time. Then, once the parameters of the porous model are calibrated, they will remain relevant when the height of the sample varies.

Parameter	θ	$S_i(\%)$
E	0.0426	8.29
ν	0.2384	56.7
k^s_{int}	-0.0430	8.74
ε	-0.0304	3.32
μ_l	0.0346	8.17
μ_g	0.0114	3.70
A_l	0.0002	1.58
B_g	0.0208	5.80
S^l_0	-0.0256	3.63

Table 4.4: **Sobol indices of the first-order local sensitivity analysis.**

Variance-based local sensitivity analysis

We performed a variance-based local sensitivity study of the finite element solution on the parameters as follows:

- A first-order analysis, the 9 parameters are disturbed one at a time respectively of $\pm 10\%$.
- Interaction analysis, the 36 parameters tuples are evaluated simultaneously disturbed.

All the results were interpreted with a polynomial model in order to quantify their weights in the solution variance, referred to as Sobol indices. The initial guess of the parameters set was: $E = 3500\,\text{Pa}$, $\nu = 0.45$, $k = 10^{-13}\,\text{m}^2$, $\varepsilon = 0.55$, $\mu_l = 8 \cdot 10^{-3}\,\text{Pa} \cdot \text{s}$, $\mu_g = 35\,\text{Pa} \cdot \text{s}$, $A_l = 1$, $B_g = 2$ and $S^l_0 = 0.012$. It gives the base error J_0.

First-order analysis

Each parameter is disturbed one at a time respectively of $\pm 10\%$, giving the corresponding error $\tilde{J}$. The relative variations of the error were calculated as follows:

$$\text{Var} = \frac{\tilde{J} - J_0}{J_0} \tag{4.18}$$

where J_0 is the error with the parameters at their initial values. In order to quantify the impact of each parameter, the following linear model was set:

$$\text{Var} = 1 + \sum_i \theta_i \alpha_i \tag{4.19}$$

where α_i is an auxiliary parameter $\in [-1, +1]$ representing the perturbations of $\pm 10\%$ of the i^{th} parameter and θ_i the slope of the variation.

In a first-order analysis, the influence of the i^{th} parameter is given by the Sobol indices:

$$S_i = \frac{\theta_i^2}{\sum_i \theta_i^2} \tag{4.20}$$

The results of the first-order analysis are reported in Table 4.4.

Interaction analysis

We evaluate the correlation between parameters. The 36 tuples $(\alpha_i, \alpha_j)_{i>j}$ have been evaluated at $\pm 10\%$. The corresponding polynomial model becomes:

$$\text{Var} = 1 + \sum_i \theta_i \alpha_i + \sum_{ij, i>j} \theta_{ij} \alpha_i \alpha_j \tag{4.21}$$

with the respective Sobol indices:

$$S_i = \frac{\theta_i^2}{\sum_i \theta_i^2 + \sum_{ij,i>j} \theta_{ij}^2} \quad \text{and} \quad S_{ij} = \frac{\theta_{ij}^2}{\sum_i \theta_i^2 + \sum_{ij,i>j} \theta_{ij}^2} \tag{4.22}$$

The results are reported in Table 4.5.

Parameters correlation						**Parameters independence**	
Tissue specific 49.5%	$S_{ij}(\%)$	Tissue/Sample 35.4%	$S_{ij}(\%)$	Sample specific 2.1%	$S_{ij}(\%)$	12.8%	$S_i(\%)$
$(\nu,\, \varepsilon)$	5.34	$(E,\, \nu)$	8.07	$(E,\, k)$	0.45	E	1.01
$(\nu,\, \mu_l)$	7.59	$(E,\, \varepsilon)$	$0,31$	$(E,\, S_0^l)$	0.26	ν	6.96
$(\nu,\, \mu_g)$	6.59	$(E,\, \mu_l)$	1.83	$(k_{\mathsf{int}}^s,\, S_0^l)$	1.36	k_{int}^s	1.07
$(\nu,\, A_l)$	6.19	$(E,\, \mu_g)$	$1,22$			ε	0.40
$(\nu,\, B_g)$	7.14	$(E,\, A_l)$	0.90			μ_l	1.00
$(\nu,\, a)$	7.06	$(E,\, a)$	1.40			a	0.60
$(\varepsilon,\, \mu_l)$	0.31	$(E,\, B_g)$	1.44			μ_g	0.45
$(\varepsilon,\, \mu_g)$	0.33	$(k_{\mathsf{int}}^s,\, \nu)$	4.13			A_l	0.19
$(\varepsilon,\, A_l)$	0.37	$(k_{\mathsf{int}}^s,\, \varepsilon)$	1.87			B_g	0.71
$(\varepsilon,\, B_g)$	0.37	$(k_{\mathsf{int}}^s,\, \mu_l)$	0.44			S_0^l	0.44
$(\varepsilon,\, a)$	0.43	$(k_{\mathsf{int}}^s,\, a)$	0.72				
$(\mu_l,\, \mu_g)$	1.16	$(k_{\mathsf{int}}^s,\, \mu_g)$	1.01				
$(\mu_l,\, A_l)$	0.88	$(k_{\mathsf{int}}^s,\, A_l)$	1.28				
$(\mu_l,\, B_g)$	1.38	$(k_{\mathsf{int}}^s,\, B_g)$	0.77				
$(\mu_l,\, a)$	1.37	$(S_0^l,\, \nu)$	5.15				
$(\mu_g,\, A_l)$	0.30	$(S_0^l,\, \varepsilon)$	0.28				
$(\mu_g,\, B_g)$	0.81	$(S_0^l,\, \mu_l)$	0.25				
$(\mu_g,\, a)$	0.77	$(S_0^l,\, a)$	3.23				
$(A_l,\, B_g)$	1.14	$(S_0^l,\, \mu_g)$	0.32				
$(A_l,\, a)$	0.49	$(S_0^l,\, A_l)$	0.61				
$(B_g,\, a)$	1.40	$(S_0^l,\, B_g)$	1.29				

Table 4.5: **Sobol indices of the second-order local sensitivity analysis.**

Chapter 5

Patient-specific glioblastoma IDH wild type imaging-informed poromechanical modeling

Contribution (CRediT author statement)

Conceptualization, Methodology, Software, Validation, Investigation, Writing – original draft, Visualization

Non-operable glioblastoma IDH wild type: proposition of a patient-specific forecasting by imaging-informed poromechanical model

Urcun Stéphane[1,2,3], Davide Baroli[4,5], Rohan Pierre-Yves[2], Wafa Skalli[2], Vincent Lubrano[6], Bordas Stéphane P.A.[1], Sciumè Giuseppe[3*]

1 Institute for Computational Engineering Sciences, Department of Engineering Sciences, Faculté des Sciences de la Technologie et de Médecine, Université du Luxembourg, Campus Belval, Luxembourg

2 Institut de Biomécanique Humaine Georges Charpak, Arts et Metiers Institute of Technology, Paris, France

3 Institut de Mécanique et d'Ingénierie, Université de Bordeaux, Talence, France

4 Università della Svizzera Italiana, Euler Institute, Lugano

5 Aachen Institute for Advanced Study in Computational Engineering Science, Rheinisch-Westfälische Technische Hochschule Aachen, Aachen

6 Hôpital Pierre-Paul Riquet, Toulouse

* giuseppe.sciume@u-bordeaux.fr

Abstract

We propose a novel imaging-informed glioblastoma model within a reactive multiphase poromechanical framework. Poromechanics offers to model in a monolithic manner both tissue deformation and pressure-driven fluid flows, these phenomena existing simultaneously in cancer disease. The model also relies on two mechano-biological hypotheses responsible of the heterogeneity of the GBM: the hypoxia signaling cascade and interaction between extra-cellular matrix and tumor cells. The model belongs to the category of patient-specific imaging-informed models as it is initialized and calibrated by the means of patient imaging data. Sensitivity solution on the parameters and on boundary conditions are provided. As this work is only a first step of the inclusion of poromechanics in imaging-informed glioblastoma models, means of improving are provided in the discussion.

5.1 Introduction

In global cancer statistics, primary brain tumors have the 21^{th} rank of incidence but reach the 14^{th} rank of mortality [238]. Glioma represents the large majority of malignant primary brain tumors. The group of diffuse glioma - 'diffuse' being opposed to 'circumscribed' - is the one with the worst prognosis. The diagnosis of diffuse glioma was first based on histological features as infiltrative glioma cells along pre-existing tissue elements, historically known as secondary Scherer's structures. The staging of the World Health Organisation (WHO) of diffuse glioma is based on specific and cumulative histological features: nuclear atypia for stage II, mitotic activity for stage III denoted anaplasic, necrosis and/or microvascular proliferation for stage IV, denoted glioblastoma multiforme (GBM). This study is interested on the WHO highest grade, grade IV GBM. This stage has the poorest prognosis with a median survival around 15 months, and a 5-year survival rate at 5.8%, constant since the year 2000 [241]. The update of the WHO classification in 2016 [154], which includes molecular biomarkers, now differentiates the diffuse gliomas into sub-types. We are specifically interested in the isocitrate dehydrogenase (IDH) wild-type. In clinical literature, between 16% and 40% of GBM are considered non-operable [168, 79], because of a functional critical location which impedes the resection, or because of patient comorbidity. Non-operable cases allow longitudinal data of glioblastoma evolution, on a patient specific basis. Hence, they are of critical interest for modeling and forecasting processes.

GBM have received a large attention of the modeling community. In 2021, an efficient review of glioblastoma modeling was made by Falco *et al.* in [76]. New hypotheses may emerge from *in silico* studies and treatment personalization may be facilitated by the exploration *in silico* of the parameters' space of the patient. This highly lethal disease and the absence of improvement of its survival rate made these two challenges particularly urgent. The authors of [76] reviewed 295 articles published between 2001 and 2020, and defined three categories, continuous, discrete and hybrid. The continuous models considered the disease as a collection of tissue and the targets of this type of model is the invasion pattern and the

treatment response at the macroscale (for instance, see [61, 246]). The discrete models are tailored for the description of intra-cellular phenomena and interaction at the cellular level. They target genetic and immunological properties. Hybrid modeling tries to retrieve the best of both approaches, by informing the models with multi-scale data, such as histological staining, genetic markers and clinical imaging (for discrete and hybrid categories, see [67, 130]). Some of these models, whatever their category, may be initialized and calibrated by clinical imaging data. By this means, they aim to patient-specific results. This supra-category is termed as imaging-informed model. This modeling framework was first developed in 2002, and applied to low- and high-grade gliomas, by Swanson *et al.* in [239], and after in [240, 178, 202]. Since 2013, with the progress of imaging methods, this framework has been developed by Yankeelov *et al.* (see [268]), and applied with clinically-relevant results in various locations such as breast cancer [122] or prostate cancer [151]. imaging-informed glioblastoma modeling has been extensively used in the last decades, and have led to personalized modeling in tumor forecasting and treatment response [2, 112, 147], and to the inclusion of tissue anisotropy [10], among other hypotheses. In 2020, a specific review of imaging-informed glioblastoma modeling was made by Mang *et al.* in [160].

We propose in this article a novel imaging-informed glioblastoma model within a continuous multiphase poromechanical framework. Poromechanics offers to model the coupling between tissue deformation and pressure-driven fluid flows, these phenomena existing simultaneously in cancer disease. Poromechanics is already applied in cancer modeling, *in vitro* [216, 247] and in animal models [91]. However, except a proposition of patient-specific imaging-informed modeling in [73] with only qualitative results, to our knowledge, there is no example of this framework applied to glioblastoma modeling in a clinically-relevant and patient-specific basis. Additionally to the description of the brain tissue as a porous medium, our model relies on two mechano-biological hypotheses responsible of the heterogeneity of the GBM: the hypoxia signaling cascade [173] and interaction between extra-cellular matrix and tumor cells [17]. A subset of the parameters of the model is initialized with the first time point of the patient imaging data, performed during pre-operative examination. The simulation outputs are calibrated against the patient's imaging after 6 cycles of concomitant radiotherapy-temozolomide chemotherapy (RT-TMZ), performed 63 days after the initial time. Through patient's segmentation, the quantities evaluated are the overlapping of the clinical and numerical tumors.

In the article, we briefly present the GBM IDH wild-type and its management, followed by the presentation of the mathematical model, the patient dataset, and the calibration process of the simulation. The results section gives the solution sensitivity on parameters variation and error of the model measured against patient imaging. Mathematical verification, such as solution sensitivity on boundary conditions are provided. As this work is only a first step of the inclusion of poromechanics in imaging-informed glioblastoma modeling, we discuss the improvements and further propositions for this inspiring modeling framework.

5.2 Description of the GBM IDH wild type

Glioma may originate from three sources [276]:

- neural stem cells, embryonic cells located in ventricular and subventricular zones of the brain, which give rise to both neurons and glial cells.
- oligodendrocyte precursor cells, a subset of glial cells precursor specific to oligodendrocytes.
- astrocyte, for which a specific precursor is not yet identified.

Therefore, the determination of the origin the cellular population, and mutations is this population, that give rise to glioma remains the open debate [276]. However, already developed GBM have an astrocytic profile. This profile is characterized by a high heterogeneity both genetic and phenotypic, which creates difficulties both in origin determination and therapeutic design. Among diffuse glioma, GBM is by far the most common (90%). Its incidence represents the majority all kinds of glioma and almost the majority of all primary malignant brain tumor. The median age at diagnosis is 65 years and the incidence is 50% higher for male patients. Except radiation and rare genetic syndromes, there is not validated risk factors. Since 2005, its standard of care is, if possible, surgical resection followed by a six 1-week cycles of concomitant radiotherapy and temozolomide chemotherapy [233], denoted RT-TMZ treatment. The TMZ is used as a radio sensitizer, and after the 6 cycles, TMZ is used as maintenance from six to twelve months. Despite improvement of the median survival, now > 15 months, glioblastoma still has a poor prognosis, with a 5-year survival rate at 5.8%, constant since 2000 [241].

The 2016 WHO classification now includes molecular biomarkers, which define GBM subtypes. The first subtype is defined by the status of isocytrate dehydrogenase (IDH). Non-mutated, the subtype is termed wild-type, other subtypes are mutated IDH-1 or IDH-2. IDH 1, 2 or 3 are enzymes involved in cell metabolism. Mutation of IDH 1 or 2 lead to the accumulation of an inhibitor of glioma stem cell differentiation, but also can promote tumor microenvironment. However, IDH mutants represent 10% of glioblastoma and have a better prognosis, as they are less resistant to chemotherapy and provoke better immune response [116]. It should be noted that the inevitable recurrence of the GBM will ultimately lead to a dominant wild-type *i.e.*, non-mutated IDH. For the sake of brevity, GBM IDH wild-type will be thereafter abbreviated GBMwt. The second subtype is defined by the status of the O^6-methylguanine–DNA methyltransferase (MGMT), methylated or non-methylated. The MGMT gene encodes a DNA-repair protein, therefore a high MGMT activity in cancer creates a resistant phenotype both on chemo- and radiotherapy. MGMT activity can be silenced by methylation and it decreases the DNA-repair activity [106]. The methylation of MGMT, termed m-MGMT, represents around 25% of GBM cases. This marker will influence the patient response to the RT-TMZ treatment, as a m-MGMT profile will be more sensitive to RT effect [41]. The IDH mutations and the MGMT methylation status are not correlated, both types of markers can co-exist.

The staging of GBM is first based on the presence of a necrotic core and/or an abnormal micro-vasculature. These characteristics indicate that hypoxia management is a key feature of GBM. Barnes *et al.* show in [17] that hypoxia applied on GBMwt cells provokes structural changes on the surrounding ECM. The brain ECM has a specific composition. Conversely to the usual rich fibrillar component such as collagen, brain ECM is almost entirely composed of glycosaminoglycans, a non-fibrous component which plays the mechanical role of shock-absorber. GBMwt cells subjected to a hypoxic environment modify the structure of glycosaminoglycans. Hypoxia signaling is made through hypoxia-inducible factor-1α (HIF1α), which provokes the production by the GBMwt cells of the glycoprotein tenascin-C. The tenascin-C modifies the surrounding glycosaminoglycans, leading to a cross-linked, stiffer ECM. This ECM stiffening will ultimately lead to an environment with a higher mechanical stress. Conversely, GBM cells with IDH mutated status have a reduced capacity to produce both HIF1α and tenascin-C. Therefore, this high stiffness of the tumorous tissue is characteristic of GBMwt.

5.3 Reactive poromechanical modeling of GBM IDH wild-type

The model presented in this section belongs to the category termed as imaging-informed reactive multiphase poromechanics. Let us describe each part of this category:

- poromechanics: the physical system is considered as a composite continuum composed of a permeable and deformable solid scaffold in which and through which fluid flows.

- multiphase: solid and fluid compartments are composites. The solid fraction, which could be compared to the medical definition of the stroma, is made of different and distinct materials (epithelial tissue, ECM - itself composite -, wall vessels, to name a few). Likewise, the fluid fraction is composed of different phases (interstitial fluid, immune cells, tumor cells). It should be noted that the blood is not modeled as a circulating fluid in this model.

- reactive: the modeling of living tissue implies the biological interactions of many diffusive chemical agents (oxygen, cytokines), which can belong to any phase of the system. Their own dynamics are strongly coupled with the poromechanical system. The model also includes non-diffusive reaction as mechanically-induced phenotype switch and hypoxic-induced necrosis.

- imaging-informed: in order to simulate patient-specific cases, the initial conditions and the boundary conditions of the problem are provided by the patient MRI measurements. A subset of the model's parameters is fixed by these measurements, another subset is calibrated with them.

General framework

Phases

s	solid
l	lymphatic/interstitial fluid
h	healthy cells
t	tumor cells

Volume fraction

ε^s	solid scaffold: stroma and vascular network
ε	porosity
ε^l	lymphatic/interstitial fluid fraction
ε^h	healthy cells volume fraction
ε^t	tumor cells volume fraction

Species

ω^{bs}	vascular fraction of solid scaffold
ω^{nl}	nutrient fraction of interstitial fluid
$\omega^{\rho t}$	fraction of GBM cells expressing a malignant phenotype
ω^{Nt}	fraction of necrotic GBM cells

Mass terms and coefficients

$\overset{i\to j}{M}$	mass exchange from phase i to phase j
$\overset{i\to j}{\gamma}$	mass exchange rate from phase i to phase j
$\overset{i\to j}{\zeta}$	dimensionless coefficient from phase i to phase j
r^i	intra-phase mass exchange of phase i
ζ^i	intra-phase dimensionless coefficient of phase i

Font

Italic	scalar quantity s
Bold	vectorial quantity $\mathbf{v}$
$n > 1$ overlines	n^{th} order tensorial quantity, *e.g.*, 2$^{\text{nd}}$ order $\bar{\bar{T}}$
One overline	homogenized quantity

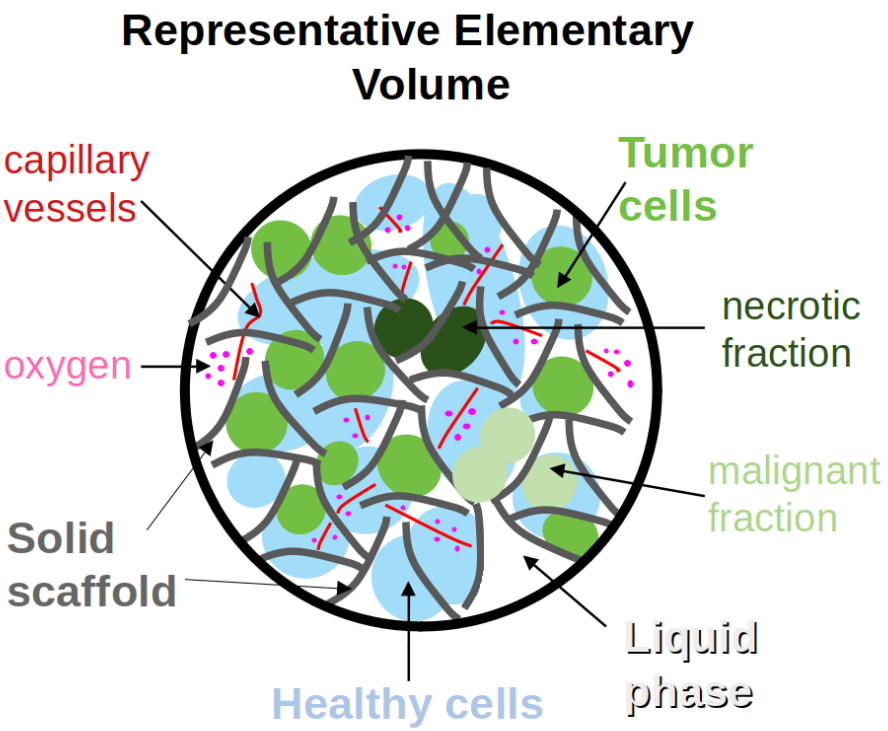

Figure 5.1: **Representative elementary volume of the modeling.** Phases are in bold font: solid scaffold (grey), liquid phase (white), healthy cells (blue) tumor cells (green). Species: of the solid scaffold, capillary vessels (red); of the liquid phase, oxygen (pink); of the tumor cells, necrotic (dark green), malignant (light green).

Let ε^s, the volume fraction occupied by the solid scaffold and ε, the volume fraction occupied by the fluid phases.

$$\varepsilon + \varepsilon^s = 1 \tag{5.1}$$

The vascular network ω^{bs} is considered as a fraction of the solid scaffold, its volume fraction is denoted $\varepsilon^s\omega^{bs}$.

Considering the fluid phases (t, tumor, h, healthy and l, fluid) and defining their own saturation degree as $S^\beta = \varepsilon^\beta/\varepsilon$ (with $\beta = t, h, l$ the index associated to extra-vascular fluids), we obtain:

$$S^l + S^t + S^h = 1 \tag{5.2}$$

Their respective volume fractions are defined by $\varepsilon^\beta = \varepsilon S^\beta$.

To facilitate the understanding of the terms of the governing equations, we report the general form the mass conservation equations for a phase and a species provided by the thermodynamically constrained averaging theory (TCAT) [99]

framework. The spatial form of the mass balance equation for an arbitrary phase reads α

$$\underbrace{\frac{\partial\left(\varepsilon^{\alpha}\rho^{\alpha}\right)}{\partial t}}_{\text{Accumulation rate}}+\underbrace{\nabla\cdot\left(\varepsilon^{\alpha}\rho^{\alpha}\mathbf{v}^{\overline{\alpha}}\right)}_{\text{Outward of phase flow}}-\underbrace{\sum_{\kappa\in\Im_{c\alpha}}\overset{\kappa\rightarrow\alpha}{M}}_{\text{Interphase mass transport}}=0 \tag{5.3}$$

where ρ^{α} is the density, $\mathbf{v}^{\overline{\alpha}}$ is the local velocity vector, $\overset{\kappa\rightarrow\alpha}{M}$ are the mass exchange terms accounting for transport of mass at the $\kappa\alpha$ interface from phase κ to phase α, and $\sum_{\kappa\in\Im_{c\alpha}}$ is the summation over all the phases sharing interfaces with the phase α.

An arbitrary species i dispersed within the phase α has to satisfy mass conservation too. The following spatial equation is derived following TCAT

$$\underbrace{\frac{\partial\left(\varepsilon^{\alpha}\rho^{\alpha}\omega^{\overline{i\alpha}}\right)}{\partial t}}_{\text{Accumulation rate}}+\underbrace{\nabla\cdot\left(\varepsilon^{\alpha}\rho^{\alpha}\omega^{\overline{i\alpha}}\mathbf{v}^{\overline{\alpha}}\right)}_{\substack{\text{Outward of species}\\ \text{advective transport}}}+\underbrace{\nabla\cdot\left(\varepsilon^{\alpha}\rho^{\alpha}\omega^{\overline{i\alpha}}\mathbf{u}^{\overline{i\alpha}}\right)}_{\substack{\text{Outward of species}\\ \text{diffusive transport}}}-\underbrace{\varepsilon^{\alpha}r^{i\alpha}}_{\substack{\text{Intraphase reactive}\\ \text{exchange of mass}}}+\underbrace{\sum_{\kappa\in\Im_{c\alpha}}\overset{i\alpha\rightarrow i\kappa}{M}}_{\substack{\text{Interphase mass transport}\\ \text{of the species}}}=0 \tag{5.4}$$

where $\omega^{\overline{i\alpha}}$ identifies the mass fraction of the species i dispersed with the phase α, $\varepsilon^{\alpha}r^{i\alpha}$ is a reaction term that allows to take into account the reactions between the species i and the other chemical species dispersed in the phase α, and $\mathbf{u}^{\overline{i\alpha}}$ is the diffusive velocity of the species i. $\overset{i\alpha\rightarrow i\kappa}{M}$ are mass exchange terms accounting for mass transport of species i at the $\kappa\alpha$ interface from phase α to phase κ.

Governing equations

The solid scaffold being deformable, we use the chain rule to define the material derivative:

$$\frac{D^{\alpha}f^{\pi}}{Dt}=\frac{\partial f^{\pi}}{\partial t}+\nabla f^{\pi}\cdot\mathbf{v}^{\alpha} \tag{5.5}$$

And apply it to Eq.5.3 and 5.4

We define the mass conservation of phases by using Eq.5.5 to express derivatives with respect to the solid phase ε^{s}. Introducing porosity ε and the saturation degrees of its phases t, h, and l, the mass balance equations of s, t, h and l phases read respectively:

$$\frac{\mathrm{D}^{s}}{\mathrm{D}t}\left(\rho^{s}\varepsilon^{s}\right)+\rho^{s}\varepsilon^{s}\nabla\cdot\mathbf{v}^{\overline{s}}=\overset{t\rightarrow s}{M} \tag{5.6}$$

$$\frac{\mathrm{D}^{s}}{\mathrm{D}t}\left(\rho^{t}\varepsilon S^{t}\right)+\nabla\cdot\left(\rho^{t}\varepsilon S^{t}\mathbf{v}^{\overline{ts}}\right)+\rho^{t}\varepsilon S^{t}\nabla\cdot\mathbf{v}^{\overline{s}}=\overset{l\rightarrow t}{M}-\overset{t\rightarrow s}{M} \tag{5.7}$$

$$\frac{\mathrm{D}^s}{\mathrm{Dt}}\left(\rho^h \varepsilon S^h\right) + \nabla \cdot \left(\rho^h \varepsilon S^h \mathbf{v}^{\overline{hs}}\right) + \rho^h \varepsilon S^h \nabla \cdot \mathbf{v}^{\overline{s}} = 0 \tag{5.8}$$

$$\frac{\mathrm{D}^s}{\mathrm{Dt}}\left(\rho^l \varepsilon S^l\right) + \nabla \cdot \left(\rho^l \varepsilon S^l \mathbf{v}^{\overline{ls}}\right) + \rho^l \varepsilon S^l \nabla \cdot \mathbf{v}^{\overline{s}} = -\overset{l\to t}{M} \tag{5.9}$$

This system can be resumed as follow:

- tumorous phase takes its mass from interstitial fluid phase $\overset{l\to t}{M}$
- tumorous phase produce solid (fibrous) components $\overset{t\to s}{M}$
- healthy cellular phase is considered at the equilibrium

Mass conservation equations of species The only diffusive species considered is the oxygen, dissolved in the interstitial fluid phase l, its mass fraction denoted $\omega^{\overline{nl}}$. It motion is governed by advection-diffusion equation. The species is produced by micro-capillaries of the solid fraction phase ω^b, and absorbed by t and h, tumor and healthy cells, its mass balance reads

$$\rho\varepsilon^l \frac{\partial^s \omega^{\overline{nl}}}{\partial \mathrm{t}} + \nabla \cdot \left(\rho\varepsilon^l \omega^{\overline{nl}} \mathbf{u}^{\overline{\overline{nl}}}\right) + \varepsilon^l \rho \mathbf{v}^{\overline{ls}} \cdot \nabla \omega^{\overline{nl}} = \overset{b\to nl}{M} - \overset{nl\to t}{M} - \overset{nl\to h}{M} + \omega^{\overline{nl}} \overset{l\to t}{M} \tag{5.10}$$

The necrotic fraction of tumor cells $\omega^{\bar{N}t}$ is a non-diffusive species. We obtain:

$$\frac{D^s}{Dt}\left(\rho^t \omega^{\bar{N}t} \varepsilon S^t\right) + \nabla \cdot (\rho^t \omega^{\bar{N}t} \varepsilon S^t \mathbf{v}^{\bar{ts}}) + \rho^t \omega^{\bar{N}t} \varepsilon S^t \nabla \cdot \mathbf{v}^{\bar{s}} = \varepsilon S^t r^{Nt} \tag{5.11}$$

with the constitutive equation of the necrotic growth rate r^{Nt} Eq.5.40 to calibrate.

Momentum equations The porous system is modeled as a continuum, under the linear momentum conservation:

$$\nabla \cdot \mathbf{t}^{\bar{\bar{T}}} = 0 \tag{5.12}$$

Where $\mathbf{t}^{\bar{\bar{T}}}$ is the total Cauchy stress tensor. We assume here that all phases are incompressible. However, the overall multiphase system is not incompressible, because of the presence of porosity that evolves according to the scaffold deformation. As all phases are incompressible, their densities ρ^α (with $\alpha = s, t, l$) are constant and the Biot's coefficient $\beta = 1$. With these premises, the total Cauchy stress tensor appearing in Eq.5.12 is related to the Biot's effective stress as follows

$$\mathbf{t}^{\bar{\bar{E}}} = \mathbf{t}^{\bar{\bar{T}}} + \beta p^s \bar{\bar{\mathbf{1}}}, \tag{5.13}$$

where $p^s = S^l p^l + S^t p^h + S^t p^h$ is denoted the solid pressure, describing the interaction between the fluids and the solid scaffold.

Internal variables

ECM stiffening One internal variable, the Young's Modulus of the ECM E^{ECM}, is updated every 250 minutes, *i.e.* every 10 iterations. This corresponds to a physical quantity that has a slower evolution than the primary unknowns (the displacement field, the pressures of the fluids and the level of oxygen). In the following equations, $T = 250\,\text{min}$. The stiffening of the ECM reads is modeled as follows:

$$E^{ECM}_{t+T} = E^{ECM}_t + (1 - \frac{E^{ECM}_t}{E_{\text{idh}}})\mathcal{H}(E_t, E_{\text{min}}, E_{\text{idh}})\langle \omega_{\text{crit}} - \omega^{\bar{nl}} \rangle^+ \tag{5.14}$$

with E_{min} is fixed at the lower bound of the stiffness measured in the cortex tissue $E_{\text{min}} = 1.2\text{kPa}$ and E_{idh}, the stiffness of cross-linked ECM, to calibrate. The regularized step function $\mathcal{H}$ is used in several constitutive equations and presented Eq.5.34.

Malignant fraction and RT-TMZ treatment Two other internal variables, the fraction of GBMwt cells expressing a malignant phenotype $\omega^{\rho t}$ and the administration of the RT-TMZ treatment are updated on a daily basis. $\omega^{\rho t}$ is updated every 4.5 days, which corresponds to 260 iterations. We note a lack of quantitative information about phenotype switch in experimental literature. However, we found that at the cell's scale, phenotype switch can be measured in minutes or in hours [21]. The only example we found at the macroscale is about lung cancer cells, where the effects of a phenotype switch is observable after a minimum of 72 hours [176]. In the absence of further information on GBMwt cells, we keep our range $T = 4.5$ days. If tumorous area undergoes a high osmotic pressure,*i.e.* greater than the threshold p_{idh}, and a chronic hypoxia, during the period T, a fraction of IDH wild-type cells $\omega^{\rho t}$ changes their phenotype. This fraction is updated as follows:

$$\omega^{\rho t}_{t+T} = \omega^{\rho t}_t + \zeta^{\rho}(1 - \omega^{\rho t}_t)\langle p^t - p_{\text{idh}} \rangle^+ \langle \omega_{\text{crit}} - \omega^{\bar{nl}} \rangle^+ \varepsilon S^t \tag{5.15}$$

with ζ^{ρ} the phenotype switch rate, εS^t the volume fraction of GBM cells, and $\langle \alpha - \beta \rangle^+ = 0$ if $\alpha < \beta$ and 1 else.

The RT-TMZ treatment is administrered by following the standard of care defined in 2005 in [233]: before 1 month after diagnosis, the patient started 6 weekly cycles: 5 daily doses of 2 Gray radiotherapy (RT) concomitant with a daily dose of Temozolomide (TMZ). The second part of the standard treatment, 24 weeks of daily TMZ, is not simulated in this article because there is no patient data at this time point. The patient has a non-methylated MGMT profile, which is more resistant to the RT-TMZ treatment [41]. The treatment is modeled by a long and a short effect. The long effect only affects the tumor growth rate:

$$\tilde{\gamma}^t_g = \gamma_{\text{RT}} \gamma^t_g \tag{5.16}$$

The short effect provokes the necrosis of the tissues, and preferentially the tumorous ones. In this article, we only model necrosis of GBMwt cells, with two dependencies. First, the TMZ being transmitted through the vascular network, its effect is increased accordingly. Second, the density of tumor cells are known to have a more resistant profile [208]. These two dependencies are modeled by the following equations:

$$f_{\mathsf{b}} = \zeta^{kill}\omega^{bs} \tag{5.17}$$

f_{b} represents the vascular dependency of RT-TMZ. ζ^{kill} is the optimal killing rate of cells by RT, ω^{bs} the vascular fraction of the stroma.

$$f_{\mathsf{t}} = \zeta^{kill}\varepsilon S^h \tag{5.18}$$

f_{t} represents the TC density dependency of RT-TMZ. εS^h is the fraction of healthy cells.
RT-TMZ short effect on the necrotic fraction $\omega^{\bar{N}t}$ is modeled by the following equation, the period $T = 1$ days, 5 days per week:

$$\omega_{t+T}^{\bar{N}t} = \omega_t^{\bar{N}t}(1 - \omega_t^{\bar{N}t})(f_{\mathsf{b}} + \mathsf{N}_{\mathsf{mgmt}} f_{\mathsf{t}}) \tag{5.19}$$

with $\mathsf{N}_{\mathsf{mgmt}}$, the negative status of the methylation of MGMT.

Constitutive relationships

Stress-strain relationship For the solid scaffold deformation, the chosen closure relationship for the effective stress $\mathbf{t}^{\bar{\bar{E}}}$ is linear elastic:

$$\mathbf{t}^{\bar{\bar{E}}} = \lambda tr(\epsilon)\bar{\bar{\mathbf{1}}} + 2\mu\epsilon \tag{5.20}$$

with $\bar{\bar{\mathbf{1}}}$ the identity tensor, $\epsilon(\mathbf{u^s}) = \frac{1}{2}(\nabla\mathbf{u}^s + (\nabla\mathbf{u}^s)^T)$ the linearized strain tensor, and the Lamé constant $\lambda = \dfrac{E\nu}{(1+\nu)(1-2\nu)}$ and $\mu = \dfrac{E}{2(1+\nu)}$.

Generalized Darcy's law The interaction between fluid phases and the solid scaffold are modeled by a generalized Darcy's flow, deduced from the linear momentum conservation of fluid phases. The details of this constitutive relationship are provided in [220] and [247].

$$-\frac{k_{\mathsf{rel}}^{\alpha} k_{\mathsf{int}}^{s}}{\mu^{\alpha}}\nabla p^{\alpha} = \varepsilon S^{\alpha}(\mathbf{v}^{\bar{\alpha}s}) \qquad \alpha = g, l \tag{5.21}$$

where k_{int}^{s} is the intrinsic permeability of the solid scaffold, μ^{α}, $k_{\mathsf{rel}}^{\alpha}$ and p^{α} are respectively the dynamic viscosity, relative permeability and the pressure of each fluid phase $\alpha = l, h, t$. The three fluid phases have their own relative permeabilities:

$$k_{\mathsf{rel}}^{l} = (S^l)^{A_l} \qquad k_{\mathsf{rel}}^{h} = (S^h)^{B_g} \qquad k_{\mathsf{rel}}^{t} = (S^t)^{B_g} \tag{5.22}$$

with A_l and B_g - common to the glial and glioma cells - to be calibrated.

Pressure-saturation relationships The porosity is saturated by three immiscible fluid phases, and each phase having its own pressure, three capillary pressures p^{ij}, *i.e.* pressure difference between fluid i and fluid j, can be defined

$$p^{hl} = p^h - p^l \qquad p^{th} = p^t - p^h \qquad p^{tl} = p^t - p^l \tag{5.23}$$

As in [215], we assume here that IF is the wetting fluid, HC is the intermediate-wetting fluid and TC the non-wetting one. Only two between the previously defined capillary pressures are independent since

$$p^{tl} = p^{hl} + p^{th} \tag{5.24}$$

The two capillary pressure-saturation relationships read

$$S^l = 1 - \left[\frac{2}{\pi}\arctan\left(\frac{p^{hl}}{a}\right)\right] \tag{5.25}$$

$$S^t = \frac{2}{\pi}\arctan\left(\Gamma\frac{p^{th}}{a}\right) \tag{5.26}$$

where a is a constant parameter depending on ECM microstructure, and Γ is the ratio of HC-IF and TC-HC interfacial tensions. In the literature, a generic value for an invasive tumor cell line was previously fixed at 6 [216]. Experimental measurements of surface tension of astrocytes and different glioblastoma cell lines [105, 270] give the ratio between 1.3 and 4.8, a higher ratio characterizing a higher invasiveness.

Malignant cells mobility The fraction of GBMwt cells that expressed a malignant phenotype, $\omega^{\rho t}$, influences the dynamic viscosity of the GBM phase, these cells being more mobile. Beforehand, the dynamic viscosity of the GBM phase is the same than healthy glial cells μ_h, the influence of the malignant cells fraction follows this equation:

$$\mu_t = \mu_h(1 - \zeta_\mu^{\rho t}\omega^{\rho t}) \tag{5.27}$$

where $\zeta_\mu^{\rho t}$ is the coefficient representative of the malignant fraction influence, to calibrate.

ECM degradation and permeability

$$k^s_{\text{int}}(\omega^\rho) = (k_{\text{max}} - k^s_{\text{int0}})\omega^\rho + k^s_{\text{int0}} \tag{5.28}$$

where $k^s_{\text{int}0}$ is the intrinsic permeability deduced from imaging data and bounded by experimental literature and k_{max}, corresponding to the permeability of an ECM fully degraded, to calibrate.

Nutrient diffusion The tumor cell growth, metabolism and necrosis are regulated by a variety of nutrient species and intracellular signaling. Two pathways are proposed in the models: one considered nutrient, the oxygen, regulating growth, hypoxia and neo-angiogenesis, and IDH phenotype switch, regulating apoptosis inhibition and cell mobility. For the oxygen diffusion, the Fick's law adapted to a porous medium, was adopted to model diffusive flow of oxygen Eq.5.10:

$$\omega^{\bar{nl}}\mathbf{u}^{\bar{nl}} = -D^{nl}\nabla\omega^{\bar{nl}} \tag{5.29}$$

where D^{nl} the diffusion coefficient for oxygen in the interstitial fluid is defined by the constitutive equation from [215]

$$D^{nl} = D^{nl}_0(\varepsilon S^l)^\delta, \tag{5.30}$$

where $D^{nl}_0 = 2.5 \cdot 10^{-9}$ corresponding to the ideal case of oxygen diffusion in pure water, *i.e.* with $\varepsilon S^l = 1$, at $37°$ [265]. The exponent δ is equal to 2, to account for the tortuosity of cell-cell interstitium where oxygen diffuse [216].

Tumor cells growth and metabolism Tumor cell growth is related, for its main part, to the exchange allowed by oxygen between the IF and the living fraction of the tumor. For its smaller part, it is related to the exchange allowed by other nutrients (*e.g.* glucose, lipid) in hypoxic situation, between the IF and the positive phenotype IDH fraction of the living tumor. The total mass exchange from IF to the tumor cell phase is defined as

$$\sum_{i\in l} \overset{i\to t}{M} = \underset{\text{Oxy}}{\overset{i\to t}{M}} + \underset{\text{Fat}}{\overset{i\to t}{M}} \tag{5.31}$$

$$\underset{\text{Oxy}}{\overset{i\to t}{M}} = \overset{l\to t}{\gamma}\varepsilon S^t(1-\omega^N)\mathcal{H}_p(p^t)\mathcal{H}(\omega^{\bar{nl}}) \tag{5.32}$$

$$\underset{\text{Fat}}{\overset{i\to t}{M}} = \overset{l\to t}{\gamma}\varepsilon S^t(1-\omega^N)\zeta^{\rho t}_A\omega^{\rho t}\mathcal{H}_p(p^t) \tag{5.33}$$

where $\underset{\text{Oxy}}{\overset{i\to t}{M}}$ represents the nutrient pathway of TC metabolism and $\underset{\text{Fat}}{\overset{i\to t}{M}}$ the anoxic growth part due to lipid synthesis of GBMwt malignant cells [8].

$\overset{l\to t}{\gamma}$ is the tumor growth rate parameter, $\varepsilon S^t(1-\omega^N)$ is the living fraction of the tumor, $\omega^{\rho t}$, its positive IDH phenotype fraction and $\zeta^{\rho t}_A$, their apoptosis inhibited fraction.

$\mathcal{H}$ and $\mathcal{H}_p$ are regularized step functions varying between 0 and 1, with two threshold parameters σ_1, σ_2, *i.e.* $\mathcal{H} =$

$\mathcal{H}(\sigma, \sigma_1, \sigma_2)$. When the variable σ is greater than σ_2, $\mathcal{H}$ is equal to 1, it decreases progressively when the variable is between σ_1 and σ_2 and is equal to zero when the variable is lower than σ_1. $\mathcal{H}$ represents the growth dependency on oxygen:

$$\mathcal{H}(\omega^{\bar{nl}}, \omega_{\text{crit}}, \omega_{\text{env}}) = \begin{cases} 0 \quad \text{if} \quad \omega^{\bar{nl}} \leq \omega_{\text{crit}} \\ \\ \dfrac{1}{2} - \dfrac{1}{2}\cos\left(\pi \dfrac{\omega^{\bar{nl}} - \omega_{\text{crit}}}{\omega_{\text{env}} - \omega_{\text{crit}}}\right) \quad \text{if} \quad \omega_{\text{crit}} \leq \omega^{\bar{nl}} \leq \omega_{\text{env}} \\ \\ 1 \quad \text{if} \quad \omega^{\bar{nl}} \geq \omega_{\text{env}} \end{cases} \tag{5.34}$$

ω_{env}, the optimal oxygen mass fraction, is set to $4.2 * 10^{-6}$ which corresponds, according to Henry's law, to 90mmHg, the usual oxygen mass fraction in arteries (see [188]). ω_{crit}, the hypoxia threshold, is cell-line dependent, for tumor cells, it has been set to a very low value: 10^{-6} (≈ 20mmHg, for common human tissue cells, hypoxic level is defined between 10 and 20mmHg [128]) Function $\mathcal{H}_p$ represents the dependency on pressure:

$$\mathcal{H}_p(p^\alpha, p_{\text{idh}}, p_{\text{crit}}) = \begin{cases} 1 \quad \text{if} \quad p^\alpha \leq p_{\text{idh}} \\ \\ \sqrt{\dfrac{p_{\text{crit}} - p^\alpha}{p_{\text{crit}} - p_{\text{idh}}}} \quad \text{if} \quad p_{\text{idh}} \leq p^\alpha \leq p_{\text{crit}} \\ \\ 0 \quad \text{if} \quad p^\alpha \geq p_{\text{crit}} \end{cases} \tag{5.35}$$

Before phenotype switch, IDH wild-type GBM cells are known to produce an important quantity of stroma [17]. Hence, a part of the mass growth term related to oxygen metabolism $\underset{\text{Oxy}}{\overset{l\to t}{M}}$ is converted into stroma:

$$\overset{t\to s}{M} = \overset{t\to sl\to t}{\zeta} \underset{\text{Oxy}}{\overset{}{M}} \tag{5.36}$$

As tumor grows, oxygen is taken up from the IF and produce by the vascular fraction of the solid scaffold, so that the sink and source terms in Eq.5.10 take the following form:

$$\overset{nl\to t}{M} = \overset{nl\to t}{\gamma} \varepsilon S^t (1 - \omega^N) \langle \omega^{\bar{nl}} - \omega_{\text{crit}} \rangle^+ \mathcal{H}_p(p^t), \tag{5.37}$$

$$\overset{nl\to h}{M} = \overset{nl\to h}{\gamma} \varepsilon S^h \langle \omega^{\bar{nl}} - \omega_{\text{crit}} \rangle^+ \mathcal{H}_p(p^h), \tag{5.38}$$

$$\overset{b\to nl}{M} = \overset{b\to nl}{\gamma} \varepsilon^s \omega^{bs} \langle \omega_{\text{env}} - \omega^{\bar{nl}} \rangle^+ \tag{5.39}$$

with $\overset{i\to j}{\gamma}$ the correspond mass exchange rate form phase i to phase j, where the term $\varepsilon S^t(1-\omega^N)$ is the volume fraction of living tumor cells, εS^h the volume fraction of healthy cells and $\varepsilon^s\omega^{bs}$ the volume fraction of vascularized stroma.

The necrotic growth rate r^{Nt} is defined by:

$$\varepsilon S^t r^{Nt} = \gamma^{Nt}(1-\tilde{\mathcal{H}}(\omega^{\bar{nl}}))(1-\omega^{\bar{N}t})\varepsilon S^t, \tag{5.40}$$

where $\gamma^{Nt}=0.01$ is the necrotic growth rate. The parameters to calibrate are summarized in Table 5.3.

5.4 Patient specific imaging-informed modeling

Patient dataset

The dataset is composed of MRI methods with a resolution of $256\times256\times200$. They are displayed Fig.5.2. The dataset contains:

- a segmentation, Fig.5.2A, by the Deep Medic convolutional neural network [126], cleaned by authors of this article. The segmentation gives edema, tumor and necrosis. The segmentation is performed by using the T1 Gadolinium contrast enhanced (T1-CE) method, Fig.5.2C, and the very long sequence T2 fluid attenuated inversion recovery (FlAIR) method, Fig.5.2D.
- a registration, Fig.5.2B, by FAST hidden Markov chain [274], which only inform about grey and white matter, as the tumor tissue is partially misinterpreted as CSF. FAST uses T1-CE method for its registration.
- a diffusion weighted MRI method, termed as apparent diffusion coefficient (ADC) of water, Fig.5.2E.
- a perfusion MRI method, termed as relative cerebral blood volume (rCBV), Fig.5.2F.

This dataset is given at two time points: pre-operative examination and after the 6 cycles of RT-TMZ therapy. 63 days separates the two time points. The first point is used for initial conditions of the model, the second point for the calibration of the parameters.

The region of interest (ROI) shown Fig.5.3A is defined in accordance with the surgical practice [224]. The ROI corresponds to the segmented volume of the contrast-enhanced tumor plus 2 cm margin around this volume, where a GBM has the greater probability to progress. Nevertheless, this clinical margin does not presume of the size of the computational domain, shown Fig.5.3B. The influence of the prescribed boundary conditions on the GBM evolution is measured separately (see Appendix 5.7). The size of the computational domain is defined by a negligible influence of the boundary conditions on the numerical results.

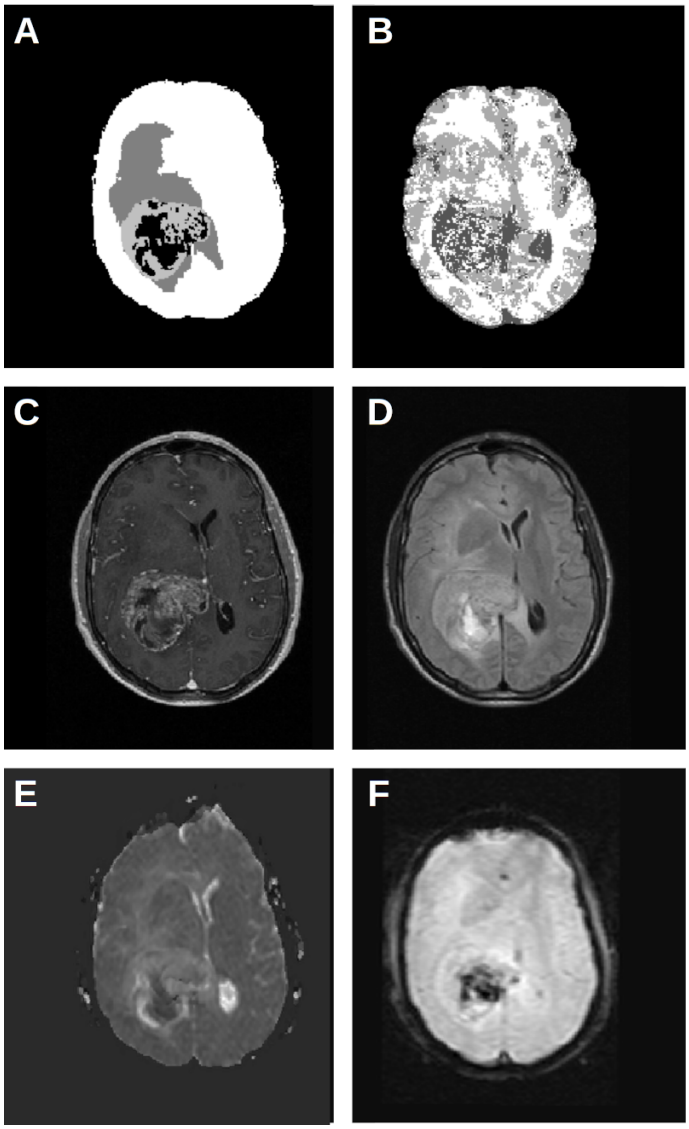

Figure 5.2: **Patient imaging dataset. A** Deep Medic segmentation gives brain mask (white), edema (dark grey), tumor (light grey) and necrotic (black) zones. **B** FAST segmentation gives only grey and white matter zones, as the tumor tissue is partially misinterpreted as CSF (dark grey). **C** T1-CE method gives the density of solid components (brighter contrast, higher density). **D** FlAIR method gives the density of fluid components (brighter contrast, higher density). **E** ADC method gives the diffusion coefficient of water (brighter contrast, higher coefficient). **F** r-CVB method gives the permeability between intra- and extra-vascular space (brighter contrast, higher permeability).

Initial parameters settings

The quantities and methods are summarized Tables in 5.1, 5.2 and 5.3. These tables represent the parameters obtained by *ex vivo* mechanical testing, informed by clinical imaging and for the calibration respectively.

Segmentation Tumor segmentation with Deep Medic and brain registration with FAST give two distinct partitions of the computational domain Ω:

- Deep Medic partition gives Ω_{CE}, the GBM Contrast Enhanced non-necrotic domain, Ω_N, the GBM necrotic domain, Ω_E the GBM edema domain and Ω_O the outer segmentation domain. The Deep Medic partition is defined by $\Omega_{CE} \cup \Omega_N \cup \Omega_E \cup \Omega_O = \Omega$
- FAST partition gives Ω_{CSF}, the CSF compartment of the patient brain -which cannot be exploited due to tumor tissue-, Ω_G, the grey matter subdomain and Ω_W the white matter subdomain. The FAST partition is defined by

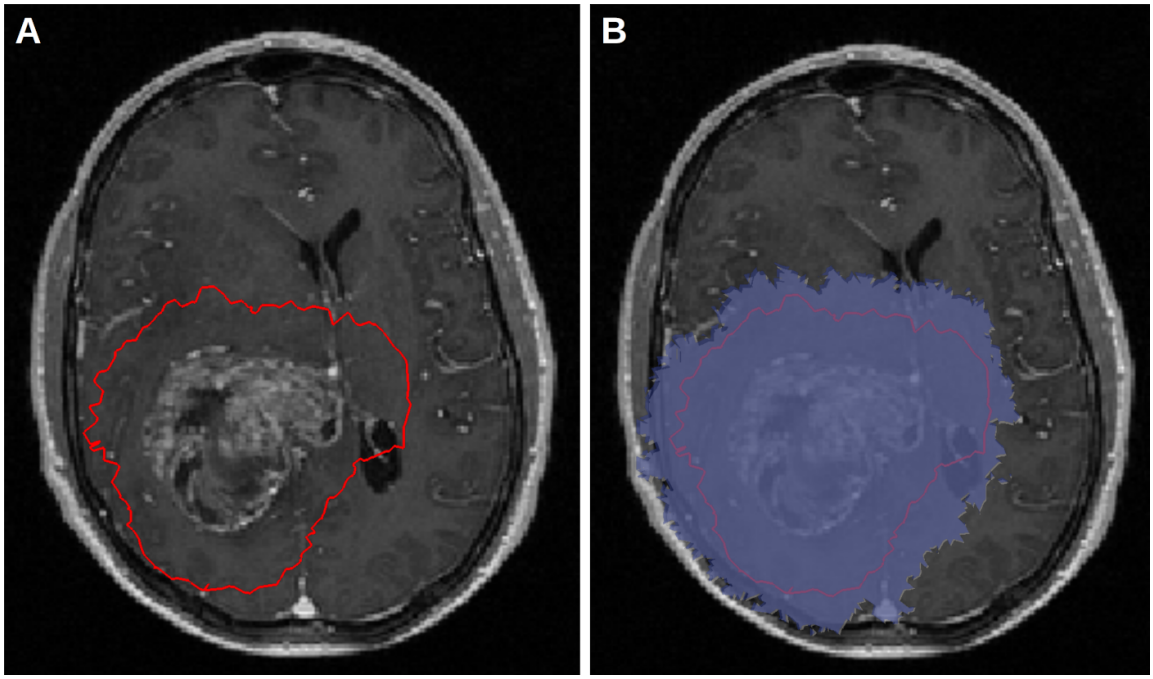

Figure 5.3: **Definition of the region of interest (ROI). A** ROI defined by the clinical margin ($\approx 2\,$cm around the tumor zone). **B** Computational domain defined by boundary conditions ($2.27 \pm 0.3\,$cm around the tumor zone) with a negligible sensitivity on the tumor evolution, for further details see appendix 5.7.

$$\Omega_{CSF} \cup \Omega_G \cup \Omega_W = \Omega$$

ADC method gives diffusion coefficient of water and it is inversely correlated to cellularity [268]. For this reason, we choose to consider the interstitial fluid (IF) saturation S^l proportional to ADC contrast. As there is the presence of an edema, the maximum contrast ADC_{max} corresponds to a pathological value of IF pressure. We have set it to $p_{\text{max}} = 400$Pa and the minimal value ADC_{min}, which correspond to the maximum cellularity (*e.g.*, the tumor necrotic zones), at a value below normal pressure $p_{\text{min}} = 40$Pa. Then, we obtain the linear function to prescribe the initial conditions for IF pressure:

$$p_0^l(x,y,z) = \frac{p^l_{\text{max}} - p^l_{\text{min}}}{\text{ADC}_{\text{max}} - \text{ADC}_{\text{min}}} \left(\text{ADC}(x,y,z) - \text{ADC}_{\text{min}}\right) + p^l_{\text{min}} \tag{5.41}$$

The tumor quantities are defined over $\Omega_{CE} \cup \Omega_N$ so they need both segmentation and MRI methods to be prescribed. In [271], histological cuts on 7 patients with GBMwt gives a volume fraction of GBMwt cells of $\varepsilon S^t = 0.12 \pm 0.07$. With the porosity estimation in [248], $\varepsilon = 0.55 \pm 0.05$, it gives the following range of tumor cells saturation S^t between 0.24 and 0.115 As base values, we chose the maximum saturation in the necrotic core $S^t_N = 0.24 \in \Omega_N$ and a value slightly below average in the contrast-enhanced zone $S^t_{CE} = 0.165 \in \Omega_{CE}$. The relationship between S^t and TC pressure difference p^{th} depends on two parameters a and Γ. With $a = 550$ and $\Gamma = 6$, we obtain $p^{th}_N = 34$Pa and $p^{th}_{CE} = 22$Pa. These base

values are tuned by the means of the ADC mapping:

$$p_0^{th}(x,y,z) = \begin{cases} p_N^{th}\left(1 - \dfrac{p_0^l(x,y,z)}{p_{\mathsf{max}}^l}\right) & \text{in } \Omega_N \\ \\ p_{CE}^{th}\left(1 - \dfrac{p_0^l(x,y,z)}{p_{\mathsf{max}}^l}\right) & \text{in } \Omega_{CE} \end{cases} \tag{5.42}$$

As the saturation of healthy glial cells S^h is constrained by Eq.5.2, this saturation is not directly linked by the capillary pressure p^{hl} of glial cells. Nevertheless, the IF saturation S^l is subjected to p^{hl} by the Eq.5.25. The initial mapping of p^{hl} with Deep Medic segmentation and ADC method respects the range of physical values deduced from [248]. In edema zone Ω_E, the base value of p_E^{hl} is fixed at $800\,\mathsf{Pa}$, which gives a pathological value of $S^l = 0.39$. In the rest of the domain $\Omega \setminus \Omega_E$, the base value p_R^{hl} is fixed at $1.6\,\mathsf{kPa}$, which gives a physiological value of $S^l = 0.11$.

$$p_0^{hl}(x,y,z) = \begin{cases} p_E^{hl}\left(1 - \dfrac{p_0^l(x,y,z)}{p_{\mathsf{max}}^l}\right) & \text{in } \Omega_E \\ \\ p_R^{hl}\left(1 - \dfrac{p_0^l(x,y,z)}{p_{\mathsf{max}}^l}\right) & \text{in } \Omega \setminus \Omega_E \end{cases} \tag{5.43}$$

The initial value of p^{hl} also sustains the intracranial pressure p^s (see Eq.5.13) which is defined all over the domain. With the initial mapping of p^{hl}, we obtain an average intracranial pressure p^s of $7.75\mathsf{mmHg}$, and of $12.5\mathsf{mmHg}$ in the inner core of the tumor. These values are in balance with clinical measurements [39].

The mapping of the intrinsic permeability of the stroma k_{int}^s is performed through FAST registration, as the white matter tracks has a higher permeability [120], and through the ADC method, because we interpret the zones of accumulation of fluids as zones with a higher permeability. As the patient data does not contain a diffusion tensor imaging method, k_{int}^s remains a scalar and heterogeneous quantity, but not a vectorial one. The determination of intrinsic permeability of the brain is a very difficult experimental task, and the wide range of values obtained remains an open debate (see [248] for details). For k_{min}^s, we choose one order lower value than we found in [248], $k_{\mathsf{min}}^s = 10^{-14}\,\mathsf{m}^2$. For k_{max}^s, we choose the lower bound of [248], $k_{\mathsf{max}}^s = 10^{-13}\,\mathsf{m}^2$, as the grey and white matter were not distinguished. Where the voxels are labeled as white matter, we follow the trends of the results of Jamal *et al.* [120] by prescribing a 15 fold higher value, *i.e.* the maximum value of k_{int}^s is $1.5 \cdot 10^{-12}\,\mathsf{m}^2$.

$$k_{\mathsf{int}\,0}^s(x,y,z) = \begin{cases} \dfrac{k_{\mathsf{max}}^s - k_{\mathsf{min}}^s}{\mathsf{ADC}_{\mathsf{max}} - \mathsf{ADC}_{\mathsf{min}}}\left(\mathsf{ADC}(x,y,z) - \mathsf{ADC}_{\mathsf{min}}\right) + k_{\mathsf{min}}^s & \text{in } \Omega \setminus \Omega_W \\ \\ 15\left(\dfrac{k_{\mathsf{max}}^s - k_{\mathsf{min}}^s}{\mathsf{ADC}_{\mathsf{max}} - \mathsf{ADC}_{\mathsf{min}}}\left(\mathsf{ADC}(x,y,z) - \mathsf{ADC}_{\mathsf{min}}\right) + k_{\mathsf{min}}^s\right) & \text{in } \Omega_W \end{cases} \tag{5.44}$$

rCBV method is treated the same way as ADC method. It gives the vascular fraction ω^{bs} of the solid scaffold ε^s. The maximum contrast rCBV_{max}, which corresponds to a neo-vascular network, sets the vascular fraction to ω^{bs}_{max}. From early work in angiogenesis, Folkman *et al.* in [85] estimated the vascularized fraction of a subcutaneous tissue undergoing angiogenesis to 1.5%, which is 400 fold higher than healthy tissue. However, cortex tissue is already a highly vascularized tissue, with a volume fraction estimated between 3% and 5% (see Yiming *et al.* in [139]). We chose to set $\omega^{bs}_{\text{max}} = 0.075$, 50% higher than maximal healthy value, and $\omega^{bs}_{\text{min}} = 0.003$, 10 fold lower than minimal healthy value for poorly vascularized zones. We obtain for the vascular fraction of the solid scaffold:

$$\omega^{bs}(x,y,z) = \frac{\omega^{bs}_{\text{max}} - \omega^{bs}_{\text{min}}}{\text{rCBV}_{\text{max}} - \text{rCBV}_{\text{min}}} \left(\text{rCBV}(x,y,z) - \text{rCBV}_{\text{min}}\right) + \omega^{bs}_{\text{min}} \tag{5.45}$$

General mechanical parameters of cortex tissue were prescribed by a previous article by Urcun *et al.* in [248]. It consisted of the reproduction of two mechanical tests of healthy cortex human and animal: confined compression ($N = 6$), *i.e.* consolidation tests [89] and unconfined compression ($N = 6$), *i.e.* indentation tests with several load rates and diameters ($N = 1$). The local sensitivity of the parameters were measured, a part of the results were calibrated and another part validated on external data ($N = 3$). All the details are provided in [248]. Regarding this article, it allows reducing the wide range the mechanical parameters of cortex tissue assumed in the literature [262, 226, 127], and more specifically in the poromechanical literature [230, 120]. Although individual variation could be considered, these parameters are related to the general mechanical behavior of healthy tissue. They are presented in Table 5.1. These background parameters will be thereafter considered as fixed.

Partial resolution of the mathematical system Imaging data or mechanical tests do not give information on the initial state of the oxygen fraction $\omega^{\bar{nl}}$. Physiology literature gives information on the bounds of the tumor growth metabolism in Eq.5.34. The hypoxia threshold ω_{crit}, in a brain tumor environment, is estimated to an oxygen fraction between $4.5 \cdot 10^{-7}$ and 10^{-6} [128]. These values correspond, according to Henry's law, to an oxygen partial pressure between $10\,\text{mmHg}$ and $22.5\,\text{mmHg}$. The clinical measurements in [187] gives the following range $[30; 48]\,\text{mmHg}$ for physiological values in brain tissue. Therefore, we set the oxygen fraction of healthy brain tissue ω_{env} to $1.9 \cdot 10^{-6}$, which corresponds, according to Henry's law, to $42.5\,\text{mmHg}$. Nevertheless, between the two bounds defined by ω_{crit} and ω_{env}, the fraction of oxygen at each voxel of the domain is not known. To fix this, the mathematical system is partially solved. The oxygen fraction is set to 10^{-6} in $\Omega_{CE} \cup \Omega_N$ and to $1.9 \cdot 10^{-6}$ in the remaining part. With these initial conditions, the system is solved with a very small increment of time ($dt = 1\,\text{s}$), as this initial state is very unstable. Since the system becomes steady, *i.e.* the variation of the oxygen fraction in one second becomes negligible, the simulation is stopped and the solution of $\omega^{\bar{nl}}$ is conserved as initial condition for this unknown. The computation lasts for 90 seconds of simulated time.

The same situation appears for the displacement field $\mathbf{u^s}$, as the pre-existing deformation of the organ is not recorded.

Moreover, one can argue that an original displacement field for an organ has no meaning. As the fluid phases exert pressure on the stroma, the same process than for $\omega^{\bar{nl}}$ is adopted. Since the mechanical steady state is reach between fluid pressures and stroma displacement, the simulation is stopped and the resulting displacement field $\mathbf{u^s}$ is conserved as initial solution for this vectorial unknown. The computation lasts for 6 minutes of simulated time, the initial $\mathbf{u^s}$ reaches a maximum displacement between $50\,\mu$m and $60\,\mu$m.

Clinical literature Kitange *et al.* in [131], showed by *in vitro* experiments and animal models that MGMT activity greatly increase the GBM resistance to TMZ treatment, whereas the methylation of MGMT decrease its activity and allows for a better response. Their statistical analysis of *in vitro* results showed an increase between 50% and 60% of the surviving GBM cells fraction with a non-methylated (n-)MGMT marker. Based on these findings, we set the resistant fraction of n-MGMT marker to 0.5 as initial guess in Eq.5.19.

Symb.	Value	Unit	Meaning	Range in literature
ε	0.55 ± 0.05	$[1]$	Porosity	0.595 ± 0.165
ν	0.48 ± 0.01	$[1]$	Poisson's ratio	0.47 ± 0.02
E_{Cortex}	3.23 ± 2.8	kPa	Young's Modulus of Cortex tissue	4.5 ± 3.5
k_{Cortex}	$1.5 \pm 1.4 \cdot 10^{-12}$	m^2	Permeability of Cortex tissue	from 10^{-17} to 10^{-13}
S^l	0.07 ± 0.043	$[1]$	IF saturation	0.149 ± 0.084
μ_l	$5.5 \pm 2.5 \cdot 10^{-3}$	Pa·s	Dynamic viscosity of IF	$0.85 \pm 0.15 \cdot 10^{-3}$
A^l	1	$[1]$	Exponent of tortuosity for IF	No expe. data
μ_h	32.5 ± 2.5	Pa·s	Dynamic viscosity of HC	No expe. data
B^h	2 or 1	$[1]$	Exponent of tortuosity for HC	No expe. data
a	600 ± 200	Pa	Cell-ECM ground interaction	No expe. data

Table 5.1: **Model's parameters estimation by ex vivo mechanical testing [248].** For the sources of the literature values, see [248].

Type	Symb.	Unit	Method(s)	Parameter
Material parameters	$k()$	m^2	ADC, Segment.[274]	Permeability mapping
	D_0^{nl}	$\text{m}^2 s^{-1}$	ADC	O_2 diffusion coefficient
	$E()$	Pa	Segment.[126]	Young's Modulus mapping
Initial conditions	p^l	Pa	ADC	Interstitial fluid pressure
	p^{hl}	Pa	ADC, Segment.[126]	Healthy cells pressure
	p^{th}	Pa	ADC, Segment.[126]	Tumor cells pressure
	ω^{bs}	[1]	rCVB	Vascular fraction

Table 5.2: **Parameters deduced from MRI methods**

Type	Symb.	Value	Unit	Meaning	Source
Poromechanical	E_{IDH}	4000	Pa	Young's Modulus of Cross-linked ECM	
	p_{crit}	1530	Pa	Critical threshold of mechanical inhibition	
	Γ	6	$[1]$	Interfacial tension ratio between HC-IF and TC-HC	
Oxygen biology	$\overset{l\to t}{\gamma}$	$2.16 \cdot 10^{-2}$	kg/(m^3.s)	TC growth rate	
	$\overset{nl\to t}{\gamma}$	3.5	s^{-1}	TC oxygen consumption rate	
	$\overset{nl\to h}{\gamma}$	$2.5 \cdot 10^{-1}$	s^{-1}	HC oxygen consumption rate	
	$\overset{b\to nl}{\gamma}$	$1.44 \cdot 10^{-2}$	s^{-1}	Capillaries oxygen production rate	
	ω_{crit}	$8 \cdot 10^{-7}$	kg/m^3	Hypoxic threshold oxygen mass fraction	
ECM mechano-biology	p_{idh}	770	Pa	Phenotype switch mechanical threshold	
	$\zeta_A^{\rho t}$	$1 \cdot 10^{-1}$	$[1]$	TC apoptosis inhibited fraction	
	$\zeta_\mu^{\rho t}$	$9 \cdot 10^{-1}$	$[1]$	TC dynamic viscosity loss fraction	
	$\overset{t\to s}{\zeta}$	$4 \cdot 10^{-1}$	$[1]$	Stroma production coefficient	
	ζ^{ρ}	6	$[1]$	Phenotype switch coefficient	
RT-TMZ treatment	ω_{TMZ}^{bs}	0.1	$[1]$	Vascular threshold for TMZ effect	
	N_{mgmt}	0.6	$[1]$	Resistant fraction of GBMwt cells to RT-TMZ treatment	

Table 5.3: **Model's parameters to be calibrated, initial values, and sources**

In silico reproduction process

Finite element formulation We implemented the above model with Dolfin, the C++ libraries of the FEniCS framework [7]. We used an incremental formulation, *i.e.* $\bar{X}_{n+1} = \bar{X}_n + \delta\bar{X}$, for the mixed finite element (FE) formulation. We resolve the system by the means of a fixed-stress staggered scheme: the pressures are solved with a fixed stress tensor, the stress tensor is solved with the updated pressures, and the loop is subjected to the norm of the solution increment as convergence criterion (for instance, see [63]). All the codes used in this article can be provided upon request.

Boundary conditions All unknowns are subjected to a homogeneous Dirichlet conditions on the domain boundary. This is a consequence of the incremental formulation. For each unknown α, we prescribed $\delta X_\alpha = 0$ on $\partial\Omega$, the boundary of the domain. In other words, the initial settings of the unknowns remain unchanged at the boundary of the domain during the simulation. The influence of the boundary distance on the FE solution is studied Appendix 5.7.

Quantities evaluated In a multiphase system, grasp the relevant quantities is not always straightforward, for instance, the saturation of tumor cells S^t could be meaningless without the indication of the porosity ε. If we want to delineate a tumor area, the significance of a high S^t could be diminished by a small ε. Hence, we adopt the following measure for the

interpretation of the results: the volume fraction of tumor cells:

$$\mathsf{Vol}_{\mathsf{TC}} = \varepsilon S^t \tag{5.46}$$

$\mathsf{Vol}_{\mathsf{TC}}$ can be separate in three relevant quantities, the living tumor cells:

$$\mathsf{Vol}_{\mathsf{LC}} = \varepsilon S^t (1 - \omega^{Nt}) \tag{5.47}$$

The malignant tumor cells:

$$\mathsf{Vol}_{\mathsf{mal}} = \varepsilon S^t (1 - \omega^{Nt}) \omega^{\rho t} \tag{5.48}$$

The necrotic tumor cells:

$$\mathsf{Vol}_{\mathsf{nec}} = \varepsilon S^t \omega^{Nt} \tag{5.49}$$

Error measure To measure the quality of the numerical results, we followed the prescription of [22]: the root mean square error (RMSE) relative to a reference, which is specified accordingly. The RMSE of the numerical quantity ξ_{num} relative to an experimental reference ξ_{ex}, evaluated at n points is computed as:

$$RMSE(\xi_{\mathsf{num}}, \xi_{\mathsf{ex}}, n) = \sqrt{\frac{1}{n} \sum_{k=1}^{n} \left(\frac{\xi_{\mathsf{ex}}(k) - \xi_{\mathsf{num}}(k)}{\xi_{\mathsf{ex}}(k)} \right)^2} \tag{5.50}$$

Sensitivity analysis: cost functions and Sobol indices. We performed a local sensitivity analysis to estimate Sobol sensitivity indices on the patient calibration dataset, to assess the sensitivity of the computational outputs to the input parameters. First, we designed the cost function J_{over}, which quantifies the error between the numerical results and the patient calibration dataset, by measuring the spatial overlapping.

$$J_{\mathsf{over}} = \frac{\sum_j | (\mathbb{1}_{\mathsf{exp}}(j) - \mathbb{1}_{\mathsf{num}}(\mathsf{Vol}_{TC\,j})) | \Delta_j}{\sum_i \Delta_i} \quad j \in \Omega \tag{5.51}$$

with

$$\mathbb{1}_{\mathsf{num}}(\mathsf{Vol}_{\mathsf{TC}}) \begin{cases} 0 & \text{if} \quad \mathsf{Vol}_{\mathsf{TC}} \leq 0.001 \\ 1 & \text{else} \end{cases} \qquad \mathbb{1}_{\mathsf{exp}}(j) \begin{cases} 0 & \text{if} \quad j \notin \Omega_{CE} \cup \Omega_N \\ 1 & \text{else} \end{cases} \tag{5.52}$$

where Δ_i is the volume of the i^{th} tetrahedron, where $\mathbb{1}_{\mathsf{exp}}(j)$ is the characteristic function of the patient segmentation at the second time point - the calibration dataset -, and $\mathbb{1}_{\mathsf{num}}(\mathsf{Vol}_{\mathsf{TC}})$ the characteristic function of the computational GBM at the same time point.

The 13 parameters at their initial values give J^0_{over} (see Table 5.3). Then, the 13 parameters are perturbed one at a time

of $\pm 10\%$. The cost variation $V_{\text{over}}^{\alpha \pm 10\%}$ of a parameter α is defined by:

$$V_{\text{over}}^{\alpha \pm 10\%} = \frac{J_{\text{over}}^{\alpha \pm 10\%} - J_{\text{over}}^{0}}{J_{\text{over}}^{0}} \tag{5.53}$$

Then, the points of the variation are linearly interpolated. The influence of the parameter α is deduced from the slope θ_α of the linear fit. The first-order Sobol index S_α is calculated as follows:

$$S_\alpha = \frac{\theta_\alpha^2}{\sum_\alpha \theta_\alpha^2} \tag{5.54}$$

Calibration To minimize J_{over}, we chose the parameters set α_i that gather 90% of the variance, *i.e.* $\sum_i S_{\alpha_i} \geq 0.9$ for the calibration. This parameters set is then calibrated using a classical Newton-Raphson algorithm.

5.5 Results

Local sensitivity analysis

The results of the first order sensitivity analysis are shown Fig.5.4, and the values of the Sobol indices Table 5.4. Two parameters, $\overset{nl\to t}{\gamma}$ and $\overset{nl\to h}{\gamma}$, have a negligible influence on the solution. The parameter p_{idh}, the pressure threshold that mechanically induced the malignant phenotype switch of GBMwt cells is largely dominant in comparison to the other parameters. Finally, only 8 parameters gather 97.5% of the variance: $p_{\text{idh}}\,(0.505)$, $\omega_{\text{crit}}\,(0.223)$,$\Gamma\,(0.068)$, $p_{\text{crit}}\,(0.058)$, $E_{\text{idh}}\,(0.038)$, $\omega_A^{\rho t}\,(0.028)$, $\zeta^\rho\,(0.028)$ and $\overset{l\to t}{\gamma}\,(0.027)$. This subset of parameters is calibrated, and the others are fixed.

Type	Symb.	Value	Sobol indices
Poromechanical	E_{idh}	4000	0.038
	p_{crit}	1530	0.058
	Γ	6	0.068
Oxygen biology	$\overset{l\to t}{\gamma}$	$2.16 \cdot 10^{-2}$	0.027
	$\overset{nl\to t}{\gamma}$	4.3	$< 10^{-4}$
	$\overset{nl\to h}{\gamma}$	$2.5 \cdot 10^{-1}$	$< 10^{-4}$
	$\overset{b\to nl}{\gamma}$	$1.44 \cdot 10^{-2}$	0.006
	ω_{crit}	$8 \cdot 10^{-7}$	0.223
ECM mechano-biology	p_{idh}	770	0.505
	$\zeta_A^{\rho t}$	$2 \cdot 10^{-1}$	0.028
	$\zeta_\mu^{\rho t}$	$9 \cdot 10^{-1}$	0.002
	$\overset{t\to s}{\zeta}$	$4 \cdot 10^{-1}$	0.001
	ζ^ρ	6	0.028

Table 5.4: **Sobol indices of the parameters at their initial values.** $J_{\text{over}} = 0.581$

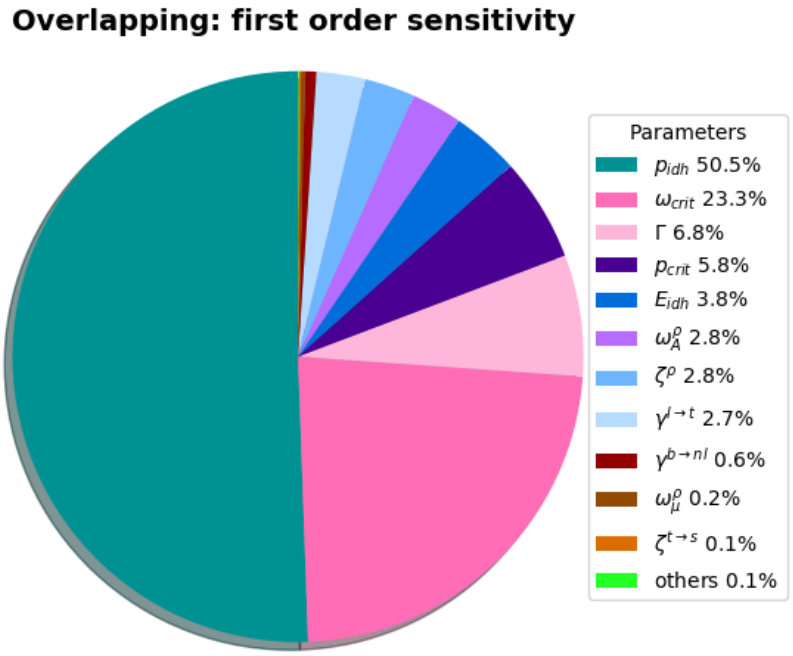

Figure 5.4: **Sobol indices of the parameters at their initial values.** Details of the parameters Table 5.4. 8 parameters gather 97.5% of the variance: $p_{\text{idh}}\,(0.505)$, $\omega_{\text{crit}}\,(0.223)$,$\Gamma\,(0.068)$, $p_{\text{crit}}\,(0.058)$, $E_{\text{idh}}\,(0.038)$, $\omega_A^{\rho t}\,(0.028)$, $\zeta^\rho\,(0.028)$ and $\overset{l\to t}{\gamma}\,(0.027)$. They constitute the parameters subset to calibrate

Calibration

The 8 parameters were identified with a Newton-Raphson algorithm, only 5 iterations were performed for a duration of 20 days of computational time, with the following overlapping errors: $J^0_{\text{over}} = 0.581$, $J^1_{\text{over}} = 0.333$, $J^2_{\text{over}} = 0.270$, $J^3_{\text{over}} = 0.188$, $J^4_{\text{over}} = 0.185$ and $J^5_{\text{over}} = 0.183$. Their values are given in Table 5.5. The 3D results at J^5_{over} are shown Fig.5.5. At the fifth iteration, the volume of the simulated tumor is of $119.1\,\text{cm}^3$, the volume of the patient tumor being of $122.5\,\text{cm}^3$. Then, we obtained a tumor with 2.7% of error in volume and which overlaps 81.7% of the patient tumor.

Symb.	Value
p_{idh}	910
ω_{crit}	$7 \cdot 10^{-7}$
Γ	4.5
p_{crit}	1450
E_{idh}	3730
$\zeta_A^{\rho t}$	$1.5 \cdot 10^{-1}$
ζ_A^{ρ}	2.5
$\overset{l\to t}{\gamma}$	$2.6 \cdot 10^{-2}$

Table 5.5: **Parameters calibration,** $J_{\text{over}} = 0.183$**.**

Qualitative results

Mechanical inhibition of tumor growth This phenomenon is well documented *in vitro* [107, 48, 4] *in vivo* [28], and already used in imaging-informed model for breast [122] or prostate [151] cancers and were comprehensively reviewed by Jain *et al.* in [119] and more recently by Nia *et al.* [180]. Even if each cell line has its own conditions (inhibiting pressure threshold, share stress dependency, phenotype switch window, coupling phenomena with hypoxia), the mechanical inhibition of tumor growth is now accepted as a shared phenomenon in cancer. Specifically in GBM mechanical growth inhibition, to our knowledge, we report only one quantitative study of Kalli *et al.* [125], which estimates for the GBM A172 cell line an inhibiting threshold $\approx 3.5\,$kPa. After our calibration of the inhibiting pressure threshold p_{crit}, we see in Fig.5.5A3 and C3 that several large zones with no progression in the patient data which undergo, in the corresponding simulated zones, a pressure at least equal to p_{crit}. They are termed inhibited zones. However, few zones of progression in the patient data (see Fig.5.5B3) correspond to a numerical progression despite the inhibiting pressure. These zones are termed invasive zones. The details on each of these zones is provided in Fig.5.6, where three kinds of zones are distinguished: inhibited, proliferating and invasive zones. If proliferating zones correspond to a TC growth which is not impeded by mechanical pressure, invasive zones correspond to TC migration, as the proliferation is impeded by mechanical pressure. The mechanism of this migration is explained in detail Fig.5.7 and 5.8.

Malignant phenotype in tumor growth and treatment response Several studies [245, 17] suggest that this phenotype switch is resulting of an increase of internal stress, denoted tensional homeostasis, coupled with an hypoxic environment. We proposed to model this phenomenon at the macroscale, Fig.5.7 shows the qualitative results of this modeling. At $T_0 + 21\,$days (Fig.5.7A1, B1, C1) before RT-TMZ treatment, the malignant GBMwt cells are almost nonexistent. The resistance of the malignant fraction $\omega^{\rho t}$ is given by the fixed parameter N_{mgmt} (see section 5.4, subsection *Initial parameters setting*, and Eq.5.19). Therefore, the volume fraction of malignant cells Vol_{mal} initially very law $\approx 10^{-5}$ is multiply by 50 fold during the 3 first RT-TMZ cycles, and by 10 fold during the 3 latter cycles. Fig.5.8 shows the details of the consequences of this phenotype switch. When GBMwt cells are under a mechanical pressure at least equal to p_{idh} and in an hypoxic area sustained long enough (the phenotype switch is updated every 4.5 days), the development of a malignant zone occurs. Once they have their phenotype switch, GBWwt malignant cells change their properties. Their viscosity decrease (see Eq.5.27, *i.e.* they become more mobile and the emission of MMP degrades the ECM and increase the intrinsic permeability of the solid scaffold (see Eq.5.28). Both phenomena allow the GBWwt malignant cells for a rapid invasion of the surrounding tissue (see Fig.5.8B, C).

5.6 Discussion

In this study we proposed to model a patient-specific non-operable glioblastoma, which subtype is termed as isocitrate dehydrogenase wild-type. The disease was first modeled within a porous medium, pre-calibrated for brain tissue in [248] by

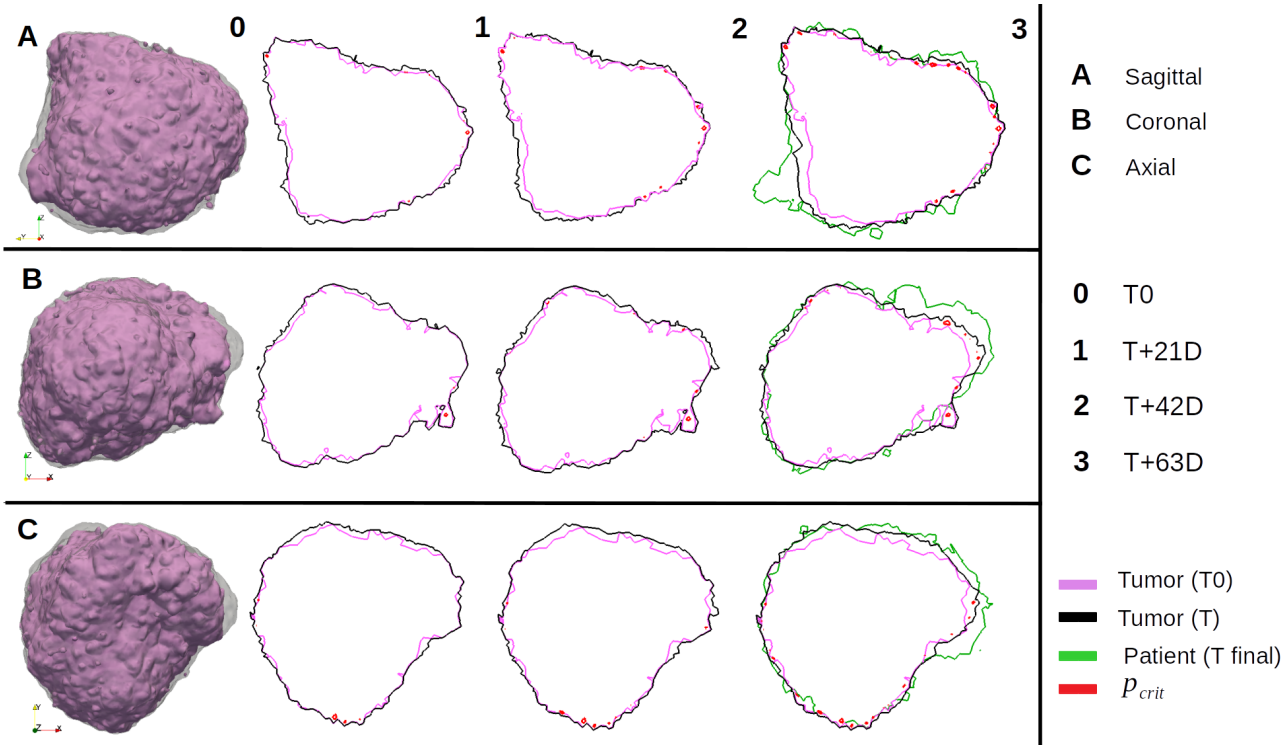

Figure 5.5: **Influence of mechanical inhibition of tumor growth.** **A** Sagittal view (along x axis). **B** Coronal view (along y axis). **C** Axial view (along z axis).**0** **0** 3D isosurface $\text{Vol}_{\text{TC}} = 0.001$ at T_0 (purple) and at $T_0 + 63$ days (grey transparent); isoline of inhibiting pressure p_{crit} (red). **1**, **2**, **3** slices centered at $x = -0.0180$, $y = -0.0104$, $z = 0.0416$; isoline $\text{Vol}_{\text{TC}} = 0.001$ at T_0 (purple). **1** isoline $\text{Vol}_{\text{TC}} = 0.001$ at $T_0 + 21$ days (black). **2** isoline $\text{Vol}_{\text{TC}} = 0.001$ at $T_0 + 42$ days (black) after 3 cycles of RT-TMZ treatment. **3** isoline $\text{Vol}_{\text{TC}} = 0.001$ at $T_0 + 63$ days (black); isoline of patient data $\text{Vol}_{\text{TC}} = 0.001$ at $T_0 + 63$ days (green) after 6 cycles of RT-TMZ treatment. The numerical results show almost no progression, with the exception of a few zones. These zones correspond to the major progression zones in the patient data. Detail of the mechanism underlying these numerical progression are given Fig.5.6.

the same authors of this study. We hypothesized that two phenomena drive the malignant evolution of the disease: hypoxia and cell-ECM signaling. To assess patient-specific measurement, we adopted the imaging-informed framework. The same clinical imaging dataset (MRI methods and segmentation), at two time points, was used to initialize and calibrate the parameters. The first point was the pre-operative checkpoint and the second was performed after 6 cycles of concomitant radio-chemotherapy. A last subset of parameters, which do not belong to brain tissue material properties and can not be assessed by imaging, was fixed by clinical and experimental literature. After calibration, we obtained a simulated tumor with a 3.5% error in volume, comparatively to the patient tumor, and which overlaps 81.8% of the patient tumor.

Qualitatively, we showed that the mechanical inhibition of the tumor growth describes well the stable zones of the patient tumor, and can partially reproduce the progression zones of the patient tumor. We note that the calibrated parameter $p_{\text{crit}} = 1.4$ kPa is lower than the only other example, to our knowledge, in the literature, estimated with the GBM cell line A172 by Kalli *et al.* in [125], $p_{\text{crit}} = 3.5$ kPa. We also showed that our modeling of the GBMwt phenotype switch behave accordingly to the experimental findings. It has been shown that an ECM stiffer than usual brain ECM is correlated with GBM cells proliferation *and* migration [245]. The same phenomena are reported under compressive stress and hypoxic

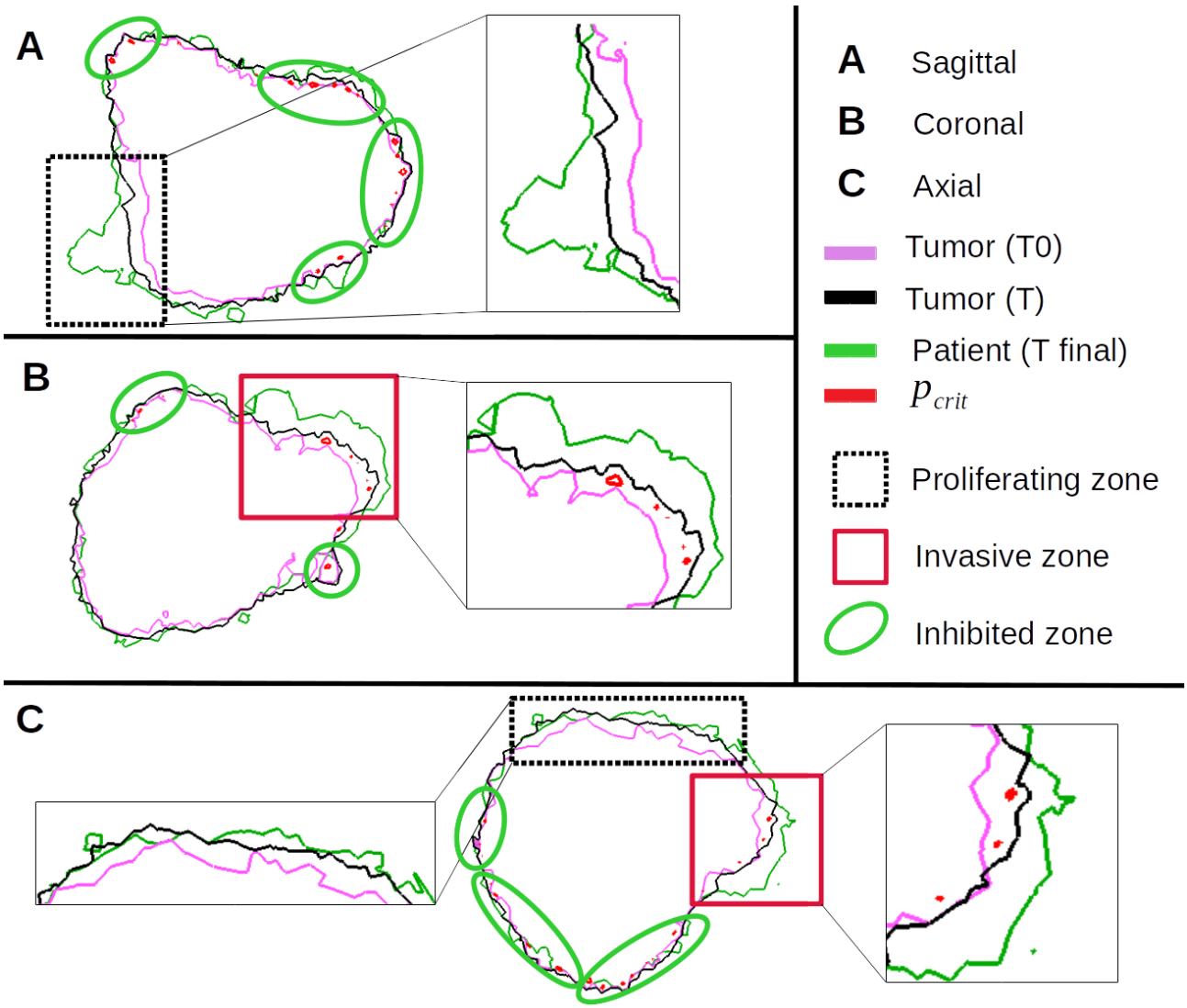

Figure 5.6: **Influence of mechanical inhibition of tumor growth, focus.** **A** Sagittal view (along x axis). **B** Coronal view (along y axis). **C** Axial view (along z axis). Isoline $\text{Vol}_{\text{TC}} = 0.001$ at T_0 (purple). At $T_0 + 63$ days after 6 cycles of RT-TMZ treatment: isoline $\text{Vol}_{\text{TC}} = 0.001$ (black); isoline of patient data $\text{Vol}_{\text{TC}} = 0.001$ (green); isoline of inhibiting pressure p_{crit} (red); proliferating zone (black dotted square); invasive zone (red square); inhibited zone (green ellipse). Almost all inhibited zones correspond to patient data with no growth. Proliferating zones correspond to a TC growth which is not impeded by mechanical pressure, 2 zones of progression in the patient data correspond to this definition in the numerical results (one in sagittal view, one in axial view). Invasive zones correspond to TC migration, as the proliferation is impeded by mechanical pressure, 2 zones of progression in the patient data correspond to this definition in the numerical results (one in coronal view, one in axial view). This migration is explained in detail Fig.5.7 and 5.8.

environment [17]. ECM stiffness and compressive stress are linked, as in a proliferative environment, a stiffer matrix will provoke a higher internal stress. An inhibiting pressure threshold and an internal stress, resulting of a stiffened ECM, which provokes a malignant phenotype switch are not contradictory. They suggest it exists a window of mechanical signaling where GBM can dramatically evolve. Before the phenotype switch, GBMwt cells produce a stiffer, cross-linked, ECM. This stiffening, accompanied by the GBMwt proliferation, increases the internal pressure. If the pressure undergone by the GBMwt reaches the threshold p_{idh} and the level of oxygen is pathologically low (threshold ω_{crit}), the affected GBMwt cells

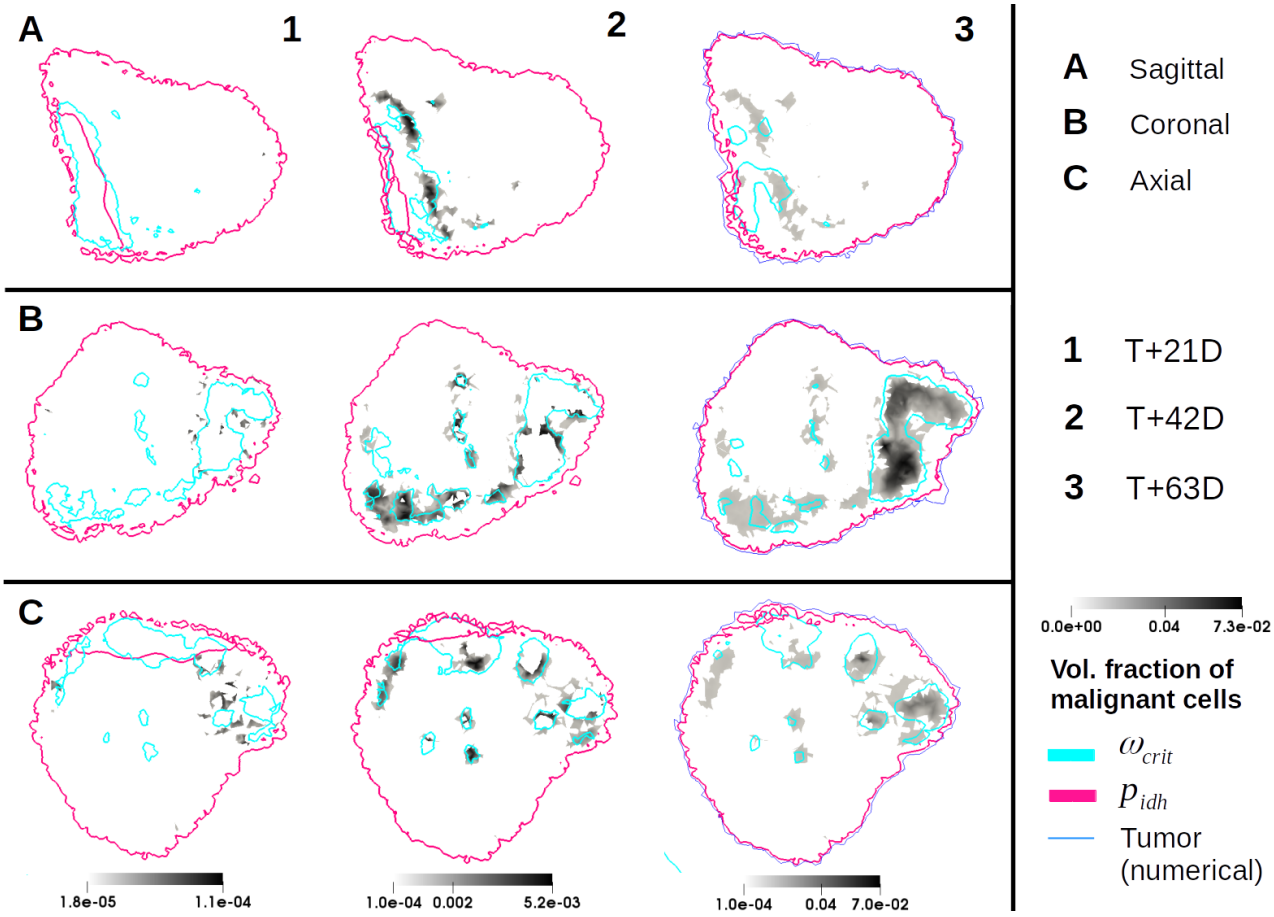

Figure 5.7: **Influence of malignant phenotype in tumor growth and treatment response. A** Sagittal view (along x axis). **B** Coronal view (along y axis). **C** Axial view (along z axis). **1**, **2**, **3** slices centered at $x = -0.0180$, $y = -0.0104$, $z = 0.0416$; volume fraction of malignant GBMwt cells (grey level); isoline of phenotype switch pressure p_{idh} (fuchsia); isoline of hypoxia threshold ω_{crit} (cyan). **1** $T_0 + 21$ days; **2** $T_0 + 42$ days after 3 cycles of RT-TMZ treatment; **3** isoline $Vol_{\text{TC}} = 0.001$ (blue); $T_0 + 63$ days after 6 cycles of RT-TMZ treatment. The malignant phenotype switch is dependent of two concomitant phenomena: a high mechanical pressure inside a hypoxic environment. During the first 3 cycles of RT-TMZ treatment, Vol_{mal} is multiply by 50 fold, during the last 3 cycles Vol_{mal} is multiply by 10 fold. The details of the progression zones are shown Fig.5.8.

change their phenotype. They become much more mobile, which is translated at the macroscale by a reduction of the dynamic viscosity of three orders and they acquire an anaerobic metabolism pathway, which allow for escaping an hypoxic environment by metabolising lipids [194].

However, this study apply to only one patient, and a third time point of patient data after the temozolomide maintenance, which was necessary to validate the parameters and calibrate the treatment response, was not available. Therefore, we only aim to a proposition of modeling of this disease, *via* porous mechanics and mechano-biology. Two leads are available to improve this proposition. Firstly, the parameters specific to the patient's cell line could be pre-calibrated by exploiting the *in vitro* results of [125]. A study was already done on encapsulation in alginate of colon carcinoma spheroids, and the parameters were validated with a multiphase poromechanical model in [247] by the same authors of this study.

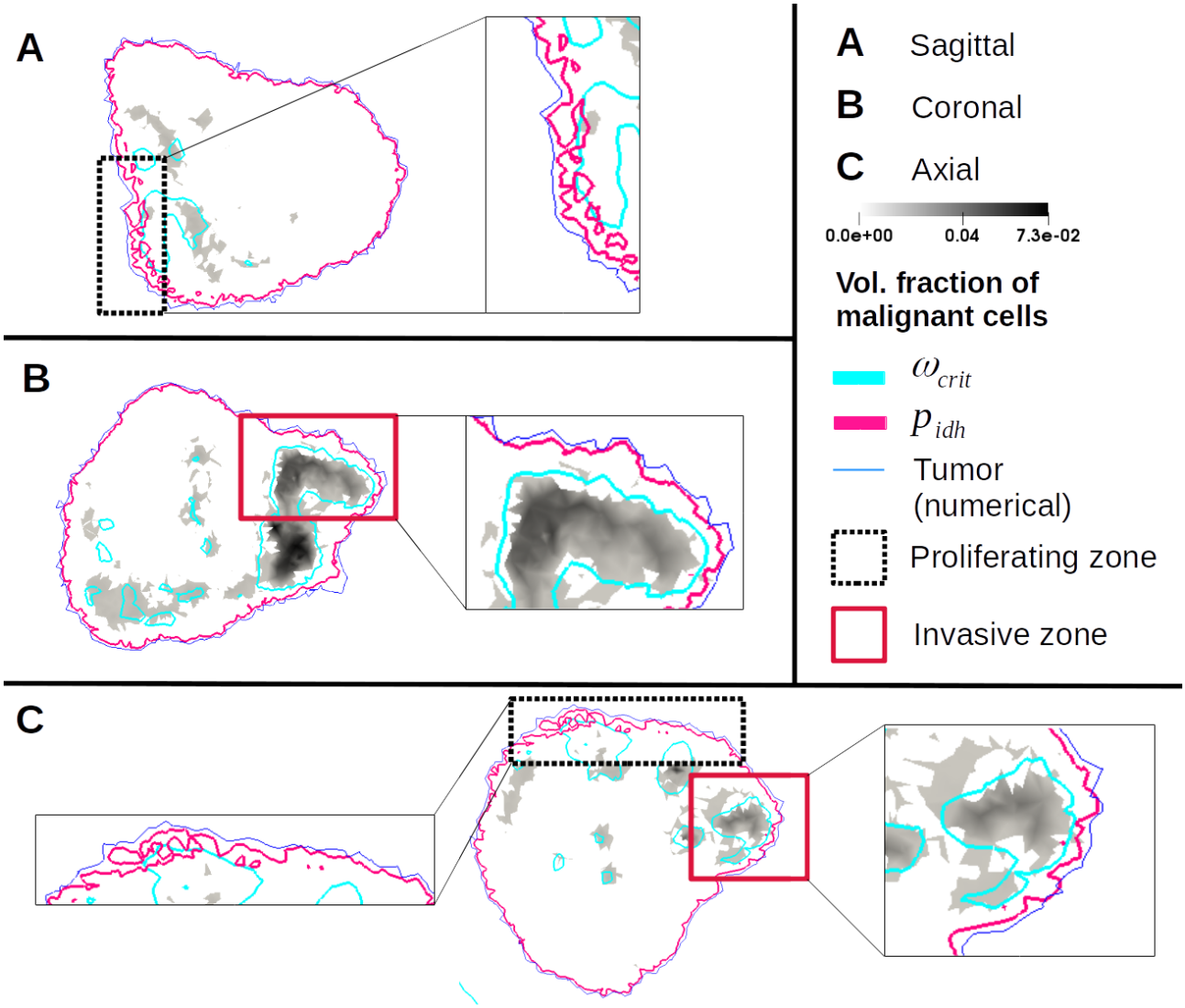

Figure 5.8: **Influence of malignant phenotype in tumor growth and treatment response, focus. A** Sagittal view (along x axis). **B** Coronal view (along y axis). **C** Axial view (along z axis). At $T_0 + 63$ days after 6 cycles of RT-TMZ treatment. Volume fraction of malignant GBMwt cells (grey level); isoline of phenotype switch pressure p_{idh} (fuchsia); isoline of hypoxia threshold ω_{crit} (cyan); isoline $Vol_{\text{TC}} = 0.001$ (blue); proliferating zone (black dotted square); invasive zone (red square). Proliferating zones correspond to a TC growth which is not impeded by mechanical pressure, 2 zones of progression in the patient data correspond to this definition in the numerical results (one in sagittal view, one in axial view). From the point of view of the malignant evolution of the disease, numerical results show that the two mechanisms required for the phenotype switch (hypoxia and mechanical pressure) have almost no intersection in these zones. However, the zone of the sagittal view shows a beginning of an intersection. If this intersection is maintained long enough (the phenotype switch is updated every 4.5 days), it could lead to an invasive progression. Invasive zones correspond to TC migration, as the proliferation is impeded by mechanical pressure, 2 zones of progression in the patient data correspond to this definition in the numerical results (one in coronal view, one in axial view). These 2 progression zones in the patient data show a correlation between malignancy and progression in numerical results. Indeed, both mechanisms required in the phenotype switch are effective in these zones.

Secondly, the addition of diffusion tensor imaging method, which allows for retrieving the white matter fiber direction, would grant access to an anisotropic permeability. This imaging method is currently a promising lead for modeling the heterogeneous progression of glioblastoma [10, 191, 166].

This study is only a first step of the inclusion of poromechanics in imaging-informed glioblastoma models, we hope the community will find it inspiring.

Acknowledgments

The results presented in this paper were carried out using the HPC facilities of the University of Luxembourg [251] (see https://hpc.uni.lu).

5.7 Supporting information: solution's sensitivity on the ROI size

Dirichlet conditions are prescribed at the ROI boundary:

- No displacement
- Fixed pressure
- Fixed oxygen level
- No necrosis

The sensitivity of these boundary conditions is evaluated on tumor evolution. We compare the capillary pressure of the tumor phase p^{th} at each voxel of the domains with four margin sizes: 1.52 ± 0.2cm, 1.77 ± 0.3cm, 2.27 ± 0.3cm, 2.45 ± 0.4cm, denoted margin 1, 2, 3 and 4 respectively. These margins defined 4 computational domains $\Omega_i \in [1,4]$ respectively. These domains contain 392 k, 425 k, 465 k and 511 k tetrahedrons respectively. The larger domain Ω_4 is used as the reference. The RMSE, without normalization, is computed as follows:

$$RMSE(p_i^{th}, p_4^{th}, n) = \sqrt{\frac{1}{n}\sum_{k=1}^{n}\left(p_4^{th}(k) - p_i^{th}(k)\right)^2} \qquad n = \mathsf{Card}(\Omega_i) \quad i \in [1,3] \tag{5.55}$$

The results of the model are evaluated by the tumor cells volume fraction $\mathsf{Vol}_{\mathsf{TC}}$ and its threshold is $\mathsf{Vol}_{\mathsf{TC}} \geq 10^{-3}$. This value corresponds, *via* l'Eq.5.26 for S^t and the range of value for the porosity, to 1.4 ± 0.1 Pa. Therefore, we consider that the RMSE in $textPa$ presented Eq.5.55 above 1.4 Pa is not negligible. At day 18, the RMSE between margins 1 and 4 reaches 0.4 Pa, the RMSE between margins 2 and 4 reaches 0.17 Pa and the RMSE between margins 3 and 4 reaches 0.1 Pa. Therefore, we consider that the boundary conditions of the domain Ω_3 have a negligible influence on the numerical solution.

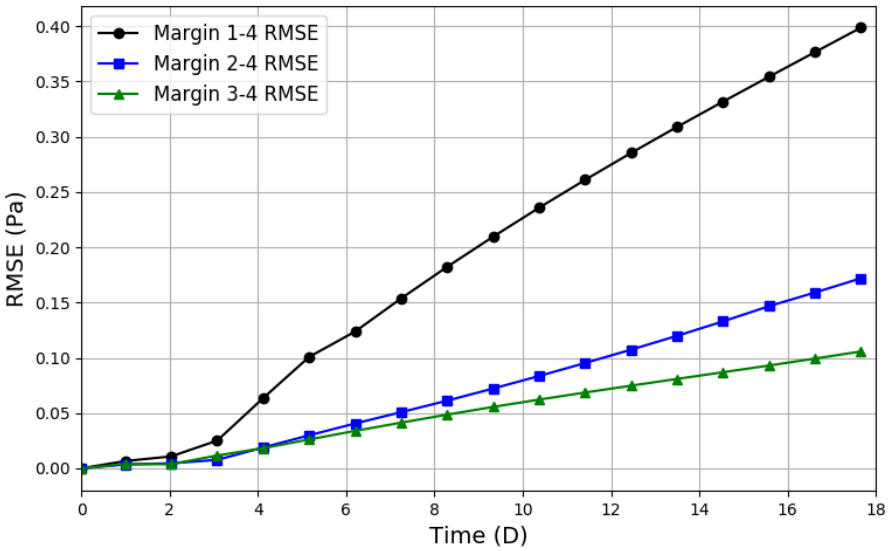

Figure 5.9: **Influence of the Dirichlet boundary distance on the tumor evolution.** RMSE between margins 1 and 4 (black line, circle marker); RMSE between margins 3 and 4 (green line, triangle marker). To be acceptable, the RMSE should remain below $1.4\,\text{Pa}$. At day 18, the RMSE between margins 1 and 4 reaches $0.4\,\text{Pa}$, the RMSE between margins 2 and 4 reaches $0.17\,\text{Pa}$, and the RMSE between margins 3 and 4 reaches $0.1\,\text{Pa}$

Chapter 6

Perspective and future works

Along this thesis, we transformed a physical model with the aim of clinical applications. We built a robust process composed of variance-based sensitivity analysis of the parameters, their gradient-based calibration and their validation on external data, if any. First, the model were validated on *in vitro* experimental data: the digital twinning of cellular capsule technology (CCT) [247]. Then, the model was validated on *ex vivo* experimental data: the reproduction of mechanical tests on cortex tissue [248], as the ability of the model to reproduce healthy tissue behavior was a prerequisite to model a pathology. On this robust basis, the next step to the clinical application was to build a pipeline from clinical data to finite element simulation. This Python pipeline is free and open-source. Then, we had to reach the organ scale for clinical simulation. To do so, the previous finite element codes were converted into C++ language to allow parallel computing.

Additionally to these computational and qualitative concerns, the core of the genuine model has been widely adapted to our purpose. First, it gained the ability to reproduce both mechanical-driven and hypoxic-driven growth inhibition. The solid scaffold of the porous model being deformable, it might describe the cell-ECM interplay. Hence, during the research process, emphasize was put on the stroma mechano-biology. Several consequences of the cell-ECM interplay are now included is the model: stroma production, ECM stiffening and mechanical-induced phenotype switch. As we aimed a clinical application in neurosurgery, the model was adapted to the complexity of brain tissue. General mechanical parameters are now calibrated for this tissue, which is heterogeneous in several ways: porosity, stiffness and permeability. The disease we aimed to model with a clinical relevancy was the glioblastoma multiforme isocitrate dehydrogenase wild-type (GBMwt). The model was adapted to its malignancy: evolution of the production of the glycosaminoglycans - a large part of the brain ECM -, evolution of the GBMwt cells mobility and of their metabolism under hypoxic environment, and modeling of their resistance against concomitant radio-chemo-therapy. Nevertheless, two things could greatly improve this modeling without the necessity of in-depth modifications. Firstly, the CCT experiment could be done on GBMwt cell line (commercial at least, or patient-specific). A commercial GBMwt cell line A172 were already tested in agarose spheroids in [125]. This kind of model pre-calibration for patient-specific cases has already been proposed by Hormuth *et al.* in [111]. The results of

chapter 3 on colon carcinoma cell line showed an inhibition pressure p_{crit} 3 fold higher than the one calibrated on GBMwt cells. As colon cells experience much higher mechanical solicitations than glial cells, these results seem coherent. However, reproduce this experiment of GBMwt cell line could confirm this hypothesis. Secondly, the addition of the diffusion tensor imaging (DTI) MRI method would allow for modeling the anisotropic permeability of the brain tissue, particularly for white matter. This method is already used in the glioblastoma modeling community [10, 191, 166], and within a multiphase reactive porous medium, it could raise new insights.

Beyond these considerations, the remaining work is vast, as only a few phenomena of GBMwt disease were modeled. The focus was on the multiscale mechanical interplay, but a large part of the phenomena set is ignored. One of the key features of GBMwt staging is a proliferative micro-vasculature, which is also a common characteristic of many malignant cancers. Modeling neo-angiogenesis would require a meticulous interest in the inflammatory process, which could be another consequence of hypoxia in cancer. This modeling would require the description of inflammatory cytokines as tumor necrosis factor α within this porous system, and also the description of the vascular endothelial growth factor emitted by the recruited macrophages in the GBMwt microenvironment [194].

From the computational point of view, the challenge of personalized medicine with this framework is still ongoing. If *in vitro* and *ex vivo* validations can help for the calibration of the cell line parameters and of the general mechanical properties, several governing parameters remain to be identified. A simulation of the disease for 63 days is necessary to obtain the outputs of the model, and the corresponding computational cost is still high. On a hundred recent cores, these 63 days are simulated in 4 days. Hence, the calibration of a few parameters take several weeks, which is not compatible with the clinical tempo. During the last year of the thesis, this computational time was divided by ten: by local mesh refinement, by decoupling the pressures and the stress tensor, by linearized constitutive relationships, by reducing the number of modeled phenomena. However, it was not sufficient. The lead of a discontinuous Galerkin formulation was explored, with not satisfying results for the analytical Terzaghi's problem, but remain open in case of the fixed stress staggered scheme applied to the patient-specific system. Currently, colleagues test the dynamic modal decomposition method on the *in vitro* model presented chapter 3. This could be a way to greatly reduce the computational cost, if applied to the patient-specific system.

If the modeling would contained the necessary inflammatory process and the computational time reduced enough to fit the clinical needs, the road would still be long. The outputs should be calibrated on several non-operable patients and, when it is possible, validated twelve months after diagnosis, at the end of the temozolomide maintenance. Reach the next stage would require the collaboration of several clinical centers. The situation then would be: the same mechanical-based framework informed with the same MRI methods (ADC, rCVB and DTI) but performed by different operators on different engines; the same type of segmentation inputs, but classified by different neural networks trained with their own dataset. If such a model, with these various inputs, can give robust patient-specific outputs, then we could claim that we reach

personalized medicine, through mechanical-based modeling.

List of publications and congress

Urcun S, Rohan PY, Skalli W, Nassoy P, Bordas SPA, et al. (2021) Digital twinning of Cellular Capsule Technology: Emerging outcomes from the perspective of porous media mechanics. PLOS ONE 16(7): e0254512. URL https://doi.org/10.1371/journal.pone.0254512

S. Urcun, P.-Y. Rohan, G. Sciumè, and S. P. Bordas. Cortex tissue relaxation and slow to medium load rates dependency can be captured by a two-phase flow poroelastic model. Journal of the Mechanical Behavior of Biomedical Materials, 126:104952, 2022. ISSN 1751-6161. URL https://www.sciencedirect.com/science/article/pii/S175161612100583X.

14th World Congress on Computational Mechanics (WCCM)
ECCOMAS Congress 2020
19–24 July 2020, Paris, France

BRAIN TISSUE POROMECHANICAL MODELING: CLINICAL DATA ASSIMILATION AND GROWTH SIMULATION OF NON-OPERABLE GLIOMAS

Stéphane Urcun[1,2*], Giuseppe Sciumè[3], Pierre-Yves Rohan[4], Davide Baroli[5], Ruairidh Howells[6], Vincent Lubrano[7], Wafa Skalli[8] and Stéphane P.A. Bordas[9]

[1] Institut de Biomécanique Humaine Georges Charpak, 151 Boulevard de l'Hôpital 75013 Paris, stephane.urcun@ensam.eu and http://biomecanique.ensam.eu/

[2] Université du Luxembourg, 2 avenue de l'Université L-4365 Esch-sur-Alzette, stephane.urcun001@student.uni.lu and https://wwwen.uni.lu/

[3] Université de Bordeaux, 351 Cours de la Libération 33400 Talence, giuseppe.sciume@u-bordeaux.fr and https://www.u-bordeaux.fr/

[4] Institut de Biomécanique Humaine Georges Charpak, 151 Boulevard de l'Hôpital 75013 Paris, pierre-yves.rohan@ensam.eu and http://biomecanique.ensam.eu/

[5] Aachen Institute for Advanced Study in Computational Engineering Science, Schinkelstraße 2 52062 Aachen, baroli@aices.rwth-aachen.de, https://www.aices.rwth-aachen.de

[6] Toulouse NeuroImaging Centre, INSERM UMR 1214 CHU Purpan, 31024 Toulouse, ruairidh.howells@inserm.fr, https://tonic.inserm.fr/en/

[7] Hôpital Pierre-Paul Riquet, Place du Docteur Baylac TSA 40031 31059 Toulouse cedex 9, lubrano.v@chu-toulouse.fr, https://www.chu-toulouse.fr/-neurochirurgie-159-

[8] Institut de Biomécanique Humaine Georges Charpak, 151 Boulevard de l'Hôpital 75013 Paris, wafa.skalli@ensam.eu and http://biomecanique.ensam.eu/

[9] Université du Luxembourg, 2 avenue de l'Université L-4365 Esch-sur-Alzette, stephane.bordas@uni.lu and https://wwwen.uni.lu/

Key Words: Multiphase Poromechanics, Neuro-oncology, FEniCS computing, Patient specific simulation

More than one third glioblastoma WHO IV are still non-operable and the operable ones are almost hundred percent recurrent. The interplay between extra-cellular matrix and interstitial fluid flux could reveal of fundamental understanding of the invasion patterns. Poromechanical modelling, coupled with mechanobiology, is particularly suited to this framework for reproducing structural shaped infiltration. The physical quantities, the initial and boundary conditions of the model are given by patient specific multi-modal MRI sets and brain atlases. They are fully translated into the finite element framework of FEniCS by a pipeline from Nifti format to tetrahedral meshes, thus the model inputs and outputs can be readily measured and compared in clinic. To monitor the whole invasion process and control the model dynamics, data sets of non-operable patients are used. Clinical measurements, multicellular spheroids culture, ex-vivo mechanical tests and in-vivo perfusion are used to tune parameters of the model. The simulations of the mechanobiology of the tissue are validated on patient-specific scenario.

REFERENCES

[1] Sciumè G., Santagiuliana R., Ferrari M., Decuzzi P., Schrefler BA. *A tumor growth model with deformable ECM*. Phys Biol. Nov 26;11(6):065004. doi: 10.1088/1478-3975/11/6/065004. (2014)

[2] Barnes JM., Przybyla L., Weaver VM. *Tissue mechanics regulate brain development, homeostasis and disease.* Journal of Cell Science 130, 71-82 doi:10.1242/jcs.191742 (2017)

[3] Budday S., Nay R., de Rooij R., Steinmann P., Wyrobek T., Ovaert TC., Kuhl E. *Mechanical properties of gray and white matter brain tissue by indentation.* J Mech Behav Biomed Mater. Jun;46:318-30. doi: 10.1016/j.jmbbm.2015.02.024 (2015)

[4] M. S. Alnaes, J. Blechta, J. Hake, A. Johansson, B. Kehlet, A. Logg, C. Richardson, J. Ring, M. E. Rognes and G. N. Wells, *The FEniCS Project Version 1.5*, Archive of Numerical Software, vol. 3, doi: 10.11588/ans.2015.100.20553 (2015)

Bibliography

[1] A. Agosti, C. Giverso, E. Faggiano, A. Stamm, and P. Ciarletta. A personalized mathematical tool for neuro-oncology: A clinical case study. *Int. J. Non Linear Mech.*, 107:170–181, 2018.

[2] A. Agosti, P. Ciarletta, H. Garcke, and M. Hinze. Learning patient-specific parameters for a diffuse interface glioblastoma model from neuroimaging data. *Mathematical Methods in the Applied Sciences*, 43(15):8945–8979, 2020. doi: https://doi.org/10.1002/mma.6588. URL https://onlinelibrary.wiley.com/doi/abs/10.1002/mma.6588.

[3] H. Akaike. A new look at the statistical model identification. *IEEE Trans. Autom. Control*, 19(6):716–723, 1974.

[4] K. Alessandri, B. R. Sarangi, V. V. Gurchenkov, B. Sinha, T. R. Kießling, and L. t. Fetler. Cellular capsules as a tool for multicellular spheroid production and for investigating the mechanics of tumor progression in vitro. *Proceedings of the National Academy of Sciences*, 110(37):14843–14848, 2013. ISSN 0027-8424. URL https://www.pnas.org/content/110/37/14843.

[5] A. L. Alexander, J. E. Lee, M. Lazar, and A. S. Field. Diffusion tensor imaging of the brain. *Neurotherapeutics*, 4: 316–329, 2007. doi: 10.1016/j.nurt.2007.05.011. URL https://doi.org/10.1016/j.nurt.2007.05.011.

[6] A. Almuhaideb, N. Papathanasiou, and J. Bomanji. ¡sup¿18¡/sup¿f-fdg pet/ct imaging in oncology. *Annals of Saudi Medicine*, 31(1):3–13, 2011. doi: 10.4103/0256-4947.75771. URL https://www.annsaudimed.net/doi/abs/10.4103/0256-4947.75771.

[7] M. Alnæs, J. Blechta, J. Hake, A. Johansson, B. Kehlet, A. Logg, C. Richardson, J. Ring, M. Rognes, and G. Wells. The fenics project version 1.5. *Archive of Numerical Software*, 3(100), 2015. ISSN 2197-8263. URL http://journals.ub.uni-heidelberg.de/index.php/ans/article/view/20553.

[8] G. Alzial, O. Renoult, F. Paris, C. Gratas, A. Clavreul, and C. Pecqueur. Wild-type isocitrate dehydrogenase under the spotlight in glioblastoma. *Oncogene*, 2021. doi: https://doi.org/10.1038/s41388-021-02056-1.

[9] G. L. Andriole, D. G. Bostwick, O. W. Brawley, L. G. Gomella, M. Marberger, F. Montorsi, C. A. Pettaway, T. L.

Tammela, C. Teloken, D. J. Tindall, M. C. Somerville, T. H. Wilson, I. L. Fowler, and R. S. Rittmaster. Effect of dutasteride on the risk of prostate cancer. *N. Engl. J. Med.*, 362(13):1192–1202, 2010.

[10] S. Angeli, K. E. Emblem, P. Due-Tonnessen, and T. Stylianopoulos. Towards patient-specific modeling of brain tumor growth and formation of secondary nodes guided by DTI-MRI. *NeuroImage: Clinical*, 20:664–673, 2018.

[11] D. N. Arnold, F. Brezzi, B. Cockburn, and L. D. Marini. Unified analysis of discontinuous galerkin methods for elliptic problems. *SIAM Journal on Numerical Analysis*, 39(5):1749–1779, 2002. doi: 10.1137/S0036142901384162. URL https://doi.org/10.1137/S0036142901384162.

[12] N. C. Atuegwu, L. R. Arlinghaus, X. Li, E. B. Welch, A. B. Chakravarthy, J. C. Gore, and T. E. Yankeelov. Integration of diffusion-weighted MRI data and a simple mathematical model to predict breast tumor cellularity during neoadjuvant chemotherapy. *Magn. Reson. Med.*, 66(6):1689–1696, 2011.

[13] K. N. Aycock and R. V. Davalos. Irreversible electroporation: Background, theory, and review of recent developments in clinical oncology. *Bioelectricity*, 1(4):214–234, 2019. doi: 10.1089/bioe.2019.0029. URL https://doi.org/10.1089/bioe.2019.0029.

[14] F. A. Azevedo, L. R. Carvalho, L. T. Grinberg, J. M. Farfel, R. E. Ferretti, R. E. Leite, W. J. Filho, R. Lent, and S. Herculano-Houzel. Equal numbers of neuronal and nonneuronal cells make the human brain an isometrically scaled-up primate brain. *Journal of Comparative Neurology*, 513(5):532–541, 2009. doi: https://doi.org/10.1002/cne.21974.

[15] S. Bakas, M. Reyes, A. Jakab, S. Bauer, M. Rempfler, A. Crimi, and R. T. Shinohara. Identifying the best machine learning algorithms for brain tumor segmentation, progression assessment, and overall survival prediction in the brats challenge, 2019.

[16] V. Baliyan, C. J. Das, R. Sharma, and A. K. Gupta. Diffusion weighted imaging: Technique and applications. *World journal of radiology*, 8:785–798, 2016. doi: 10.4329/wjr.v8.i9.785.

[17] J. M. Barnes, L. Przybyla, and V. M. Weaver. Tissue mechanics regulate brain development, homeostasis and disease. *Journal of Cell Science*, 130(1):71–82, 2017. ISSN 0021-9533. doi: 10.1242/jcs.191742. URL https://jcs.biologists.org/content/130/1/71.

[18] A. V. Basilio, P. Xu, Y. Takahashi, T. Yanaoka, H. Sugaya, G. A. Ateshian, and B. M. III. Simulating cerebral edema and delayed fatality after traumatic brain injury using triphasic swelling biomechanics. *Traffic Injury Prevention*, 20 (8):820–825, 2019. doi: 10.1080/15389588.2019.1663347. URL https://doi.org/10.1080/15389588.2019.1663347. Publisher: Taylor & Francis _eprint: https://doi.org/10.1080/15389588.2019.1663347.

[19] J. Bauer, M. A. B. Emon, J. J. Staudacher, A. L. Thomas, J. Zessner-Spitzenberg, G. Mancinelli, N. Krett, M. T. Saif, and B. Jung. Increased stiffness of the tumor microenvironment in colon cancer stimulates cancer associated fibroblast-mediated prometastatic activin a signaling. *Nature Scientific Reports*, 10(50), 2020. doi: https://doi.org/10.1038/s41598-019-55687-6.

[20] B. Bender and U. Klose. Cerebrospinal fluid and interstitial fluid volume measurements in the human brain at 3t with epi. *Magnetic Resonance in Medicine*, 61(4):834–841, 2009. doi: https://doi.org/10.1002/mrm.21915.

[21] K. Bentley and S. Chakravartula. The temporal basis of angiogenesis. *Philosophical Transactions of the Royal Society B: Biological Sciences*, 372(1720):20150522, 2017. doi: 10.1098/rstb.2015.0522. URL `https://royalsocietypublishing.org/doi/abs/10.1098/rstb.2015.0522`.

[22] S. Benzekry, C. Lamont, A. Beheshti, A. Tracz, J. M. L. Ebos, L. Hlatky, and P. Hahnfeldt. Classical mathematical models for description and prediction of experimental tumor growth. *PLOS Computational Biology*, 10(8):1–19, 08 2014. doi: 10.1371/journal.pcbi.1003800. URL `https://doi.org/10.1371/journal.pcbi.1003800`.

[23] M. A. Biot. General theory of three-dimensional consolidation. *Journal of Applied Physics*, 12(2):155–164, 1941. doi: 10.1063/1.1712886. URL `https://doi.org/10.1063/1.1712886`.

[24] S. Bisdas, M. Kirkpatrick, P. Giglio, C. Welsh, M. Spampinato, and Z. Rumboldt. Cerebral blood volume measurements by perfusion-weighted mr imaging in gliomas: Ready for prime time in predicting short-term outcome and recurrent disease? *American Journal of Neuroradiology*, 30(4):681–688, 2009. ISSN 0195-6108. doi: 10.3174/ajnr.A1465. URL `http://www.ajnr.org/content/30/4/681`.

[25] D. Boffi, F. Brezzi, and M. Fortin. *Mixed Finite Element Methods and Applications*. Springer, 2013. ISBN 978-3-642-36519-5.

[26] R. Brady and H. Enderling. Mathematical models of cancer: When to predict novel therapies, and when not to. *Bulletin of Mathematical Biology*, 2019. doi: https://doi.org/10.1007/s11538-019-00640-x.

[27] A. Briganti, F. K.-H. Chun, N. Suardi, A. Gallina, J. Walz, M. Graefen, S. Shariat, A. Ebersdobler, P. Rigatti, P. Perrotte, F. Saad, F. Montorsi, H. Huland, and P. I. Karakiewicz. Prostate volume and adverse prostate cancer features: Fact not artifact. *Eur. J. Cancer*, 43(18):2669–2677, 2007.

[28] R. Brossel, A. Yahi, S. David, L. Moreno Velasquez, and J.-M. Guinebretière. Mechanical signals inhibit growth of a grafted tumor in vivo: Proof of concept. *PLOS ONE*, 11:1–17, 04 2016. doi: 10.1371/journal.pone.0152885.

[29] S. Budday, C. Raybaud, and E. Kuhl. A mechanical model predicts morphological abnormalities in the developing human brain. *Scientific Reports*, 4:266–273, 2014. doi: 10.1038/srep05644.

[30] S. Budday, C. Raybaud, and E. Kuhl. A mechanical model predicts morphological abnormalities in the developing human brain. *Scientific Reports*, 4(1):5644, July 2014. ISSN 2045-2322. doi: 10.1038/srep05644. URL https://doi.org/10.1038/srep05644.

[31] S. Budday, R. Nay, R. de Rooij, P. Steinmann, T. Wyrobek, T. C. Ovaert, and E. Kuhl. Mechanical properties of gray and white matter brain tissue by indentation. *Journal of the mechanical behavior of biomedical materials*, 46:318—330, June 2015. ISSN 1751-6161. doi: 10.1016/j.jmbbm.2015.02.024. URL https://europepmc.org/articles/PMC4395547.

[32] S. Budday, G. Sommer, G. Holzapfel, P. Steinmann, and E. Kuhl. Viscoelastic parameter identification of human brain tissue. *Journal of the Mechanical Behavior of Biomedical Materials*, 74:463 – 476, 2017. ISSN 1751-6161. doi: https://doi.org/10.1016/j.jmbbm.2017.07.014.

[33] S. Budday, G. Sommer, F. Paulsen, G. A. Holzapfel, P. Steinmann, and E. Kuhl. Region- and loading-specific finite viscoelasticity of human brain tissue. *PAMM*, 18(1):e201800169, 2018. doi: https://doi.org/10.1002/pamm.201800169. URL https://onlinelibrary.wiley.com/doi/abs/10.1002/pamm.201800169.

[34] S. Budday, T. C. Ovaert, G. A. Holzapfel, P. Steinmann, and E. Kuhl. Fifty shades of brain: A review on the mechanical testing and modeling of brain tissue. *Archives of Computational Methods in Engineering*, 14:931–965, 2019. doi: 10.1007/s11831-019-09352-w.

[35] H. P. Bui, S. Tomar, H. Courtecuisse, M. Audette, S. Cotin, and S. P. Bordas. Controlling the error on target motion through real-time mesh adaptation: Applications to deep brain stimulation. *International Journal for Numerical Methods in Biomedical Engineering*, 34(5):e2958, 2018. doi: https://doi.org/10.1002/cnm.2958. URL https://onlinelibrary.wiley.com/doi/abs/10.1002/cnm.2958. e2958 cnm.2958.

[36] H. P. Bui, S. Tomar, H. Courtecuisse, S. Cotin, and S. P. A. Bordas. Real-time error control for surgical simulation. *IEEE Transactions on Biomedical Engineering*, 65(3):596–607, 2018. doi: 10.1109/TBME.2017.2695587.

[37] B. Burbach, S. O'Flanagan, Q. Shao, P. Roy, K. Young, J. Slaughter, M. Rollins, T. J. Street, V. Granger, L. Beura, S. Azarin, S. Ramadhyani, B. Forsyth, and J. C. B. Y. Shimizu. Irreversible electroporation augments checkpoint immunotherapy in prostate cancer and promotes tumor antigen-specific tissue-resident memory cd8+ t cells. *Nature Communications*, 12:3862, 2021.

[38] H. Byrne and L. Preziosi. Modelling solid tumour growth using the theory of mixtures. *Mathematical Medicine and Biology: A Journal of the IMA*, 20(4):341–366, 12 2003. ISSN 1477-8599. URL https://doi.org/10.1093/imammb/20.4.341.

[39] N. Canac, J. K. Jalaleddini, S. G. Thorpe, C. M. Thibeault, and R. B. Hamilton. Review: pathophysiology of intracranial hypertension and noninvasive intracranial pressure monitoring. *Fluids and Barriers of the CNS*, 17(1): 40, 2020. doi: 10.1186/s12987-020-00201-8.

[40] J. J. Casciari, S. V. Sotirchos, and R. M. Sutherland. Mathematical modelling of microenvironment and growth in emt6/ro multicellular tumour spheroids. *Cell Proliferation*, 25(1):1–22, 1992. doi: 10.1111/j.1365-2184.1992.tb01433.x. URL https://onlinelibrary.wiley.com/doi/abs/10.1111/j.1365-2184.1992.tb01433.x.

[41] A. Chakravarti, M. G. Erkkinen, U. Nestler, R. Stupp, M. Mehta, K. Aldape, M. R. Gilbert, P. M. Black, and J. S. Loeffler. Temozolomide-mediated radiation enhancement in glioblastoma: A report on underlying mechanisms. *Clinical Cancer Research*, 12(15):4738–4746, 2006. ISSN 1078-0432. doi: 10.1158/1078-0432.CCR-06-0596. URL https://clincancerres.aacrjournals.org/content/12/15/4738.

[42] S. Chatelin, A. Constantinesco, and R. Willinger. Fifty years of brain tissue mechanical testing: From in vitro to in vivo investigations. *Biorheology*, 47(5-6):255–276, 2010. URL https://hal.archives-ouvertes.fr/hal-00591614.

[43] V. P. Chauhan, Z. Popović, O. Chen, J. Cui, D. Fukumura, M. G. Bawendi, and R. K. Jain. Fluorescent nanorods and nanospheres for real-time in vivo probing of nanoparticle shape-dependent tumor penetration. *Angewandte Chemie International Edition*, 50(48):11417–11420, 2011. doi: https://doi.org/10.1002/anie.201104449. URL https://onlinelibrary.wiley.com/doi/abs/10.1002/anie.201104449.

[44] V. P. Chauhan, T. Stylianopoulos, J. D. Martin, Z. Popović, O. Chen, W. S. Kamoun, and M. G. t. Bawendi. Normalization of tumour blood vessels improves the delivery of nanomedicines in a size-dependent manner. *Nature Nanotechnology*, 7:383–388, 2012. doi: 10.1038/nnano.2012.45.

[45] J. Chen, Z. Wan, J. Zhang, W. Li, Y. Chen, Y. Li, and Y. Duan. Medical image segmentation and reconstruction of prostate tumor based on 3d alexnet. *Computer Methods and Programs in Biomedicine*, 200:105878, 2021. ISSN 0169-2607. doi: https://doi.org/10.1016/j.cmpb.2020.105878. URL https://www.sciencedirect.com/science/article/pii/S0169260720317119.

[46] W. Chen, M. L. Giger, and U. Bick. A fuzzy c-means (FCM)-based approach for computerized segmentation of breast lesions in dynamic contrast-enhanced MR images. *Acad. Radiol.*, 13(1):63–72, 2006.

[47] X. Chen, R. M. Summers, and J. Yao. Kidney tumor growth prediction by coupling reaction–diffusion and biomechanical model. *IEEE Transactions on Biomedical Engineering*, 60(1):169–173, Jan 2013. ISSN 1558-2531. doi: 10.1109/TBME.2012.2222027.

[48] G. Cheng, J. Tse, R. K. Jain, and L. L. Munn. Micro-environmental mechanical stress controls tumor spheroid size and morphology by suppressing proliferation and inducing apoptosis in cancer cells. *PLOS ONE*, 4(2):1–11, 02 2009. doi: 10.1371/journal.pone.0004632. URL https://doi.org/10.1371/journal.pone.0004632.

[49] S. Cheng and L. E. Bilston. Unconfined compression of white matter. *Journal of Biomechanics*, 40(1):117–124, 2007. ISSN 0021-9290. doi: https://doi.org/10.1016/j.jbiomech.2005.11.004. URL https://www.sciencedirect.com/science/article/pii/S002192900500521X.

[50] R. Chignola, A. Schenetti, G. Andrighetto, E. Chiesa, R. Foroni, S. Sartoris, G. Tridente, and D. Liberati. Forecasting the growth of multicell tumour spheroids: implications for the dynamic growth of solid tumours. *Cell Proliferation*, 33 (4):219–229, 2000. URL https://onlinelibrary.wiley.com/doi/abs/10.1046/j.1365-2184.2000.00174.x.

[51] L. S. Chung, Y.-g. Man, and G. P. Lupton. Wt-1 expression in a spectrum of melanocytic lesions: Implication for differential diagnosis. *J Cancer*, 1:120–125, 2010. doi: 10.7150/jca.1.120. URL https://www.jcancer.org/v01p0120.htm.

[52] P. G. Ciarlet. *The Finite Element Method for Elliptic Problems*. Society for Industrial and Applied Mathematics, 2002. doi: 10.1137/1.9780898719208. URL https://epubs.siam.org/doi/abs/10.1137/1.9780898719208.

[53] P. Cignoni, M. Callieri, M. Corsini, M. Dellepiane, F. Ganovelli, and G. Ranzuglia. Meshlab: an open-source mesh processing tool. In E. U. Scarano V, Chiara RD, editor, *Eurographics Italian chapter conference*, pages 129–136. The Eurographics Association, 2008.

[54] O. Clatz, M. Sermesant, P.-Y. Bondiau, H. Delingette, S. K. Warfield, G. Malandain, and N. Ayache. Realistic simulation of the 3-D growth of brain tumors in MR images coupling diffusion with biomechanical deformation. *IEEE Trans. Med. Imaging*, 24(10):1334–1346, 2005.

[55] B. Cockburn and C.-W. Shu. The local discontinuous galerkin method for time-dependent convection-diffusion systems. *SIAM Journal on Numerical Analysis*, 35(6):2440–2463, 1998. doi: 10.1137/S0036142997316712. URL https://doi.org/10.1137/S0036142997316712.

[56] P. Colli, H. Gomez, G. Lorenzo, G. Marinoschi, A. Reali, and E. Rocca. Mathematical analysis and simulation study of a phase-field model of prostate cancer growth with chemotherapy and antiangiogenic therapy effects. *Math. Models Methods Appl. Sci.*, 30(07):1253–1295, 2020.

[57] M. Colombié, S. Gouard, M. Frindel, A. Vidal, M. Chérel, F. Kraeber-Bodéré, C. Rousseau, and M. Bourgeois. Focus on the controversial aspects of 64cu-atsm in tumoral hypoxia mapping by pet imaging. *Frontiers in Medicine*, 2: 58, 2015. ISSN 2296-858X. doi: 10.3389/fmed.2015.00058. URL https://www.frontiersin.org/article/10.3389/fmed.2015.00058.

[58] C. Colpaert, P. Vermeulen, E. Van Marck, and L. Dirix. The presence of a fibrotic focus is an independent predictor of early metastasis in lymph node-negative breast cancer patients. *The American Journal of Surgical Pathology*, 25, 2001. doi: 10.1097/00000478-200112000-00016.

[59] E. Comellas, S. Budday, J.-P. Pelteret, G. A. Holzapfel, and P. Steinmann. Modeling the porous and viscous responses of human brain tissue behavior. *Computer Methods in Applied Mechanics and Engineering*, 369:113128, 2020. ISSN 0045-7825. doi: https://doi.org/10.1016/j.cma.2020.113128. URL https://www.sciencedirect.com/science/article/pii/S0045782520303133.

[60] J. A. Cottrell, T. J. R. Hughes, and Y. Bazilevs. *Isogeometric analysis: toward integration of CAD and FEA*. John Wiley & Sons, 2009.

[61] V. Cristini, X. Li, J. S. Lowengrub, and S. M. Wise. Nonlinear simulations of solid tumor growth using a mixture model: invasion and branching. *Journal of Mathematical Biology*, 58(4):723, 2008. doi: 10.1007/s00285-008-0215-x.

[62] E. Cukierman, R. Pankov, D. R. Stevens, and K. M. Yamada. Taking cell-matrix adhesions to the third dimension. *Science*, 294(5547):1708–1712, 2001. ISSN 0036-8075. URL https://science.sciencemag.org/content/294/5547/1708.

[63] S. Dana and M. F. Wheeler. Design of convergence criterion for fixed stress split iterative scheme for small strain anisotropic poroelastoplasticity coupled with single phase flow, 2021.

[64] R. V. Davalos, L. M. Mir, and B. Rubinsky. Tissue ablation with irreversible electroporation. *Annals of Biomedical Engineering*, 33:223, 2005. doi: 10.1007/s10439-005-8981-8.

[65] F. Debruyne, J. Barkin, P. van Erps, M. Reis, T. L. Tammela, and C. Roehrborn. Efficacy and safety of long-term treatment with the dual 5alpha-reductase inhibitor dutasteride in men with symptomatic benign prostatic hyperplasia. *Eur. Urol.*, 46(4):488–495, 2004. ISSN 0302-2838.

[66] E. DETOURNAY and A. H.-D. CHENG. 5 - fundamentals of poroelasticity. In C. FAIRHURST, editor, *Analysis and Design Methods*, pages 113–171. Pergamon, Oxford, 1993. ISBN 978-0-08-040615-2. doi: https://doi.org/10.1016/B978-0-08-040615-2.50011-3. URL https://www.sciencedirect.com/science/article/pii/B9780080406152500113.

[67] D. Dionysiou, G. Stamatakos, D. Gintides, N. Uzunoglu, and N. Kyriaki. Critical parameters determining standard radiotherapy treatment outcome for glioblastoma multiforme: a computer simulation. *The open biomedical engineering journal*, 2:43–51, 2008. doi: 10.2174/1874120700802010043.

[68] Y. Dong, A. M. Skelley, K. D. Merdek, K. M. Sprott, C. Jiang, W. E. Pierceall, J. Lin, M. Stocum, W. P. Carney, and D. A. Smirnov. Microfluidics and circulating tumor cells. *The Journal of Molecular Diagnostics*, 15(2):149–157, 2013. ISSN 1525-1578. doi: https://doi.org/10.1016/j.jmoldx.2012.09.004. URL https://www.sciencedirect.com/science/article/pii/S1525157812003078.

[69] J. Dusheck. Oncology: Getting physical. *Nature*, 491, 2012. URL https://doi.org/10.1038/491S50a.

[70] T. Dutta-Roy, A. Wittek, and K. Miller. Biomechanical modelling of normal pressure hydrocephalus. *Journal of Biomechanics*, 41(10):2263–2271, 2008. ISSN 0021-9290. doi: https://doi.org/10.1016/j.jbiomech.2008.04.014. URL https://www.sciencedirect.com/science/article/pii/S0021929008001966.

[71] M. E. Edgerton, Y.-L. Chuang, P. Macklin, W. Yang, E. L. Bearer, and V. Cristini. A novel, patient-specific mathematical pathology approach for assessment of surgical volume: Application to ductal carcinoma *in situ* of the breast. *Analytical Cellular Pathology*, 34, 2011.

[72] W. Ehlers. Foundations of multiphasic and porous materials. In *Porous media: theory, experiments and numerical applications*, pages 3–86. Springer-Verlag Berlin Heidelberg, 2002.

[73] W. Ehlers and A. Wagner. Multi-component modelling of human brain tissue: a contribution to the constitutive and computational description of deformation, flow and diffusion processes with application to the invasive drug-delivery problem. *Computer Methods in Biomechanics and Biomedical Engineering*, 18(8):861–879, 2015. doi: 10.1080/10255842.2013.853754. URL https://doi.org/10.1080/10255842.2013.853754. PMID: 24261340.

[74] M. Essig, M. S. Shiroishi, T. B. Nguyen, M. Saake, J. M. Provenzale, D. Enterline, N. Anzalone, A. Dörfler, and A. Rovira. Perfusion mri: The five most frequently asked technical questions. 200:24–34, 2013. doi: 10.2214/AJR.12.9543.

[75] A. C. Evans, A. L. Janke, D. L. Collins, and S. Baillet. Brain templates and atlases. *NeuroImage*, 62(2):911–922, 2012. ISSN 1053-8119. doi: https://doi.org/10.1016/j.neuroimage.2012.01.024. URL https://www.sciencedirect.com/science/article/pii/S1053811912000419. 20 YEARS OF fMRI.

[76] J. Falco, A. Agosti, I. G. Vetrano, A. Bizzi, F. Restelli, M. Broggi, M. Schiariti, F. DiMeco, P. Ferroli, P. Ciarletta, and F. Acerbi. In silico mathematical modelling for glioblastoma: A critical review and a patient-specific case. *Journal of Clinical Medicine*, 10(10), 2021. ISSN 2077-0383. doi: 10.3390/jcm10102169. URL https://www.mdpi.com/2077-0383/10/10/2169.

[77] L. Falzone, S. Salomone, and M. Libra. Evolution of cancer pharmacological treatments at the turn of the third millennium. *Frontiers in Pharmacology*, 9:1300, 2018. ISSN 1663-9812. doi: 10.3389/fphar.2018.01300. URL https://www.frontiersin.org/article/10.3389/fphar.2018.01300.

[78] H. Fang, Z. Wang, Z. Lin, and M. Liu. Lattice boltzmann method for simulating the viscous flow in large distensible blood vessels. *Phys. Rev. E*, 65:051925, May 2002. doi: 10.1103/PhysRevE.65.051925. URL https://link.aps.org/doi/10.1103/PhysRevE.65.051925.

[79] B. Fazeny-Dörner, C. Wenzel, M. Veitl, M. Piribauer, K. Roessler, K. Dieckmann, K. Ungersböck, and C. Marosi. Survival and prognostic factors of patients with unresectable glioblastoma multiforme. *Anti-cancer drugs*, 14:305–12, 04 2003. doi: 10.1097/01.cad.0000065040.82984.bb.

[80] A. Fedorov, R. Beichel, J. Kalpathy-Cramer, J. Finet, J.-C. Fillion-Robin, S. Pujol, C. Bauer, D. Jennings, F. Fennessy, M. Sonka, J. Buatti, S. Aylward, J. V. Miller, S. Pieper, and R. Kikinis. 3d slicer as an image computing platform for the quantitative imaging network. *Magn. Reson. Imaging*, 30(9):1323–1341, 2012.

[81] C. Festuccia, G. L. Gravina, P. Muzi, R. Pomante, A. Angelucci, C. Vicentini, and M. Bologna. Effects of dutasteride on prostate carcinoma primary cultures: A comparative study with finasteride and MK386. *J. Urol.*, 180(1):367–372, 2008. ISSN 0022-5347.

[82] D. Fink, A. Wagner, and W. Ehlers. Application-driven model reduction for the simulation of therapeutic infusion processes in multi-component brain tissue. *Journal of Computational Science*, 24:101–115, 2018. ISSN 1877-7503. doi: https://doi.org/10.1016/j.jocs.2017.10.002. URL `https://www.sciencedirect.com/science/article/pii/S1877750317310840`.

[83] T. L. Fletcher, A. G. Kolias, P. J. A. Hutchinson, and M. P. F. Sutcliffe. Development of a finite element model of decompressive craniectomy. *PLOS ONE*, 9(7):1–9, 07 2014. doi: 10.1371/journal.pone.0102131. URL `https://doi.org/10.1371/journal.pone.0102131`.

[84] M. S. Floater and K. Hormann. Surface parameterization: a tutorial and survey. In N. A. Dodgson, M. S. Floater, and M. A. Sabin, editors, *Advances in Multiresolution for Geometric Modelling*, pages 157–186. Springer, Berlin, Heidelberg, 2005.

[85] J. Folkman. Tumor angiogenesis: Therapeutic implications. *New England Journal of Medicine*, 285(21):1182–1186, 1971. doi: 10.1056/NEJM197111182852108. URL `https://doi.org/10.1056/NEJM197111182852108`. PMID: 4938153.

[86] G. Follain, D. Herrmann, S. Harlepp, V. Hyenne, N. Osmani, S. C. Warren, P. Timpson, and J. G. Goetz. Fluids and their mechanics in tumour transit: shaping metastasis. *Nature Reviews Cancer*, 20:107 – 124, 2020. doi: 10.1038/s41568-019-0221-x. URL `https://hal.archives-ouvertes.fr/hal-01573589`.

[87] A. E. Forte, S. M. Gentleman, and D. Dini. On the characterization of the heterogeneous mechanical response of human brain tissue. *Biomechanics and Modeling in Mechanobiology*, 16:907–920, 2017. doi: 10.1007/s10237-016-0860-8.

[88] M. Fraldi and A. R. Carotenuto. Cells competition in tumor growth poroelasticity. *Journal of Mechanics Physics of Solids*, 112:345–367, Mar. 2018. doi: 10.1016/j.jmps.2017.12.015.

[89] G. Franceschini, D. Bigoni, P. Regitnig, and G. Holzapfel. Brain tissue deforms similarly to filled elastomers and follows consolidation theory. *Journal of the Mechanics and Physics of Solids*, 54:2592–2620, 2006. ISSN 0022-5096.

[90] S. J. Freedland, W. B. Isaacs, E. A. Platz, M. K. Terris, W. J. Aronson, C. L. Amling, J. C. Presti Jr, and C. J. Kane. Prostate size and risk of high-grade, advanced prostate cancer and biochemical progression after radical prostatectomy: a search database study. *J. Clin. Oncol.*, 23(30):7546–7554, 2005.

[91] H. B. Frieboes, B. R. Smith, Y.-L. Chuang, K. Ito, A. M. Roettgers, S. S. Gambhir, and V. Cristini. An integrated computational/experimental model of lymphoma growth. *PLOS Computational Biology*, 9(3):1–13, 03 2013. doi: 10.1371/journal.pcbi.1003008.

[92] R. Gatenby, P. Maini, and E. Gawlinski. Analysis of tumor as an inverse problem provides a novel theoretical framework for understanding tumor biology and therapy. *Appl. Math. Lett.*, 15(3):339–345, 2002. ISSN 0893-9659.

[93] P. Gerard, A. Léonard, J.-P. Masekanya, R. Charlier, and F. Collin. Study of the soil–atmosphere moisture exchanges through convective drying tests in non-isothermal conditions. *International Journal for Numerical and Analytical Methods in Geomechanics*, 34(12):1297–1320, 2010. doi: https://doi.org/10.1002/nag.866. URL `https://onlinelibrary.wiley.com/doi/abs/10.1002/nag.866`.

[94] A. Gertych, Z. Swiderska-Chadaj, Z. Ma, N. Ing, T. Markiewicz, S. Cierniak, H. Salemi, S. Guzman, A. E. Walts, and B. S. Knudsen. Convolutional neural networks can accurately distinguish four histologic growth patterns of lung adenocarcinoma in digital slides. *Scientific Reports*, 9:1483, 2019. doi: 10.1038/s41598-018-37638-9.

[95] C. Geuzaine and J.-F. Remacle. Gmsh: A 3-d finite element mesh generator with built-in pre- and post-processing facilities. *International Journal for Numerical Methods in Engineering*, 79(11):1309–1331, 2009. doi: https://doi.org/10.1002/nme.2579. URL `https://onlinelibrary.wiley.com/doi/abs/10.1002/nme.2579`.

[96] M. Giladi, R. S. Schneiderman, T. W. Voloshin, Y. Porat, M. Munster, R. Blat, and S. Sherbo. Mitotic spindle disruption by alternating electric fields leads to improper chromosome segregation and mitotic catastrophe in cancer cells. *Scientific Reports*, 5, 2015. doi: https://doi.org/10.1038/srep18046.

[97] H. Gomez and K. G. van der Zee. Computational phase-field modeling. In E. Stein, R. de Borst, and T. J. R. Hughes, editors, *Encyclopedia of Computational Mechanics Second Edition*, pages 1–35. 2017. ISBN 9781119176817.

[98] Y. Gordon, S. Partovi, M. Müller-Eschner, E. Amarteifio, T. Bäuerle, M.-A. Weber, H.-U. Kauczor, and F. Rengier. Dynamic contrast-enhanced magnetic resonance imaging: fundamentals and application to the evaluation of the peripheral perfusion. *Cardiovascular Diagnosis and Therapy*, 4(2), 2014. ISSN 2223-3660. URL `https://cdt.amegroups.com/article/view/3640`.

[99] W. G. Gray and C. T. Miller. *Introduction to the Thermodynamically Constrained Averaging Theory for Porous Medium Systems*. Springer, 2014. ISBN 978-3-319-04010-3.

[100] Y. Guéguen, L. Dormieux, and M. Boutéca. Chapter 1 fundamentals of poromechanics. In Y. Guéguen and M. Boutéca, editors, *Mechanics of Fluid-Saturated Rocks*, volume 89 of *International Geophysics*, pages 1–54. Academic Press, 2004. doi: https://doi.org/10.1016/S0074-6142(03)80017-7. URL https://www.sciencedirect.com/science/article/pii/S0074614203800177.

[101] S. Hakim, J. Venegas, and J. Burton. The physics of the cranial cavity, hydrocephalus and normal pressure hydrocephalus: mechanical interpretation and mathematical model. *Surgical neurology*, 5(3):187—210, March 1976. ISSN 0090-3019. URL http://europepmc.org/abstract/MED/1257894.

[102] H. W. Haslach, L. N. Leahy, P. Riley, R. Gullapalli, S. Xu, and A. H. Hsieh. Solid–extracellular fluid interaction and damage in the mechanical response of rat brain tissue under confined compression. *Journal of the Mechanical Behavior of Biomedical Materials*, 29:138–150, 2014. ISSN 1751-6161. doi: https://doi.org/10.1016/j.jmbbm.2013.08.027. URL https://www.sciencedirect.com/science/article/pii/S1751616113002981.

[103] R. Hass, J. von der Ohe, and H. Ungefroren. Impact of the tumor microenvironment on tumor heterogeneity and consequences for cancer cell plasticity and stemness. *Cancers*, 12(12), 2020. ISSN 2072-6694. doi: 10.3390/cancers12123716. URL https://www.mdpi.com/2072-6694/12/12/3716.

[104] C. He, J. Wang, S. Sun, Y. Zhang, and S. Li. Immunomodulatory effect after irreversible electroporation in patients with locally advanced pancreatic cancer. *Journal of Oncology*, 2019. doi: 10.1155/2019/9346017.

[105] B. Hegedüs, F. Marga, K. Jakab, K. L. Sharpe-Timms, and G. Forgacs. The interplay of cell-cell and cell-matrix interactions in the invasive properties of brain tumors. *Biophysical Journal*, 91(7):2708–2716, 2006. ISSN 0006-3495. doi: https://doi.org/10.1529/biophysj.105.077834. URL https://www.sciencedirect.com/science/article/pii/S000634950671983X.

[106] M. E. Hegi, A.-C. Diserens, T. Gorlia, M.-F. Hamou, N. de Tribolet, M. Weller, J. M. Kros, J. A. Hainfellner, W. Mason, L. Mariani, J. E. Bromberg, P. Hau, R. O. Mirimanoff, J. G. Cairncross, R. C. Janzer, and R. Stupp. Mgmt gene silencing and benefit from temozolomide in glioblastoma. *New England Journal of Medicine*, 352 (10):997–1003, 2005. doi: 10.1056/NEJMoa043331. URL https://doi.org/10.1056/NEJMoa043331. PMID: 15758010.

[107] G. Helmlinger, P. A. Netti, H. C. Lichtenbeld, R. J. Melder, and R. K. Jain. Solid stress inhibits the growth of multicellular tumor spheroids. *Nature Biotechnology*, 15(21):778–783, 1997.

[108] S. B. Hladky and M. A. Barrand. Mechanisms of fluid movement into, through and out of the brain: evaluation of the evidence. *Fluids and Barriers of the CNS*, 11:26, 2014. doi: https://doi.org/10.1186/2045-8118-11-26. URL 10.1186/2045-8118-11-26.

[109] D. A. Hormuth, S. L. Eldridge, J. A. Weis, M. I. Miga, and T. E. Yankeelov. Mechanically coupled reaction-diffusion model to predict glioma growth: Methodological details. In L. von Stechow, editor, *Cancer Systems Biology: Methods and Protocols*, pages 225–241. Springer New York, 2018.

[110] D. A. Hormuth, A. M. Jarrett, X. Feng, and T. E. Yankeelov. Calibrating a predictive model of tumor growth and angiogenesis with quantitative mri. *Annals of Biomedical Engineering*, 47:1539–1551, 2019. doi: 10.1007/s10439-019-02262-9.

[111] D. A. Hormuth, A. M. Jarrett, E. A. Lima, M. T. McKenna, D. T. Fuentes, and T. E. Yankeelov. Mechanism-based modeling of tumor growth and treatment response constrained by multiparametric imaging data. *JCO Clinical Cancer Informatics*, (3):1–10, 2019. doi: 10.1200/CCI.18.00055.

[112] D. A. Hormuth, K. A. Al Feghali, A. M. Elliott, T. E. Yankeelov, and C. Chung. Image-based personalization of computational models for predicting response of high-grade glioma to chemoradiation. *Sci. Rep.*, 11:8520, 2021.

[113] D. A. Hormuth II, J. A. Weis, S. L. Barnes, M. I. Miga, E. C. Rericha, V. Quaranta, and T. E. Yankeelov. Predicting in vivo glioma growth with the reaction diffusion equation constrained by quantitative magnetic resonance imaging data. *Phys. Biol.*, 12(4):046006, 2015.

[114] S. S. Hossain, Y. Zhang, X. Liang, F. Hussain, M. Ferrari, T. J. Hughes, and P. Decuzzi. In silico vascular modeling for personalized nanoparticle delivery. *Nanomedicine*, 8(3):343–357, 2013. doi: 10.2217/nnm.12.124. URL https://doi.org/10.2217/nnm.12.124. PMID: 23199308.

[115] M. Hosseini-Farid, M. Ramzanpour, J. McLean, M. Ziejewski, and G. Karami. A poro-hyper-viscoelastic rate-dependent constitutive modeling for the analysis of brain tissues. *Journal of the Mechanical Behavior of Biomedical Materials*, 102:103475, 2020. ISSN 1751-6161. doi: https://doi.org/10.1016/j.jmbbm.2019.103475. URL https://www.sciencedirect.com/science/article/pii/S1751616119305764.

[116] J. Huang, J. Yu, L. Tu, N. Huang, H. Li, and Y. Luo. Isocitrate dehydrogenase mutations in glioma: From basic discovery to therapeutics development. *Frontiers in Oncology*, 9:506, 2019. ISSN 2234-943X. doi: 10.3389/fonc.2019.00506. URL https://www.frontiersin.org/article/10.3389/fonc.2019.00506.

[117] R. Jain and L. Baxter. Mechanisms of heterogeneous distribution of monoclonal antibodies and other macromolecules in tumors: significance of elevated interstitial pressure. *Cancer research*, 48 24 Pt 1:7022–32, 1988.

[118] R. K. Jain. Normalization of tumor vasculature: An emerging concept in antiangiogenic therapy. *Science*, 307 (5706):58–62, 2005. ISSN 0036-8075. doi: 10.1126/science.1104819. URL https://science.sciencemag.org/content/307/5706/58.

[119] R. K. Jain, J. D. Martin, and T. Stylianopoulos. The role of mechanical forces in tumor growth and therapy. *Annual Review of Biomedical Engineering*, 16(1):321–346, 2014. URL https://doi.org/10.1146/annurev-bioeng-071813-105259.

[120] A. Jamal, M. T. Mongelli, M. Vidotto, M. Madekurozwa, A. Bernardini, D. R. Overby, E. De Momi, F. Rodriguez y Baena, J. M. Sherwood, and D. Dini. Infusion mechanisms in brain white matter and their dependence on microstructure: An experimental study of hydraulic permeability. *IEEE Transactions on Biomedical Engineering*, 68 (4):1229–1237, 2021. doi: 10.1109/TBME.2020.3024117.

[121] A. M. Jarrett, D. A. Hormuth, S. L. Barnes, X. Feng, W. Huang, and T. E. Yankeelov. Incorporating drug delivery into an imaging-driven, mechanics-coupled reaction diffusion model for predicting the response of breast cancer to neoadjuvant chemotherapy: theory and preliminary clinical results. *Phys. Med. Biol.*, 63(10):105015, 2018.

[122] A. M. Jarrett, D. A. Hormuth, C. Wu, A. S. Kazerouni, D. A. Ekrut, J. Virostko, A. G. Sorace, J. C. DiCarlo, J. Kowalski, D. Patt, B. Goodgame, S. Avery, and T. E. Yankeelov. Evaluating patient-specific neoadjuvant regimens for breast cancer via a mathematical model constrained by quantitative magnetic resonance imaging data. *Neoplasia*, 22(12):820–830, 2020.

[123] H. Jiang, S. Hegde, B. L. Knolhoff, Y. Zhu, J. M. Herndon, M. A. Meyer, T. M. Nywening, W. G. Hawkins, I. M. Shapiro, and D. T. Weaver. Targeting focal adhesion kinase renders pancreatic cancers responsive to checkpoint immunotherapy. *Nature Medicine*, 22(8):851–860, 2016. doi: https://doi.org/10.1038/nm.4123.

[124] M.-Z. Jin and W.-L. Jin. The updated landscape of tumor microenvironment and drug repurposing. *Signal Transduction and Targeted Therapy*, 5:166, 2020. doi: 10.1038/s41392-020-00280-x.

[125] M. Kalli, C. Voutouri, A. Minia, V. Pliaka, C. Fotis, L. G. Alexopoulos, and T. Stylianopoulos. Mechanical compression regulates brain cancer cell migration through mek1/erk1 pathway activation and gdf15 expression. *Frontiers in Oncology*, 9:992, 2019. ISSN 2234-943X. doi: 10.3389/fonc.2019.00992. URL https://www.frontiersin.org/article/10.3389/fonc.2019.00992.

[126] K. Kamnitsas, E. Ferrante, S. Parisot, C. Ledig, A. V. Nori, A. Criminisi, D. Rueckert, and B. Glocker. Deepmedic for brain tumor segmentation. In A. Crimi, B. Menze, O. Maier, M. Reyes, S. Winzeck, and H. Handels, editors, *Brainlesion: Glioma, Multiple Sclerosis, Stroke and Traumatic Brain Injuries*, pages 138–149, Cham, 2016. Springer International Publishing.

[127] T. Kaster, I. Sack, and A. Samani. Measurement of the hyperelastic properties of ex vivo brain tissue slices. *Journal of Biomechanics*, 44(6):1158–1163, 2011. ISSN 0021-9290. doi: https://doi.org/10.1016/j.jbiomech.2011.01.019. URL https://www.sciencedirect.com/science/article/pii/S0021929011000492.

[128] N. Khan, B. B. Williams, H. Hou, H. Li, and H. M. Swartz. Repetitive tissue po2 measurements by electron paramagnetic resonance oximetry: current status and future potential for experimental and clinical studies. *Antioxidants & redox signaling*, 9(8):1169–1182, 2007.

[129] J. Kim, J. W. Davis, E. A. Klein, C. Magi-Galluzzi, Y. Lotan, J. F. Ward, L. L. Pisters, J. W. Basler, C. A. Pettaway, A. Stephenson, E. M. Li Ning Tapia, E. Efstathiou, X. Wang, K.-A. Do, J. J. Lee, I. P. Gorlov, L. A. Vornik, A. M. Hoque, I. N. Prokhorova, H. L. Parnes, S. M. Lippman, I. M. Thompson, P. H. Brown, C. J. Logothetis, and P. Troncoso. Tissue effects in a randomized controlled trial of short-term finasteride in early prostate cancer. *EBioMedicine*, 7:85–93, 2016. ISSN 2352-3964.

[130] Y. Kim and S. Roh. A hybrid model for cell proliferation and migration in glioblastoma. *Discrete & Continuous Dynamical Systems - B*, 18(4):969–1015, 2013.

[131] G. J. Kitange, B. L. Carlson, M. A. Schroeder, P. T. Grogan, J. D. Lamont, P. A. Decker, W. Wu, C. D. James, and J. N. Sarkaria. Induction of MGMT expression is associated with temozolomide resistance in glioblastoma xenografts. *Neuro-Oncology*, 11(3):281–291, 06 2009. ISSN 1522-8517. doi: 10.1215/15228517-2008-090. URL https://doi.org/10.1215/15228517-2008-090.

[132] E. J. Koay, M. J. Truty, V. Cristini, R. M. Thomas, R. Chen, D. Chatterjee, Y. Kang, P. R. Bhosale, E. P. Tamm, C. H. Crane, M. Javle, M. H. Katz, V. N. Gottumukkala, M. A. Rozner, H. Shen, J. E. Lee, H. Wang, Y. Chen, W. Plunkett, J. L. Abbruzzese, R. A. Wolff, G. R. Varadhachary, M. Ferrari, and J. B. Fleming. Transport properties of pancreatic cancer describe gemcitabine delivery and response. *The Journal of clinical investigation*, 124(4): 1525–1536, 2014.

[133] X. Kong, M. S. Moran, N. Zhang, B. Haffty, and Q. Yang. Meta-analysis confirms achieving pathological complete response after neoadjuvant chemotherapy predicts favourable prognosis for breast cancer patients. *Eur. J. Cancer*, 47(14):2084–2090, 2011.

[134] P. Koumoutsakos, I. Pivkin, and F. Milde. The fluid mechanics of cancer and its therapy. *Annual Review of Fluid Mechanics*, 45(1):325–355, 2013. doi: 10.1146/annurev-fluid-120710-101102.

[135] A. K. Laird. Dynamics of tumor growth. *British Journal of Cancer*, 18:490–502, 1964. doi: 10.1038/bjc.1964.55.

[136] G. E. Lang, P. S. Stewart, D. Vella, S. L. Waters, and A. Goriely. Is the donnan effect sufficient to explain swelling in brain tissue slices? *Journal of The Royal Society Interface*, 11(96):20140123, 2014. doi: 10.1098/rsif.2014.0123. URL https://royalsocietypublishing.org/doi/abs/10.1098/rsif.2014.0123.

[137] V. Le Maout, K. Alessandri, B. Gurchenkov, H. Bertin, P. Nassoy, and G. Sciumè. Role of mechanical cues and hypoxia on the growth of tumor cells in strong and weak confinement: A dual in vitro–in silico approach. *Science Advances*, 6, 2020.

[138] J. A. Lefever, J. Jaime García, and J. H. Smith. A patient-specific, finite element model for noncommunicating hydrocephalus capable of large deformation. *Journal of Biomechanics*, 46(8):1447–1453, 2013. ISSN 0021-9290. doi: https://doi.org/10.1016/j.jbiomech.2013.03.008. URL https://www.sciencedirect.com/science/article/pii/S0021929013001243.

[139] Y. Lei, H. Han, F. Yuan, A. Javeed, and Y. Zhao. The brain interstitial system: Anatomy, modeling, in vivo measurement, and applications. *Progress in Neurobiology*, 157:230 – 246, 2017. ISSN 0301-0082. doi: https://doi.org/10.1016/j.pneurobio.2015.12.007. New Perspectives on Healthy Aging.

[140] G. Lemaître. *Computer-Aided Diagnosis for Prostate Cancer using Multi-Parametric Magnetic Resonance Imaging*. PhD thesis, Universitat de Girona and Université de Bourgogne, 2016.

[141] G. Lemaître, R. Martí, J. Freixenet, J. C. Vilanova, P. M. Walker, and F. Meriaudeau. Computer-Aided Detection and diagnosis for prostate cancer based on mono and multi-parametric MRI: A review. *Comput. Biol. Med.*, 60: 8–31, 2015. ISSN 0010-4825.

[142] X. Li, B. M. Dawant, E. B. Welch, A. B. Chakravarthy, L. Xu, I. Mayer, M. Kelley, I. Meszoely, J. Means-Powell, J. C. Gore, and T. E. Yankeelov. Validation of an algorithm for the nonrigid registration of longitudinal breast MR images using realistic phantoms. *Med. Phys.*, 37(6Part1):2541–2552, 2010.

[143] X. Li, H. von Holst, and S. Kleiven. Influences of brain tissue poroelastic constants on intracranial pressure (icp) during constant-rate infusion. *Computer Methods in Biomechanics and Biomedical Engineering*, 16(12):1330–1343, 2013. doi: 10.1080/10255842.2012.670853. URL https://doi.org/10.1080/10255842.2012.670853. PMID: 22452461.

[144] M. Lin, X. Zhang, S. Liang, X. Li, H. Luo, M. Alnaggar, A. Liu, and Z. Yin. Irreversible electroporation plus allogenic vγ9vδ2 t cells enhances antitumor effect for locally advanced pancreatic cancer patients. *Signal Transduction and Targeted Therapy*, 5:215, 2020. doi: https://doi.org/10.1038/s41392-020-00260-1.

[145] S. Lindsey and S. A. Langhans. Chapter one - epidermal growth factor signaling in transformed cells. volume 314 of *International Review of Cell and Molecular Biology*, pages 1–41. Academic Press, 2015. doi: https://doi.org/10.1016/bs.ircmb.2014.10.001. URL https://www.sciencedirect.com/science/article/pii/S1937644814000045.

[146] J. L. Lions. *Problemes aux Limites non Homogenes a Donnees Irregulieres*, pages 283–292. Springer Berlin Heidelberg, Berlin, Heidelberg, 2010. ISBN 978-3-642-11057-3. doi: 10.1007/978-3-642-11057-3_12. URL https://doi.org/10.1007/978-3-642-11057-3_12.

[147] J. Lipková, P. Angelikopoulos, S. Wu, E. Alberts, B. Wiestler, C. Diehl, C. Preibisch, T. Pyka, S. E. Combs, P. Hadjidoukas, K. Van Leemput, P. Koumoutsakos, J. Lowengrub, and B. Menze. Personalized radiotherapy

design for glioblastoma: Integrating mathematical tumor models, multimodal scans, and Bayesian inference. *IEEE Transactions on Medical Imaging*, 38(8):1875–1884, 2019.

[148] J. Liu and L. Guo. An improved k-means algorithm for brain MRI image segmentation. In *3rd International Conference on Mechatronics, Robotics and Automation*. 2015.

[149] A. Logg and G. N. Wells. Dolfin: Automated finite element computing. *ACM Trans. Math. Softw.*, 37(2), apr 2010. ISSN 0098-3500. doi: 10.1145/1731022.1731030. URL https://doi.org/10.1145/1731022.1731030.

[150] G. Lorenzo, M. A. Scott, K. Tew, T. J. R. Hughes, Y. J. Zhang, L. Liu, G. Vilanova, and H. Gomez. Tissue-scale, personalized modeling and simulation of prostate cancer growth. *Proc. Natl. Acad. Sci. U.S.A.*, 113(48): E7663–E7671, 2016.

[151] G. Lorenzo, T. J. R. Hughes, P. Dominguez-Frojan, A. Reali, and H. Gomez. Computer simulations suggest that prostate enlargement due to benign prostatic hyperplasia mechanically impedes prostate cancer growth. *Proceedings of the National Academy of Sciences*, 116(4):1152–1161, 2019. ISSN 0027-8424. URL https://www.pnas.org/content/116/4/1152.

[152] G. Lorenzo, T. Hughes, A. Reali, and H. Gomez. A numerical simulation study of the dual role of 5alpha-reductase inhibitors on tumor growth in prostates enlarged by benign prostatic hyperplasia via stress relaxation and apoptosis upregulation. *Comput. Methods Appl. Mech. Eng.*, 362:112843, 2020. ISSN 0045-7825.

[153] G. Lorenzo, D. A. Hormuth II, A. M. Jarrett, E. A. Lima, S. Subramanian, G. Biros, J. T. Oden, T. J. Hughes, and T. E. Yankeelov. Quantitative in vivo imaging to enable tumor forecasting and treatment optimization. *arXiv preprint arXiv:2102.12602*, 2021.

[154] D. Louis, A. Perry, and G. Reifenberger. The 2016 world health organization classification of tumors of the central nervous system: a summary. *Acta Neuropathol.*, 131:803–820, 2016. doi: 10.1007/s00401-016-1545-1.

[155] J. S. Lowengrub, H. B. Frieboes, F. Jin, Y.-L. Chuang, X. Li, P. Macklin, S. M. Wise, and V. Cristini. Nonlinear modelling of cancer: bridging the gap between cells and tumours. *Nonlinearity*, 23(1), 2010.

[156] J. Lu, D. Dean, Yu, R. T. Bonnecaze, and M. H. Zaman. Cancer cell stiffness: integrated roles of three-dimensional matrix stiffness and transforming potential. *Biophysical journal*, 99:2048–57, 2010. ISSN 2296-634X. doi: 10.3389/fcell.2018.00017.

[157] P. Macklin, M. E. Edgerton, A. M. Thompson, and V. Cristini. Patient-calibrated agent-based modelling of ductal carcinoma in situ (dcis): From microscopic measurements to macroscopic predictions of clinical progression. *Journal of Theoretical Biology*, 301:122 – 140, 2012.

[158] D. B. MacManus, B. Pierrat, J. G. Murphy, and M. D. Gilchrist. A viscoelastic analysis of the p56 mouse brain under large-deformation dynamic indentation. *Acta Biomaterialia*, 48:309–318, 2017. ISSN 1742-7061. doi: https://doi.org/10.1016/j.actbio.2016.10.029. URL https://www.sciencedirect.com/science/article/pii/S1742706116305566.

[159] A. Malandrino and E. Moeendarbary. Poroelasticity of living tissues. In R. Narayan, editor, *Encyclopedia of Biomedical Engineering*, pages 238–245. Elsevier, Oxford, 2019. ISBN 978-0-12-805144-3. doi: https://doi.org/10.1016/B978-0-12-801238-3.99932-X. URL https://www.sciencedirect.com/science/article/pii/B978012801238399932X.

[160] A. Mang, S. Bakas, S. Subramanian, C. Davatzikos, and G. Biros. Integrated biophysical modeling and image analysis: application to neuro-oncology. *Annu. Rev. Biomed. Eng.*, 22:309–341, 2020.

[161] A. Marusyk and K. Polyak. Tumor heterogeneity: Causes and consequences. *Biochimica et Biophysica Acta (BBA) - Reviews on Cancer*, 1805(1):105–117, 2010. ISSN 0304-419X. doi: https://doi.org/10.1016/j.bbcan.2009.11.002. URL https://www.sciencedirect.com/science/article/pii/S0304419X09000742.

[162] P. Mascheroni, C. Stigliano, M. Carfagna, D. P. Boso, L. Preziosi, P. Decuzzi, and B. A. Schrefler. Predicting the growth of glioblastoma multiforme spheroids using a multiphase porous media model. *Biomechanics and Modeling in Mechanobiology*, 15(1):1215–1228, 2016.

[163] R. McBeath, D. M. Pirone, C. M. Nelson, K. Bhadriraju, and C. S. Chen. Cell shape, cytoskeletal tension, and rhoa regulate stem cell lineage commitment. *Developmental Cell*, 6(4):483–495, 2004. ISSN 1534-5807. doi: https://doi.org/10.1016/S1534-5807(04)00075-9. URL https://www.sciencedirect.com/science/article/pii/S1534580704000759.

[164] J. D. McConnell, R. Bruskewitz, P. Walsh, G. Andriole, M. Lieber, H. L. Holtgrewe, P. Albertsen, C. G. Roehrborn, J. C. Nickel, D. Z. Wang, A. M. Taylor, and J. Waldstreicher. The effect of finasteride on the risk of acute urinary retention and the need for surgical treatment among men with benign prostatic hyperplasia. *N. Engl. J. Med.*, 338 (9):557–563, 1998.

[165] E. A. Meroi and B. A. Schrefler. *Large Strain Static and Dynamic Hydro-Mechanical Analysis of Porous Media*, pages 397–447. Springer Vienna, Vienna, 1995.

[166] M.-C. Metz, M. Molina-Romero, J. Lipkova, J. Gempt, F. Liesche-Starnecker, P. Eichinger, L. Grundl, B. Menze, S. E. Combs, C. Zimmer, and B. Wiestler. Predicting glioblastoma recurrence from preoperative mr scans using fractional-anisotropy maps with free-water suppression. *Cancers*, 12(3), 2020. ISSN 2072-6694. doi: 10.3390/cancers12030728. URL https://www.mdpi.com/2072-6694/12/3/728.

[167] F. Michor, J. Liphardt, M. Ferrari, and J. Widom. What does physics have to do with cancer? *Nature reviews. Cancer*, 11(3):657–670, 2011. doi: 10.1038/nrc3092.

[168] R.-O. Mirimanoff, T. Gorlia, W. Mason, M. J. Van den Bent, R.-D. Kortmann, B. Fisher, M. Reni, A. A. Brandes, J. Curschmann, S. Villa, G. Cairncross, A. Allgeier, D. Lacombe, and R. Stupp. Radiotherapy and temozolomide for newly diagnosed glioblastoma: Recursive partitioning analysis of the eortc 26981/22981-ncic ce3 phase iii randomized trial. *Journal of Clinical Oncology*, 24(16):2563–2569, 2006. doi: 10.1200/JCO.2005.04.5963. URL https://doi.org/10.1200/JCO.2005.04.5963. PMID: 16735709.

[169] A. Mohanty, R. R. Pharaon, A. Nam, S. Salgia, P. Kulkarni, and E. Massarelli. Fak-targeted and combination therapies for the treatment of cancer: an overview of phase i and ii clinical trials. *Expert Opinion on Investigational Drugs*, 29(4):399–409, 2020. doi: 10.1080/13543784.2020.1740680. URL https://doi.org/10.1080/13543784.2020.1740680. PMID: 32178538.

[170] F. Morin, M. Chabanas, H. Courtecuisse, and Y. Payan. *Biomechanical modeling of brain soft tissues for medical applications*. Academic Press, 2017. ISBN 978-1-119-00379-3. doi: 10.1016/B978-0-12-804009-6.00006-7.

[171] M. Mostavi, Y.-C. Chiu, Y. Huang, and Y. Chen. Convolutional neural network models for cancer type prediction based on gene expression. *BMC Medical Genomics*, 13:44, 2020. doi: 10.1186/s12920-020-0677-2.

[172] J. Munger, X. Huang, H. Kawakatsu, M. J. Griffiths, S. L. Dalton, J. Wu, J.-F. Pittet, N. Kaminski, C. Garat, and M. A. Matthay. A mechanism for regulating pulmonary inflammation and fibrosis: The integrin $\alpha v\beta 6$ binds and activates latent tgf $\beta 1$. *Cell*, 96:319–328, 1999. doi: https://doi.org/10.1016/S0092-8674(00)80545-0.

[173] B. Muz, P. de la Puente, F. Azab, and A. Azab. The role of hypoxia in cancer progression, angiogenesis, metastasis, and resistance to therapy. *Hypoxia (Auckl)*, 3:83–92, 2015. doi: https://doi.org/10.2147/HP.S93413.

[174] T. Nagashima, N. Tamaki, S. Matsumoto, B. Horwitz, and Y. Seguchi. Biomechanics of Hydrocephalus: A New Theoretical Model. *Neurosurgery*, 21(6):898–904, 04 1987. ISSN 0148-396X. doi: 10.1227/00006123-198712000-00019. URL https://doi.org/10.1227/00006123-198712000-00019.

[175] S. Nagrath, L. V. Sequist, , D. W. Bell, D. Irimia, L. Ulkus, and M. R. Smith. Isolation of rare circulating tumour cells in cancer patients by microchip technology. *Nature*, 450:1235–1239, 2007. doi: 10.1038/nature06385.

[176] A. Nam, A. Mohanty, S. Bhattacharya, S. Kotnala, S. Achuthan, K. Hari, and A. Nathan. Suppressing chemoresistance in lung cancer via dynamic phenotypic switching and intermittent therapy. *bioRxiv*, 2020. doi: 10.1101/2020.04.06.028472. URL https://www.biorxiv.org/content/early/2020/04/30/2020.04.06.028472.

[177] M. L. Neal, A. D. Trister, T. Cloke, R. Sodt, S. Ahn, A. L. Baldock, C. A. Bridge, A. Lai, T. F. Cloughesy, M. M. Mrugala, J. K. Rockhill, R. C. Rockne, and K. R. Swanson. Discriminating survival outcomes in patients with glioblastoma using a simulation-based, patient-specific response metric. *PLoS ONE*, 8(1):e51951, 2013.

[178] M. L. Neal, A. D. Trister, T. Cloke, R. Sodt, S. Ahn, A. L. Baldock, C. A. Bridge, A. Lai, T. F. Cloughesy, M. M. Mrugala, J. K. Rockhill, R. C. Rockne, and K. R. Swanson. Discriminating survival outcomes in patients with glioblastoma using a simulation-based, patient-specific response metric. *PLoS ONE*, 8(1):e51951, 2013.

[179] E. Neuhaus, L. Zirjacks, K. Ganser, L. Klumpp, U. Schüler, D. Zips, F. Eckert, and S. M. Huber. Alternating electric fields (ttfields) activate cav1.2 channels in human glioblastoma cells. *Cancers*, 11(1), 2019. ISSN 2072-6694. doi: 10.3390/cancers11010110. URL https://www.mdpi.com/2072-6694/11/1/110.

[180] H. T. Nia, L. L. Munn, and R. K. Jain. Physical traits of cancer. *Science*, 370(6516), 2020. ISSN 0036-8075. doi: 10.1126/science.aaz0868. URL https://science.sciencemag.org/content/370/6516/eaaz0868.

[181] X. Ning, Q. Zhu, Y. Lanir, and S. S. Margulies. A Transversely Isotropic Viscoelastic Constitutive Equation for Brainstem Undergoing Finite Deformation. *Journal of Biomechanical Engineering*, 128(6):925–933, 06 2006. ISSN 0148-0731. doi: 10.1115/1.2354208. URL https://doi.org/10.1115/1.2354208.

[182] N. I. Nissen, M. Karsdal, and N. Willumsen. Collagens and cancer associated fibroblasts in the reactive stroma and its relation to cancer biology. *Journal of Experimental & Clinical Cancer Research*, 38:115, 2019. doi: 10.1186/s13046-019-1110-6.

[183] J. Nitsche. Über ein variationsprinzip zur lösung von dirichlet-problemen bei verwendung von teilräumen, die keinen randbedingungen unterworfen sind. *Abhandlungen aus dem Mathematischen Seminar der Universität Hamburg*, 36: 9–15, 1971. doi: 10.1007/BF02995904.

[184] J. M. Northcott, I. S. Dean, J. K. Mouw, and V. M. Weaver. Feeling stress: The mechanics of cancer progression and aggression. *Frontiers in Cell and Developmental Biology*, 6:17, 2018. ISSN 2296-634X. doi: 10.3389/fcell.2018.00017.

[185] R. W. Ogden and R. Hill. Large deformation isotropic elasticity – on the correlation of theory and experiment for incompressible rubberlike solids. *Proceedings of the Royal Society of London. A. Mathematical and Physical Sciences*, 326(1567):565–584, 1972. doi: 10.1098/rspa.1972.0026. URL https://royalsocietypublishing.org/doi/abs/10.1098/rspa.1972.0026.

[186] A. Omuro and L. M. DeAngelis. Glioblastoma and other malignant gliomas: A clinical review. *JAMA*, 310(17): 1842–1850, 11 2013.

[187] E. Ortiz-Prado, J. F. Dunn, J. Vasconez, D. Castillo, and G. Viscor. Partial pressure of oxygen in the human body: a general review. *American journal of blood research*, 9(1):1–14, 2019. URL https://pubmed.ncbi.nlm.nih.gov/30899601.

[188] E. Ortiz-Prado, J. F. Dunn, J. Vasconez, D. Castillo, G. Viscor, F. Warner, and S. W. Zucker. Partial pressure of oxygen in the human body: a general review. *American journal of blood research*, 9(1):1–14, 2019.

[189] B. K. Owler, A. Pena, S. Momjian, Z. Czosnyka, M. Czosnyka, N. G. Harris, P. Smielewski, T. Fryer, T. Donvan, A. Carpenter, and J. D. Pickard. Changes in cerebral blood flow during cerebrospinal fluid pressure manipulation in patients with normal pressure hydrocephalus: A methodological study. *Journal of Cerebral Blood Flow & Metabolism*, 24(5):579–587, 2004. doi: 10.1097/00004647-200405000-00012. URL https://doi.org/10.1097/00004647-200405000-00012. PMID: 15129190.

[190] A. R. Padhani, K. A. Krohn, J. S. Lewis, and M. Alber. European radiology. *European Urology Focus*, 17:861–872, 2007. doi: https://doi.org/10.1007/s00330-006-0431-y.

[191] K. Painter and T. Hillen. Mathematical modelling of glioma growth: The use of diffusion tensor imaging (dti) data to predict the anisotropic pathways of cancer invasion. *Journal of Theoretical Biology*, 323:25–39, 2013. ISSN 0022-5193. doi: https://doi.org/10.1016/j.jtbi.2013.01.014. URL https://www.sciencedirect.com/science/article/pii/S0022519313000398.

[192] M. J. Paszek, N. Zahir, K. R. Johnson, J. N. Lakins, G. I. Rozenberg, A. Gefen, C. A. Reinhart-King, S. S. Margulies, M. Dembo, D. Boettiger, D. A. Hammer, and V. M. Weaver. Tensional homeostasis and the malignant phenotype. *Cancer cell*, 8:241–254, 2005.

[193] M. T. Prange and S. S. Margulies. Regional, Directional, and Age-Dependent Properties of the Brain Undergoing Large Deformation . *Journal of Biomechanical Engineering*, 124(2):244–252, 03 2002. ISSN 0148-0731. doi: 10.1115/1.1449907. URL https://doi.org/10.1115/1.1449907.

[194] I. Prionisti, L. H. Bühler, P. R. Walker, and R. B. Jolivet. Harnessing microglia and macrophages for the treatment of glioblastoma. *Frontiers in Pharmacology*, 10:506, 2019. ISSN 1663-9812. doi: 10.3389/fphar.2019.00506. URL https://www.frontiersin.org/article/10.3389/fphar.2019.00506.

[195] P. P. Provenzano and P. J. Keely. Mechanical signaling through the cytoskeleton regulates cell proliferation by coordinated focal adhesion and Rho GTPase signaling. *Journal of Cell Science*, 124(8):1195–1205, 04 2011. ISSN 0021-9533. doi: 10.1242/jcs.067009. URL https://doi.org/10.1242/jcs.067009.

[196] H. Rappel, L. Beex, L. Noels, and S. Bordas. Identifying elastoplastic parameters with bayes' theorem considering output error, input error and model uncertainty. *Probabilistic Engineering Mechanics*, 55:28–41, 2019. ISSN 0266-8920. doi: https://doi.org/10.1016/j.probengmech.2018.08.004. URL https://www.sciencedirect.com/science/article/pii/S0266892018300547.

[197] B. Rashid, M. Destrade, and M. D. Gilchrist. Mechanical characterization of brain tissue in compression at dynamic strain rates. *Journal of the Mechanical Behavior of Biomedical Materials*, 10:23–38, 2012. ISSN 1751-6161. doi: https://doi.org/10.1016/j.jmbbm.2012.01.022. URL https://www.sciencedirect.com/science/article/pii/S1751616112000744.

[198] P. Rawla, T. Sunkara, and A. Barsouk. Epidemiology of colorectal cancer: incidence, mortality, survival, and risk factors. *Gastroenterology Review/Przeglad Gastroenterologiczny*, 14(2):89–103, 2019. ISSN 1895-5770. doi: 10.5114/pg.2018.81072. URL http://dx.doi.org/10.5114/pg.2018.81072.

[199] P. Rawla, T. Sunkara, and V. Gaduputi. Epidemiology of pancreatic cancer: Global trends, etiology and risk factors. *World Journal of Oncology*, 10(1), 2019.

[200] A. J. Rice, E. Cortes, D. Lachowski, B. C. H. Cheung, S. A. Karim, J. P. Morton, and A. del Río Hernández. Matrix stiffness induces epithelial–mesenchymal transition and promotes chemoresistance in pancreatic cancer cells. *Oncogenesis*, 6:e352, 2017. doi: https://doi.org/10.1038/oncsis.2017.54.

[201] R. C. Rockne, A. D. Trister, J. Jacobs, A. J. Hawkins-Daarud, M. L. Neal, K. Hendrickson, M. M. Mrugala, J. K. Rockhill, P. Kinahan, K. A. Krohn, and K. R. Swanson. A patient-specific computational model of hypoxia-modulated radiation resistance in glioblastoma using (18)F-FMISO-PET. *J. R. Soc. Interface*, 12(103):20141174, 2015.

[202] R. C. Rockne, A. D. Trister, J. Jacobs, A. J. Hawkins-Daarud, M. L. Neal, K. Hendrickson, M. M. Mrugala, J. K. Rockhill, P. Kinahan, K. A. Krohn, and K. R. Swanson. A patient-specific computational model of hypoxia-modulated radiation resistance in glioblastoma using (18)F-FMISO-PET. *J. R. Soc. Interface*, 12(103):20141174, 2015.

[203] R. C. Rockne, A. Hawkins-Daarud, K. R. Swanson, J. P. Sluka, J. A. Glazier, P. Macklin, D. A. Hormuth, A. M. Jarrett, E. ABF. Lima, J. Tinsley Oden, G. Biros, T. E. Yankeelov, K. Curtius, I. Al Bakir, D. Wodarz, N. Komarova, L. Aparicio, M. Bordyuh, R. Rabadan, S. D. Finley, H. Enderling, J. Caudell, E. G. Moros, A. RA. Anderson, R. A. Gatenby, A. Kaznatcheev, P. Jeavons, N. Krishnan, J. Pelesko, R. R. Wadhwa, N. Yoon, D. Nichol, A. Marusyk, M. Hinczewski, and J. G. Scott. The 2019 mathematical oncology roadmap. *Phys. Biol.*, 16(4):41005, 2019.

[204] A. Rolong, R. V. Davalos, and B. Rubinsky. *History of Electroporation*, pages 13–37. Springer International Publishing, Cham, 2018. ISBN 978-3-319-55113-5. doi: 10.1007/978-3-319-55113-5_2. URL https://doi.org/10.1007/978-3-319-55113-5_2.

[205] M. A. F. Rueda, L. Cui, and M. D. Gilchrist. Finite element modelling of equestrian helmet impacts exposes the need to address rotational kinematics in future helmet designs. *Computer Methods in Biomechanics and Biomedical Engineering*, 14(12):1021–1031, 2011. doi: 10.1080/10255842.2010.504922. URL https://doi.org/10.1080/10255842.2010.504922. Publisher: Taylor & Francis _eprint: https://doi.org/10.1080/10255842.2010.504922.

[206] B. Rybinski, J. Franco-Barraza, and E. Cukierman. The wound healing, chronic fibrosis, and cancer progression triad. *Physiological Genomics*, 46(7):223–244, 2014. doi: 10.1152/physiolgenomics.00158.2013. PMID: 24520152.

[207] N. S, L. M, and W. R. Shear properties of brain tissue over a frequency range relevant for automotive impact situations: new experimental results. *Stapp car crash journal*, pages 239–258, 11 2004.

[208] H. Sabelström, D. A. Quigley, T. Fenster, D. J. Foster, C. A. Fuchshuber, S. Saxena, E. Yuan, N. Li, F. Paterno, J. J. Phillips, C. D. James, B. Norling, M. S. Berger, and A. I. Persson. High density is a property of slow-cycling and treatment-resistant human glioblastoma cells. *Experimental Cell Research*, 378(1):76–86, 2019. ISSN 0014-4827. doi: https://doi.org/10.1016/j.yexcr.2019.03.003. URL `https://www.sciencedirect.com/science/article/pii/S0014482719300916`.

[209] F. Saeg and M. Anbalagan. Breast cancer stem cells and the challenges of eradication: a review of novel therapies. *Stem Cell Investigation*, 5, 2018.

[210] A. Saltelli, P. Annoni, I. Azzini, F. Campolongo, M. Ratto, and S. Tarantola. Variance based sensitivity analysis of model output. design and estimator for the total sensitivity index. *Computer Physics Communications*, 181(2):259–270, 2010. ISSN 0010-4655. doi: https://doi.org/10.1016/j.cpc.2009.09.018. URL `https://www.sciencedirect.com/science/article/pii/S0010465509003087`.

[211] R. Santagiuliana, M. Milosevic, B. Milicevic, G. Sciumè, V. Simic, A. Ziemys, M. Kojic, and B. A. Schrefler. Coupling tumor growth and bio distribution models. *Biomedical microdevices*, 21, 2019.

[212] P. Schiavone, F. Chassat, T. Boudou, E. Promayon, F. Valdivia, and Y. Payan. In vivo measurement of human brain elasticity using a light aspiration device. *Medical Image Analysis*, 13(4):673 – 678, 2009. ISSN 1361-8415. doi: https://doi.org/10.1016/j.media.2009.04.001.

[213] N. Schlömer, A. Cervone, G. McBain, tryfon mw, R. van Staden, and F. Gokstorp. nschloe/pygmsh v6.1.1, Apr. 2020. URL `https://doi.org/10.5281/zenodo.3764683`.

[214] G. Sciumè, S. Shelton, W. G. Gray, C. T. Miller, F. Hussain, M. Ferrari, P. Decuzzi, and B. A. Schrefler. A multiphase model for three-dimensional tumor growth. *New Journal of Physics*, 15(1):015005, jan 2013.

[215] G. Sciumè, W. G. Gray, F. Hussain, M. Ferrari, P. Decuzzi, and B. A. Schrefler. Three phase flow dynamics in tumor growth. *Computational Mechanics*, 53(3):465–484, 2014.

[216] G. Sciumè, R. Santagiuliana, M. Ferrari, P. Decuzzi, and B. A. Schrefler. A tumor growth model with deformable ecm. *Physical biology*, 11(6), 2014.

[217] G. Sciumè. Mechanistic modeling of vascular tumor growth: an extension of biot's theory to hierarchical bi-compartment porous medium systems. *Acta Mechanica*, 232:1445–1478, 2021. doi: https://doi.org/10.1007/s00707-020-02908-z.

[218] G. Sciumè, D. P. Boso, W. G. Gray, C. Cobelli, and B. A. Schrefler. A two-phase model of plantar tissue: a step toward prediction of diabetic foot ulceration. *International Journal for Numerical Methods in Biomedical Engineering*, 30(11):1153–1169, 2014. URL `https://onlinelibrary.wiley.com/doi/abs/10.1002/cnm.2650`.

[219] G. Sciumè, M. Ferrari, and B. A. Schrefler. Saturation–pressure relationships for two- and three-phase flow analogies for soft matter. *Mechanics Research Communications*, 62:132–137, 2014. ISSN 0093-6413. doi: https://doi.org/10.1016/j.mechrescom.2014.10.001. URL https://www.sciencedirect.com/science/article/pii/S009364131400130X.

[220] G. Sciumè, M. Ferrari, and B. A. Schrefler. Saturation–pressure relationships for two- and three-phase flow analogies for soft matter. *Mechanics Research Communications*, 62:132 – 137, 2014. ISSN 0093-6413. doi: https://doi.org/10.1016/j.mechrescom.2014.10.001.

[221] H. Seo, D. Kim, and S. C. Jun. Effect of Anatomically Realistic Full-Head Model on Activation of Cortical Neurons in Subdural Cortical Stimulation-A Computational Study. *Scientific reports*, 6:27353–27353, June 2016. ISSN 2045-2322. doi: 10.1038/srep27353. URL https://pubmed.ncbi.nlm.nih.gov/27273817. Publisher: Nature Publishing Group.

[222] F. A. Shaikh, B. J. Kolowitz, O. Awan, H. J. Aerts, A. von Reden, S. Halabi, S. A. Mohiuddin, S. Malik, R. B. Shrestha, and C. Deible. Technical challenges in the clinical application of radiomics. *JCO Clinical Cancer Informatics*, (1):1–8, 2017. doi: 10.1200/CCI.17.00004. URL https://doi.org/10.1200/CCI.17.00004. PMID: 30657374.

[223] Q. Shao, S. O'Flanagan, T. Lam, P. Roy, F. Pelaez, B. J. Burbach, S. M. Azarin, Y. Shimizu, and J. C. Bischof. Engineering t cell response to cancer antigens by choice of focal therapeutic conditions. *International Journal of Hyperthermia*, 36(1):130–138, 2019. doi: 10.1080/02656736.2018.1539253. URL https://doi.org/10.1080/02656736.2018.1539253. PMID: 30676126.

[224] J. Sherriff, J. Tamangani, L. Senthil, G. Cruickshank, D. Spooner, B. Jones, C. Brookes, and P. Sanghera. Patterns of relapse in glioblastoma multiforme following concomitant chemoradiotherapy with temozolomide. *The British Journal of Radiology*, 86(1022):20120414, 2013. doi: 10.1259/bjr.20120414. URL https://doi.org/10.1259/bjr.20120414. PMID: 23385995.

[225] A. Shetty and M. Saber. Positron emission tomography. https://radiopaedia.org/articles/29716, 2021. URL https://radiopaedia.org/articles/29716.

[226] A. D. C. Smith, W. R. Crum, D. L. G. Hill, N. A. Thacker, and P. A. Bromiley. Biomechanical simulation of atrophy in MR images. In M. Sonka and J. M. Fitzpatrick, editors, *Medical Imaging 2003: Image Processing*, volume 5032, pages 481 – 490. International Society for Optics and Photonics, SPIE, 2003. doi: 10.1117/12.480412. URL https://doi.org/10.1117/12.480412.

[227] M. A. Smith, N. L. Seibel, S. F. Altekruse, L. A. Ries, D. L. Melbert, M. O'Leary, F. O. Smith, and G. H. Reaman. Outcomes for children and adolescents with cancer: Challenges for the twenty-first century. *Journal of Clinical Oncology*, 28(15):2625–2634, 2010. doi: 10.1200/JCO.2009.27.0421. PMID: 20404250.

[228] I. Sobey, A. Eisentraeger, B. Wirth, and M. Czosnyka. Simulation of cerebral infusion tests using a poroelastic model. *International Journal of Numerical Analysis and Modeling, Series B*, 3:52–64, 01 2012.

[229] A. G. Sorace, C. Wu, S. L. Barnes, A. M. Jarrett, S. Avery, D. Patt, B. Goodgame, J. J. Luci, H. Kang, R. G. Abramson, T. E. Yankeelov, and J. Virostko. Repeatability, reproducibility, and accuracy of quantitative MRI of the breast in the community radiology setting. *J. Magn. Reson. Imaging*, 48(3):695–707, 2018.

[230] D. R. Sowinski, M. D. J. McGarry, E. E. W. Van Houten, S. Gordon-Wylie, J. B. Weaver, and K. D. Paulsen. Poroelasticity as a model of soft tissue structure: Hydraulic permeability reconstruction for magnetic resonance elastography in silico. *Frontiers in Physics*, 8:637, 2021. ISSN 2296-424X. doi: 10.3389/fphy.2020.617582. URL https://www.frontiersin.org/article/10.3389/fphy.2020.617582.

[231] E. Stein, R. de Borst, and T. J. R. Hughes. *Encyclopedia of Computational Mechanics, Vol. 1*. Wiley, 2017. ISBN 978-1-119-00379-3.

[232] S. L. Stott, C.-H. Hsu, D. I. Tsukrov, M. Yu, D. T. Miyamoto, B. A. Waltman, and S. M. Rothenberg. Isolation of circulating tumor cells using a microvortex-generating herringbone-chip. *Proceedings of the National Academy of Sciences*, 107(43):18392–18397, 2010. ISSN 0027-8424. doi: 10.1073/pnas.1012539107. URL https://www.pnas.org/content/107/43/18392.

[233] R. Stupp, W. P. Mason, M. J. van den Bent, M. Weller, B. Fisher, M. J. Taphoorn, K. Belanger, A. A. Brandes, C. Marosi, U. Bogdahn, J. Curschmann, R. C. Janzer, S. K. Ludwin, T. Gorlia, A. Allgeier, D. Lacombe, J. G. Cairncross, E. Eisenhauer, and R. O. Mirimanoff. Radiotherapy plus concomitant and adjuvant temozolomide for glioblastoma. *New England Journal of Medicine*, 352(10):987–996, 2005. doi: 10.1056/NEJMoa043330. URL https://doi.org/10.1056/NEJMoa043330. PMID: 15758009.

[234] R. Stupp, S. Taillibert, A. Kanner, W. Read, D. M. Steinberg, B. Lhermitte, S. Toms, A. Idbaih, and M. S. Ahluwalia. Effect of Tumor-Treating Fields Plus Maintenance Temozolomide vs Maintenance Temozolomide Alone on Survival in Patients With Glioblastoma: A Randomized Clinical Trial. *JAMA*, 318(23):2306–2316, 12 2017. ISSN 0098-7484. doi: 10.1001/jama.2017.18718.

[235] T. Stylianopoulos, J. D. Martin, M. Snuderl, F. Mpekris, S. R. Jain, and R. K. Jain. Coevolution of solid stress and interstitial fluid pressure in tumors during progression: Implications for vascular collapse. *Cancer Research*, 73(13):3833–3841, 2013. ISSN 0008-5472. doi: 10.1158/0008-5472.CAN-12-4521. URL https://cancerres.aacrjournals.org/content/73/13/3833.

[236] R. Stämpfli and M. Willi. Membrane potential of a ranvier node measured after electrical destruction of its membrane. *Experientia*, 13:297–298, 1957. doi: 10.1007/BF02158430.

[237] P. Suetens. *Fundamentals of Medical Imaging*. Cambridge University Press, 2 edition, 2009. doi: 10.1017/CBO9780511596803.

[238] H. Sung, J. Ferlay, R. L. Siegel, M. Laversanne, I. Soerjomataram, A. Jemal, and F. Bray. Global cancer statistics 2020: Globocan estimates of incidence and mortality worldwide for 36 cancers in 185 countries. *CA: A Cancer Journal for Clinicians*. doi: https://doi.org/10.3322/caac.21660.

[239] K. R. Swanson, E. C. Alvord, and J. D. Murray. Virtual brain tumours (gliomas) enhance the reality of medical imaging and highlight inadequacies of current therapy. *British Journal of Cancer*, 86:14–18, 2002. doi: 10.1038/sj.bjc.6600021.

[240] K. R. Swanson, R. C. Rostomily, and E. C. Alvord. A mathematical modelling tool for predicting survival of individual patients following resection of glioblastoma: A proof of principle. *Br. J. Cancer*, 98(1):113–119, 2008.

[241] A. C. Tan, D. M. Ashley, G. Y. López, M. Malinzak, H. S. Friedman, and M. Khasraw. Management of glioblastoma: State of the art and future directions. *CA: A Cancer Journal for Clinicians*, 70(4):299–312, 2020. doi: https://doi.org/10.3322/caac.21613. URL `https://acsjournals.onlinelibrary.wiley.com/doi/abs/10.3322/caac.21613`.

[242] I. M. Thompson, P. J. Goodman, C. M. Tangen, M. S. Lucia, G. J. Miller, L. G. Ford, M. M. Lieber, R. D. Cespedes, J. N. Atkins, S. M. Lippman, S. M. Carlin, A. Ryan, C. M. Szczepanek, J. J. Crowley, and C. A. Coltman. The influence of finasteride on the development of prostate cancer. *N. Engl. J. Med.*, 349(3):215–224, 2003. PMID: 12824459.

[243] A. Trushko, I. Di Meglio, A. Merzouki, C. Blanch-Mercader, S. Abuhattum, J. Guck, K. Alessandri, P. Nassoy, K. Kruse, B. Chopard, and A. Roux. Buckling of an epithelium growing under spherical confinement. *Developmental Cell*, 54:655–668, 2020. doi: 10.1016/j.devcel.2020.07.019.

[244] D. S. Tuch, V. J. Wedeen, A. M. Dale, J. S. George, and J. W. Belliveau. Conductivity tensor mapping of the human brain using diffusion tensor mri. *Proceedings of the National Academy of Sciences*, 98(20):11697–11701, 2001. ISSN 0027-8424. doi: 10.1073/pnas.171473898. URL `https://www.pnas.org/content/98/20/11697`.

[245] T. A. Ulrich, E. M. de Juan Pardo, and S. Kumar. The mechanical rigidity of the extracellular matrix regulates the structure, motility, and proliferation of glioma cells. *Cancer Research*, 69(10):4167–4174, 2009. doi: 10.1158/0008-5472.CAN-08-4859.

[246] J. Unkelbach, B. H. Menze, E. Konukoglu, F. Dittmann, N. Ayache, and H. A. Shih. Radiotherapy planning for glioblastoma based on a tumor growth model: implications for spatial dose redistribution. *Physics in Medicine and Biology*, 59(3):771–789, jan 2014. doi: 10.1088/0031-9155/59/3/771. URL `https://doi.org/10.1088/0031-9155/59/3/771`.

[247] S. Urcun, P.-Y. Rohan, W. Skalli, P. Nassoy, S. P. A. Bordas, and G. Sciumè. Digital twinning of cellular capsule technology: Emerging outcomes from the perspective of porous media mechanics. *PLOS ONE*, 16(7):1–30, 07 2021. doi: 10.1371/journal.pone.0254512. URL https://doi.org/10.1371/journal.pone.0254512.

[248] S. Urcun, P.-Y. Rohan, G. Sciumè, and S. P. Bordas. Cortex tissue relaxation and slow to medium load rates dependency can be captured by a two-phase flow poroelastic model. *Journal of the Mechanical Behavior of Biomedical Materials*, 126:104952, 2022. ISSN 1751-6161. doi: https://doi.org/10.1016/j.jmbbm.2021.104952. URL https://www.sciencedirect.com/science/article/pii/S175161612100583X.

[249] R. C. van den Bergh, S. Loeb, and M. J. Roobol. Impact of early diagnosis of prostate cancer on survival outcomes. *European Urology Focus*, 1:137–146, 2015. doi: 10.1016/j.euf.2015.01.002.

[250] M. T. van Genuchten. A closed-form equation for predicting the hydraulic conductivity of unsaturated soils. *Soil Science Society of America Journal*, 44(5):892–898, 1980. doi: https://doi.org/10.2136/sssaj1980.03615995004400050002x. URL https://acsess.onlinelibrary.wiley.com/doi/abs/10.2136/sssaj1980.03615995004400050002x.

[251] S. Varrette, P. Bouvry, H. Cartiaux, and F. Georgatos. Management of an academic hpc cluster: The ul experience. In *2014 International Conference on High Performance Computing Simulation (HPCS)*, pages 959–967, 2014. doi: 10.1109/HPCSim.2014.6903792.

[252] V. Vavourakis, B. Eiben, J. H. Hipwell, N. R. Williams, M. Keshtgar, and D. J. Hawkes. Multiscale mechano-biological finite element modelling of oncoplastic breast surgery—numerical study towards surgical planning and cosmetic outcome prediction. *PLOS One*, 11(7):e0159766, 2016.

[253] A. Verruijt. *Theory and Problems of Poroelasticity*. 2013. URL https://geo.verruijt.net/.

[254] P. Villalobos and I. I. Wistuba. Lung cancer biomarkers. *Hematology/Oncology Clinics of North America*, 31(1):13–29, 2017. ISSN 0889-8588. doi: https://doi.org/10.1016/j.hoc.2016.08.006. URL https://www.sciencedirect.com/science/article/pii/S0889858816301204. Lung Cancer.

[255] C. H. Wang, J. K. Rockhill, M. Mrugala, D. L. Peacock, A. Lai, K. Jusenius, J. M. Wardlaw, T. Cloughesy, A. M. Spence, R. Rockne, E. C. Alvord, and K. R. Swanson. Prognostic significance of growth kinetics in newly diagnosed glioblastomas revealed by combining serial imaging with a novel biomathematical model. *Cancer Res.*, 69(23):9133–9140, 2009.

[256] V. Weaver, O. Petersen, F. Wang, C. Larabell, P. Briand, C. Damsky, and M. Bissell. Reversion of the Malignant Phenotype of Human Breast Cells in Three-Dimensional Culture and In Vivo by Integrin Blocking Antibodies. *Journal of Cell Biology*, 137(1):231–245, 04 1997. ISSN 0021-9525. doi: 10.1083/jcb.137.1.231. URL https://doi.org/10.1083/jcb.137.1.231.

[257] A. J. Wein, L. R. Kavoussi, A. C. Novick, A. W. Partin, and C. A. Peters. *Campbell-Walsh Urology: Expert Consult Premium Edition: Enhanced Online Features and Print, 4-Volume Set*. Elsevier Saunders, 10th edition, 2012.

[258] J. A. Weis, M. I. Miga, L. R. Arlinghaus, X. Li, A. B. Chakravarthy, V. Abramson, J. Farley, and T. E. Yankeelov. A mechanically coupled reaction-diffusion model for predicting the response of breast tumors to neoadjuvant chemotherapy. *Phys. Med. Biol.*, 58(17):5851–5866, 2013.

[259] J. A. Weis, M. I. Miga, L. R. Arlinghaus, X. Li, V. Abramson, A. B. Chakravarthy, P. Pendyala, and T. E. Yankeelov. Predicting the response of breast cancer to neoadjuvant therapy using a mechanically coupled reaction–diffusion model. *Cancer Research*, 75(22):4697–4707, 2015. ISSN 0008-5472. doi: 10.1158/0008-5472.CAN-14-2945. URL https://cancerres.aacrjournals.org/content/75/22/4697.

[260] J. A. Weis, M. I. Miga, and T. E. Yankeelov. Three-dimensional image-based mechanical modeling for predicting the response of breast cancer to neoadjuvant therapy. *Computer Methods in Applied Mechanics and Engineering*, 314:494–512, 2017. ISSN 0045-7825. doi: https://doi.org/10.1016/j.cma.2016.08.024. Special Issue on Biological Systems Dedicated to William S. Klug.

[261] J. G. Whisenant, G. D. Ayers, M. E. Loveless, S. L. Barnes, D. C. Colvin, and T. E. Yankeelov. Assessing reproducibility of diffusion-weighted magnetic resonance imaging studies in a murine model of HER2+ breast cancer. *Magn. Reson. Imaging*, 32(3):245–249, 2014.

[262] A. Wittek, T. Hawkins, and K. Miller. On the unimportance of constitutive models in computing brain deformation for image-guided surgery. *Biomechanics and modeling in mechanobiology*, 8:77–84, 2009. doi: 10.1007/s10237-008-0118-1.

[263] K. C. L. Wong, R. M. Summers, E. Kebebew, and J. Yoa. Pancreatic tumor growth prediction with elastic-growth decomposition, image-derived motion, and FDM-FEM coupling. *IEEE Trans. Med. Imaging*, 36(1):111–123, 2017.

[264] C. Wu, F. Pineda, D. A. Hormuth II, G. S. Karczmar, and T. E. Yankeelov. Quantitative analysis of vascular properties derived from ultrafast DCE-MRI to discriminate malignant and benign breast tumors. *Magn. Reson. Med.*, 81(3):2147–2160, 2019.

[265] W. Xing, M. Yin, Q. Lv, Y. Hu, C. Liu, and J. Zhang. 1 - oxygen solubility, diffusion coefficient, and solution viscosity. In W. Xing, G. Yin, and J. Zhang, editors, *Rotating Electrode Methods and Oxygen Reduction Electrocatalysts*, pages 1–31. Elsevier, Amsterdam, 2014. ISBN 978-0-444-63278-4. doi: https://doi.org/10.1016/B978-0-444-63278-4.00001-X. URL https://www.sciencedirect.com/science/article/pii/B978044463278400001X.

[266] W.-k. Xing, C. Shao, Z.-y. Qi, C. Yang, and Z. Wang. The role of Gliadel wafers in the treatment of newly diagnosed GBM: a meta-analysis. *Drug design, development and therapy*, 9:3341–3348, 2015. doi: 10.2147/DDDT.S85943.

[267] T. E. Yankeelov and J. C. Gore. Dynamic contrast enhanced magnetic resonance imaging in oncology: theory, data acquisition, analysis, and examples. *Curr. Med. Imaging Rev.*, 3(2):91–107, 2007.

[268] T. E. Yankeelov, N. Atuegwu, D. Hormuth, J. A. Weis, S. L. Barnes, M. I. Miga, E. C. Rericha, and V. Quaranta. Clinically relevant modeling of tumor growth and treatment response. *Science Translational Medicine*, 5(187), 2013. doi: 10.1126/scitranslmed.3005686.

[269] O. Yeoh. Some forms of the strain energy function for rubber. *Rubber Chemistry and Technology*, 66:754–771, 1993.

[270] M. Yu, A. Mahtabfar, P. Beelen, Y. Demiryurek, D. I. Shreiber, J. D. Zahn, R. A. Foty, L. Liu, and H. Lin. Coherent timescales and mechanical structure of multicellular aggregates. *Biophysical Journal*, 114:2703–2716, 2018. doi: doi:10.1016/j.bpj.2018.04.025.

[271] F. Zaccagna, F. Riemer, A. N. Priest, M. A. McLean, K. Allinson, J. T. Grist, C. Dragos, T. Matys, J. H. Gillard, C. Watts, S. J. Price, M. J. Graves, and F. A. Gallagher. Non-invasive assessment of glioma microstructure using verdict mri: correlation with histology. *European Radiology*, 29:5559–5566, 2019. doi: https://doi.org/10.1007/s00330-019-6011-8.

[272] D. Zardavas and M. Piccart. Neoadjuvant therapy for breast cancer. *Annu. Rev. Med.*, 66(1):31–48, 2015.

[273] M. Zeraatpisheh, S. P. Bordas, and L. A. Beex. Bayesian model uncertainty quantification for hyperelastic soft tissue models. *Data-Centric Engineering*, 2:e9, 2021. doi: 10.1017/dce.2021.9.

[274] Y. Zhang, M. Brady, and S. Smith. Segmentation of brain mr images through a hidden markov random field model and the expectation-maximization algorithm. *IEEE Transactions on Medical Imaging*, 20(1):45–57, 2001. doi: 10.1109/42.906424.

[275] Y. J. Zhang. *Geometric Modeling and Mesh Generation from Scanned Images*. Chapman & Hall/CRC Mathematical and Computational Imaging Sciences Series. CRC Press, 2018.

[276] H. Zong, L. F. Parada, and S. J. Baker. Cell of origin for malignant gliomas and its implication in therapeutic development. *Cold Spring Harbor Perspectives in Biology*, 7(5), 2015. doi: 10.1101/cshperspect.a020610. URL http://cshperspectives.cshlp.org/content/7/5/a020610.abstract.

Titre: Mécano-biologie de la croissance tumorale orientée vers l'application clinique, une approche poromécanique multiphase réactive

Mots clés: Mécano-biologie, Oncologie, Poromécanique

Résumé: Nous proposons une modélisation du glioblastome isocitrate déhydrogénase type naturel (GBMtn) bâtie sur les hypothèse suivantes : le tissu cérébral est un milieu poreux, le couplage des conséquences de l'hypoxie et des interactions mécaniques entre les cellules tumorales et la matrice extra-cellulaire est le phénomène gouvernant de l'évolution maligne de la maladie. Une revue de littérature, avec un spectre large, a été faite sur les applications de la mécanique dans la gestion clinique du cancer. Le modèle a d'abord été validé sur des expériences in vitro d'encapsulation de sphéroides multi-cellulaires. Ensuite, une collaboration clinique a été initiée avec le centre de neuro-imagerie de Toulouse, et la cible de la modélisation a été définie comme étant les cas de GBMtn non-opérables. Dans ce but, le modèle a été au préalable adapté aux spécificités de la mécanique du tissu cérébral. Les caractéristiques de la maladie ont été modélisées : le cœur nécrotique, la production altérée de matrice extra-cellulaire, l'émergence d'un phénotype malin et l'invasion. Les données d'imagerie clinique ont été pré-traitées pour informer le modèle sur une base spécifique au patient. Une proposition de modélisation est fournie et évaluée au regard des données cliniques.

Title: Mechano-biology of tumor growth with the aim of clinical applications, a reactive multiphase poromechanical approach

Keywords: Mechano-biology, Oncology, Poromechanics

Abstract: We propose the modeling of glioblastoma isocitrate dehydrogenase wild-type (GBMwt) build on the following hypotheses: the brain tissue is a porous medium, the coupling of hypoxia consequences and mechanical interplay between extra-cellular matrix and tumor cells is the driver of the malignant evolution of the disease. In this thesis, a poromechanical model is developed with the aim of a clinical application in oncology. A review, with a large scope, is done on mechanical applications in clinical management of cancer. The model is first validated on in vitro experimental data of encapsulated multi-cellular spheroids. Then, a clinical collaboration is initiated with the Neuro-imaging center of Toulouse, and the targeted clinical application is the modeling of non-operable GBMwt. To this end, the model is first adapted to the specificity of brain tissue mechanics. Characteristic features of the disease are modeled: necrotic core, modified extra-cellular matrix production, emerging malignant phenotype and invasion. Clinical imaging data are pre-treated to inform the model in a patient specific basis. A proposition of modeling is provided with an evaluation against clinical data.